Modelling of urban micro-climates forbuilding applications : A non-transparentradiative transfer approach

Feng Wang

N°d'ordre NNT : 2021LYSEI013

THESE de DOCTORAT DE L'UNIVERSITE DE LYON
opérée au sein de
INSA LYON

Ecole Doctorale N° ED162
Mécanique, Energétique, Génie civil et Acoustique

Spécialité de doctorat : Thermique énergétique

Soutenue publiquement le 19/02/2021, par :
Feng WANG

Modelling of urban micro-climates for building applications:a non-transparent radiative transfer approach

---

Devant le jury composé de :

MUSY, Marjorie	Directrice de recherche	Rapportrice
LEMONNIER, Denis	Directeur de recherche	Rapporteur
MENEZO, Christophe	Professeur des Universités	Examinateur
KUZNIK, Frédéric	Professeur des Universités	Directeur de thèse
VERGNAULT, Etienne	Maître de conférences	Co-directeur de thèse
ANDRE, Frédéric	Directeur de recherche	Co-directeur de thèse
BOUQUEREL, Mathias	Ingénieur chercheur	Invité

Département FEDORA – INSA Lyon - Ecoles Doctorales – Quinquennal 2016-2020

SIGLE	ECOLE DOCTORALE	NOM ET COORDONNEES DU RESPONSABLE
CHIMIE	**CHIMIE DE LYON** http://www.edchimie-lyon.fr Sec. : Renée EL MELHEM Bât. Blaise PASCAL, 3e étage secretariat@edchimie-lyon.fr INSA : R. GOURDON	**M. Stéphane DANIELE** Institut de recherches sur la catalyse et l'environnement de Lyon IRCELYON-UMR 5256 Équipe CDFA 2 Avenue Albert EINSTEIN 69 626 Villeurbanne CEDEX directeur@edchimie-lyon.fr
E.E.A.	**ÉLECTRONIQUE, ÉLECTROTECHNIQUE, AUTOMATIQUE** http://edeea.ec-lyon.fr Sec. : M.C. HAVGOUDOUKIAN ecole-doctorale.eea@ec-lyon.fr	**M. Gérard SCORLETTI** École Centrale de Lyon 36 Avenue Guy DE COLLONGUE 69 134 Écully Tél : 04.72.18.60.97 Fax 04.78.43.37.17 gerard.scorletti@ec-lyon.fr
E2M2	**ÉVOLUTION, ÉCOSYSTÈME, MICROBIOLOGIE, MODÉLISATION** http://e2m2.universite-lyon.fr Sec. : Sylvie ROBERJOT Bât. Atrium, UCB Lyon 1 Tél : 04.72.44.83.62 INSA : H. CHARLES secretariat.e2m2@univ-lyon1.fr	**M. Philippe NORMAND** UMR 5557 Lab. d'Ecologie Microbienne Université Claude Bernard Lyon 1 Bâtiment Mendel 43, boulevard du 11 Novembre 1918 69 622 Villeurbanne CEDEX philippe.normand@univ-lyon1.fr
EDISS	**INTERDISCIPLINAIRE SCIENCES-SANTÉ** http://www.ediss-lyon.fr Sec. : Sylvie ROBERJOT Bât. Atrium, UCB Lyon 1 Tél : 04.72.44.83.62 INSA : M. LAGARDE secretariat.ediss@univ-lyon1.fr	**Mme Sylvie RICARD-BLUM** Institut de Chimie et Biochimie Moléculaires et Supramoléculaires (ICBMS) - UMR 5246 CNRS - Université Lyon 1 Bâtiment Curien - 3ème étage Nord 43 Boulevard du 11 novembre 1918 69622 Villeurbanne Cedex Tel : +33(0)4 72 44 82 32 sylvie.ricard-blum@univ-lyon1.fr
INFOMATHS	**INFORMATIQUE ET MATHÉMATIQUES** http://edinfomaths.universite-lyon.fr Sec. : Renée EL MELHEM Bât. Blaise PASCAL, 3e étage Tél : 04.72.43.80.46 infomaths@univ-lyon1.fr	**M. Hamamache KHEDDOUCI** Bât. Nautibus 43, Boulevard du 11 novembre 1918 69 622 Villeurbanne Cedex France Tel : 04.72.44.83.69 hamamache.kheddouci@univ-lyon1.fr
Matériaux	**MATÉRIAUX DE LYON** http://ed34.universite-lyon.fr Sec. : Stéphanie CAUVIN Tél : 04.72.43.71.70 Bât. Direction ed.materiaux@insa-lyon.fr	**M. Jean-Yves BUFFIÈRE** INSA de Lyon MATEIS - Bât. Saint-Exupéry 7 Avenue Jean CAPELLE 69 621 Villeurbanne CEDEX Tél : 04.72.43.71.70 Fax : 04.72.43.85.28 jean-yves.buffiere@insa-lyon.fr
MEGA	**MÉCANIQUE, ÉNERGÉTIQUE, GÉNIE CIVIL, ACOUSTIQUE** http://edmega.universite-lyon.fr Sec. : Stéphanie CAUVIN Tél : 04.72.43.71.70 Bât. Direction mega@insa-lyon.fr	**M. Jocelyn BONJOUR** INSA de Lyon Laboratoire CETHIL Bâtiment Sadi-Carnot 9, rue de la Physique 69 621 Villeurbanne CEDEX jocelyn.bonjour@insa-lyon.fr
ScSo	**ScSo*** http://ed483.univ-lyon2.fr Sec. : Véronique GUICHARD INSA : J.Y. TOUSSAINT Tél : 04.78.69.72.76 veronique.cervantes@univ-lyon2.fr	**M. Christian MONTES** Université Lyon 2 86 Rue Pasteur 69 365 Lyon CEDEX 07 christian.montes@univ-lyon2.fr

*ScSo : Histoire, Géographie, Aménagement, Urbanisme, Archéologie, Science politique, Sociologie, Anthropologie

Acknowledgement

First of all, I want to express my thanks to my family members for their support during my 28 years life. Since 2010 when I arrived in France for the first time, they have been encouraged and motivated me in my study and daily life. Without their support, there could be no chance for me to become a PhD student. Especially for my Mum and Dad who dedicate half of their lives to educate me and lead me into the right direction.

At the same time, I really appreciate the help of my best friend Shaoran WANG and Weiyang ZHAO. Although our communication has become less than before because of the different countries we live in, you are still my best friend. Thanks very much for the talks, which helps me a lot to come over my frustration during the last 10 years.

I would also like to thank my supervisors of the thesis: M.Étienne VERGNAULT, with whom I get along for the longest time since 2013, thank you very much for your course during my bachelor and master degree. Also without you I would not get the chance for this thesis. M.Frédéric KUZNIK,the director of my thesis, who has been my professor since my master degree, thank you very much for your kind advise and patience to lead me when I could not find a direction. Thank you for giving me this opportunity to become a PhD student. For M.Frédéric ANDRE, even if you joined my thesis in the second year, your aid on the 'air characteristic' and 'discrete ordinates method' are extremely import for my thesis. Your patient interpretation helps me a lot for this thesis. Once again, for all of my advisors, my deepest thanks for your valuable advises and discussion to lead me finishing my thesis.

I am also grateful to M.BOUQUEREL Mathias who helped me at the application software HélioBIM. At the same time, your advises during our discussion and for my scientific paper helps me a a lot. MERLIER Lucie, who kindly and patiently introduce the acknowledgement of microclimate modelling at the beginning of the thesis.RAYBAUD Blaise, who is also a PhD student for its patience on communicating with me. Your works on radiation part provide an important benchmark for me. I really enjoy working with you.

Also my gratefulness to the laboratory CETHIL, CNRS and EDF. Without their support this project even wont existed. Thanks for all the members in laboratory CETHIL for their warm welcoming during the last three years. Especially for DUSSOUILLEZ Julie and LUCCHESI Christophe with whom I shared the office for the most of the time. Thanks for your help in all matters during the three year. I will always remember the time we spent in the office 315B.

Warmest thanks to the IUT of Saint Nazaire and UCBL. The three year I spent in Saint Nazaire is still in my memory. Thanks for teaching me in my speciality and French cultural to help me to adapt my life in French. For the UCBL, thanks a lot for the bachelor and master curriculum which helps me to get my master degree, which is essential for my thesis.

Last but not the least, I would like to express my thanks to the jury to give me an opportunity to discuss my PhD work. It is my honor to have you participated on my jury. Your comments and advise will be important for me to become a real researcher in science.

2020 is the tenth year I spend in France. It means a third of my life is highly related to this country. I still remember the day when I decided to go to France for the University Education. To be frank, I never excepted to go this far like today. From a child who knew nothing about French language and culture, to a man who can communicate with French fluently(almost), from a middle school student who did not have a conception about thermal energy, to a PhD student who is becoming a researcher in this field, my experience in France has offered me too much, too much from what I expected. I do not know whether it will be an end for my life in France, as I always expect to work with these kind people for longer. But even it does, this ten years life will be my treasure that always be kept in mind. At last, I want to thanks again for all the kind people I encountered in the last ten years, it is my pleasure and honor to meet up with you. Thank you very much!

Abstract

Urbanisation has been a growing trend for several decades. With the rapidly increasing population, urban areas expand significantly. At the same time, problems related to a higher energy demand and local climate changes have been disturbing the entire humankind. During the last two decades, thermal regulation has been well developed in France for all the new constructions, as well as for building retrofit. The objectives are to reduce the energy consumption principally due to heating and to increase the building thermal comfort especially in Summer. Usually, the effort is focused on increasing the building insulation and air sealing, in order to reduce the need of air heating or air conditioning. The calculation of the energy consumption is often based on tabulated weather data outside buildings: some of the calculation parameters thus stay the same during a part of or the whole simulation period or are not specific to the location of interest (e.g. urban areas). Real urban conditions are far more complex than what is usually assumed in the simulations. Furthermore, a precise knowledge of the real operating conditions outside the buildings is difficult to ensure due to the interactions between the buildings and the urban environment, through a large range of possible heat and mass transfer phenomena, together with the complex urban morphology.

The objective of this PhD work is to develop a tool devoted to an accurate description of the thermal environment outside of buildings. Among the three energy transfer modes considered here, i.e. conduction, convection and radiation, we focus on thermal radiation which is usually the most time consuming and less detailed part in building studies. The main idea is to put the widely used assumption of transparent air into perspective for thermal building simulations. With several air absorption models and different algorithms to evaluate the radiative transfer in the urban area, we are able to analyse the influence of some modeling assumptions (in particular related to thermal radiation) and compare their orders of magnitude.

This PhD thesis is divided in three mains parts. The first one focuses on the medium in which the radiation propagates, viz. the air in the urban canopy. Different factors have been taken into consideration for the absorption and scattering properties of urban atmosphere. With the help of high resolution spectra based on the spectroscopic database HITRAN, several chemical compositions of air have been modeled with a full spectrum k-distribution method. The goal of this part of the study is to evaluate the impact of water vapour on the radiative heat transfer at a urban scale. The second part involves two algorithms to calculate the thermal radiation transfer: the radiosity method, which is a popular method in urban studies, and the Discrete Ordinates Method (DOM) which is widely used in mechanical engineering, for combustion reactor calculations for instance. The main advantage of DOM is to allow the calculation of the thermal radiation propagation through the air volume, while the radiosity method is mostly a surface-to-surface method in which air is treated as a transparent medium. Different aspects of each technique have been developed and compared in order to propose a method providing accurate results at a reasonable computational cost. The last part is dedicated to simulations in real cases. The objective is to determine the variations of temperatures at the external surface of a set of buildings over a one week period. With the help of mea-

sured weather data, we analyze the influence of air absorptivity on the external temperature of buildings and determine the most appropriate method to calculate the radiation transfer in the urban area.

The results of the numerical simulations exhibit a difference of $2\ ^{\circ}C$ on the building surface temperature in Summer, which suggests that the absorption of thermal radiation by air needs to be taken into account for accurate heat budget predictions. Compared to surface-to-surface methods, the Discrete Ordinates Method allows dealing with the urban atmosphere treated as an absorbing medium in micro-climate modelling. Widespread use of the method will depend on further numerical implementation developments, while taking into account air as an absorptive medium is only meaningful if a tighter than usual control of the whole modelling chain (thermal and radiative boundary conditions, among others) can be ensured.

Key words: Microclimate; building energy consumption; Radiation; Air absorption; Radiosity; Discrete ordinates method;

Résumé

Ca fait longtemps que l'urbanisation devient un mot-clé. Avec l'augmentation rapide de la population, les zones urbaines se développent très rapidement. Les problèmes liés à la demande d'énergie et aux changements climatiques dérange tout l'humanité à la fois. Depuis l'année 1974, la régulation thermique est bien développée en France pour toutes les constructions neuves, ainsi que pour la rénovation des bâtiments. Les objectifs sont de réduire la consommation d'énergie principalement liée au chauffage et d'augmenter le confort thermique des bâtiments, notamment en été. L'effort est généralement concentré sur l'augmentation de l'isolation du bâtiment et de l'étanchéité à l'air, afin de réduire le besoin de chauffage de l'air ou de climatisation.Le calcul de la consommation d'énergie est souvent basé sur des données météorologiques mesurés à l'extérieur des bâtiments: certains des paramètres de calcul restent donc les mêmes pendant une partie ou toute de la période de simulation, ou ne sont pas spécifiques au lieu d'étudié (par exemple, les zones urbaines).Conditions urbaines réelles sont beaucoup plus complexes que ce que l'on suppose habituellement dans les simulations. De plus, une connaissance précise des conditions réelles à l'extérieur des bâtiments est difficile à assurer en raison des interactions entre les bâtiments et l'environnement urbain, avec une grand quantitéde transfert de chaleur et masse, ainsi que la morphologie urbaine complexe.

L'objectif de cette thèse est de développer un outil dédié à une description précise de l'environnement thermique à l'extérieur des bâtiments.Parmi les trois modes majors de transfert d'énergie: la conduction, la convection et le rayonnement, nous nous concentrons sur le rayonnement thermique qui est généralement le plus coûteuse en temps de calcul et moins détaillée dans les études de bâtiments. L'idée principale est faire le simulation avec difference modèle de l'air autre que le modèle transparent, par rapport les differents algorithms. Afin de analyser l'influence de certaines hypothèses de modélisation (liées notamment au rayonnement thermique) et de comparer leurs ordres de grandeur.

Cette thèse de doctorat est divisée en trois parties principales. La première porte sur le milieu dans lequel le rayonnement se propage: l'air dans la canopée urbaine. Différents facteurs ont été pris en compte pour les propriétés d'absorption et de diffusion de l'atmosphère urbaine. à l'aide sur la base de données spectroscopiques HITRAN. Le but de cette partie de l'étude est d'évaluer l'impact de la vapeur d'eau sur le transfert de chaleur radiatif à l'échelle urbaine. La deuxième partie implique deux algorithmes pour calculer le transfert de rayonnement thermique: la méthode de radiosité, qui est une méthode populaire dans les études urbaines, et la méthode ordonnée discrète (DOM) qui est largement utilisée en génie mécanique, pour les calculs des réacteurs de combustion par exemple. Le principal avantage de DOM est de permettre de calcul la propagation du rayonnement thermique dans le volume d'air, tandis que la méthode Radiosité est principalement une méthode de surface à surface, dans laquelle l'air est traité comme un milieu transparent.Différents aspects de chaque technique ont été développés et comparés afin de proposer une méthode fournissant des résultats précis à un coût de calcul raisonnable. La dernière partie est dédié à des simulations en cas réel. L'objectif est de déterminer les variations de températures à la surface extérieure d'un ensemble

de bâtiments sur une période d'une semaine.À l'aide de données météorologiques mesurées, nous analysons l'influence de l'absorption de l'air sur la température extérieure des bâtiments et déterminer la méthode la plus appropriée pour calculer le transfert de rayonnement dans la zone urbaine.

Les résultats des simulations numériques montrent une différence de $2\ ^{\circ}C$ sur la température de surface du bâtiment en été, ce qui suggère que l'absorption du rayonnement thermique par l'air doit être prise en compte pour des prévisions précises du bilan thermique.Par rapport aux méthodes de surface à surface, la méthode des ordonnées discrètes permet de traiter l'atmosphère urbaine traitée comme un milieu absorbant dans la modélisation du microclimat. Par contre, il y a pas trop de sens de tenant en compte l'air comme un milieu participative si les autres parameters sont pas bien modelisé.

Mot clé: Microclimate;consumation énergétique du batîment; Transfert du rayonnement; L'absorption de l'air; Radiosité; Méthode ordonnées discretes;

Contents

List of Figures

List of Tables

Nomenclature

Abbreviation specific

$ALBDF$ Absorption line blackbody distribution function

DCI Double contour integral

DOM Discrete ordinate method

DSI Double surface integral

ISA Infinitesimal surface approximation

MC Monte Carlo

PDF Probability density function

qMC Quasi Monte Carlo

RTE Radiation transfer equation

SLW Spectral line weighted-sum-of-gray-gases method

GHG Greenhouse gas

LBL Line-by-line

S2S Surface to surfqce

Greek symbol

β_λ	Air extension coefficient	m^{-1}
η	Wavenumber	m^{-1}
$\kappa_{\lambda,abs}$	Air absorption coefficient	m^{-1}
$\kappa_{\lambda,sca}$	Air scattering coefficient	m^{-1}
$\kappa_{a,\lambda}$	Gas spectral absorption coefficient	m^{-1}
$\kappa_{abs,gas}$	Air gas absorption coefficient	m^{-1}
$\kappa_{abs,part}$	Air partial Editor: Please ensure that the intended meaning has been maintained in this edit, which was made below as well. absorption coefficient	m^{-1}
$\kappa_{sca,gas}$	Air gas diffusion coefficient	m^{-1}
$\kappa_{sca,part}$	Air partial diffusion coefficient	m^{-1}

λ	Wavelength	m
ω	Solid angle	sr
Φ	Flux	W
ρ	Reflectivity of a surface	
σ	Stefan-Boltzmann constant	$W.m^{-2}.K^{-4}$
θ	Angle between the normal and ray directions	sr
I_s	Luminous intensity in the direction s	$W.sr^{-1}$
I_s	Luminous intensity in the normal direction	$W.sr^{-1}$
L_s	Isotropic luminance of the surface	$W.m^{-2}.sr^{-1}$

Symbol

C	Contour	m
c	Light velocity	$m.s^{-1}$
h	Planck constant	$J.s$
$I_\lambda(\Omega)$	Monochromatic intensity in direction Ω	$W.m^{-2}.sr^{-1}.\mu m^{-1}$
$I_b(T)$	Total radiative intensity	$W.m^{-2}.sr^{-1}$
$I_{b,\lambda}$	Monochromatic luminance of the blackbody	$W.m^{-3}.sr^{-1}$
J	Radiosity of a surface	$W.m^{-2}$
k	Boltzmann constant	$J.K^{-1}$
M_j	Exitance of surface j	$W.m^{-2}$
Q_{dif}	Diffuse shortwave radiation	
Q_{dir}	Direct shortwave radiation	
Q_{enf}	Environment longwave radiation	
Q_{lw}	Longwave radiation	
Q_{ref}	Reflected longwave radiation	
Q_{ref}	Reflected shortwave radiation	
Q_{sky}	Downward-oriented sky radiation	
Q_{sw}	Shortwave radiation	
R_ϕ	Random number to generate the polar azimuthal angle	
R_θ	Random number to generate the polar angle	
T	Temperature	K
X_{water}	Volume ratio of water vapor in the air	

Chapter 1

Introduction

Contents

1.1 Context: urbanization growth & climate change

1.1.1 General facts about urbanization

According to the 'Our world in data' website [7], only 4 million people lived on Earth 12000 years ago. The rate of increase in this value remained at a very low level over centuries; an average growth rate of 0.04 % for the population on Earth was estimated until the 18^{th} century [7]. However, the industrial revolution brought enormous changes to the status quo. For instance, before 1750, the population of England stayed stagnant with a very small rate of increase [8]. Then, during the next half of that century, this value experienced a demographic explosion [9] as the population doubled. This explosion has not stopped. Currently, the population on Earth is approximately 8 billion, which is 1840 times that 12 millennia ago [7].

Moreover, the urbanized population has been undergoing a corresponding increase since the industrial revolution. Because of science and technology developments, it became possible to build factories away from rivers. A rising number of industrial sites was constructed near cities, which led to the population shifting from rural villages to urban areas. Currently, over half of the population on Earth lives in urban areas (Figure 1.1). By the end of 2050, this value is expected to increase to 68% [10], which—according to the estimation made by the United Nations—means that over 7 billion people will settle in cities.

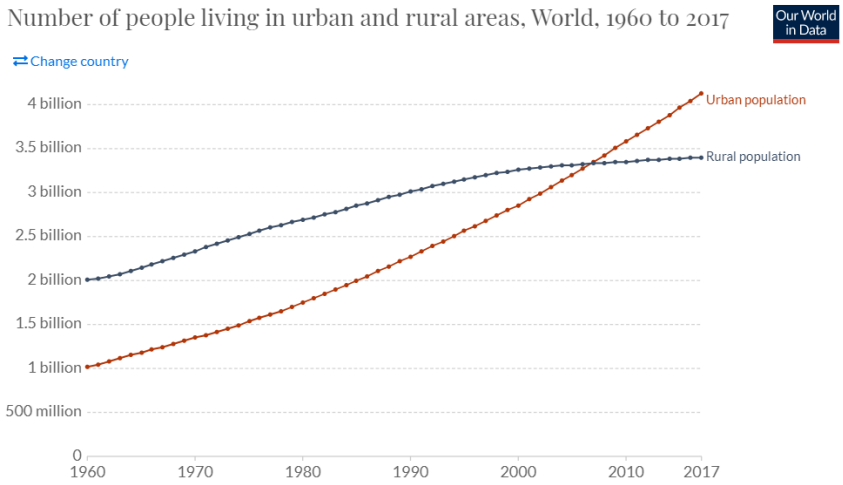

Figure 1.1: The urban population growth [1]

Population explosion involves not only significantly higher energy needs and resource consumption but also a larger production of waste and greenhouse gases (GHGs) that ultimately becomes an important factor in climate change and global warming. The relationship between the growth of population, economy and carbon emissions has become increasingly evident [11; 12; 13]. For example, in China, the population increased from 960 million to 1.4 billion from 1978 to 2010, the primary energy requirement increased from approximately 570 to just over 3200 million tons of coal equivalent (Mtce) [14], and China's carbon emissions overtook the US's leading place in 2009 [15; 16]. Not only the population amount but also its structure affects carbon emissions [17]. Because of the increasing carbon emissions as well as the other GHGs, the Earth surface temperature is rising by approximately 0.2 °C per decade [18]. The global temperature has reached its highest level in the past millennium [19]. A more worrying effect is that the trend is not even close to stopping in this century. A stronger variation in the Earth surface temperature is incoming, which should be acknowledged and

addressed by all humankind. Among the factors that contribute to GHG emissions, buildings are a leading factor, consuming approximately 36% of the global energy and reportedly accounting for approximately 39% of energy-related GHG emissions [20]. In France, building energy consumption accounted for approximately 44.5% of the total consumption in 2012 [21]. Furthermore, the building sector is responsible for 22% of CO_2 emissions [21]. These data mean that the building field is joining the high-consumption and high-emission group already occupied by industry and transportation.

1.1.2 Facing climate change: the building field

The building field is not only a contributor to climate change but also suffers from it. The impact of climate change on buildings is concentrated at two points: the thermal comfort of the building and its energy consumption.

1.1.2.1 Thermal comfort

The thermal comfort of a building can be expressed by the satisfaction or dissatisfaction of an occupant. It has been reported that a healthy and comfortable indoor thermal environment can help occupants improve their work efficiency [22]. Because comfort is highly dependent on personal feelings, it can vary greatly from person to person, physiologically and psychologically. It is difficult to satisfy everyone in a space and even to define this satisfaction through a regulatory standard. As described by the ASHRAE standard 55 [23], six primary factors should be addressed for thermal comfort:

- Metabolic rate
- Clothing insulation
- Air temperature
- Radiant temperature
- Air speed
- Humidity

In France, thermal regulation, for example, RT2012, is controlled by an indoor conventional temperature in summer (Tic). Due to climate change, the higher outdoor temperature can provoke an overheating problem in summer, especially in the case of internal loads and an absence of window aeration [24]. In Frank's study [25], substantial overheating was found for a climate change variant of 4.4 °C for the period 2050 to 2100, particularly for the case without nighttime ventilation. This overheating problem can lead to occupant discomfort.

To solve the overheating problem in summer to improve human comfort, a cooling system is required, which leads to the second impact of climate change on individual buildings: energy consumption.

1.1.2.2 Building energy

Building energy demands can vary in response to climate change. Because of the increasing temperature, the heating energy requirements are lowered, while the cooling energy requirements increase [24]. The net increase or decrease in the energy demand of the building depends strongly on the region's cooling or heating demand dominance [26]. Varying building locations can lead to benefits from climate change and temperature rise [27].

For example, Wang and Chen [28] calculated the annual heating and cooling demand of nine different kinds of buildings in 15 US cities located in different climate zones. They found a reduction in net energy use by heating and cooling sources for cities in cold climates (such as Minneapolis and Portland ME). However, in warm or hot cities such as Houston and Miami, net energy consumption greatly increases. Furthermore, variation exists in the cooling demand of different building types. The amount of cooling increase of buildings such as single families and restaurants is almost twice that of hospitals and hotels.

Not only annual consumption but also peak demand is influenced by climate change. This aspect is a critical element in the long-term planning of energy system capacity consisting of electricity and natural gas [26]. A study by Guido Franco and Alan H. Sanstad [29] showed a strong relationship between the peak consumption of electricity and the maximum daily temperature. Their work indicated that with the temperature rise caused by climate change, the annual consumption as well as the peak demand every day could increase for some locations.

1.2 The building environment

Two important pieces of information are required to carry out a building energy consumption simulation: the weather data of the entire duration and the environment where the building is located.

1.2.1 Weather data

The thermal performance of buildings is highly vulnerable to climate variations. Therefore, it is critical to anticipate the building performance under changing climate. Input data such as weather files are essential for simulation. We commonly use typical year weather data to represent past weather observations [30]. Two general ways exist to generate this typical year data. The first is to use a whole year or 12 consecutive months of data to represent the weather condition. The second is to select the months of different years from a data bank to assemble a whole year [31].

The creation of typical weather data depends on the building location, the available data in the data bank and the purpose of the data. The most well-known methods are the typical meteorological year (TMY) [32], test reference year [33], example weather year [34], design summer year [35], etc. These methods are useful to construct weather data for calculating and comparing the performance of buildings for different locations or types.

1.2.2 Urban microclimate

Buildings do not stand alone. To test their thermal performance and calculate the energy consumption, it is necessary to describe the environment and take the corresponding interaction into consideration. The urban area can be categorized by different scales [36]. The mesoscale represents an area with dimensions over 10 km; the microscale, dimensions less than 1 km. There is also a local scale between the two, which has dimensions of approximately several kilometers. In this thesis, we are interested in a microclimate scale that limits our area length to within 300 m. The vertical dimension is always located in the roughness sublayer.

An example of a microclimate is illustrated in Figure 1.2. Numerous physical phenomena exist in the microclimate area that involve micrometeorology, heat and mass transfer. Different interactions and multireflections and complex urban morphologies increase the difficulty of describing these physical phenomena outside of buildings. Moreover, the estimation of building energy consumption should be calculated considering the microclimate environment. Overall, there are several factors that can directly impact building energy consumption: air temperature, wind, sunlight conditions and radiative heat transfer in the region.

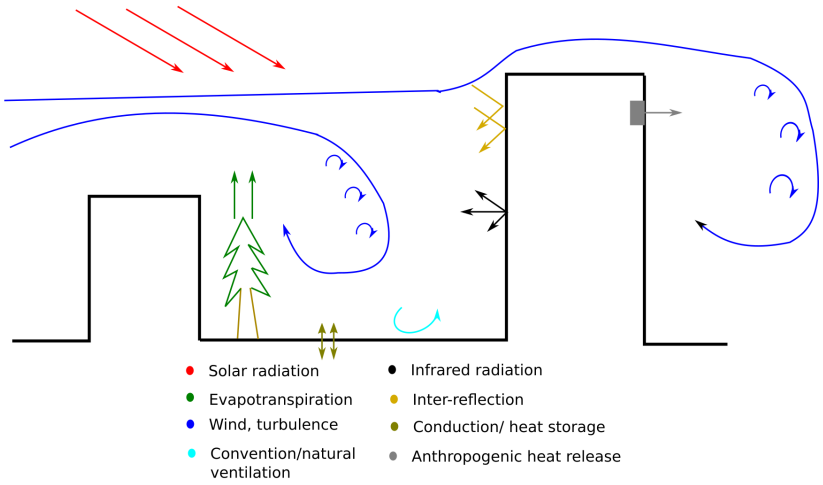

Figure 1.2: The physical phenomenons existed in a micro-climate area [2]

1.2.2.1 Air temperature

The air temperature factor is the most direct relevant factor, as it directly drives the operation of cooling and heating systems and leads to variations in the corresponding building cooling and heating energy consumption. The principle presented in part 1.1.2.2 also applies to this scale of area. Because of the increasing temperature in the microclimate urban area, the requirement of heating decreases, while the cooling demand increases. Moreover, this relationship between air temperature and building consumption has strengthened in recent years [28; 37]. This is particularly true in urban areas, where the morphology is complex and the wind is weak. The surfaces in these areas are heavily modified from the natural surface, and the complexity of the morphology substantially reduces the wind speed to evacuate heat from the area [38]. For these reasons, there is a difference in temperature between urban and rural areas, and this phenomenon is known as the urban heat island (UHI). As demonstrated by previous studies [39; 40; 41], the UHI effect is a worldwide problem regardless of the locations and sizes of urban areas. As the adverse effects of UHIs continue to grow [42], urban areas may experience a higher air temperature, with a greater impact on building energy consumption.

1.2.2.2 Wind

As one of the main reasons for the UHI mentioned in the previous part, the wind is an important factor that can affect building energy consumption in the following ways [43]:

- Air infiltration and exfiltration: The air pressure near the building surface can be affected by the wind [44]. This aspect controls the variation in heat by mass transfer through the building surface.
- Surface heat transfer: The wind flow around the building is associated with forced convection. Forced convection heat transfer can be caused by the following behavior of the air close to the building surface [43]: turbulence in the wall boundary layer; wind flow patterns around the building; and the turbulence inherent in the wind stream. Forced convection is often calculated with a convective coefficient that depends on the air temperature, wind speed and geometric configuration. Empirical models [45] are often applied to calculate the corresponding heat transfer.
- The mechanical system efficiency: The air circulation is controlled by the wind around the building, which influences the effectiveness of ventilation and air conditioning in two ways: exhaust recycling, which reduces the efficiency of the cooling and heating system, and pressure gradients, which affect the fan power requirements.

1.2.2.3 Sunlight

Sun radiation plays the most important role in urban radiation transfer. During normal daylight hours, this mode contributes most of the heat gain of a building, especially for residential buildings, where the internal energy gain is relatively low [46].

As shown in Figure 1.3, solar emissions can be regarded as black body emissions with a temperature of approximately 5900 K. The solar spectrum contains a part of the IR and ultraviolet fields, as well as the full visible field. The solar constant represents the total solar energy measured by a satellite above the atmosphere, and its value is approximately 1361 W/m^2 [47].

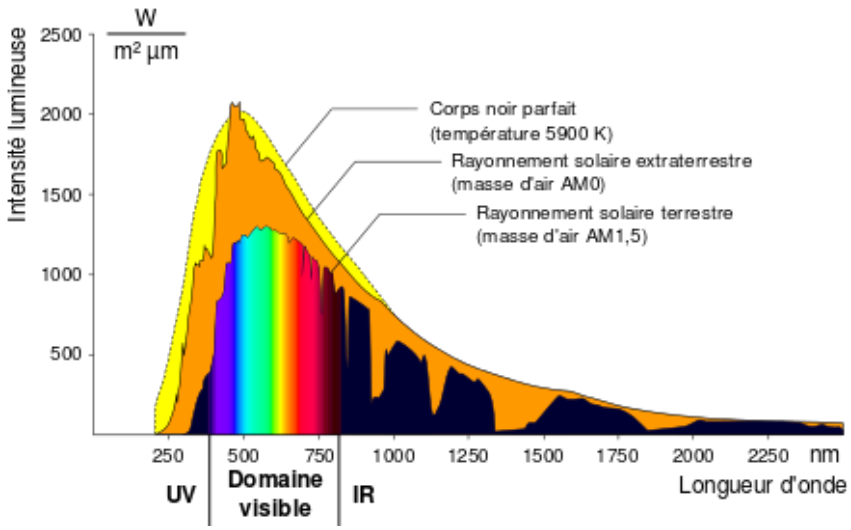

Figure 1.3: The solar spectrum [3]

During passage through the atmosphere, this radiation is attenuated by air gas scattering and absorption. The more atmosphere through which it passes, the greater the attenuation. When the radiation finishes traveling through the atmosphere, the solar spectrum can be characterized by the air mass (AM) [48]. This parameter is defined as the ratio between the path length through the atmosphere and the path length at zenith and sea level. Different AM values are calculated for different zenith angles, and AM1.5 (zenith angle equal to 48°) is applied to represent the overall yearly average for the mid-latitudes [49].

Finally, the solar beams reach the urban surface. Generally, the sun influences building thermal energy consumption in two main ways:

- The solar beam reaches the outside of the surface, providing a large amount of energy, normally representing the largest part of the thermal exchange for the outside wall. The increasing outside surface temperature can ultimately impact the indoor thermal balance by conduction, which leads to a change in the energy consumption (heater, air conditioning) of the building.
- The solar beam reaching the window is transmitted inside of the building. The solar factor, which describes the ratio between the energy transmitted through the window and the incident energy, ranges from 0.25 to 0.8. With the standard of 49%, half of the incident energy penetrating the room contributes directly to the indoor thermal environment. For a building with a glazed envelope, the impact of sun radiation can be more important [50; 51].

1.2.2.4 Radiative heat transfer

Radiation transfer is a principal energy source for an urban area. There are two terms of radiation with different wavelength bands that are involved in this energy balance: the solar irradiance (Q_{sw}) brought by the solar beam described in the previous section, which is usually the most important incoming energy with a band from 0.3 to 3 μm, and the IR radiation (Q_{lw}) with a wavelength ranging from 3 to 100 μm, which is often termed longwave radiation because its emission is concentrated within a longer-wavelength band.

Both radiation sources can generate an impact on building heating and cooling demand [52; 50], which can ultimately affect the building energy consumption.

Solar radiation (Q_{sw}) The shortwave radiation (Q_{sw}) can be calculated as:

$$Q_{sw} = Q_{dir} + Q_{dif} + Q_{ref} \tag{1.1}$$

Q_{dir} is the solar radiation that comes directly from the sun. This part of the total radiative intensity is normally the highest among all three terms. The solar beam, after passing through the atmosphere, reaches the surfaces in the sunlight direction. This part of the irradiance can be characterized at a weather station regarding intensity and direction. It can also be characterized by various methods depending on the solar constant, location, and atmospheric conditions.

Q_{dif} refers to the part of incident solar radiation scattered by the atmosphere. Air molecules, aerosols, $etc.$ scatter a part of the incident I_{dir}. Ultimately, a fraction of this

scattered energy reaches the surfaces (walls, ground, $etc.$). As direct irradiance, the diffused part can also be measured or predicted by a detailed atmosphere and sky model.

Q_{ref} is the component related to reflections by the surfaces. For a given location, this part of the energy comes from all surrounding elements. It is difficult to evaluate this energy component because of the complex morphology of urban areas. Many sky diffuse models consider that this part of irradiance depends only on the inclination of the tilt surface [53].

IR radiation (Q_{lw}) The thermal IR radiation received by a surface comes from the sky Q_{sky} and the environment Q_{env}. The amount of thermal IR radiation from the sky is approximated by an emissivity ϵ_{atm} and an effective temperature T_{atm} [54]. Numerous sky models have been developed, and it is difficult to identify the best one: All of them show scattering and uncertainty in the predicted value [53; 55].

The environmental radiation Q_{env} is equivalent to the component Q_{ref} in solar radiation and accounts for radiative thermal emission by all boundary surface elements. Because of the higher emissivity of building surfaces in cities, the value is usually more important there than in rural areas. Detailed information about building geometries and surface conditions is obviously required to allow an accurate estimation of this component.

Both parts, Q_{sky} and Q_{env}, are in practice difficult to evaluate precisely because of limited knowledge of wall and ground thermophysical properties. For instance, they are frequently idealized using Lambertian boundary surfaces with a given prescribed temperature and gray emissivity.

1.3 Modeling radiative transfer

In this thesis, we concentrate on radiation transfer in the microclimate urban area. As presented in the previous section, this transfer involves solar radiation, known as shortwave radiation, and IR radiation, which is also termed longwave radiation or thermal radiation. Moreover, it contains not only the radiation incoming for the determined microclimate area but also the radiation transfer inside the area, such as the emission of the building in IR radiation and the interreflection of solar radiation and IR radiation.

1.3.1 Sunlight simulation

The solar radiation calculation is based on sunlight simulation. It is also called daylight simulation, involving the combination of all direct and indirect sunlight during the daytime. The quality and accuracy of simulations can be influenced by multiple different factors, including the calculation method, sky model, surface properties, etc.

1.3.1.1 Sky models

The solar radiation contains a direct part, i.e., direct incident solar energy from the sun, and an indirect part, i.e., diffuse solar energy transmitted through the atmosphere. This means

that the sky model is critical to sunlight simulation because of the highly variable nature of diffuse irradiance.

There are numerous diffuse sky models for calculating this value for a tilted surface. We start from the isotropic sky model introduced by Liu and Jordan [56]. It assumes that all diffuse radiation is uniformly distributed over the sky dome. Then, the Klucher model [57] introduces the circumsolar and horizon brightening by a clearness index to calculate the diffuse solar energy. The Hay model [58] weights the isotropic diffuse radiation to include the circumsolar anisotropy. The Reindl model [59] extends the Hay model to take into account horizon brightness. The most important model is the Perez model [60], which is recognized as one of the most accurate sky models.

1.3.1.2 Surface properties

The surface properties of the object in the area are also an important factor in the sunlight calculation. The characterization of surface reflective properties can be defined by a function that determines how reflected radiance is distributed in terms of the distribution of incident radiance. This function is called the bidirectional reflectance distribution function (BRDF). This function requires four variables to define how light is reflected at an opaque surface. It considers the incoming and outgoing direction of the reflection, and it usually contains a zenith angle and an azimuth angle for each direction, bringing the total number of input variables to four. By this function, it is possible to determine the ratio of the reflected radiance exiting along the outgoing direction we define.

In general, BRDF models can be classified into three categories: empirical, theoretical and experimental.

- Empirical BRDF models: These models are designed to provide a fast calculation to mimic reflection. They do not consider the underlying physical law. Examples include the Phong [61] and Blinn-Phong [62] models.
- Theoretical BRDF models: These models apply physical laws to accurately simulate light reflection. Their expression is often complex, and the computational cost is usually high. Examples include the Torrance-Sparrow [63] and Oren-Nayar [64] models. The most common BRDFs we apply in the simulation, the specular and diffuse models, are also theoretical models.
- Experimental BRDF models: These are the models measured by a gonioreflectometer, which mechanically varies the light source and sensor positions to directly acquire the BRDF or its parameters to calculate the BRDF in different directions. The data are usually limited at specific angles. Examples include the Lafortune [65] and Ward [66] models.

1.3.1.3 Sunlight calculation methods

To simulate sunlight in a determined area, numerous sunlight transport calculation methods can be applied:

- The split flux formula method: This is the oldest method, derived from a manual calculation method established by the English Building Research Establishment (BRE).

The principle of this method is to split the solar energy incident upon a surface into three major components: direct solar incoming, reflection by an object outside of the enclosed area and reflection by an object in the area. The solar radiation is calculated separately and summed to obtain the global illumination. As the result is highly approximated, it is rare to see this method in solar simulation software.

- Radiosity method: Radiosity is a method introduced in the 1950s to calculate heat transfer. Then, in 1984, researchers at Cornell University brought this technique to the computer graphic field [67]. It has become one of the most important powerful computer graphics tools in the commercial computer graphic market [4]. Despite the initial design to study thermal transfer, this method was proven capable of handling sunlight simulations for simple scenes. These simulations are constrained by multiple factors, such as diffuse surfaces and complex descriptions of the sky [68]. In recent years, the method was developed to handle nondiffuse reflection [69], as well as hierarchical methods for more complex geometries [70]. However, these improvements made the radiosity method more computationally expensive. It is still a powerful tool to calculate the surface illumination, but favor is slowly shifting towards the ray tracing method.

- Ray tracing: The principle of ray tracing method is to calculate the distribution of a large number of rays emitted from the surface in a scene. If the ray emerges from a light source, it is called the forward ray tracing method. If the ray emerges from a surface where we wish to calculate the illumination, it is called backward ray tracing [71]. This method can also combine the two directions, termed bidirectional ray tracing [72]. The rays follow the same principles as light in the real world to ensure that the method is physically plausible [73]. When the rays encounter surface elements, they can be reflected, absorbed or transmitted. Energy conservation is maintained at every bounce of a ray. The splitting of rays can be controlled by a deterministic or stochastic (Monte Carlo, MC) method [74; 75]. At the object surface level, ray tracing can easily handle specular reflection and refraction. However, diffuse reflection requires tracing a large amount of rays whose quantity can reach millions. Hence, diffuse reflection is usually subjected to various levels of approximations and optimizations, resulting in bias [76]. Currently, hybrid methods are being developed based on the ray tracing method, such as the bidirectional ray tracing method [72] and photon mapping [77].

1.3.2 Thermal radiative heat transfer

Different from solar radiation, whose source is the sun outside of the scene, thermal radiation can be generated by an object located inside the geometry. Any surface in an urban area can emit thermal radiation and reflect and absorb incident thermal radiation. For glazed surfaces, part of the energy is transmitted through the surface. With the complexity of the geometry, the calculation of thermal radiative transfer can be difficult and computationally expensive.

Many radiation models have been developed to calculate radiation transfer, such as the discrete transfer radiation model (DTRM) [78], P-1 radiation model [79], Rosseland radiation model [79] and surface-to-surface (S2S) radiation model [79]. Each of them has advantages and limitations compared with other models. Among them, the S2S model is widely applied in software to evaluate the radiation performance of an object.

1.3.2.1 S2S models

The S2S radiation model is well known for modeling enclosure radiative transfer without participating media. In the case where the medium between the surface is considered transparent to the radiation, this model provides faster calculation time in every iteration compared with the other relevant radiation models. This model contains a calculation of the view factor, which can consume much more time than the other calculations [80]. Limitations of the S2S model are also evident:

- All the surfaces in the scene are considered perfect diffuse surfaces. It is difficult to calculate the corresponding glazed surface reflection.
- The storage and memory requirements can vastly increase with increasing surface number.
- The model neglects transfer between surfaces, indicating that it cannot be applied for the radiation problem addressed here.
- It is not applicable to problems with periodic boundary conditions.

Despite all of these limitations, the S2S method, such as the radiosity method, is still widely used to simulate radiation transfer. It is widely applied in software designed for different levels of complexity of geometry:

- At the single-building level, building energy simulation (BES) tools are capable of calculating the energy consumption of single buildings in the urban environment. However, the surroundings of buildings are usually considered nonexistent, as a general weather data file is used to model the environment. TRNSYS is a building simulation tool that uses the radiosity method to calculate both solar and thermal radiation transfer.
- To simulate all the interactions between buildings and their environment, the urban building energy simulations (UBESs) were developed. For example, SOLENE, developed by the Centre de Recherche Nantais Architectures (CEREMA), was first designed to precisely describe the solar luminance distribution in the city. After years of development, it was shown to be able to calculate building energy consumption [81]. In this radiative calculation part of this tool, radiosity is applied for all types of radiation.
- For a simulation of an area larger than UBES, tools such as 'CitySim' have been developed to support the sustainable development of urban areas [82]. The calculation of radiation interaction between the building and the environment is considered by a special radiation model designed by Robinson and Stones [83; 84], which is also an S2S-based method.

The wide applications of the S2S model show that it is still preferred by tool developers even with its limitations. In addition, problems such as surface reflection properties and storage and memory requirements have already been improved by the hybrid radiosity method [85; 69] and the cluster of surface faces method [86]. However, questions remain about radiation transfer between surfaces through air. Should air always be regarded as a transparent medium for radiation?

1.3.2.2 Air attenuation of thermal IR

In the composition of the atmosphere, gases such as nitrogen and oxygen, which contribute over 99%, hardly interact with radiation [87]. Neither incoming solar radiation nor outgoing Earth emissions are influenced by this large quantity of these air gases. Minor air gases, however, such as water vapor, carbon dioxide, ozone and methane, play an important role in the Earth's climate by radiation absorption. According to [87], 90% of Earth radiation emissions and 15% of solar incident energy are absorbed by these gases. They are called GHGs because their function is quite similar to that of glass to build greenhouses. Among these gases, water vapor is responsible for 70% of radiation absorption in the atmosphere [88], especially in the IR region. The large concentration in the atmosphere and high absorption of radiation make this the most important factor leading to the greenhouse effect and climate change.

It has already been proven that GHGs can affect radiation transfer [87; 88; 89]. Moreover, the concentration of these gases is still increasing [90], and their impact is extending. However, the S2S model when simulating radiation transfer cannot take the air impact into account, which makes the results from these simulation tools less promising.

1.4 Objectives and organization of the thesis

As described in the previous sections, building energy consumption faces additional stress from population growth and urbanization development. This energy pressure encourages us to be more cautious in energy consumption issues during building design and construction renovation. It requires not only explicit calculations regarding the building interior but also a detailed simulation of all the physical phenomena outside of the building. As the most important energy source for buildings, radiation is usually calculated by the S2S model. Even though this model has been improved in recent years in terms of surface properties and calculation time, it still cannot take air attenuation into account. Moreover, the impact of air gas on radiation transfer is becoming increasingly severe. The other software, such as DART [91], considers the air attenuation between the top of atmosphere and urban surface level only. Other software like Fluent applies a simple grey air model in the calculation for the air absorption calculation. This air model is recognised for its exaggeration of air absorption, which makes the result less promising. The air inside the urban area is considered transparent. The impact of air attenuation on the radiation transfer inside the urban area is unaddressed by these tools.

The objective of this thesis is to develop a computational tool capable of accurately describing the thermal environment outside of buildings at the microclimate scale. We concentrate on radiation transfer and the impact of air gas. We discuss the assumption of considering air as a transparent medium for the different terms of radiation heat transfer.

The second chapter introduces radiation transfer through a brief presentation of the fundamentals aspects. Then, to develop an approach to evaluate radiation transfer in a microclimate area, the radiosity method is introduced in the second half of the chapter, along with different methods to calculate the view factor. Because of the calculation time advantage of the infinitesimal surface approximation (ISA), we develop this method and aim to improve its accuracy for close surfaces with the subdivision method. An analysis of the subdivision performance is performed, with a check of the so-called $5\times$ rule. Subsequently, three methods for calculating the view factor are tested and compared in terms of both precision and time

cost.

With the transparent radiative transfer approach developed in the preceding chapter, we develop an approach that can deal with air as a participatory medium in the third chapter. This chapter starts with the basic radiation transfer equation (RTE), which it is necessary to solve to calculate the radiation transfer in the participatory medium. The characteristics of air are presented, and different air models are introduced. Finally, with the help of the HITRAN database, the air absorption coefficient is evaluated for each air sample with different configurations of temperature and humidity. The air model performance is evaluated and compared. With the incorporation of the air gas radiative property and the air model, which can describe this transfer aspect in the RTE, a method is selected to solve the equation. The method we choose is the discrete ordinate method (DOM), which method treats the RTE by using separate discretization schemes in spaces and angles. A comparison of the linear interpolation schemes is also discussed.

With the two approaches that can calculate the radiation transfer under different conditions, simulation and comparison are carried out in the fourth chapter. The first calculation involves a steady-state simulation with a typical geometry model in an urban area: the canyon. Different modifications of both the radiosity method and the DOM are applied to simulate and compare both solar radiation and IR radiation. Then, in terms of the DOM, the critical factors, such as discretization in angle and space, are discussed with the canyon model to determine their influence on the result precision and time consumption. For the last part of this thesis, a transient simulation for a real geometry model is carried out. The objective is to determine the air impact on the building energy budget for a long time duration. We attempt to determine the energy transfer in the area for approximately one week. The first part is the presentation and modeling of this area. Then, the initial calculations are analyzed using both the radiosity method and the DOM in a transparent environment. We seek the magnitude of disparity between these methods with a transparent model to understand the level of difference in the initial air condition. Subsequently, the DOM alone is applied for determination of the air impact on the building surface because the radiosity method is not applicable with the participatory air model. Three air models tested in the second chapter are implemented in the DOM core to simulate the energy transfer in the area. Even if the model is quite simplified, the final results are still promising enough to conclude this thesis.

The thesis ends with a conclusion based on the work performed and results obtained. Because of the simplification we apply in the last part, there are still improvements available that can make our results more promising.

Chapter 2

Air as a transparent medium: the radiosity method

Contents

2.1 Definitions

Radiative heat transfer theory studies the propagation of heat by electromagnetic waves or photons/quanta. All bodies at a temperature higher than 0 K emit or absorb radiation. Unlike the other mechanisms of heat transfer, such as conduction or convection, thermal radiation can propagate at light speed in vacuum without the need for any material support.

Only part of the electromagnetic spectrum is able to produce thermal transfer: It is called thermal radiation and covers only a part of the IR, ultraviolet and visible spectra. Wavelengths that extend from 0.1μm to 100μm are considered to compose thermal radiation, as shown in Figure 2.1.

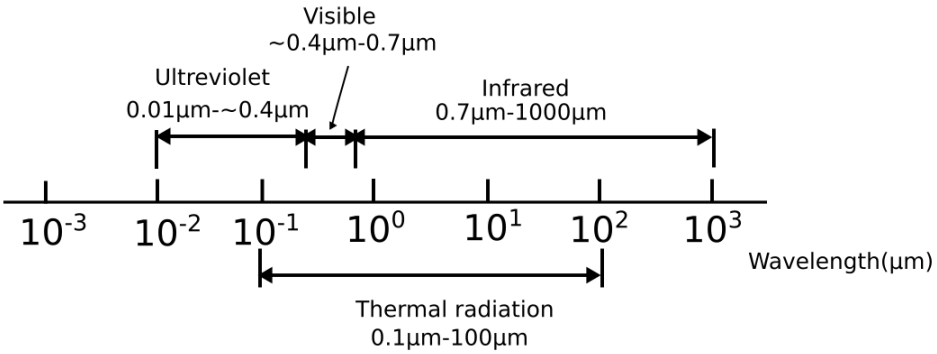

Figure 2.1: Electromagnetic radiation spectrum

2.1.1 Radiative intensity

The amount of energy emitted is a function of the temperature of the body and of its nature. Different kinds of media have different emission spectra that are characterized by comparison with a perfect radiation emitter, the blackbody, which is defined as a medium emitting, for all wavelengths, the highest radiative heat flux. The blackbody radiative intensity $I_{b,\lambda}$ $[W.m^{-3}.sr^{-1}]$ can be calculated by Planck's law as:

$$I_{b,\lambda} = \frac{2hc^2}{\lambda^5} \frac{1}{e^{\frac{hc}{\lambda kT}} - 1} \tag{2.1}$$

where h is the Planck constant $(6.63 \times 10^{-34}\, J.s)$, c represents the speed of the light in vacuum $(3 \times 10^8\, m.s^{-1})$, k is the Boltzmann constant $(1.38 \times 10^{-23}\, J.K^{-1})$ and T is the temperature of the blackbody in kelvins.

All materials can be characterized by a spectral emissivity that measures the amount of radiative energy emitted by the medium at a given temperature and a chosen wavelength compared to a perfect radiation source called the blackbody. The blackbody is also a body that can absorb all the incident radiation, regardless of its frequency and the angle of incidence.

The total radiative intensity $I_b(T)$ $[W.m^{-2}.sr^{-1}]$ emitted by a blackbody is obtained by integration of the spectral radiative intensities over the full range of wavelengths. It is given by the Stephan–Boltzmann law:

$$I_b(T) = \frac{\sigma T^4}{\pi} \tag{2.2}$$

where σ is the Stefan-Boltzmann constant, which can be obtained by:

$$\sigma = \frac{2\,\pi^5 k^4}{15\,c^2 h^3} = 5.67 \times 10^{-8}\ [W.m^{-2}.K^{-4}] \tag{2.3}$$

However, the blackbody is an idealized physical body that does not exist in nature [92]. In the real world, the radiation emitted by a body is smaller than the value corresponding to a blackbody. This emitted radiation is characterized by its surface property, which can be considered for each wavelength or as an average over the whole thermal spectrum.

2.1.2 Radiative surface properties

Real materials emit energy at a fraction of black-body energy levels. This fraction, called the surface emissivity, describes the effectiveness of surface radiation emission. Due to this definition, emissivities are always in the interval [0,1]. A blackbody has an emissivity of 1. The emissivities of other bodies are quite different from each others. The treatment of the real surfaces can be found in Ref. [93].

The spectral emissivity in a direction Ω can be evaluated by:

$$\epsilon_{\lambda,\Omega} = \frac{I_{\lambda,\Omega}}{I_{b,\lambda,\Omega}} \tag{2.4}$$

$I_{\lambda,\Omega}$: Surface spectral radiative intensity in the direction Ω

$I_{b,\lambda,\Omega}$: Spectral radiative intensity in the direction Ω of a black body at the same temperature as that surface. Often, the emissivity is assumed to be independent of the direction (for bodies with diffuse emission) and of the wavelength (gray bodies), so for diffuse gray bodies, there is only one parameter, the total emissivity of the surface, which is defined by a ratio of emitted radiative intensities as:

$$\epsilon = \frac{\pi \int \epsilon_\lambda I_{b,\lambda}(T) d\lambda}{\sigma T^4} \tag{2.5}$$

In many problems of practical interest, the total emissivity is sufficient to make radiative transfer calculations. The amount of radiative energy emitted by a surface (excluding at the moment possible effects due to reflections) is given as:

$$I = \frac{\epsilon \sigma T^4}{\pi} \tag{2.6}$$

This relationship also works for the blackbody, but in this case, ϵ=1, allowing us to retrieve Eq. 2.2.

The materials are not only sources but also receivers of thermal radiation energy. When an energy flux impinges on a body surface, it can be reflected and absorbed by that surface. Under some conditions, the flux can also transmit completely through the surface and continue to propagate. These phenomena introduce the physical values of absorbance (α), reflectance (ρ) and transmittance (τ) to describe the radiative surface properties. Conservation of energy requires the sum of these values to be 1:

$$\alpha + \rho + \tau = 1 \tag{2.7}$$

Based on Kirchhoff's law [94], the emission and absorption of thermal electromagnetic radiation at every wavelength are in thermodynamic equilibrium. This suggests that the emissivity of a surface equals its absorbance.

$$\alpha = \epsilon \tag{2.8}$$

Based on these fundamental physic laws, numerous methods have been developed to evaluate a body's radiative performance and exchange with the ambient environment. S2S methods such as radiosity are the most well-known methods to calculate radiative transfer. In this thesis, we concentrate on the radiosity method. The objective is to evaluate the radiative transfer in an urban area while considering the air as a transparent medium. The calculation result of radiosity provides a benchmark for our new approach.

2.2 The radiosity method

The fundamentals of the method are based on the numerical solution of the shading equation on a mesh of finite surfaces. The scene of the area is divided into numerous surface patches that are normally triangular and very small. The surfaces are assumed to be perfectly diffuse gray surfaces, or Lambertian surfaces, which means that their intensity is isotropic and follows Lambert's cosine law (Figure 2.2):

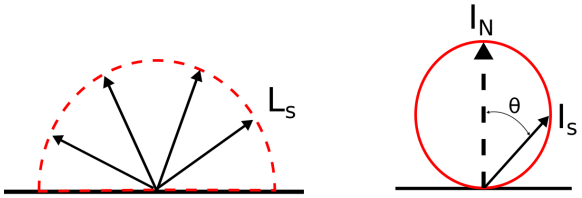

Figure 2.2: Characteristics of the Lambertian surface

$$L_s = \frac{M}{\pi} \tag{2.9}$$

$$I_s = I_N cos(\theta) \tag{2.10}$$

L_s: Isotropic luminance of the surface $[W.m^{-2}.sr^{-1}]$

M: Exitance of the surface $[W.m^{-2}]$

I_s: Luminous intensity in the direction s $[W.sr^{-1}]$

I_N: Luminous intensity in the normal direction $[W.sr^{-1}]$

θ: Angle between Ω and the surface normal

2.2.1 Definition of the radiosity

The radiosity J characterizes the heat flux leaving a surface. It is the sum of the surface self emission (radiant exitance, M) and the reflection of the incoming flux (irradiance, E_{inc}) (Figure 2.3):

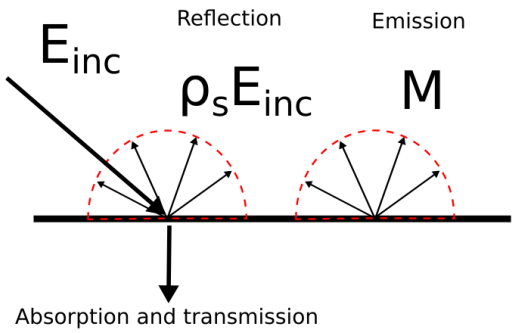

Figure 2.3: Radiosity of the surface

$$J = M + \rho E_{inc} \tag{2.11}$$

In the radiosity method 2.4, for a single mesh S_j with a surface $A_j[m^2]$, the total flux leaving Φ_j can be expressed as:

$$\Phi_j = J_j A_j \tag{2.12}$$

For a receiving surface S_i, which can see surface S_j without any obstruction, it is possible to receive flux Φ_{ji}:

$$\Phi_{ji} = J_j A_j F_{ji} \tag{2.13}$$

F_{ji} is the view factor between the surfaces S_j and S_i. Mathematically, this equals the proportion of the radiation leaving surface S_j received by surface S_i. The details of the view factor are introduced in the following section. For mesh S_i, the overall irradiance E_{inc}, which is the sum of the incident fluxes, can be written as:

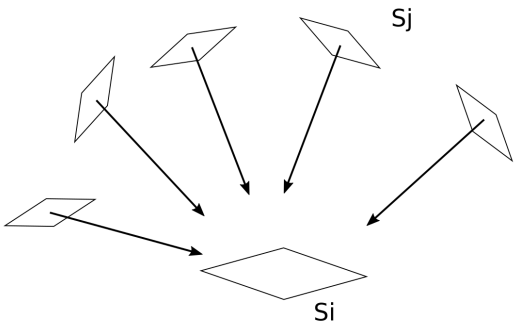

Figure 2.4: The radiosity method [4]

$$E_{inc} = \frac{\sum_{j=1}^{n} J_j A_j F_{ji}}{A_i} \tag{2.14}$$

Here, *n* is the total number of surfaces.

With the reciprocity law of the view factor,

$$A_i F_{ij} = A_j F_{ji} \tag{2.15}$$

the irradiance equation 2.14 becomes:

$$E_{inc} = \sum_{j=1}^{n} J_j F_{ij} \tag{2.16}$$

For gray diffuse materials, the final radiosity equation changes from Eq. 2.11 to:

$$J_i = \epsilon_i \sigma T^4 + (1 - \epsilon_i) \sum_{j=1}^{n} J_j F_{ij} \tag{2.17}$$

This system of *n* linear equations is too large to solve for a direct method such as Gauss elimination. The most common way to solve this system is the Jacobi and Gauss-Seidel method [95] [96]. This approach is recognized as a full radiosity algorithm. The time complexity for the full radiosity algorithm is $O(n^2)$, which means that the time consumption quadruples if the number of patches in the scene doubles. The required data storage is $O(n^2)$. These disadvantages make a full radiosity method too expensive for very large scenes with refined meshes.

Despite the cost of solving the radiosity equation, the most challenging part of this algorithm is to calculate the view factor for each pair of small patches in the mesh. The time spent on the view factor calculation can occupy over 90% of the total simulation time [80]. This information needs to be calculated only once for a determined scene, but the time required can be much more than that to solve a system of linear equations.

2.2.2 Numerical assessment of the view factors

The view factor, also known as the form factor or shape factor, is the most critical input to the radiosity method. This dimensionless parameter defines a fraction of the flux emitted by one surface patch that is received by another. For a closed environment, the sum of the view factors for S_i equals 1. The summation also includes the self-view factor F_{ii}. For a flat surface, F_{ii} equals 0.

The calculation of the view factors involves only the scene geometry and can be conducted beforehand and the result stored. Difference methods are included in the software mentioned in chapter 1 [97; 83]. In this thesis, we wish to find another method that can be implemented rapidly and precisely.

The view factor is defined by a double surface integral. Let us consider the differential regions dS_i and dS_j in the surfaces S_i and S_j, with a distance of *R* (Figure 2.5). Here, dS_j emits energy in the direction θ_j with the solid angle ω. The flux received by dS_i is:

$$d^2\Phi_{ji} = L_j dS_j cos\theta_j d\omega_j \tag{2.18}$$

With the solid angle:

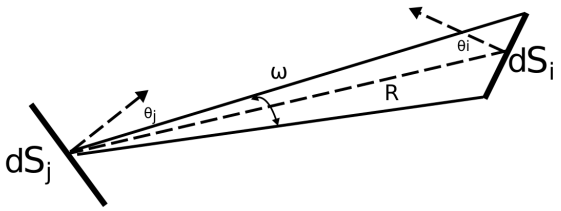

Figure 2.5: The flux emit by dS_j et received by dS_i

$$d\omega_j = \frac{dS_i cos\theta_i}{R^2} \tag{2.19}$$

Eq. 2.18 becomes:

$$d^2\Phi_{ji} = L_{j\theta_j} \frac{dS_j cos\theta_j dS_i cos\theta_i}{R^2} \tag{2.20}$$

$L_{j\theta_j}$ is the radiance in the direction θ_j. The radiosity method assumes that all the surfaces obey the Lambert law. Thus, Eq. 2.20 becomes:

$$d^2\Phi_{ji} = \frac{M_j}{\pi} \frac{dS_j cos\theta_j dS_i cos\theta_i}{R^2} \tag{2.21}$$

The flux emitted by surface S_j received by surface S_i can be obtained by integration:

$$\Phi_{ji} = M_j \int_{Sj} \int_{Si} \frac{dS_j cos\theta_j dS_i cos\theta_i}{\pi R^2} \tag{2.22}$$

The view factor, i.e., the ratio of Φ_{ji} to the total emitted flux Φ_j, can be written as:

$$F_{ji} = \frac{\Phi_{ji}}{M_j S_j} = \frac{1}{\pi S_j} \int_{Sj} \int_{Si} \frac{dS_j cos\theta_j dS_i cos\theta_i}{R^2} \tag{2.23}$$

Eq. 2.23 contains a double surface integration step that generally cannot be solved analytically. Simplification is required to obtain the view factor between every pair of patches in a geometric model.

2.2.2.1 Double contour integration (DCI)

In 1963, E. Sparrow published an article introducing the DCI method [98]. The idea is to apply the Stokes theorem to Eq. 2.23, which successfully reduces the integral degree by converting from surface to contour integration.

$$F_{ji} = \frac{1}{S_j \pi} \int_{C_j} \int_{C_i} In(R) dC_i dC_j \tag{2.24}$$

Compared with the double surface integral, this method allows determination of the view factor precisely for many different shapes of patches [79]. However, due to its time-consuming nature, it is impractical for complex areas. Nevertheless, its accuracy provides a reference for the calculations in this thesis.

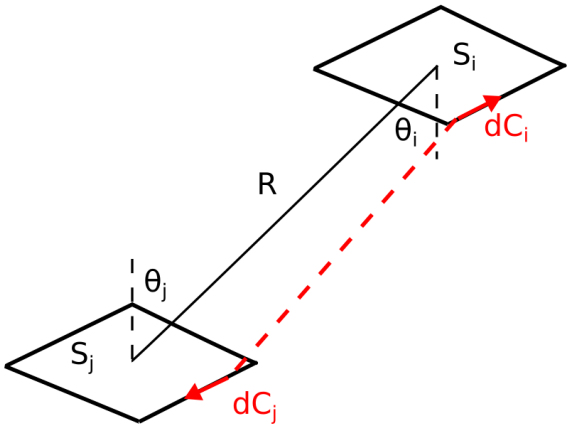

Figure 2.6: The double contour integral

2.2.2.2 The Monte Carlo(MC) method

The MC method is a statistical method that repeatedly generates random samples to obtain the equivalent to a closed numerical result. To calculate the view factor of the surfaces, numerous energy bundles are launched with random directions from one surface S_j. The view factor F_{ji} is the ratio of the bundles received by surface S_i to the number launched by surface S_j.

Consider a physical quantity $I(x)$ defined in field D by the following integration:

$$I(x) = \int_D f(x)dx \tag{2.25}$$

This integration can be estimated by a probability density function (PDF) $p(x)$, which corresponds to the variable position of x in field D:

$$I(x) = \int_D f(x)dx = \int_D p(x).g(x)dx \tag{2.26}$$

with:

$$\int_D p(x)dx = 1 \tag{2.27}$$

With the MC method, one can obtain $\widetilde{I(x)}$ by performing N random tests, following the distribution $p(x)$:

$$\widetilde{I(x)} = \frac{1}{N}\sum_{n=1}^{N} g(x) \tag{2.28}$$

The most important task is to determine the PDF of the radiation emission.

The heat flux of a surface:

$$\Phi_\lambda = \int_{2\pi} L_\lambda cos\theta d\omega \tag{2.29}$$

For integration over a hemisphere, one can add the PDF to this function:

$$\Phi_\lambda(\vec{x}) = \int_0^{2\pi}\int_0^{\frac{\pi}{2}} L_\lambda cos\theta sin\theta d\theta d\phi \tag{2.30}$$

$$= \int_0^{2\pi} p_\phi(\phi)\int_0^{\frac{\pi}{2}} p_\theta(\theta)\frac{L_\lambda cos\theta sin\theta}{p_\phi(\phi)p_\theta(\theta)}d\theta d\phi \tag{2.31}$$

Therefore, there are two relevant PDFs: one for the polar angle θ and one for the azimuths angle ϕ. For a diffuse surface, we choose $p_\phi = \frac{1}{2\pi}$, so we have:

$$\int_0^{2\pi} p_\phi(\phi) = \int_0^{2\pi}\frac{1}{2\pi} = 1 \tag{2.32}$$

For the polar angle part, we seek:

$$p_\theta(\theta) = acos\theta sin\theta \tag{2.33}$$

The integration of the PDF over the field is 1:

$$\int_0^{\frac{\pi}{2}} p_\theta(\theta) = 1 \tag{2.34}$$

We find that 'a' equals 2. A random number is generated between 0 and 1 for each angle to give a random direction for the energy bundle:

$$\theta = arcsin(\sqrt{R_\theta}) \tag{2.35}$$

$$\phi = 2\pi R_\phi \tag{2.36}$$

Because the method is a statistical method, many samples are needed to achieve satisfactory results. For simple models, the MC method is imprecise and inapplicable. However, since the complexity of the method differs from that of other methods (O(n^2)) [99], with *n* being the total number of surfaces in the model, this method may be superior to the others for complex models.

2.2.2.3 Infinitesimal Surface Approximation(ISA)

Based on this basic formulation, many methods have been developed to determine the view factor between surfaces. In 2003, J. J. MacFarlane [100] introduced four methods in the VISARD system. Three methods were developed from the DCI method. The last method, the infinitesimal surface method, contains a simple vector calculation (Figure 2.7).

The equation is given by:

$$F_{ji} = -\frac{1}{2A_j\pi}\frac{2A_jA_i}{|\vec{R}|^4}(\vec{n}_j.\vec{R})(\vec{n}_i.\vec{R}) \tag{2.37}$$

Demonstrated by J. J. MacFarlane [100], the infinitesimal surface method shows a large advantage in terms of time cost. With numerous meshes used in urban simulations, the infinitesimal surface method can reduce simulation costs. However, this method suffers from accuracy problems when the surfaces are too close. MacFarlane suggests that the application of this method should obey what is termed the $5\times$ rule.

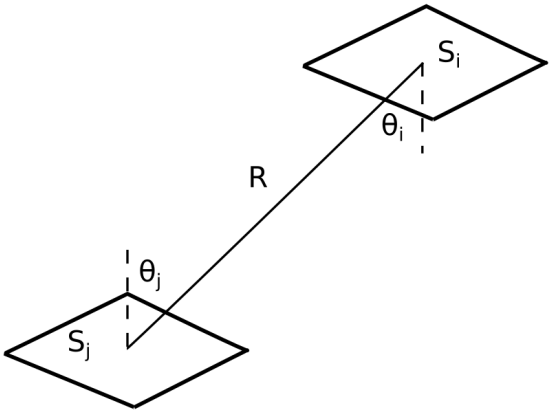

Figure 2.7: Infinitesimal surface approximation:The view factor is calculated by a simple vector calculation of position of two surfaces($\vec{R}$ and $\theta_i and \theta_j$) and the surfaces parameters(area and normal)

2.2.2.4 Local refinement to the Infinitesimal Surface Approximatio

The 5 times rule has been applied by engineers for a long time. As illustrated in Figure 2.8, much research has been done on this topic, including that by Saraiji and Mistrick [101], Emery et al. [102], Baum et al. [95], Max and Troutman [103] and Sbert [104]. This work has led to the conclusion that a finite-area Lambertian emitter should be modeled as a point source only when the distance to the receiving surface is greater than five times the maximum projected width of the emitter [4]:

$$\frac{|\vec{R}|}{l_{max}} \leq 5 \tag{2.38}$$

where l_{max} is the longest dimension of the emitter.

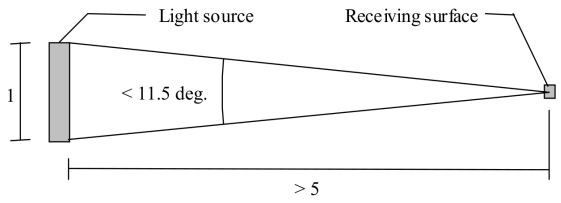

Figure 2.8: The five times rule [4]

In cases where the 5 times rule is violated, a subdivision process is necessary to keep the view factor result in good precision.

In this thesis, when using the ISA, the fraction between the maximum dimension of the source patch and the distance of two patches is evaluated. If the patches are too close, a subdivision function is useful to divide the source patch into several smaller facets to reduce its dimension (Figure 2.9). The number of division is based on the five times rule which ensure that the fraction $\frac{|\vec{R}|}{l_{max}}$ of small source patch and receiving patch is always above 5.F

The final view factor F_{ji} is given by:

$$F_{ji} = \frac{1}{N} \sum F_{ni} \tag{2.39}$$

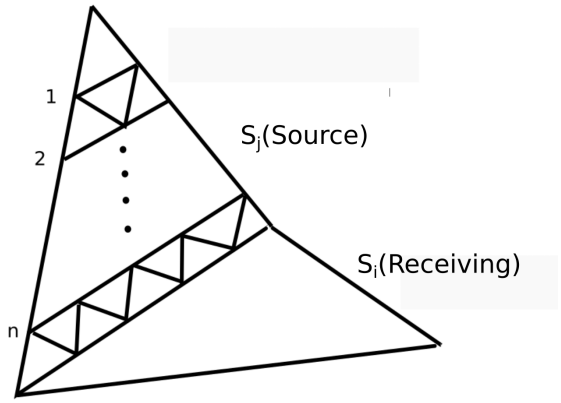

Figure 2.9: The subdivision

2.2.2.5 Intervisibility

For two surface patches chosen in an urban geometry, the following condition can be concluded:

- As shown in case 1 in Figure 2.10, the two patches are on the same planar surface. In this case, they cannot see each other, and the view factor is thus set to 0.
- Case 2 in Figure 2.10 illustrates the case with two patches on the different surfaces. This time, they still cannot see each other, indicating a null value of the view factor between the two patches. To have direct transfer between the patches, the scalar product of the surface normal and vector between the contour of the patches should be positive:

$$\langle \vec{n_i} \cdot \vec{ij} \rangle > 0 \; and \; \langle \vec{n_j} \cdot \vec{ji} \rangle > 0 \tag{2.40}$$

- Case 3 describes the condition that satisfies Eq. 2.40. In this case, there is radiation transfer between the patches if no obstruction exists between them.

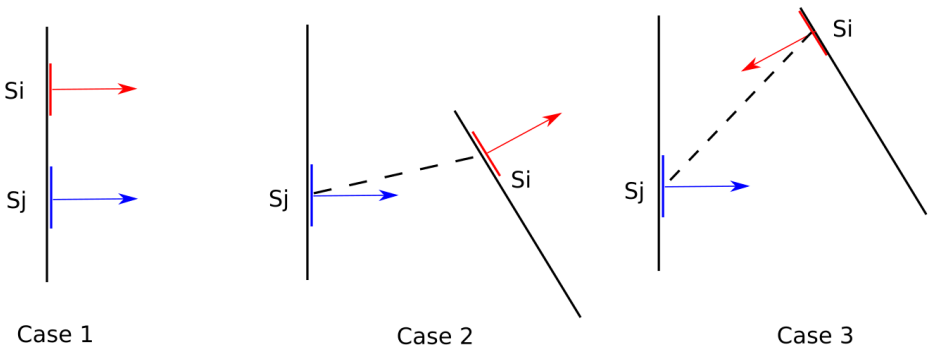

Figure 2.10: The different cases of two patches in the geometry

Obstruction detection is easier than the traditional intersection calculation in ray tracing. In the ray tracing method, it is necessary to determine whether the ray can be blocked by an object and where the intersection point is. However, in the view factor calculation, it is not important to identify which object is responsible for the intersection. In other words, we do not need to know which patch blocks sight for the two chosen patches.

Two algorithms are considered in this thesis. The first is ray axis aligned bounding box intersection tests, which is known as the AABB problem [105]. This is a common method used in ray tracing to test for intersections [106]. For buildings in cuboid shapes, the AABB test can be implemented directly. For an object with a complex shape, the bounding volume 2.11 is applied [107]. A building with a complex shape can be regarded as a cube that covers the entire body.

In this thesis, the code of Jesús Mena [108] is used for this test. The AABB method is not applied very much in this thesis, as the bounding volume is not precise when the patch size is small.

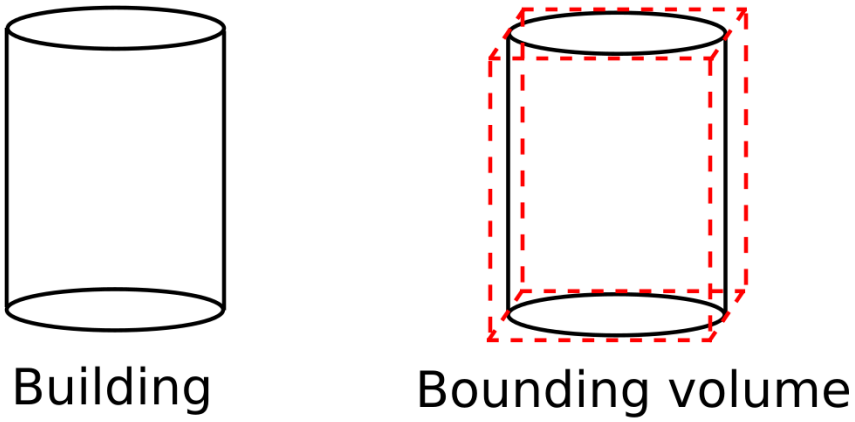

Figure 2.11: An example of the bounding volume

The second method is the main method used in this thesis. The idea is to simplify the problem from ray-box intersection to ray-surface intersection. All the surfaces of the possible obstruction objects, generally buildings, are chosen for the intersection test. This is achieved by a second (coarser) mesh for these objects. Different from the initial refined mesh, the patch size of the second mesh is far larger than that of the first mesh to reduce the patch number and thus decrease the time consumption. This step leads to the traditional ray triangle intersection step.

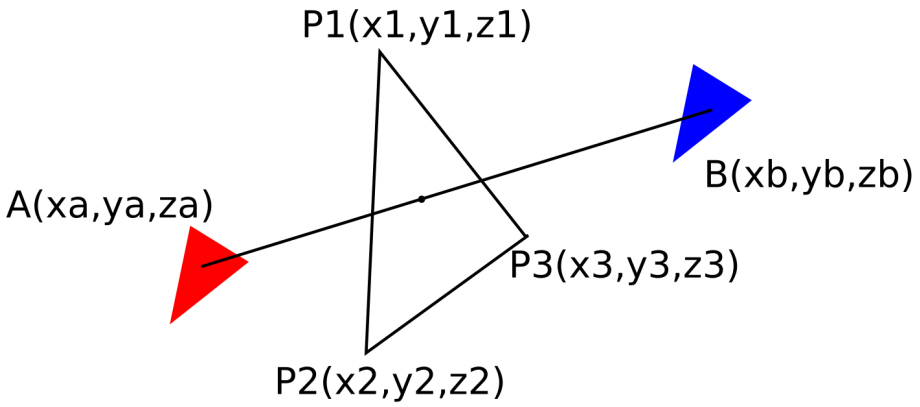

Figure 2.12: The ray surface intersection calculation

The two surfaces for the view factor calculations are presented by the red and blue triangles in Figure 2.12. The third patch located between the two is presented by a triangle with the three vortices (P1, P2, P3). The positions of the red and blue triangles are given by

their center coordinates. The line AB is defined by:

$$\begin{aligned} AB &= A + (B - A)t \\ &= \begin{bmatrix} x_a + (x_b - x_a)t \\ y_a + (y_b - y_a)t \\ z_a + (z_b - z_a)t \end{bmatrix} \qquad t \in \mathcal{R} \end{aligned} \tag{2.41}$$

The surface can also be defined by the coordinates of the vortex:

$$\begin{aligned} &P_1 + (P_2 - P_1)u + (P_3 - P_1)v \\ &= \begin{bmatrix} x_1 + (x_2 - x_1)u + (x_3 - x_1)v \\ y_1 + (y_2 - y_1)u + (y_3 - y_1)v \\ z_1 + (z_2 - z_1)u + (z_3 - z_1)v \end{bmatrix} \qquad u, v \in \mathcal{R} \end{aligned} \tag{2.42}$$

If the surface and the line are assumed to intersect:

$$\begin{aligned} A + (B - A)t &= P_1 + (P_2 - P_1)u + (P_3 - P_1)v \\ \begin{bmatrix} x_a + (x_b - x_a)t \\ y_a + (y_b - y_a)t \\ z_a + (z_b - z_a)t \end{bmatrix} &= \begin{bmatrix} x_1 + (x_2 - x_1)u + (x_3 - x_1)v \\ y_1 + (y_2 - y_1)u + (y_3 - y_1)v \\ z_1 + (z_2 - z_1)u + (z_3 - z_1)v \end{bmatrix} \qquad t, u, v \in \mathcal{R} \end{aligned} \tag{2.43}$$

Eq. 2.43 can be written as

$$\begin{bmatrix} x_a - x_1 \\ y_a - y_1 \\ z_a - z_1 \end{bmatrix} = \begin{bmatrix} (x_a - x_b) + (x_2 - x_1) + (x_3 - x_1) \\ (y_a - y_b) + (y_2 - y_1) + (y_3 - y_1) \\ (z_a - z_b) + (z_2 - z_1) + (z_3 - z_1) \end{bmatrix} \begin{bmatrix} t \\ u \\ v \end{bmatrix} \qquad u, v \in \mathcal{R} \tag{2.44}$$

If the ray is on the surface or parallel to the surface, the determinant of the matrix $\begin{bmatrix} (x_a - x_b) + (x_2 - x_1) + (x_3 - x_1) \\ (y_a - y_b) + (y_2 - y_1) + (y_3 - y_1) \\ (z_a - z_b) + (z_2 - z_1) + (z_3 - z_1) \end{bmatrix}$ should be null. Otherwise, $\begin{bmatrix} t \\ u \\ v \end{bmatrix}$ can be resolved. If *t* is between 0 and 1 ($t \in [0, 1]$), then the intersection point is located between A and B. If *u* and *v* are located between 0 and 1 ($u, v \in [0, 1]$), then the sum of these two values is not bigger than 1 ($u + v \leq 1$), and the intersection point is located inside the triangle. In this condition, the third patch $P_1P_2P_3$ is considered to block the radiation transfer between the two chosen surfaces, and the view factor F_{AB} is 0.

2.2.3 Testing the view factor calculation

In this section, all the methods presented in the previous section are evaluated with different geometric models to determine their performance on the view factor calculation. The most notable algorithm for this thesis is the ISA because of its substantial advantage in terms of time consumption and accuracy in most circumstances. The DCI method provides the best accuracy among these methods, which leads to the reference result. The MC method is also tested in several calculations to compare with the other two methods in terms of accuracy and time consumption.

The test contains two calculation parts:

- The first part concentrates on the ISA method. As Macfarlane described [100], this method suffers from the adjacent patch case, which does not satisfy the 5 times rule. Therefore, we focus on the error produced by the ISA in these cases. Different calculations are performed to determine the magnitude of error. The subdivision is engaged afterwards to determine the efficiency of the local refinement.

- The second part compares the general view factor calculation methods (DCI, MC, ISA). The test uses a cube with different geometric meshing systems. First, the performance of the methods is compared by calculating the S2S view factor. A surface normally contains several patches, which are used to characterize the global radiation transfer between the surfaces. The second part concentrates on the heat transfer between the patches. This provides an image of the error distribution at every surface.

2.2.3.1 The adjacent patches for the ISA

The first calculation involves a study of the subdivisions for the ISA method to determine the necessary fraction between the distance between two surfaces and the longest dimension of the source surface. Unlike the case of other fields, such as computer graphics, the geographic model with radiosity is quite simple here. Most of the time, the shape of the building is a hexahedron, typically a rectangular cuboid. There are also cylinder-shaped or elliptical cylinder-shaped buildings, but curved surfaces do not appear as much in the urban morphology. But at the same time, the surfaces are divided into triangle patches for the view factor calculation due to the better adaptation of different geometric size, even though the quadrilateral mesh is more accurate. This helps us classify the inappropriate cases for the ISA into two categories (Figure 2.13):

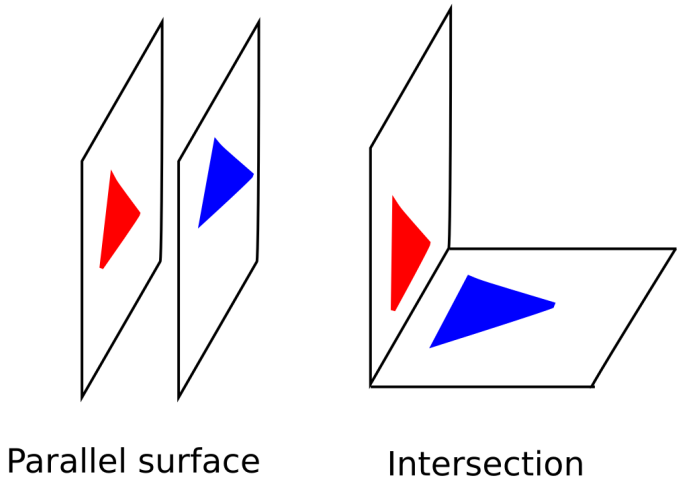

Figure 2.13: The subdivision required cases

- Parallel surfaces: This case applies when the space between two surfaces of the building is too small. Due to the cost of the simulation, the size of a surface patch is often generated with a minimum value, and sometimes the patch is not small enough.

- Perpendicular surfaces: This happens far more frequently than the parallel surface case. Almost every building view factor simulation contains this case. For the simulation of the exterior of the building, the location at the bottom of the wall that connects to the ground is associated with a calculation error for the ISA method. In the building

interior simulation, this case exists where two construction components intersect with each other, such as a wall-wall or wall-floor intersection. Because of the hexahedron shape, this case always occurs and cannot be avoided, even with well-refined meshes.

The DCI is also applied to perform the same calculation for reference. The error in percentage is calculated by Eq. 2.45.

$$Error = \frac{100(FF_{ISA} - FF_{DCI})}{FF_{DCI}} \tag{2.45}$$

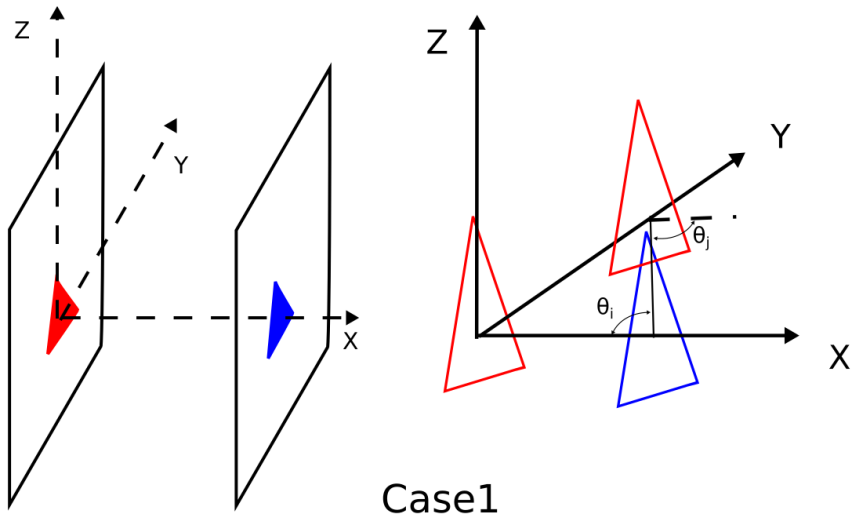

Figure 2.14: The parallel case:Only the red triangle(source patch) changes its position in the plane zOy. The blue triangle(receiving patch) stay at its initial position during the entire test

Parallel patches As shown in Figure 2.14, the source surfaces and receiving surface are parallel to each other with a distance X [m]. Equilateral triangle patches (side=1 m) are chosen on each surface (red for the source surface, blue for the receiving surface). The two triangles are located at the same position. During the calculation, the position of the red triangle on the plane zOy and the distance X changes. Because of the symmetry on the plane zOy, the red triangle moves in the area $x = X, y > 0, z > 0$ only. Its position is characterized by its center (X, y_{red}, z_{red}). To satisfy the $5\times$ rule, only the result for this field is reported:

$$X^2 + y_{red}^2 + z_{red}^2 \leq 25 \tag{2.46}$$

For each determined distance X, as shown in Figure 2.14, θ_i and θ_j are identical because the normals of the two triangles are parallel. Additionally, the modulus of $\vec{R}$ can be calculated by:

$$|\vec{R}| = \frac{X}{cos\theta_i} \tag{2.47}$$

transforming Eq. 2.37 into:

$$F_{ji} = \frac{A}{\pi X^2} cos^4\theta_i = \frac{AX^2}{\pi |\vec{R}|^4} \tag{2.48}$$

with the range of $\theta_i \in [0°, 90°)$.

Considering the distance between the coordinate center point O and the triangle center j to be marked as r:

$$\begin{aligned} r^2 &= y_{red}^2 + z_{red}^2 \\ &= |\vec{R}|^2 - X^2 \end{aligned} \tag{2.49}$$

Eq. 2.48 can finally be written as:

$$F_{ji} = \frac{AX^2}{\pi(X^2 + r^2)^2} \tag{2.50}$$

Eq. 2.50 shows that the view factor between the two triangles is a function of r, which means that the value is the central symmetry of axis *x*. In our calculation, the red patch shifts 0.1 m each time from the center point O. The distance X, which is the distance between the parallel surfaces, varies from 0.2 m to 5 m with a step of 0.2 m. The results of the percentage error compared with the DCI method are presented in Figure 2.15:

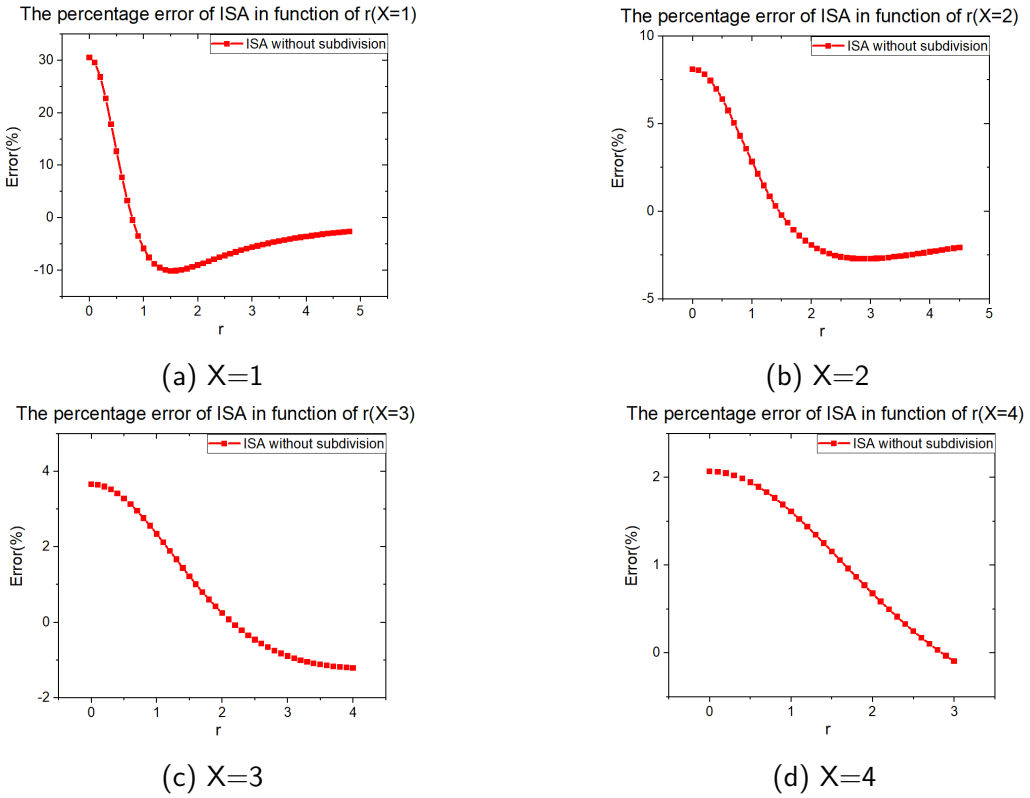

(a) X=1 (b) X=2

(c) X=3 (d) X=4

Figure 2.15: The percentage error of ASI in function of *r*

The peak of the error for each case of X located at the initial position: The closer the two surfaces are, the larger the peak value (30% when X equals 1 and 2% when X equals 4). However, the error drops sharply when the position moves towards the edge of the area, particularly for the case with small X. In Figures 2.15a and 2.15b, as the patch approaches the edge of the field, the error has already stabilized. This indicates that the factor $|\vec{R}|/l_{max}$ does not need to reach 5 to obtain a stable result. In contrast, Figure 2.15d shows that the value continues to drop when *r* reaches 3. The ratio $|\vec{R}|/l_{max}$ is larger than 5 in this case, although the error itself seems to be very small. The result at the edge of each case shows

that the stable error value decreases as the distance X increases (-2.59% for X=1; -2% for X=2; -1.2% for X=3; and -0.1% for X=4) even if the $|\vec{R}|/l_{max}$ factors are almost the same at approximately 5.

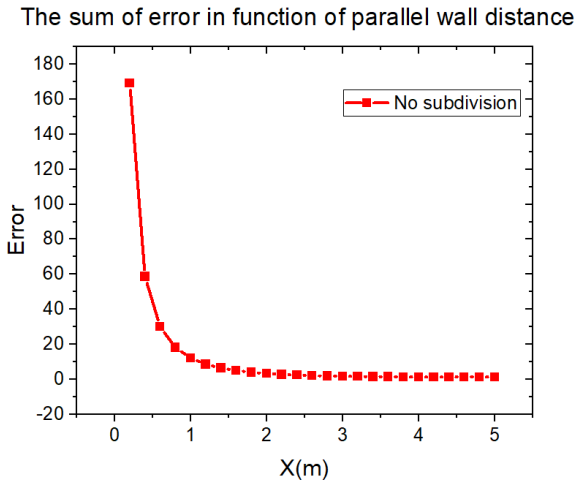

Figure 2.16: The percentage error in the sum of area $x = X, y > 0, z > 0$ in function of distance between the two parallel walls(X)

The sum of the errors in each zOy plane is also calculated for all the cases, with the aim of acknowledging the overall impact of the ISA on areas that do not satisfy the 5 times rule. The profile as a function of X for the parallel case is presented in Figure 2.16. The error for the whole area decreases to 10% when X reaches 1.2 m and to 5% when X equals 1.6 m. The decrease stops at 1.32% at the maximum X value. This error sum applies only to quadrant $x = X, y > 0, z > 0$. This means that the error of the 4 quadrants reaches 5.2% when X is 5 m.

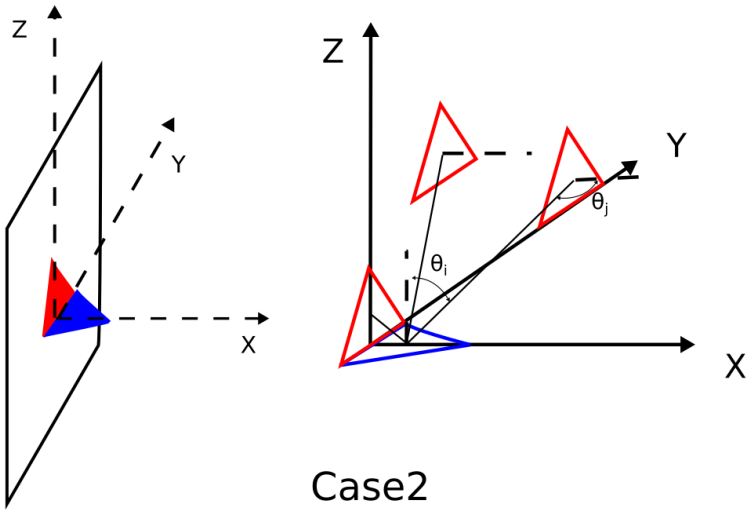

Figure 2.17: The Perpendicular case

Perpendicular patches As shown in Figure 2.17, this time, the blue patch (receiving surface) is perpendicular to the red patch (emitting surface). The initial distance of the patches is calculated by the coordinates of the two triangle centers, yielding $\frac{\sqrt{6}}{6}$. The variation in position is the same as in the parallel case. Additionally, the calculated area is limited within

$x = X, y > 0, z > 0$ because of the symmetry. The only difference is that the arbitrary point is located at the middle point of the bottom side, not the center of the triangle, as in the perpendicular case. If the center of the emitting triangle is presented by (y_j, z_j), the distances $|\vec{R}|$, θ_i and θ_j are calculated by:

$$|\vec{R}| = \sqrt{y_j^2 + z_j^2 + \frac{1}{12}} \tag{2.51}$$

$$cos(\theta_j) = \frac{\frac{\sqrt{3}}{6}}{R} \tag{2.52}$$

$$cos(\theta_i) = \frac{z_j}{R} \tag{2.53}$$

with $z_j \in [\frac{\sqrt{3}}{6}, \infty)$ and $y_j \in [0, \infty)$. Three cases are discussed:

1: The emitting triangle moves along axis *y*, which keeps z_j unchanged. The equation to calculate the view factor is then:

$$F_{ji} = \frac{A}{12\pi(y_j^2 + \frac{1}{6})^2} \tag{2.54}$$

2: The triangle moves along axis *z*, which suggests that *y* always equals 0. Eq. 2.37 changes to:

$$F_{ji} = \frac{\sqrt{3}Az_j}{6\pi(z_j^2 + \frac{1}{12})^2} \tag{2.55}$$

3: This is the general case; the triangle moves in this quadrant with $y_j > 0, z_j > \frac{\sqrt{3}}{6}$. The equation is:

$$F_{ji} = \frac{\sqrt{3}Az_j}{6\pi(z_j^2 + y_j^2 + \frac{1}{12})^2} \tag{2.56}$$

We assume that z_j can be expressed by $\frac{\sqrt{3}}{6} + y_j tan\theta'$, with θ' as the azimuth angle. The resulting equation 2.56 becomes:

$$F_{ji} = \frac{\sqrt{3}A(\frac{\sqrt{3}}{6} + y_j tan\theta')}{6\pi((\frac{\sqrt{3}}{6} + y_j tan\theta')^2 + y_j^2 + \frac{1}{12})^2} \tag{2.57}$$

A demonstration of these equations can be found in appendix 6.1.

The results are shown in Figure 2.18 The positive peak value of 85% is also at the initial position of the red patch. However, it generates a negative peak of 54% near the positive value. Moreover, it is not like the parallel case, which involves central symmetry of axis *x*. Here, the big error exists only at the horizontal level. Furthermore, this case has the same tendency as in the small-X condition in the parallel case: The 5 times rule is exaggerated. When $|\vec{R}|/l_{max}$ reaches 4, the error has stabilized. Regarding the difference in the full area that does not satisfy the 5 times rule, the value in case 2 is 44% in one quadrant and 88% for the whole surface.

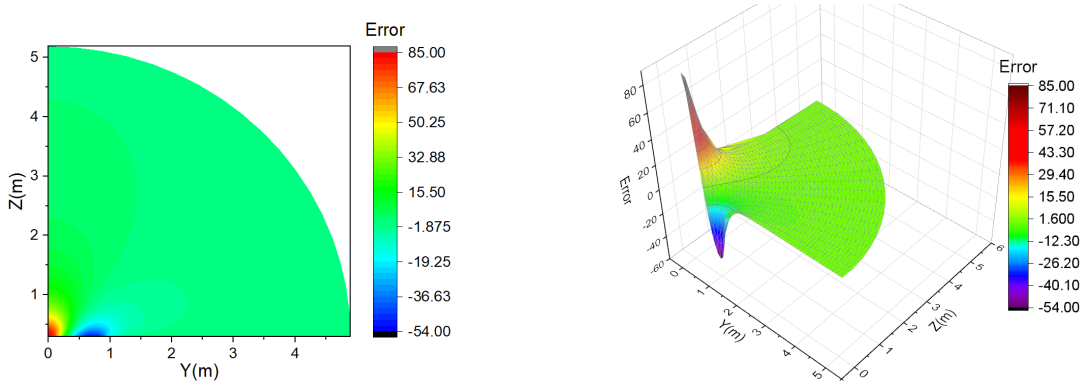

(a) Contour Colourmap (b) 3D Colourmap

Figure 2.18: The relative error for perpendicular patches

Local refinement for the ISA method Demonstrated by the calculations in the two cases, the ISA method suffers from the adjacent patch situation. For the parallel case with a small distance X and the perpendicular case, the 5 times rule is applicable because the variation stops before it reaches a factor of five. For the parallel case with a large distance X, a longer $|\vec{R}|$ is needed to establish the result. Moreover, the results indicate that a large error can be generated in the view factor calculation of adjacent patches. To reduce the error, the subdivision method is applied in this part.

The view factor calculation for each case remains the same in this part, and only the subdivision method is added. The subdivision number is calculated by the most extreme condition:

- Case 1: The smallest $|\vec{R}|/l_{max}$ factor is 0.2, which is the first calculation with X=0.2 m, and the red patch stays at the initial position. In this case, the largest dimension of the patch should be reduced to at least 0.04 m, which suggests 25 for subdivision number n_{sub}.
- Case 2: The most extreme case is also the first case, with the red patch located at the initial position. The distance between the patches is $\frac{\sqrt{6}}{6}$. In the calculation, the subdivision number n_{sub} is set to 20, which increases $|\vec{R}|/l_{max}$ to 8.2.

The results of the relative error are presented in Figures 2.19 and 2.20.

Figure 2.19 shows that the subdivision is quite effective in reducing the error for every distance X. The peak value decreases to less than 50% of the result calculated without subdivision (30% to 12% for X=1; 8% to 4% for X=2; 3.6% to 1.8% for X=3; and 2.1% to 1% for X=4). The shape of each curve does not change considerably, and the values simply converge toward 0. For perpendicular patches, the positive peak disappears, while the negative peak exhibits only a slight reduction in value.

In terms of the overall error in the area that does not satisfy the $5\times$ rule, Figure 2.21 shows that the error drops sharply from 170% to 20% when X equals 0.2 m. However, there is still a nearly 20% error, which cannot be readily decreased. Under this condition, to obtain the precise view factor, the basic mesh needs to be refined. The error decreases to 10% when X rises to 0.6 m and 5% when X equals 1 m, and it stops at 0.65% for $X = 5\ m$. This approach successfully reduces the error by half with a subdivision method. For case 2, this value decreases from 44% to -5%

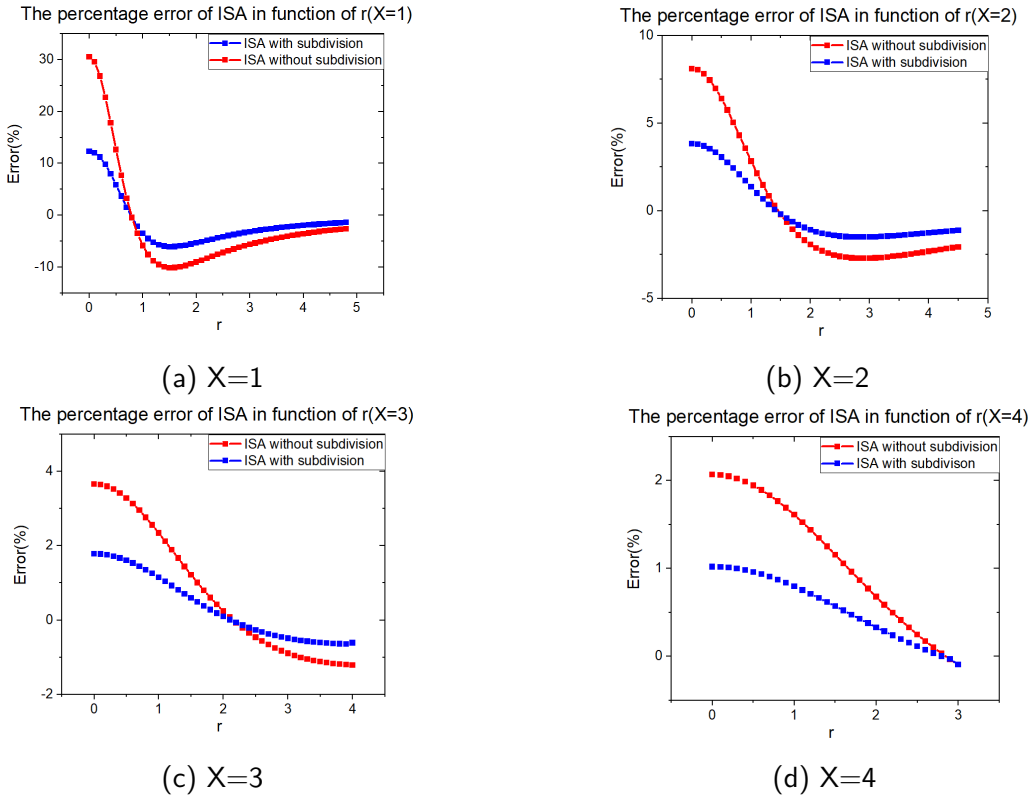

(a) X=1 (b) X=2

(c) X=3 (d) X=4

Figure 2.19: The percentage error of ASI in function of r

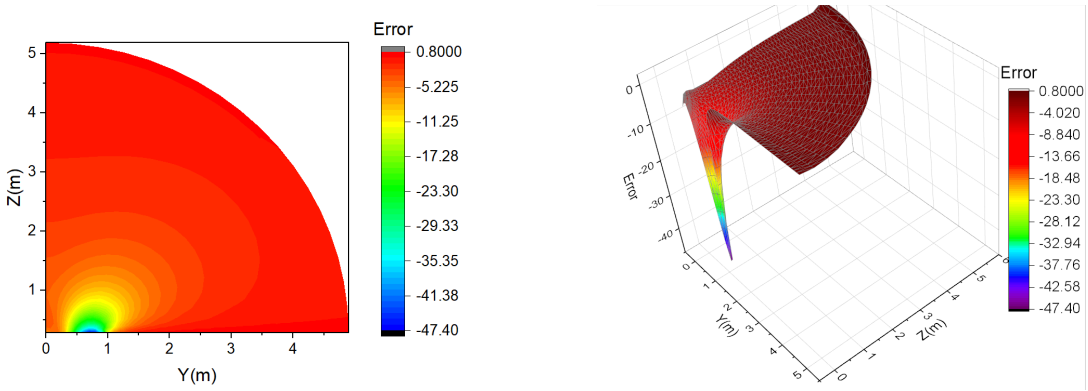

(a) Contour Colourmap (b) 3D Colourmap

Figure 2.20: The relative error for perpendicular patches with subdivision

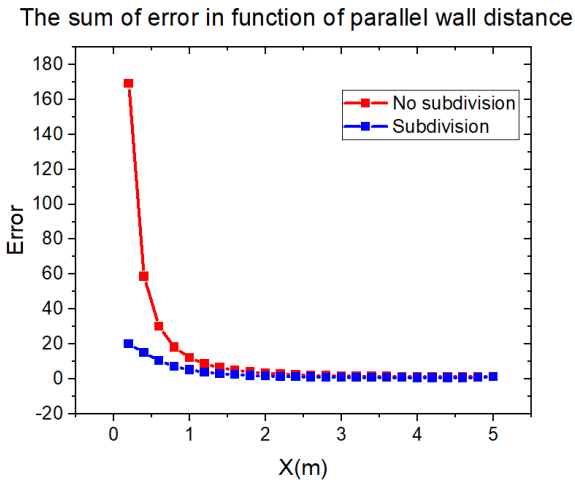

Figure 2.21: The sum of error in the area $x = X, y > 0, z > 0$ in function of distance X

To conclude, the subdivision method can help the ISA method obtain precise results. However, even with a high subdivision number, the subdivision method cannot eliminate the error in the case where the two surfaces are too close. This means that a finite error can always be expected in the calculation. To continue to reduce the error, better mesh refinement is required.

2.2.3.2 Radiation transfer in cubes

In this section, the view factor calculation methods are evaluated by the precision of the results and their time consumption. The first test is to calculate the view factor between the surfaces in a cube. This approach concentrates on the transfer from one entire surface to another. The second part specifies the difference in every single patch to determine the error distribution at every surface.

The cube dimensions are 1 m×1 m×1 m. The surfaces are perfectly diffuse with an emissivity of 0.9. There are 4 levels of mesh tested in this part, which are shown in Figure 2.22.

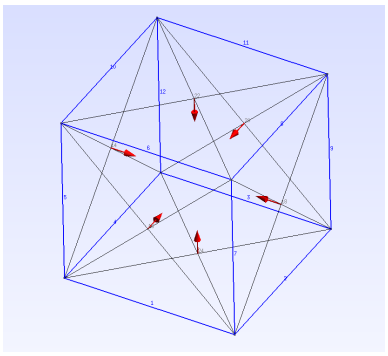

(a) 4 Patches

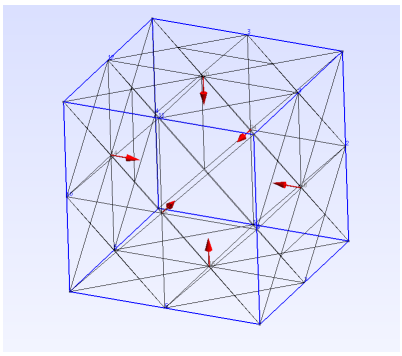

(b) 16 Patches

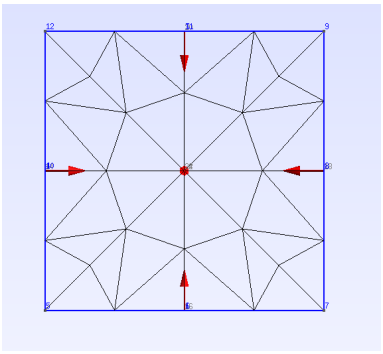

(c) 40 Patches

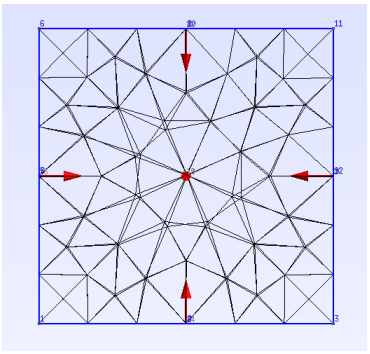

(d) 104 Patches

Figure 2.22: The different patch levels for the test cube

The mesh is generated by the software GMSH [109]. Different mesh levels are realized by adding nodes on the side of the cube (Table 2.1). For the three methods:

Patches	4	16	40	104
Node added	0	1	3	5

Table 2.1: Adding nodes on a side of cube

- ISA: The subdivision method is applied with the ISA. A detection factor of R/l_{max} is applied to each pair of two surfaces. Once R/l_{max} is below 5, the subdivision is engaged, and the emitting patch is divided into smaller patches. The division number is not a predefined input. It is calculated automatically as needed in every case, which helps enable all the smaller patches to meet the $5\times$ rule in every case without waste of time. A large default value makes it possible to perform the unnecessary calculation for the case whose R/l_{max} is just slightly smaller than 5.
- DCI: The DCI code applied in this section was developed by Nicolas Lauzier and Daniel Rousse [110], University Laval. The results serve as a reference for the other two methods.
- MC: Initially, the ray ejection number is 1000 for each patch, which remains the same during the comparison with the other two methods. Then, different ray ejection numbers are set for each mesh case (100, 500, 1000, 5000, 10000, and 50000 for each patch). According to [99], the complexity for this scenario is $O(n_{patch} \log n_{patch})$.

The calculation result of the cube is presented by a matrix with dimensions $n_{patch} \times n_{patch}$. The analysis is carried out in two parts. With the original view factor matrix, a sum of view factors of patches in a surface is calculated to determine the view factor between the surfaces. In a cube, the view factor between each pair of surfaces is a value close to 0.2. This can reveal the impact of the method on the overall surface view factor calculation. The second part concentrates on the difference distribution for each surface. This time, a full radiosity calculation is executed for each case to analyze the influence on the detailed positions of a surface.

The S2S view factor In a cube, because of the symmetry, there are only two kinds of surfaces: two parallel surfaces and two perpendicular connected surfaces. Therefore, the view factor can also be divided into these two kinds (F12 for the perpendicular case and F13 for the parallel case); the two view factors have a value very close to 0.2 [111]:

$$F12 = 0.200043777 \tag{2.58}$$

$$F13 = 0.199824896 \tag{2.59}$$

The calculation results of F12 and F13 are shown in Figure 2.23. Figure 2.24 illustrates the error of the different methods' results relative to the correct value.

For the ISA method, the error appears in the case where the number of patches is relatively small. Approximately 6% of the error is generated for F12 and over -1% for F13. The large size of the mesh leads to this error during the calculation. Even with the $5\times$ rule and the subdivision, the error is not negligible. With additional patches, the error decreases gradually from 6% to -1% for F12 and -1% to 0.5% for F13. Furthermore, the parallel case seems unlikely to converge towards the exact value. There is over -1% error that cannot be eliminated. However, the error itself is small in terms of the view factor. Its impact on the difference in incident flux is limited.

It is not surprising that the DCI method exhibits the best performance among these methods, regardless of the patch size. The maximum error is limited to 0.5%. The MC method seems to be accurate with a large patch size. When the patch number increases, its performance starts to struggle. In this case, more samples are required for the MC method to obtain a precise result.

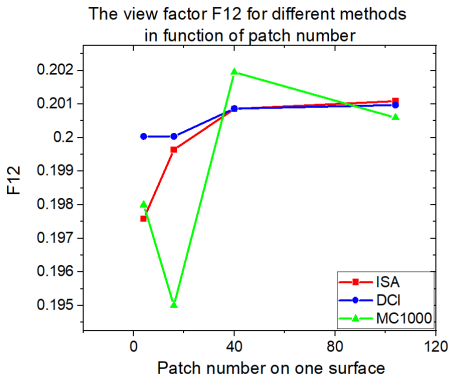

(a) F12

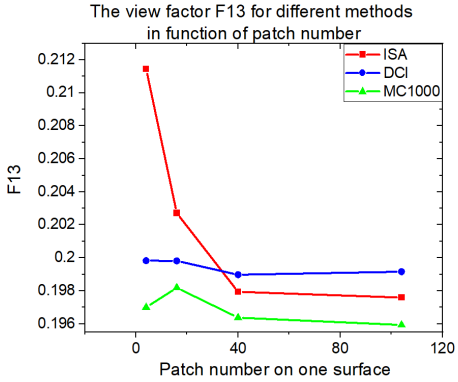

(b) F13

Figure 2.23: The view factor calculated by the different methods in function of surface patch number

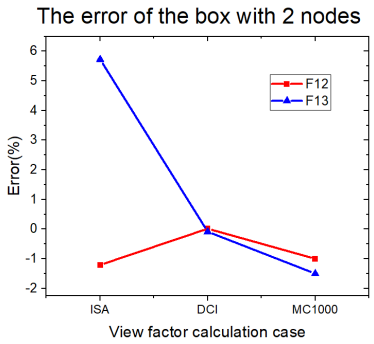

(a) 4 Patches

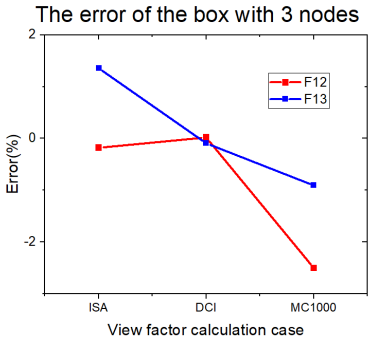

(b) 16 Patches

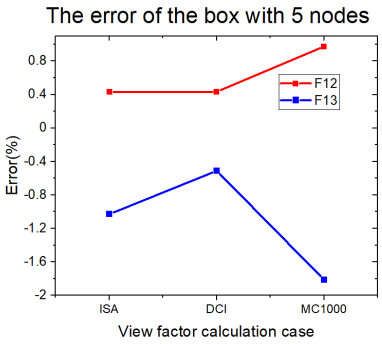

(c) 40 Patches

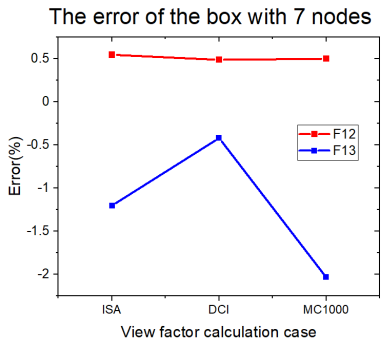

(d) 104 Patches

Figure 2.24: The comparison of the result of each method with the exact F12 and F13 value

Then, the calculation of the MC method is developed with the variation in ray number. We focus on the precision of the results and the calculation time.

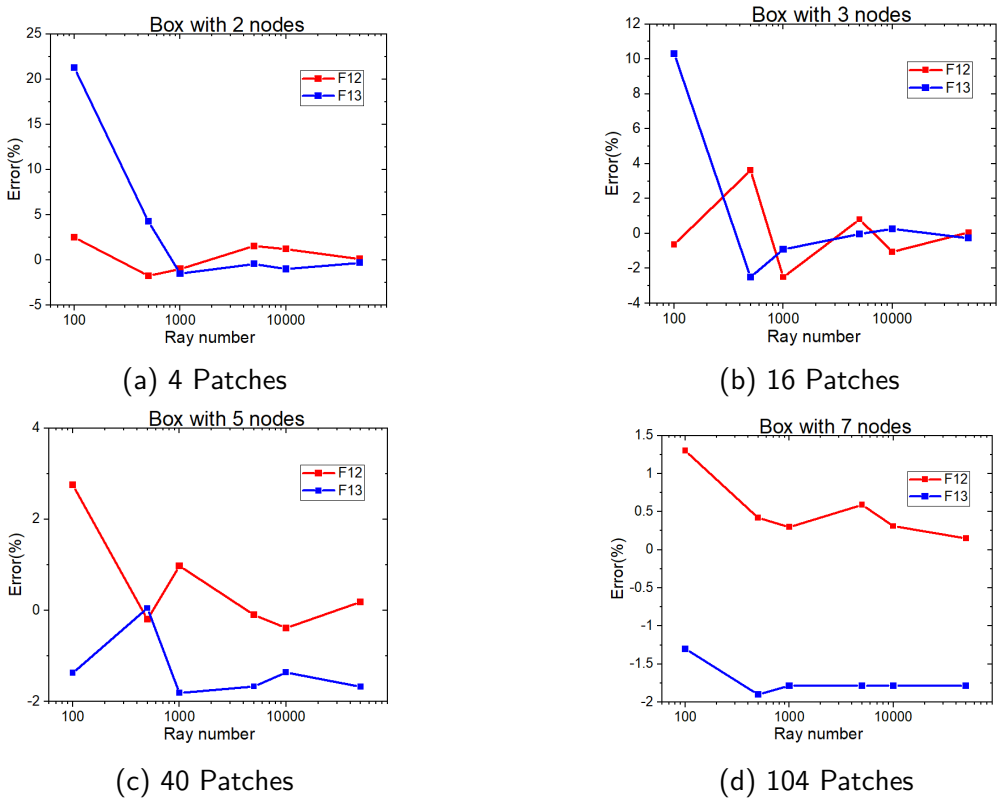

(a) 4 Patches

(b) 16 Patches

(c) 40 Patches

(d) 104 Patches

Figure 2.25: The percentage error of the MC method in function of ray ejecting number

Figure 2.25 shows that F13 converges slightly faster than F12. The amplitude decreases to a small value in each case when the ray number passes 1000. However, there is also an error for the MC method that cannot be eliminated with increasing patch number. In contrast, this error for the parallel case increases from almost 0 to -1.6%. However, similar to the ISA method, the error in the view factor is small, and its influence on the incident flux is minimal.

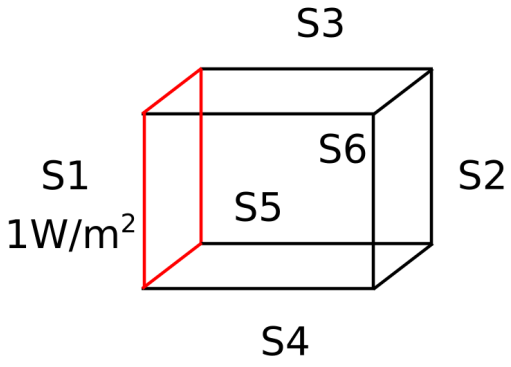

Figure 2.26: The boundary condition of cube

Patch-to-patch transfer The second part consists of a full radiosity calculation for each box with different patch numbers. As shown in Figure 2.26, we assume a surface (S1) that with normalized emission $1W/m^2$ and 0 emission for the other surfaces. The reflectivity for each surface is set to be 0.1. The view factor matrix obtained in the previous section is

substituted in this section to determine the difference in incident flux. The result of the box with 104 patches on each surface is presented here as an example. The results for the other configurations are given in appendix 6.3.

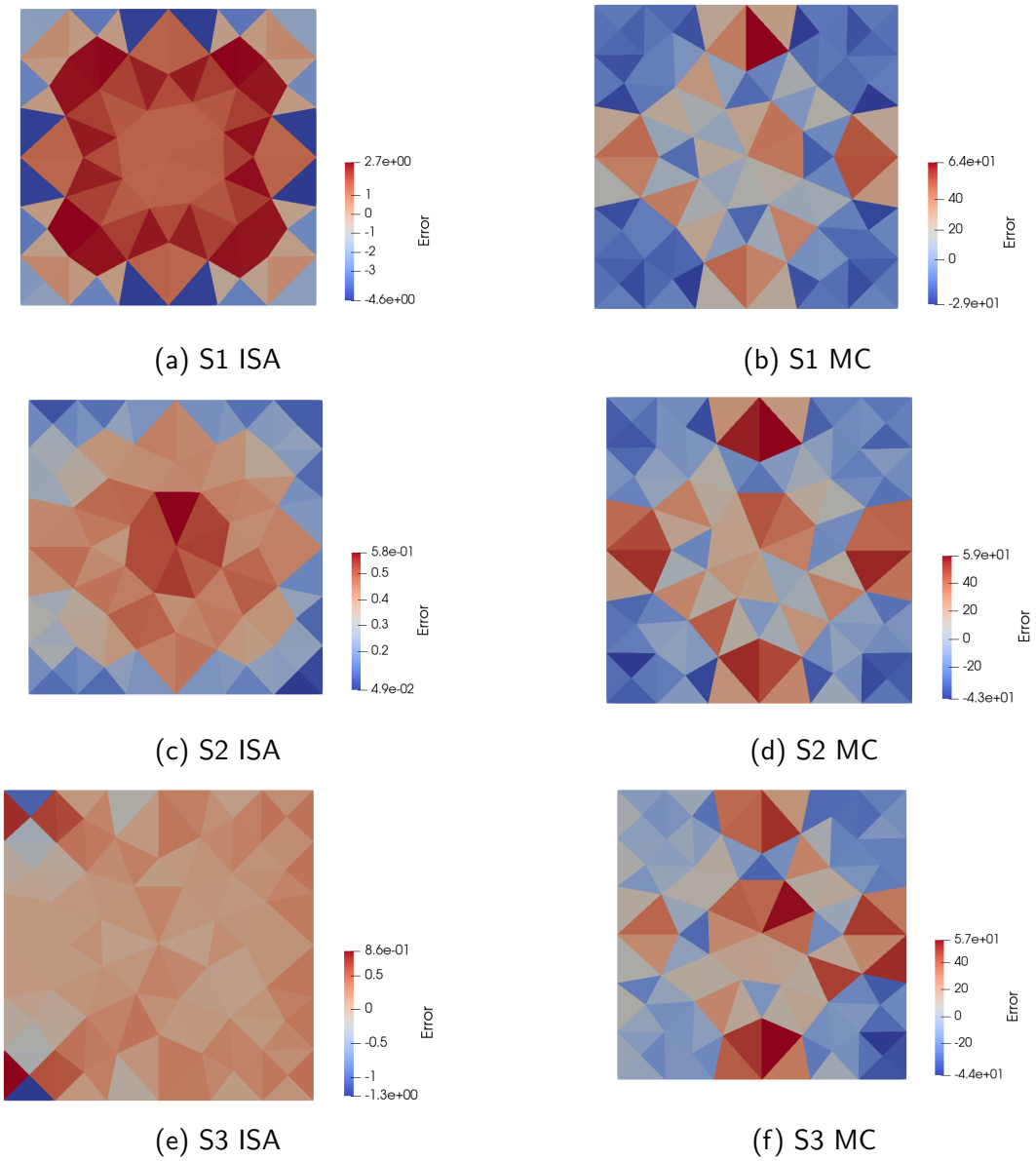

(a) S1 ISA (b) S1 MC

(c) S2 ISA (d) S2 MC

(e) S3 ISA (f) S3 MC

Figure 2.27: The percentage error of each patch on the three chosen surfaces

Because of the symmetry, the results of S3 to S6 are quite similar. There are only three surface types in this problem: the emitting surface (S1), the surface parallel to the emitting surface (S2), and the connection surface, which is positioned perpendicular to the two parallel surfaces. This time, the DCI result is set as the reference for the ISA and MC methods. The percentage error shown in Figure 2.27 is calculated with Eq. 2.45.

For the MC method, the pattern is almost identical for all three surfaces. The method seems to struggle with corners. In all cases, for the patches located near the corner, there is always a negative gap between its result and the DCI result. These differences sometimes reach 50% locally, which is quite significant. On the other hand, for the patch between the corner, this method exaggerates the incident energy, which suppresses the negative difference at the corner. There is also a slight increase at the center of the surface. The amount is not prohibitively high except for perpendicular surface S3. When using the MC method to calculate the view factor, it can be expected that the incident power is slightly diverted from

the corner to the center of the side and the center of the surface.

For the ISA method, the center of the emitting and parallel surface gathers more energy than expected. In the case with a larger mesh size, this phenomenon does not disappear. Only in S3, which is under a large flux gradient, is the large error area shifted toward the side closer to the source surface. As a result, a negative error is produced near the side to compensate for the error in the center. Compared with the MC method, the error magnitude is far smaller, which means that the performance of the ISA is more stable than that of MC.

In general, the difference in incident power for each surface in total is nearly negligible. Only the distribution of this difference differs from one method to the others. If the simulation focus on the sum or mean value of the incident energy on a building surface, this difference is meaningless. In terms of result precision, all these methods can meet the demand. Simulation method is preferred when its time consumption is lower. The MC method may be the preferred choice because of its complexity. The only problem with this method is to predict the ray number. Because of the different morphologies and patch sizes, the number can vary greatly from case to case. If we concentrate more on the distribution of the energy, corresponding to the value for a part of the surface, then the ISA may be a better choice because its variance is smaller than that of the MC method.

Time consumption From the perspective of time consumption, as presented in Figure 2.28, with additional patches or rays, the calculation time jumps from several hundred seconds to 17000 s. It is obvious that the patch number n_{patch} is more influential than the ray number. The complexity is $n_{patch}log(n_{patch})$ in this case. Among all three methods, the DCI method requires far more time than the other two if the number of patches is large. This is the reason that this method is impractical for urban radiation calculations because the patch number is usually far greater than we use in this test. The base of the ISA also provides an $O(n^2)$ complexity as the DCI method does. With the subdivision, it takes more time to calculate the view factor of the small subdivided facets. With a variable division number and an undetermined number of patches that need subdivision, it is quite difficult to estimate the time if we vary the patch number. Overall, because there is no integral in the calculation, this method can provide considerable time savings over the DCI method. The MC method has an advantage in its complexity. Additional patches can enhance this advantage. In Figure 2.28b, for the box with 104 patches on a surface, the MC method has already spent less time than the ISA. This shows that the MC method is superior if we take only the calculation time factor into consideration.

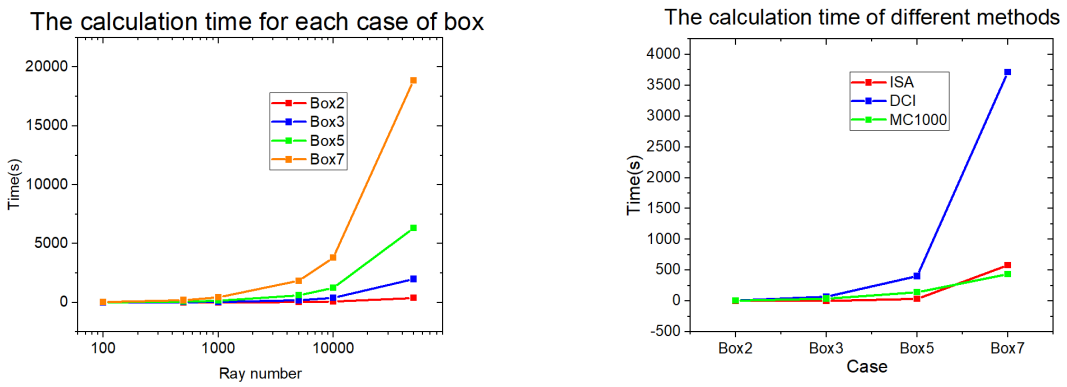

(a) MC method with different ray number

(b) All methods comparison

Figure 2.28: The relative error for case 2 with subdivision

2.3 Concluding remarks

In this chapter, an approach to calculate radiative transfer in a transparent medium was developed. The radiosity method was chosen for the calculation. Different methods of view factor calculation were discussed, and the ISA, MC and DCI methods were selected to be tested with a simple geometry.

The first study on the adjacent patches for ISA showed an error of over 170% and 44% generated in the parallel and perpendicular cases, respectively. This means that the ISA method cannot work alone and that the subdivision method is necessary to reduce this error in these cases. With the subdivision, more than half of the error was eliminated. However, even with a high subdivision number, the error could not be fully eliminated or reduced to a negligible value. To continue to decrease this error, better mesh refinement is required.

The second study contained a test with a cube. We concentrated first on the S2S view factor value and characterized the difference in transfer between the surfaces. With a high patch number for each surface, a maximum error of 1% was generated by the ISA and MC methods. This means that both of these methods can obtain precise values if the surface is well meshed. However, in the low-patch-number case, the performance of the ISA dropped due to the error in the calculation of adjacent patches mentioned in the previous paragraph. Then, a full radiosity calculation was launched with the cube to determine the difference in every single patch with these methods. Compared with the DCI result, the ISA exhibited better performance, as its difference was smaller than that of the MC method.

In terms of time consumption, the DCI method consumes far more time than the other two methods, which makes it impractical to apply to a complex geometry. With a simple geometry, the ISA took less time than the MC method, but this ordering flipped with an increasing patch number. The time consumption of the MC method depends highly on the ray number, which relates to the complexity of the geometry and is hard to predict before the simulation.

The ISA and MC methods were candidates for our view factor calculation method, considering the DCI time consumption problem. We ultimately chose the ISA method because of the uncertainty of the ray number in the MC method. This could have an impact on the heat transfer between the patches and the calculation time. Most of the time, it is not easy to predict the necessary ray number to obtain a precise result. The increasing number can substantially extend the calculation and erase its advantage in complexity. At the same time, we should be aware that even with the subdivision, the ISA still holds an absolute error of approximately 5% to calculate the view factor for the area that does not satisfy the $5\times$ rule in the adjacent case. This error can be totally erased if the mesh is well designed for the parallel wall. However, in the vertical case, the error always exists, and the refinement of the patch can decrease only the superficial area.

In this chapter, the air is considered to be a transparent medium, and an approach is developed based on this hypothesis. However, what if air plays a role in radiation transfer and its impact cannot be neglected? In the next chapter, we focus on air gas and aim to determine the answer to this problem.

Chapter 3

Air as a participating medium in radiative heat transfer

Contents

3.1 The Radiative Transfer Equation(RTE)

The previous chapter was dedicated to radiative exchanges between surfaces, assuming that atmospheric air is transparent. Here, we consider the more general case in which air interacts with the radiation field. The main tool for the present analysis is the RTE.

The RTE mathematically describes the rate of change of incident radiation propagating within a participating medium due to the interactions of the radiation field with the medium by radiative emission, absorption and scattering.

Let us define the spectral (monochromatic) intensity $I_\lambda(\Omega)$ $[W.m^{-2}.sr^{-1}.\mu m^{-1}]$ as the radiative energy dQ that exits a surface dS inside a solid angle $d\omega$ around a direction Ω, as shown in Figure 3.1, inside a small interval $d\lambda$ of wavelengths:

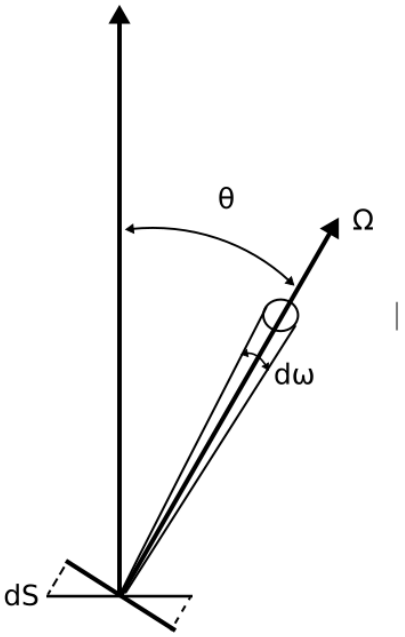

Figure 3.1: Radiative emission by an elementary surface

$$I_\lambda(\Omega) = \frac{dQ}{cos\theta dS d\omega d\lambda} \tag{3.1}$$

The RTE provides a way to calculate the rate of change of $I_\lambda(\Omega)$ along an elementary path increment, from a point s along a ray to a point $s + ds$ along the same ray, within a period of time dt, due to the interactions mentioned above. This rate of change is:

$$dI_\lambda(\Omega) = I_\lambda(s + ds, t + dt, \Omega) - I_\lambda(s, t, \Omega) \tag{3.2}$$

When an electromagnetic wave passes through a participating medium, a part of its energy can be absorbed or scattered along a distance of propagation ds, leading to a decrease (hence the negative sign) in its initial value by the following amount:

$$dI_\lambda(\Omega)_{ext} = -\beta_\lambda I_\lambda(\Omega) ds \tag{3.3}$$

where β_λ is the spectral extinction coefficient, which is the sum of the absorption $\kappa_{\lambda,abs}$ and scattering $\kappa_{\lambda,sca}$ coefficients. Both are functions of wavelength.

Over the same path increment ds, the participating medium can also emit radiation leading to a reinforcement (hence the plus sign) of the radiation field:

$$dI_\lambda(\Omega)_{emis} = \kappa_{abs} I_{b,\lambda} ds \tag{3.4}$$

where $I_{b,\lambda}$ is the given by the Planck law (Eq. 2.1).

At the same time, a portion of the radiation field coming from all possible directions (represented by the solid angle Ω') can be scattered in the direction Ω, leading to an increase in the radiative intensity along ds:

$$dI_\lambda(\Omega)_{sca} = \frac{\kappa_{\lambda,sca} ds}{4\pi} \int_{\Omega'} P(\Omega, \Omega') I_\lambda(\Omega') d\Omega' \tag{3.5}$$

where $P(\Omega, \Omega')$ is the phase function, which describes the probability of scattering incident radiation from directions Ω' to Ω.

The summation of the various sources described above allows estimating the rate of change $dI_\lambda(\Omega)$ as:

$$dI_\lambda(\Omega) = -\beta_\lambda I_\lambda(\Omega) ds + \kappa_{\lambda,abs} I_{b,\lambda} ds + \frac{\kappa_{\lambda,sca} ds}{4\pi} \int_{\Omega'} P(\Omega, \Omega') I_\lambda(\Omega') d\Omega' \tag{3.6}$$

Here, $dI_\lambda(\Omega)$ depends both on space and time. However, in our study, the term involving the time derivative can be neglected (for a small though non-null time increment Δt, $c.\Delta t$ is large compared to any spatial dimension encountered in our problem). The RTE then simplifies into:

$$\Omega.\nabla I_\lambda = -\beta_\lambda I_\lambda(\Omega) + \kappa_{\lambda,abs} I_{b,\lambda} + \frac{\kappa_{\lambda,sca}}{4\pi} \int_{\Omega'} P(\Omega, \Omega') I_\lambda(\Omega') d\Omega' \tag{3.7}$$

Note that the RTE is an integrodifferential equation in 6 dimensions (3 dimensions of space, two directions and one dimension related to the radiation wavelength). Solving this equation in a general frame is complicated and in some realistic configurations computationally expensive. However, in some situations, it is possible to skip the spectral dimension (i.e., to neglect the dependency of the RTE on the wavelength). This assumption is reasonable if the propagating medium is gray, that is, if its radiative properties do not depend on the wavelength. This assumption is incorrect in the case of gases, as seen in the next section.

3.2 Gas properties

3.2.1 Air properties: absorption coefficients

The atmosphere is a mixture of gases that covers the surface of the Earth. A typical composition of the dry air near the ground surface is given in Table 3.1:

In the table, ppmv means "parts per million by volume". Water vapor is not included in the table but is also an important component of air. In the lower layers of the atmosphere,

Gas name	Formula	Volume in ppmv	Volume %
Nitrogen	N_2	780840	78.084%
Oxygen	O_2	209460	20.946%
Argon	Ar	9340	0.934%
Carbon dioxide	CO_2	413.60	0.04136%
Neon	Ne	18.18	0.001818%
Helium	He	5.24	0.000524%
Methane	CH_4	1.87	0.000187%

Table 3.1: Composition of dry air, from [6]

near the ground surface, water vapor concentrations can vary by orders of magnitude from place to place. This spatial variability creates a fundamental problem in climate modeling due to the very high temporal and spatial resolution needed to treat all processes related to water vapor [112]. The composition of air changes with altitude, together with the total pressure of the mixture of gaseous species.

The amount of carbon dioxide and other GHGs has a significant impact on radiative transfer in the atmosphere. (The greenhouse effect is one of the consequences [113].) This is because some of the gaseous elements present in air strongly absorb radiation. Due to human activities in the past few hundreds of years, the amount of GHGs has increased greatly, and the impact on thermal radiation is significant [114]. Typical absorption spectra of molecules found in air are described in the next sections.

The extinction coefficient of air $\beta_\lambda[m^{-1}]$ is required to evaluate the attenuation of radiation by the atmosphere at the urban scale. This coefficient can be expressed as the sum of the absorption κ_{abs} and the scattering coefficients κ_{sca} of the gas/particle mixture present in air:

$$\beta_\lambda = \kappa_{abs} + \kappa_{sca} \tag{3.8}$$

Each of these coefficients accounts for contributions by the gas molecules and the particles:

$$\kappa_{air} = \kappa_{abs,gas} + \kappa_{abs,part} + \kappa_{sca,gas} + \kappa_{sca,part} \tag{3.9}$$

For solar radiation, $\kappa_{sca,gas}$ is related to Rayleigh scattering caused by oxygen and nitrogen in clean dry air. Its value is approximately $0.13 \times 10^{-1}\ km^{-1}$ at sea level [115]. In our calculations, this phenomenon is neglected for simplicity. In addition, $\kappa_{sca,part}$ is a large contributor to radiation extinction due to different kinds of aerosols in the atmosphere [116]. At the urban scale, $\kappa_{abs,part}$ is associated mainly with carbonaceous particles such as soot in the air. Furthermore, $\kappa_{abs,gas}$ is the absorption caused by several gaseous components in the air.

Meteorological parameters (temperature, humidity, etc.) can also have an impact on the extinction coefficient. The relative humidity (RH), for instance, plays an important role in this coefficient. A higher RH corresponds to more water vapor in the air, which can directly increase the amount of absorbed radiative energy. It also has an indirect impact on the radiative properties of aerosols and their capacity to scatter radiation. For instance, as

shown by Malm [116], the scattering cross section of an ammonium sulfate particle can be increased by a factor of five or more above that of the dry particle at approximately 90% RH.

GHGs are the leading contributors of anthropogenic climate change due to their strong absorption capacity (Figure 3.2). According to Ref. [117], approximately 70% of solar energy is transmitted by the atmosphere and reaches the ground. However, GHGs absorb approximately 70% of the thermal energy emitted by the Earth's surface, which leads to the greenhouse effect. Among all GHGs, water vapor has the strongest impact on thermal radiation: approximately 35% to 65% of the absorption for a sunny day and 65% to 85% for a cloudy day.

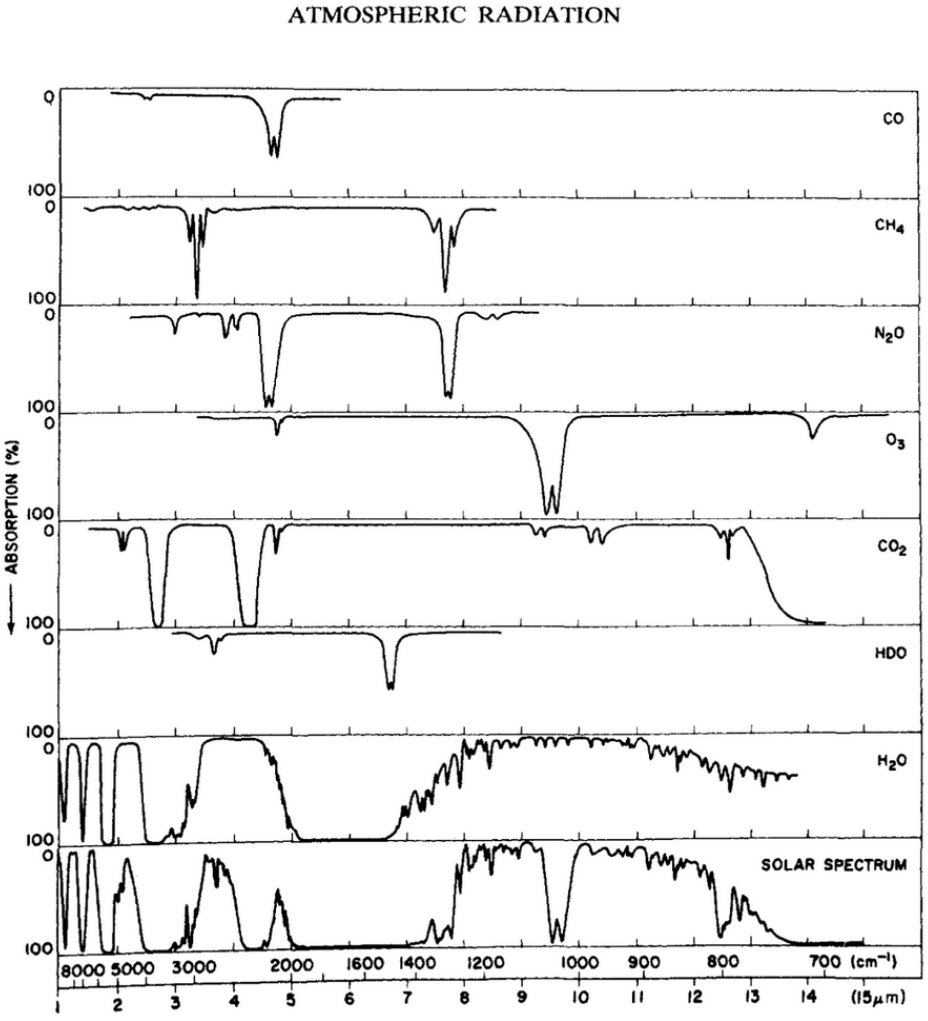

Figure 3.2: Low resolution absorption spectrum of the atmosphere[5]

In this thesis, simulations are carried out using standard conditions in the urban area. No specific weather conditions are specified (rain [118], fog [119], or snow [120] [121] were thus not considered): These situations can significantly complicate the treatment of the radiative transfer problem. Furthermore, particle pollution was not considered in the study. We focused mostly on the impact of the RH on the absorption of radiation energy (both solar and IR) and its consequences on the energy balance at building surfaces, which have a known influence on the energy consumption of buildings.

3.2.1.1 Wavelength dependence

As shown in Figure 3.2, the absorption coefficient of each gas varies strongly with respect to the wavelength. Moreover, air is a combination of all these gases, which means that the exact value of absorption of air is a sum of all these contributions at each wavelength. In this thesis, the information on the spectral absorption coefficient is calculated using the spectroscopic database HITRAN [122; 123].

HITRAN is an acronym for 'high-resolution transmission molecular absorption databases' [122]. It is a compilation of spectroscopic parameters that can be used to predict and simulate radiative behavior in the atmosphere. The database is a long-running project started by the Air Force Cambridge Research Laboratories (AFCRL) in the late 1960s in response to the need for detailed knowledge of the IR properties of the atmosphere. It also provides HITRAN online tools that allow users to customize the simulation conveniently on the Internet. Every four years, a major update of HITRAN is released, with an accompanying publication that describes the enhancement of the new HITRAN database. The latest version of the database is HITRAN 2016 [124].

With the HITRAN database, it is possible to calculate the values of the absorption coefficient ($\kappa_{a,\lambda}$) and absorption cross sections (C_λ) as functions of the wavelength (λ) or wavenumber (η). Calculations at high spectral resolution employ the line-by-line (LBL) method. The principle of LBL calculations at a fixed spectral discretization represented by wavenumbers η_i is shown in Figure 3.3 for absorption cross sections. The link between these quantities and the absorption coefficients required in the RTE is:

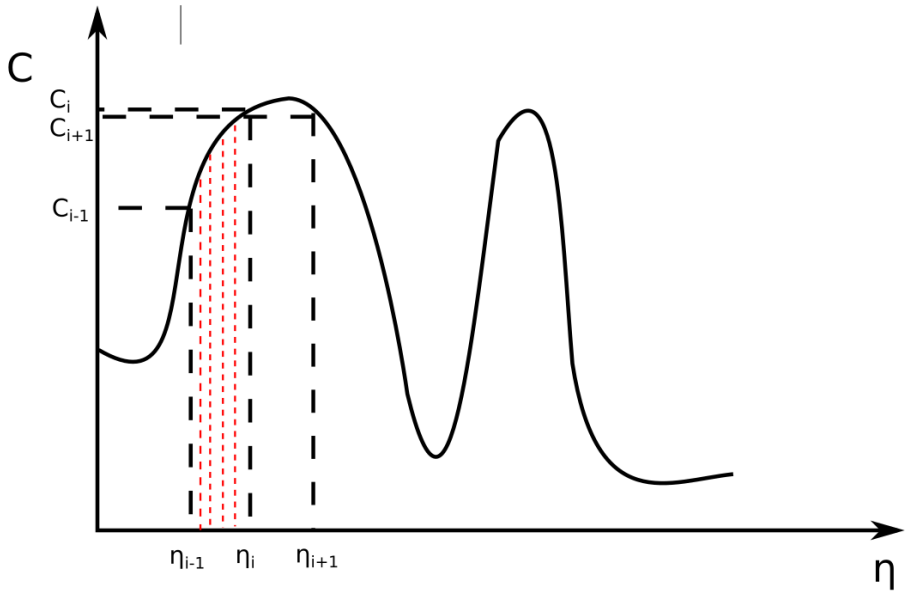

Figure 3.3: The Line-By-Line calculation

$$\kappa_{abs,\eta} = N(T_{gas}, P_{gas}) Y C_\eta \tag{3.10}$$

where N is the molar density at pressure P_{gas} and temperature T_{gas} and Y is the gas mole fraction.

The LBL model provides the most accurate representation of gas spectra, but the amount of computer resources required to apply this method in radiative transfer simulations mostly restricts its use to benchmark calculations.

To decrease the computational cost of simulations, narrow band models were introduced. These methods are based on spectral averaging techniques, allowing approximation of the radiative properties of gaseous paths over bands that extend from a few to a few dozens of cm^{-1}. Many studies have been devoted to narrow band models, such as the Malkmus narrow band model [125; 126] and the correlated–k (CK) method [127]. The computational cost of narrow band models is lower than that of the LBL method since radiative transfer is considered over bands containing many wavenumbers and not at each spectral location. These models are sufficiently accurate for most real-world applications, for which they provide an accuracy of a few percent. However, the methods are still expensive, especially in coupled simulations.

Global methods are the most widely used techniques in engineering applications. The principle of these methods is to provide gas radiative properties averaged over the full spectrum, providing a direct evaluation of the quantities of interest in coupled calculations, viz., radiative fluxes and powers. In this thesis, two global air models are considered: the gray gas and the spectral line weighted-sum-of-gray-gases (SLW) models.

3.2.1.2 Simplified absorption models

In this section, the gray gas and SLW models are presented. Both of them are realistic alternatives to the transparent model assumptions. They allow accounting for the interactions between the air and the radiation field in an efficient way. The two models are assessed against the LBL calculations in some simple test cases.

Gray gas model The gray gas model is the simplest global method. It assumes that the absorption coefficient of gases does not depend on the wavelength, which gives a constant $\kappa_{a,gray}$ $[m^{-1}]$ (often called the Planck mean absorption coefficient) over the full spectrum (Figure 3.4).

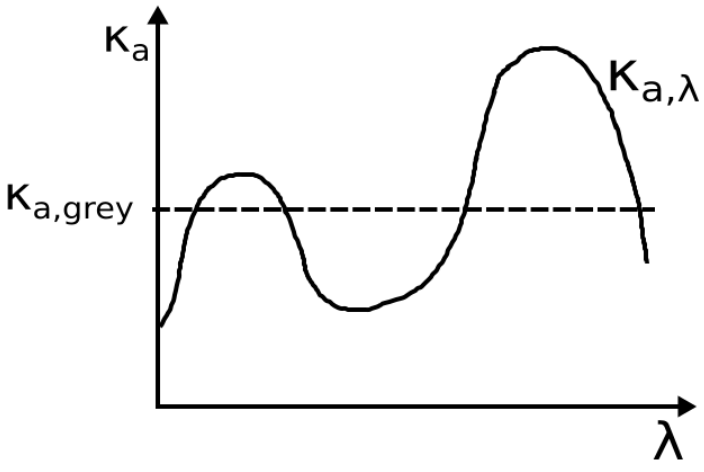

Figure 3.4: The absorption coefficient for the gray gas model

The coefficient $\kappa_{a,gray}$ can be obtained by:

$$\kappa_{a,gray} = lim_{L\to 0}\frac{\pi}{\sigma T_{gas}^4}\frac{\int(1-e^{-\kappa_{a,\lambda}L})\, I_{b,\lambda}(T)d\lambda}{L} \tag{3.11}$$

where $\kappa_{a,\lambda}$ is the spectral absorption coefficient of the gas.

In most cases, the gray model is known to provide inaccurate approximations of the radiative properties of gases. This is partly because this model does not account for possible transparency regions in the gaseous spectra. Some methods, such as the semigray or SLW-1 models, use several values of absorption coefficients instead of a single value. They are usually more accurate than the gray method but are not considered further in the present study. More details on these techniques can be found in Ref. [128].

SLW model The SLW method was the first global method based on a distribution function of the absorption coefficient weighted by the Planck function. Now, several similar techniques, such as the absorption distribution function (ADF) [129] and full-spectrum k-distribution (FSK) [130], use the same kind of formulation but mostly distinct notations. Information on the local thermodynamic state of the gas (temperature, pressure, etc.) is accounted for in the model, which is the main difference between this method and the widely used weighted sum-of-gray-gases model of Hottel and Sarofim [131], which considers fixed absorption coefficients. The distribution function needed in the method, which is called the absorption line blackbody distribution function (ALBDF) in the SLW model, was introduced by Denison and Webb in [132]. The ALBDF concept extends to the full-spectrum idea introduced by Ambartzumian [133] in 1934 and developed throughout the 20th century, leading to the so-called k-distribution methods. The ALBDF is defined as the fraction of blackbody intensity emitted in the spectral regions where the spectral absorption cross section of the gas in a given state (whose dependency is omitted here for legibility), C_η, is below a prescribed value C. From this definition, ALBDFs take values between 0 (when C is below the minimum value of absorption cross sections encountered in the gaseous spectrum) and 1 (when C approaches infinity) and can be interpreted as the probability of encountering along the full wavenumber axis a value of spectral absorption cross section lower than C. This probability is mathematically defined as:

$$F(C, \phi_{gas}, T) = \frac{\pi}{\sigma T^4} \int_{\eta:C(\eta)<C} I_{b,\eta}(T) d\eta \tag{3.12}$$

in which ϕ_{gas} is the thermophysical state of the gas, defined as a vector of parameters $\phi_{gas} = (T_{gas}, P_{gas}, Y_{gas})$, which represent the temperature, pressure and mole fraction of the gas, respectively. $I_{b,\eta}(T)$ is the spectral intensity of the blackbody at temperature T and wavenumber η. The whole method to evaluate an ALBDF and use the gas model parameters is as follows (see also Figure 3.5):

1: From the LBL absorption cross-section spectrum, find the maximum and minimum values of $C(\eta)$. Then, divide the whole absorption cross-section range into evenly spaced intervals on a logarithmic scale:

$$C_j = C_{min} \left(\frac{C_{max}}{C_{min}} \right)^{\frac{j}{n}}, \; j = 1, 2, 3...n \tag{3.13}$$

where n is the number of intervals of absorption cross sections, set to 10000 in the present work.

2: Evaluate the ALBDF $F(C, \phi_{gas}, T)$ by applying its definition 3.12 to the high-resolution LBL data.

3: Select a numerical quadrature over the [0,1] interval. The weights of the quadrature are written as ω_i, $i = 1, ..N$ and its nodes as X_i, $i = 1, ..N$. N is the order of the

quadrature ($N = 7$ was chosen in this work, as is typical in the SLW method).

4: The gray gas weights are then simply those of the quadrature set, and the corresponding gas absorption cross sections C_i are given as solutions of the following implicit equations: $F\left(C_i, \phi_{gas}, T_{gas}\right) = X_i$, where X_i are the nodes of the quadrature set.

5: Use the corresponding set of approximate model coefficients (gray gas absorption coefficients and weights) to solve the RTE:

$$\frac{\partial I_i(s,\Omega)}{\partial s} = -N(T_{gas}, P_{gas})YC_iI_i(s,\Omega) + N(T_{gas}, P_{gas})YC_iI_b \tag{3.14}$$

The total intensity can be calculated by:

$$I_{s,\Omega} = \sum_{i}^{N} \omega_i I_i(s,\Omega) \tag{3.15}$$

Figure 3.5 illustrates the flowchart of the SLW method. The process provided here is a simplified version of the full SLW method described in [128]. However, as the gas layers considered in our problem are assumed to be isothermal, the method described previously is sufficient to generate the radiative model parameters required for air in our application.

3.2.2 Comparison of the absorption models

A simple case of thermal radiation transfer was studied to evaluate the air model impact. This preliminary study compares the absorption of radiation for different conditions of air with different air models (transparent, gray, SLW). The goal of the simulation is to check whether air can be treated as a transparent medium for radiative transfer under our conditions. If the absorption is small enough that the difference between the transparent and the other absorbing models is negligible, then a method such as radiosity is likely to provide acceptable results. Otherwise, a method such as the DOM combined with a more sophisticated gas radiation model (gray or SLW) should be necessary to solve the RTE to obtain accurate results.

Different cases of air gas are distinguished based on the volume ratio of water vapor in the air (X_{water}), which can be expressed by:

$$X_{water} = \frac{m_{water}}{m_{dryair} + m_{water}} = \frac{1}{1 + \frac{m_{dryair}}{m_{water}}} \tag{3.16}$$

where m_{water} is the number of moles of water vapor in the air and m_{dryair} is the number of moles of dry air. We assumed the gas mixture to follow the perfect gas law, which allows the following to be written:

$$\frac{m_{water}}{m_{dryair}} = \frac{P_{water}}{P_{atm} - P_{water}} \tag{3.17}$$

P_{atm} is standard atmospheric pressure, taken as 101325 Pa in this calculation. The pressure of the vapor P_{water} can be obtained by the Dupré formula with the assumption that the RH for all the cases of air is 100%.

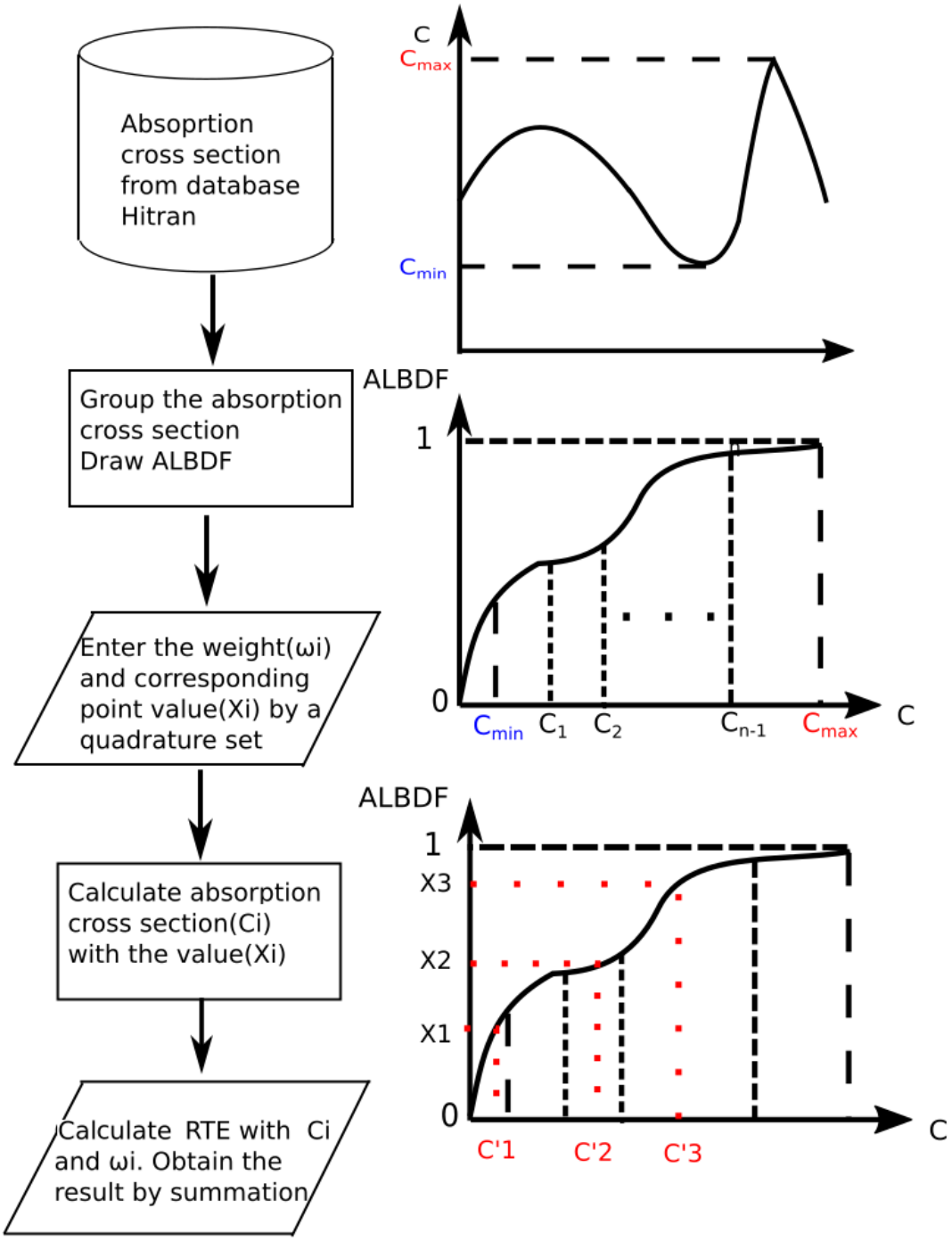

Figure 3.5: Flowchart to solve the RTE with the SLW air model, starting from HITRAN spectra

In each test case, the RH is set to 100%, and the temperature differs from one case to the other to create situations with different specific volumes of vapor. Table 3.2 shows the saturation vapor pressure for each air gas.

Temperature(°C)	Temperature(K)	Saturation vapor pressure(Pa)
-10	263	260
0	273	610
10	283	1230
20	293	2340
30	303	4240
40	313	7380

Table 3.2: Saturation vapor pressure for each case of air

We assume that air is composed only of nitrogen (N_2), oxygen (O_2), carbon dioxide (CO_2), methane (CH_4), carbon monoxide CO, nitrous oxide (N_20), ozone (O_3) and water vapor (H_20). These gases are the main air components to calculate the absorption in the HITRAN database, which provides the absorption coefficient and cross-section calculations. The volume percentage of each component in each case is shown in Table 3.3. The volume ratio of other components remains the same, while some of the nitrogen is replaced by water vapor.

Absorption cross sections of every single element of air gas was calculated in both the solar and infrared spectral ranges. The spectrum of solar radiation was calculated from 0.25 μm to 2.5 μm (corresponding to the range of wavenumbers 4000 cm^{-1} to 40000 cm^{-1} for the input wavenumbers of HITRAN). For the infrared radiation, the spectral range extended from 5 μm to 50μm (200 cm^{-1} to 2000 cm^{-1} for the input wavenumbers of HITRAN).

Temperature(K)	Vapor	CO_2	O_3	N_2O	CO	CH_4	O_2	N_2
-10	0.002566	0.00033	$3E-8$	$3.2E-7$	$1.5E-7$	$1.7E-6$	0.20900001	0.78810179
0	0.006020232	0.00033	$3E-8$	$3.2E-7$	$1.5E-7$	$1.7E-6$	0.20900001	0.784647558
10	0.012139156	0.00033	$3E-8$	$3.2E-7$	$1.5E-7$	$1.7E-6$	0.20900001	0.778528634
20	0.023094004	0.00033	$3E-8$	$3.2E-7$	$1.5E-7$	$1.7E-6$	0.20900001	0.767573786
30	0.041845547	0.00033	$3E-8$	$3.2E-7$	$1.5E-7$	$1.7E-6$	0.20900001	0.748822243
40	0.072834937	0.00033	$3E-8$	$3.2E-7$	$1.5E-7$	$1.7E-6$	0.20900001	0.717832853

Table 3.3: The composition of air

Based on the spectroscopic data provided by the HITRAN database, the absorption coefficients of several mixtures of molecular species can be obtained in every range of the spectrum needed. Figure 3.6 shows the result of the absorption coefficient of air at $T = 263\ K$. The absorption of solar radiation occurs in two portions of the spectrum, where the wavelengths are approximately 1.4 μm and 1.8 μm. Compared with the absorption coefficients of the single components of air in the same situation and the same spectral range (Figure 3.7), we can find that the absorption for these two spectral locations is caused mainly by water vapor. A comparison between Figures 3.6a and 3.7h shows that the only difference between the two figures is a sharp peak located at approximately 0.8 μm. This absorption is due to molecular oxygen (Figure 3.7b). Although components such as CH_4 and CO have a significant absorption between 2 and 3 μm, their quantity in the atmosphere is small so that their contribution to the total absorption coefficient of air is negligible.

For IR radiation, the conclusions are almost the same. Figures 3.6b and 3.8h show that most of the absorption in this spectral range is due to water vapor. The only difference

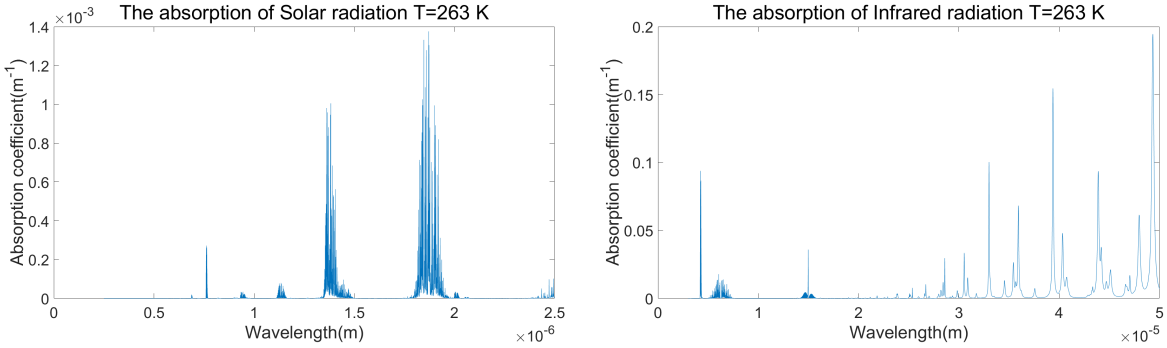

(a) Solar radiation (b) Infrared radiation

Figure 3.6: Absorption coefficient of air at T=263 K

is that at approximately 0.4 μm and 1.5 μm, strong absorption occurs due to CO_2. The large absorption ability of CO_2 in this part of the spectrum explains its impact on the overall absorption coefficient even considering its relatively small quantity.

Temperature influences absorption only indirectly through its impact on the shapes of the spectral lines (integral under a spectral line and profile). Because of the temperature change, the quantity of air components such as water varies, which eventually leads to an increase or a decrease in the absorption coefficient of air. Among all the components of air, water vapor plays a key role in the radiative properties of the gaseous mixture.

Based on these LBL calculations, simple 0D (line-of-sight) radiation transfer simulations were performed to quantify the amount of radiative energy absorbed by air for different line-of-sight geometries using different path lengths.

Blackbodies were used to represent the sun at $T = 5780\ K$ and a point source at $T = 300\ K$ in the solar and IR radiation calculations, respectively. These incident sources propagated in each air sample with distances of l =1, 10, 50 or 100 m. The Beer-Lambert law is used to calculate the spectrum after absorption by the gas layer [134; 135]:

$$I_\lambda = I_{b,\lambda} e^{-\kappa_{a,\lambda} l} \tag{3.18}$$

The transmitted and initial blackbody emissions in the case of an air layer at $T = 263\ K$ are depicted in Figures 3.9 and 3.10. The same figures for the other temperatures are presented in appendix 6.2.

For solar radiation (Figure 3.9), the spectral intensity decreases in the strongly absorbing zones of air. Even with a transfer distance of 50 m, the radiative intensity drops to nearly 0 at some spectral locations. However, the whole transmission ratio (averaged over the full spectral range of the source) remains high, approximately 0.98 for 100 m.

The situation is slightly different for IR radiation (Figure 3.10). For a gas path length of 100 m, almost all the radiative energy above 3 μm is absorbed. The strong absorption capacity of air in the IR region leads to a decrease of 37% of the incident emission.

The intensity left in all spectra for solar and IR radiation in different cases can be found in Figures 3.11 and 3.12. For the highest air temperatures considered here, the absorption by air increases together with the increase in the amount of water vapor.

The conclusion is that for solar radiation, absorption by atmospheric air at the urban surface level is nearly negligible. In the worst case considered, air absorbs less than 10% of

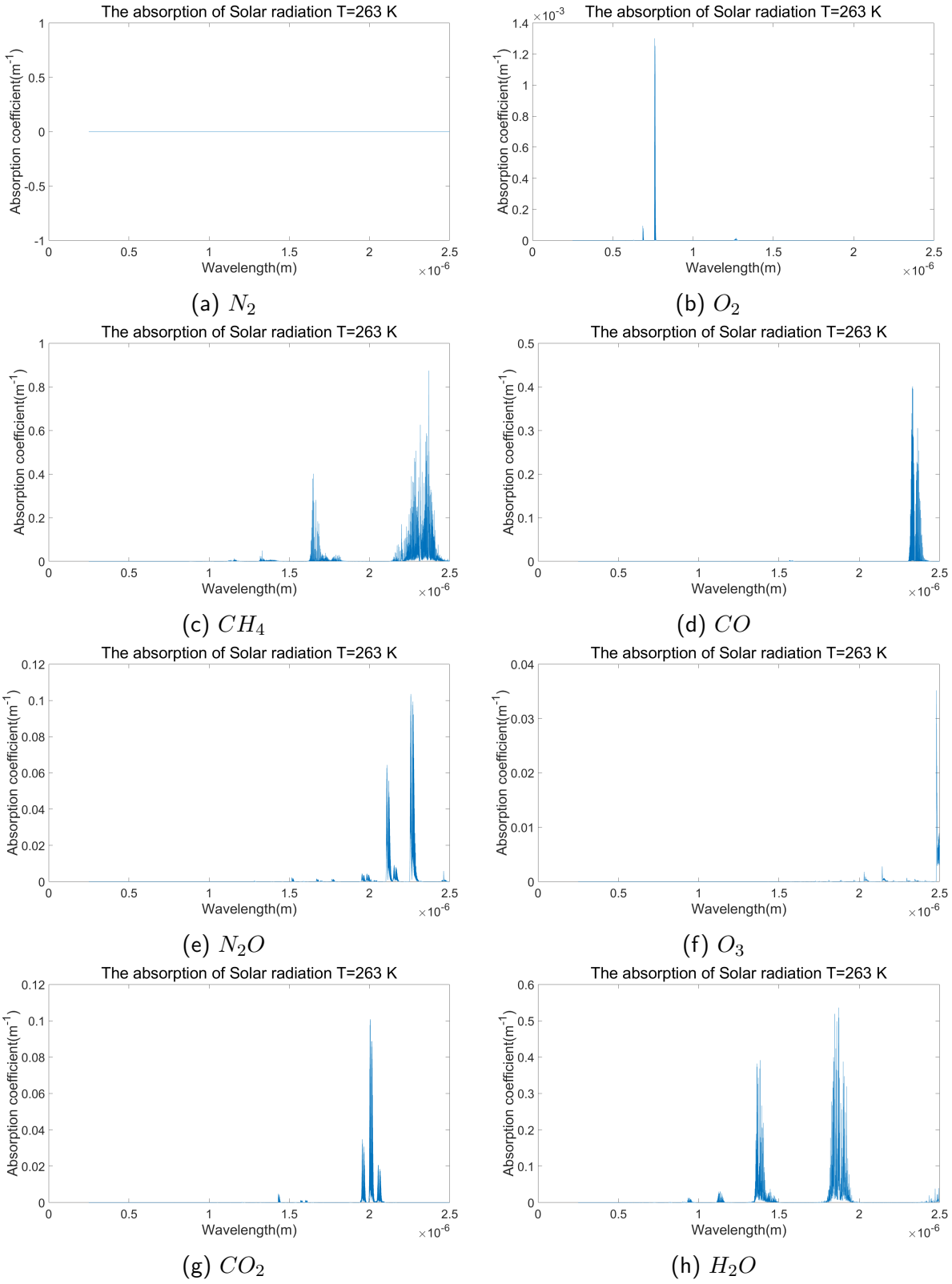

(a) N_2 (b) O_2

(c) CH_4 (d) CO

(e) N_2O (f) O_3

(g) CO_2 (h) H_2O

Figure 3.7: Absorption coefficient of single components of air in the Solar range, with air at T=263 K

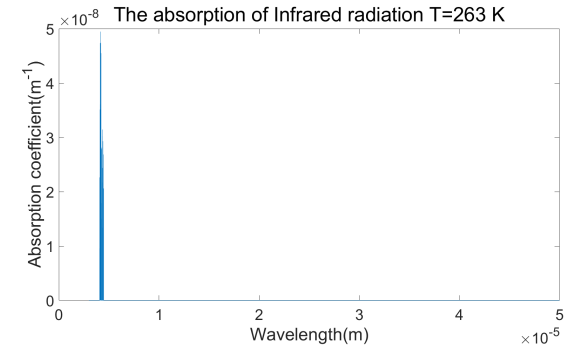

(a) N_2

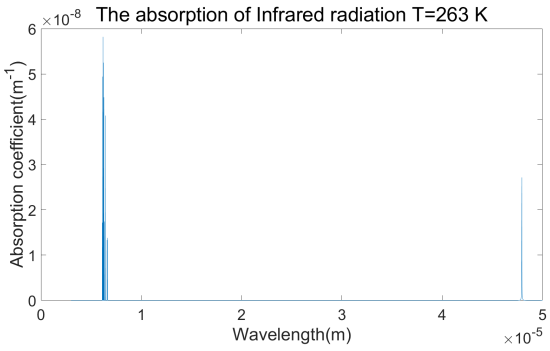

(b) O_2

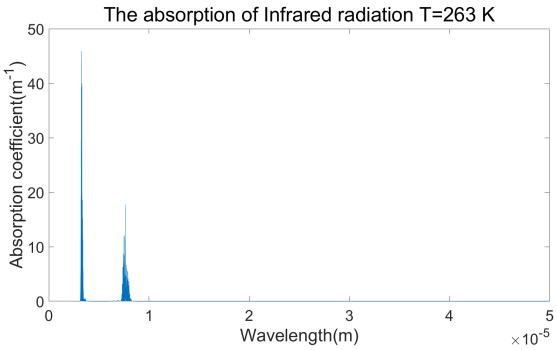

(c) CH_4

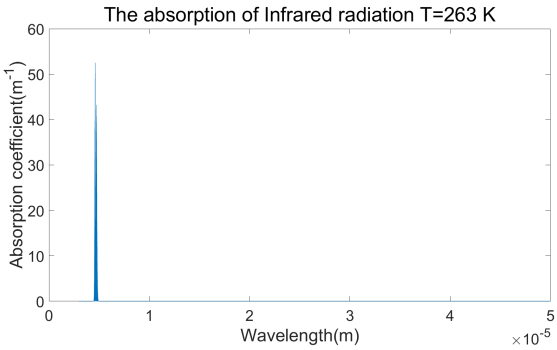

(d) CO

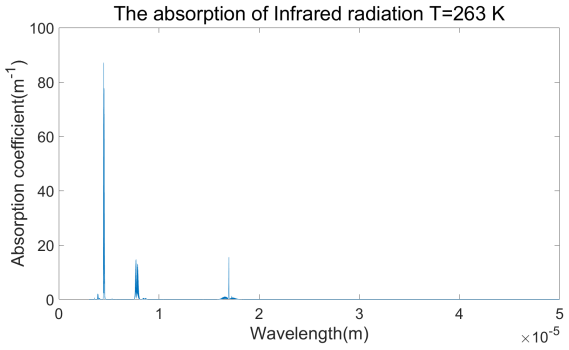

(e) N_2O

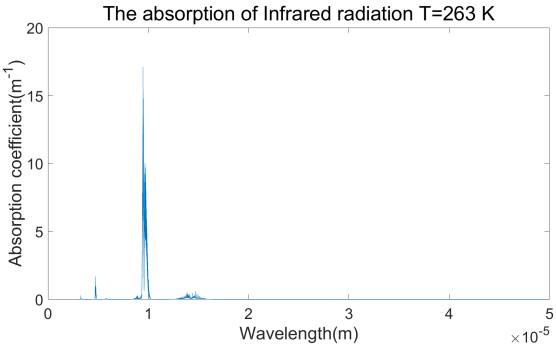

(f) O_3

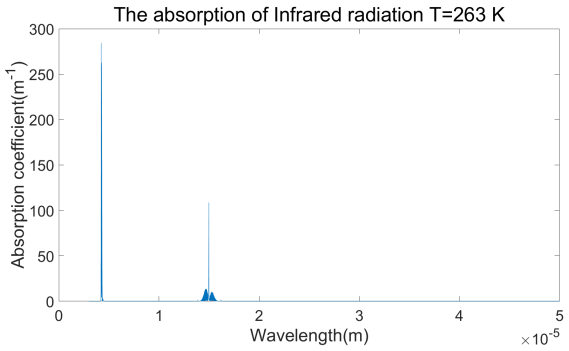

(g) CO_2

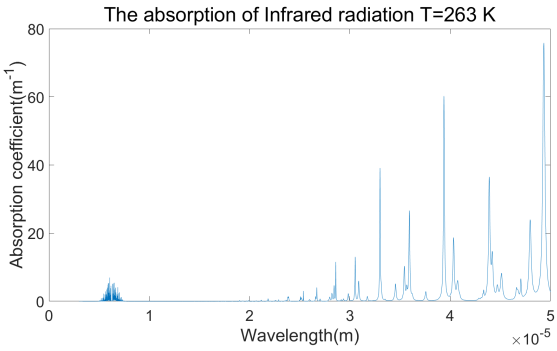

(h) H_2O

Figure 3.8: Absorption coefficient of single air components in the Infrared, with air at T=263 K

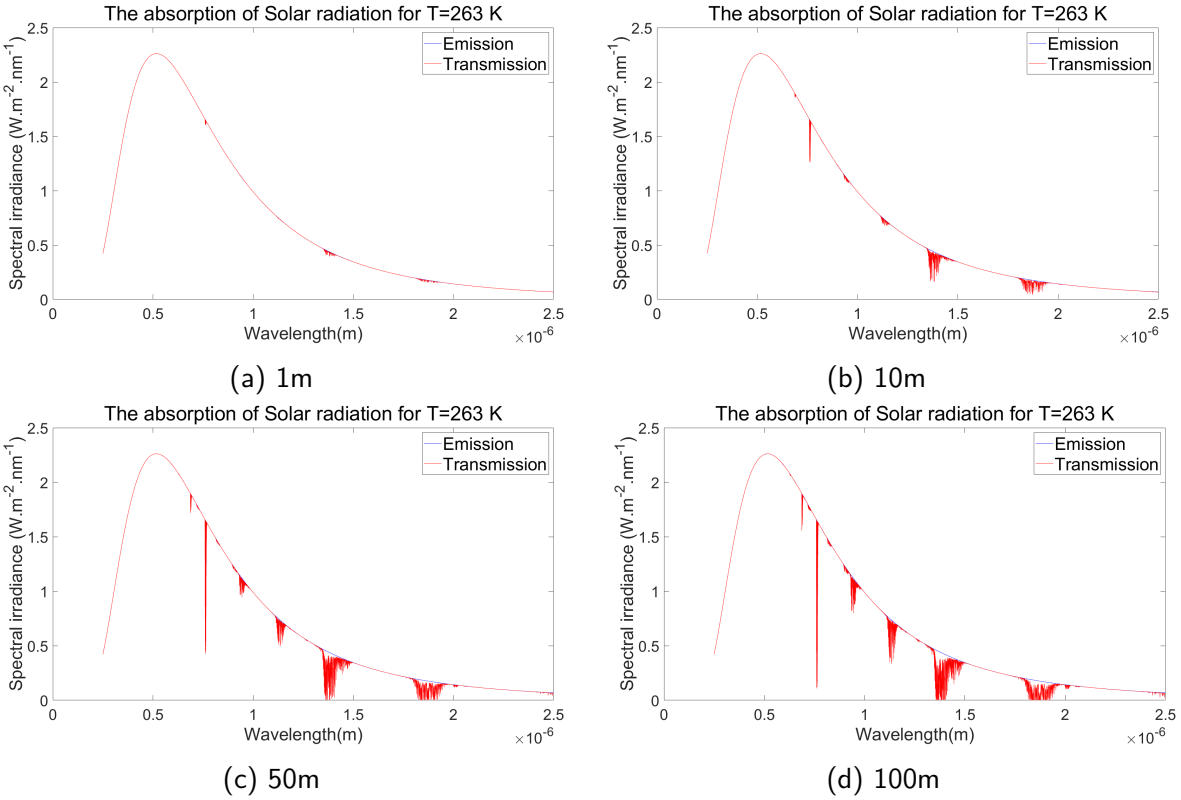

(a) 1m (b) 10m

(c) 50m (d) 100m

Figure 3.9: Transmission of Solar radiation for different air layer (at 263 K) thicknesses

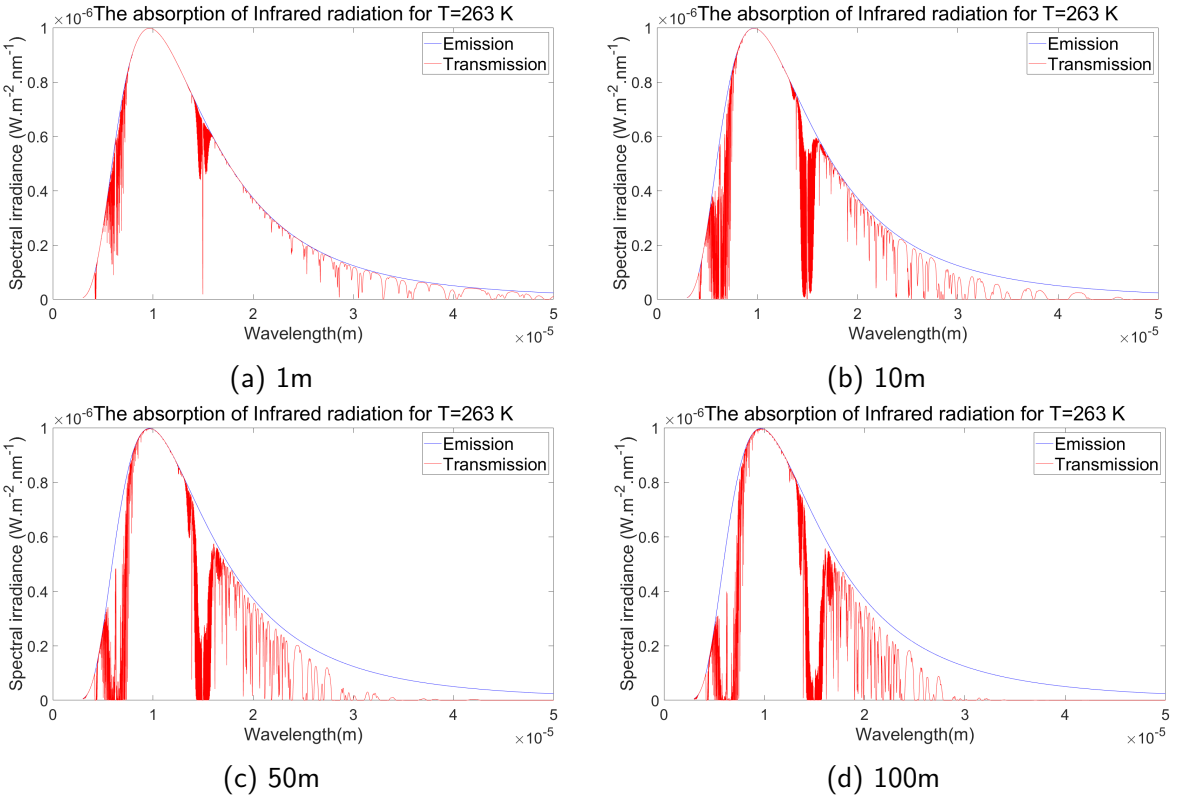

(a) 1m (b) 10m

(c) 50m (d) 100m

Figure 3.10: Transmission of infrared radiation for different air layer (at 263 K) thicknesses

the sun energy (Figure 3.11f). A transparent model for solar radiation can be reasonable in most cases of urban radiation simulations.

On the other hand, in the IR range, the situation is more complicated because of the strong radiative absorption of air. To study this problem in detail, we have chosen to treat air as an absorbing medium in the calculations discussed later. However, to account for air absorption and to avoid the use of LBL data whose cost would be too excessive for our purpose, we consider the two approximate methods for the radiative properties of air described earlier, i.e., the gray and SLW methods.

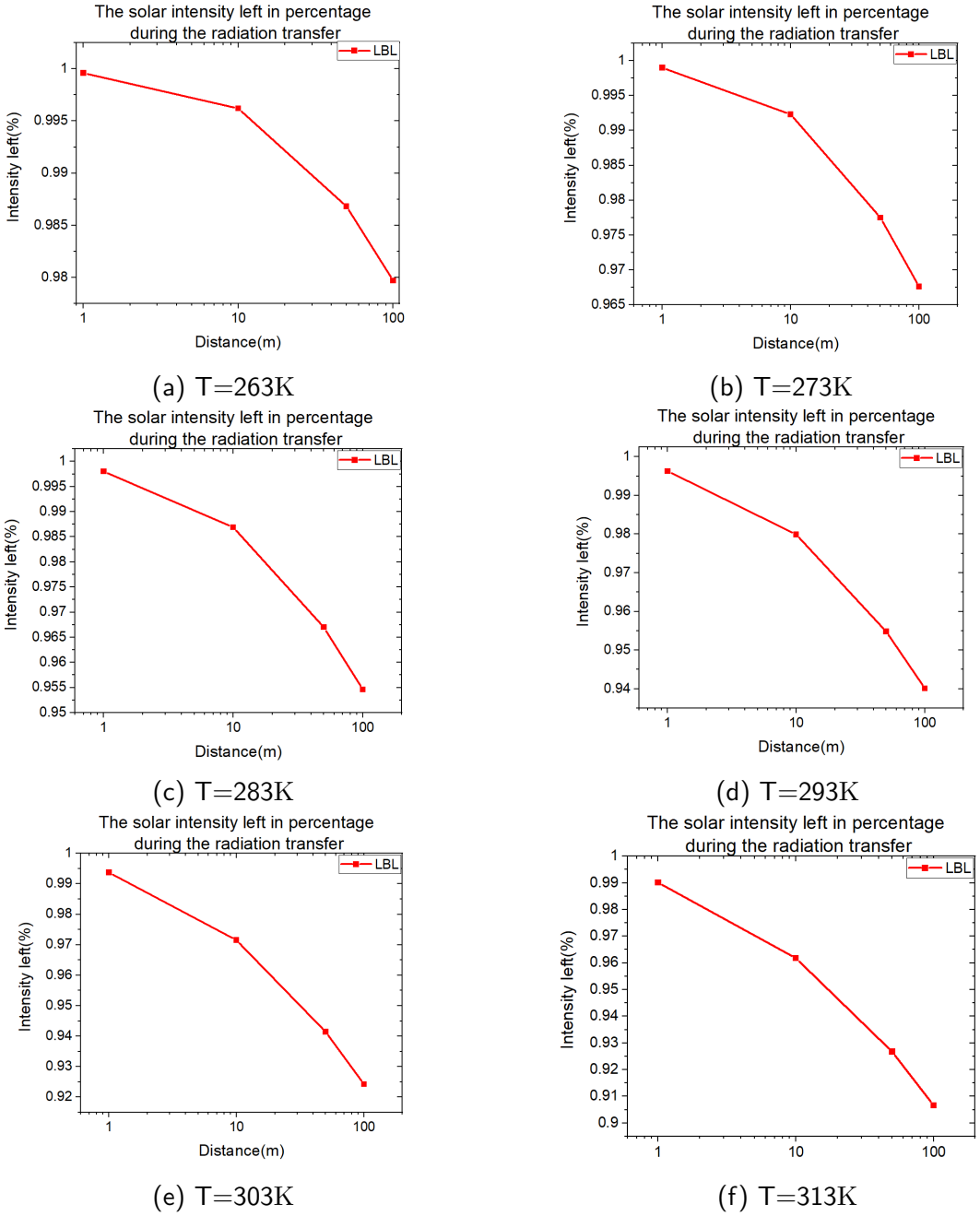

(a) T=263K (b) T=273K

(c) T=283K (d) T=293K

(e) T=303K (f) T=313K

Figure 3.11: The ratio of the solar radiation intensity left after the transfer with LBL air model

The gray model and SLW model are applied and compared with the LBL results provided previously. For the SLW model, the air absorption cross-section data are taken directly from the HITRAN LBL outputs, and the method described earlier to generate model parameters and use them in radiative transfer calculations is applied. The gray model takes the integration result of 1 m to set the absorption coefficient of each air sample (this assumes

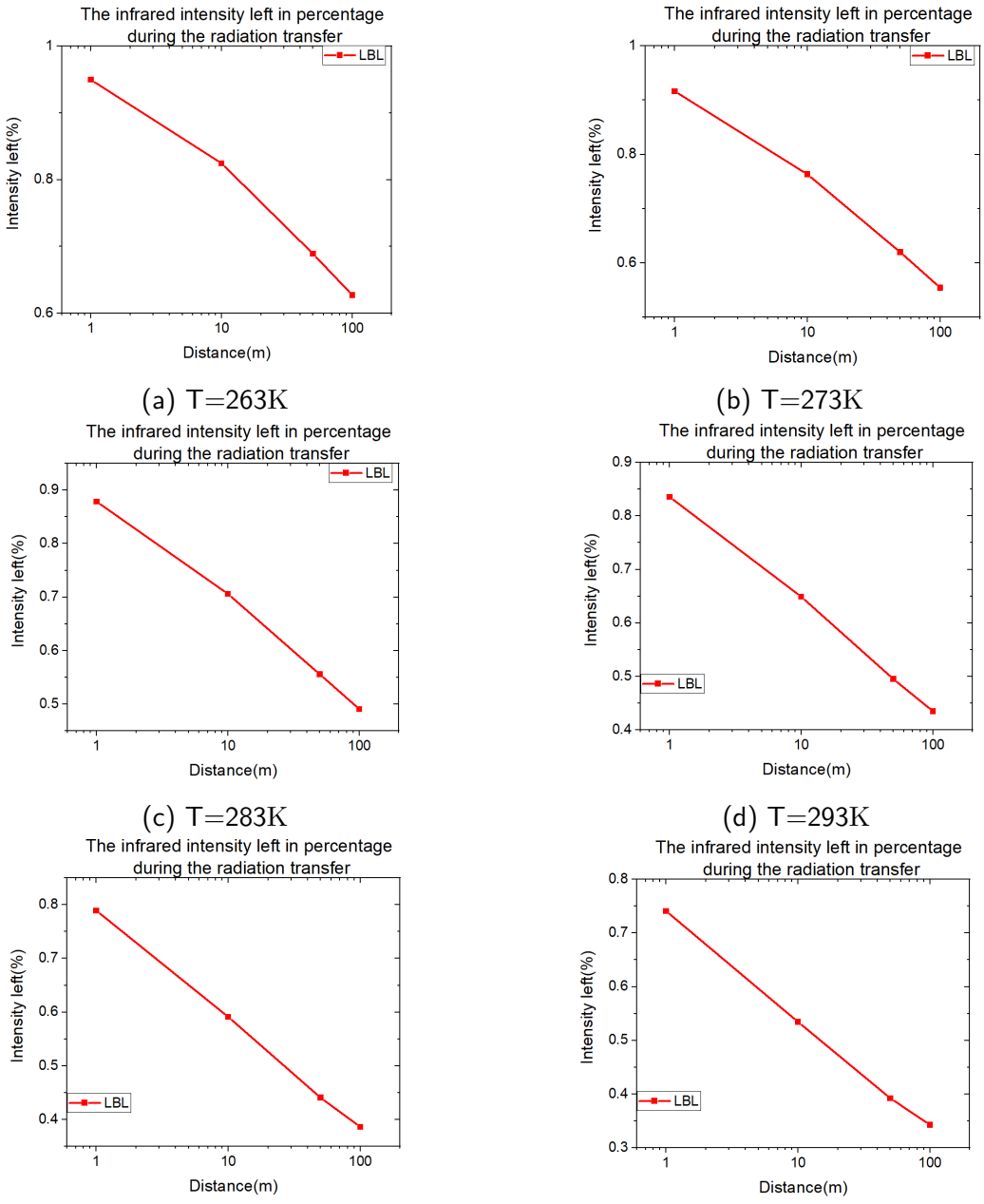

(a) T=263K (b) T=273K

(c) T=283K (d) T=293K

(e) T=303K (f) T=313K

Figure 3.12: The ratio of the infrared radiation intensity left after the transfer with LBL air model

that the corresponding value is a fair approximation of the limit when L vanishes used in the definition of the gray gas coefficient; see Eq. 3.11). Then, this coefficient is used to calculate the air absorption for 10 m, 50 m and 100 m for each air sample. The results are presented in the figures below (3.13, 3.14):

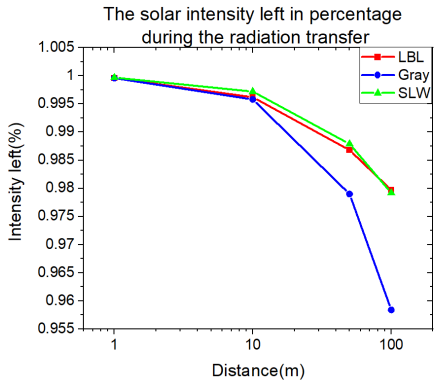

(a) T=263K

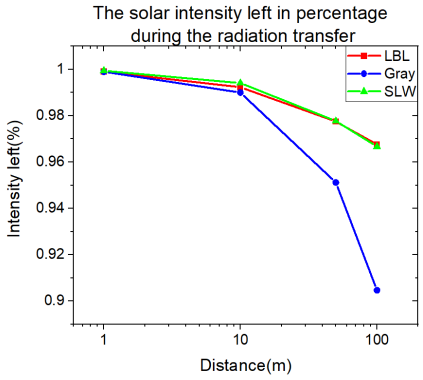

(b) T=273K

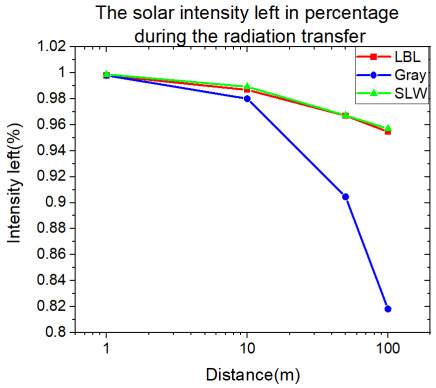

(c) T=283K

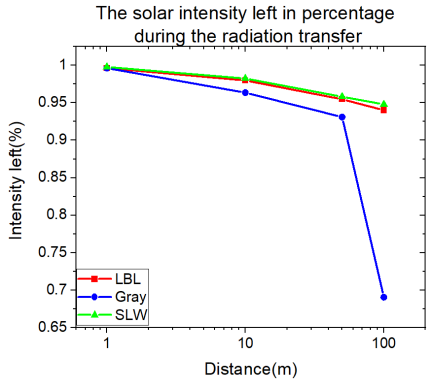

(d) T=293K

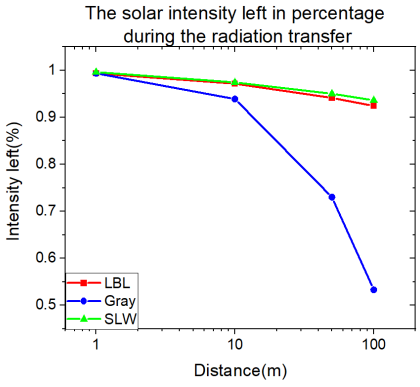

(e) T=303K

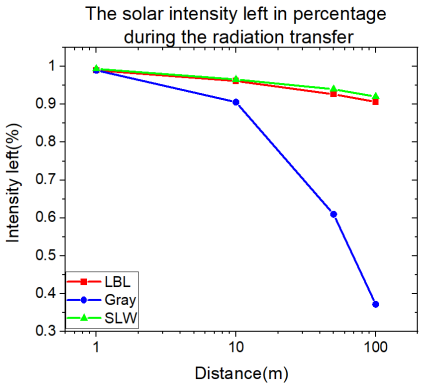

(f) T=313K

Figure 3.13: The ratio of the solar radiation intensity left after the transfer with all air models

As expected, the gray model gives the less accurate results. As said previously, the fact that no transparency region is considered in the gray model leads to an overestimation of the absorption, which explains these poor-quality results.

The results provided by the SLW model are more accurate. The difference between the LBL model and SLW model is shown in Table 3.4. Increasing the number of gray gases in SLW is likely to increase its accuracy at the expense of a higher computational cost.

Compared to transparent or gray models, the main drawback of the SLW model is its computational cost, even if it is orders of magnitude lower than LBL calculations. This

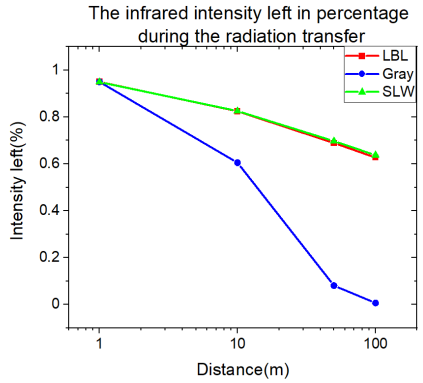

(a) T=263K

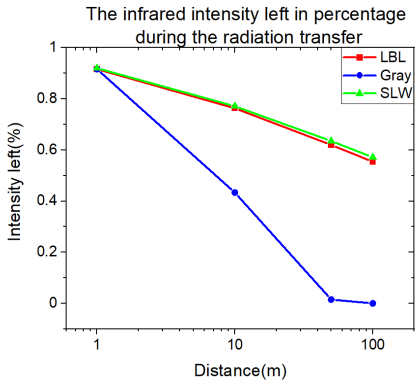

(b) T=273K

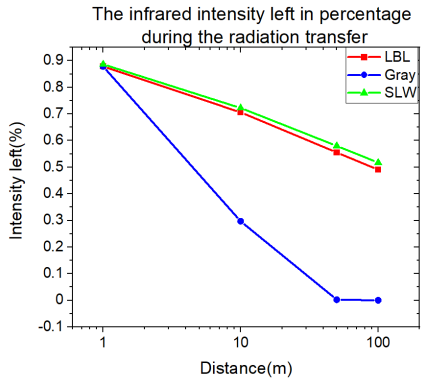

(c) T=283K

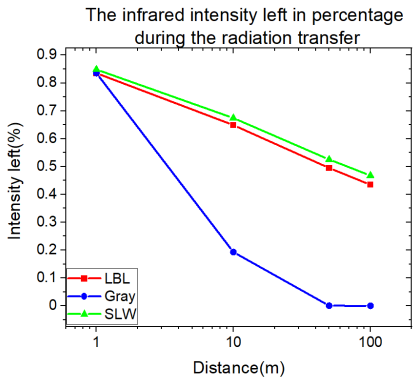

(d) T=293K

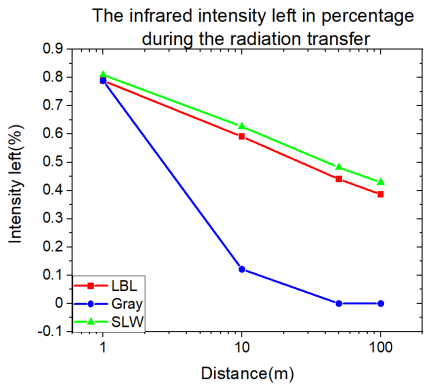

(e) T=303K

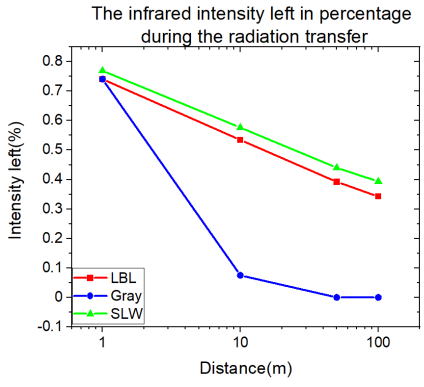

(f) T=313K

Figure 3.14: The ratio of the infrared radiation intensity left after the transfer with all air models

Solar radiation						
	263K	273K	283K	293K	303K	313K
1m	$1.38E-4$	$3.66E-4$	$7.882E-4$	0.0015	0.0025	0.0037
10m	$9.8E-4$	0.0018	0.0025	0.0026	0.0027	0.0040
50m	0.001	$1.56E-4$	$2.9E-4$	0.0033	0.0086	0.0133
100m	-$4.8E-4$	-$9.4E-4$	0.0024	0.0078	0.0120	0.0139
Infrared radiation						
	263K	273K	283K	293K	303K	313K
1m	-$6.5E-4$	0.0032	0.0080	0.0131	0.0204	0.0285
10m	0.0012	0.0080	0.0166	0.0256	0.0357	0.0422
50m	0.0083	0.0155	0.0246	0.0307	0.0414	0.0476
100m	0.0106	0.0175	0.0267	0.0331	0.0429	0.0511

Table 3.4: The difference in transmission ratio between the SLW model and LBL integration results

cost (considering the full process from the generation of the model parameters from LBL data up to their use in radiative transfer calculations) is due to two factors:

- The first is related to the time needed to calculate a series of gray absorption coefficients together with their associated weights. In this case, the whole cross-section range is in 10000 ($n = 10000$ in Eq. 3.13) logarithmically scaled intervals, and the absorption coefficient of air is then reduced, using SLW model theory, to 7 coefficients with their weights. It takes 125.25 s to calculate the IR part for a single air configuration and 721.184 s for the solar radiation part. For repetitive radiative transfer calculations, these coefficients can be generated once and then stored in tables, leading to a significant reduction in the amount of computational power needed to generate these parameters.
- The second is related to the use of these coefficients in a radiative transfer calculation. The computational cost of the present SLW model is 7 times higher than that of the gray model. Depending on the complexity of the geometry considered for the calculation, the RTE solution requirements remain demanding, especially in coupled situations.

In this part, we evaluate the air gas absorption with different transfer distances. We show that air can absorb a fraction of energy, especially IR radiation during propagation. The quantity of absorption cannot be neglected, which means that the S2S radiation transfer method is not able to give precise values in cases with high temperature and humidity. In this case, RTE solution is necessary. To this end, the DOM is introduced in the following section.

3.3 The DOM: a method to solve the RTE

3.3.1 Method presentation

The DOM is one of the most widely used techniques to solve the RTE in participating media. This technique treats the RTE by using separate discretization schemes on space (ds) and angle (dΩ). For this purpose, an angular discretization of variable Ω is used. This requires the selection of a quadrature set to numerically evaluate integrals over angles. As soon as

this set is chosen, for one single discrete direction Ω_m (characterized by a triplet of directional coefficients μ_m, η_m, ξ_m), the RTE equation 3.7 simplifies into:

$$\Omega_m.\nabla I_\lambda(s,\Omega_m) = -\kappa_\lambda I_\lambda(s,\Omega_m) + \kappa_\lambda I_{b,\lambda}\left[T(s)\right] \tag{3.19}$$

In the case of a Cartesian spatial mesh, as considered throughout the present work, the previous equation becomes:

$$\mu_m \frac{dI_\lambda(s,\Omega_m)}{dx} + \eta_m \frac{dI_\lambda(s,\Omega_m)}{dy} + \xi_m \frac{dI_\lambda(s,\Omega_m)}{dz} + \kappa_\lambda I_\lambda(s,\Omega_m) = \kappa_\lambda I_{b,\lambda}\left[T(s)\right] \tag{3.20}$$

where dx, dy, dz are local path increments that characterize the mesh over which the RTE is solved.

The previous equation can be integrated over a single Cartesian cell (as depicted in Figure 3.15), over which the absorption coefficient is assumed to be constant and divided by the volume of the cell. This provides the following discrete form:

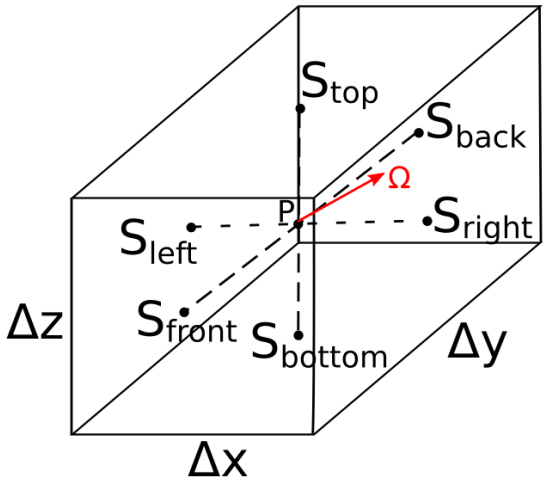

Figure 3.15: Cartesian cell considered in the Discrete Ordinate Method

$$\mu_m Ax(I_{\lambda,S_{right},m} - I_{\lambda,S_{left},m}) + \eta_m Ay(I_{\lambda,S_{back},m} - I_{\lambda,S_{front},m}) + \xi_m Az(I_{\lambda,S_{top},m} - I_{\lambda,S_{bottom},m}) + \kappa_\lambda I_{\lambda,p,m}\delta v = S_{\lambda,p}\delta v \tag{3.21}$$

where $I_{\lambda,p,m}$ is the radiative intensity at point P (center of the cell) for the m-th direction of the directional quadrature scheme and where we have used the following notations:

$$\begin{aligned} Ax &= \Delta y \times \Delta z \\ Ay &= \Delta x \times \Delta z \\ Az &= \Delta x \times \Delta y \\ \delta v &= \Delta x \times \Delta y \times \Delta z \\ S_{\lambda,p} &= \kappa_\lambda I_{b,\lambda}\left[T(s)\right] \end{aligned} \tag{3.22}$$

In the general case, for a given choice of the direction of propagation Ω_m, the intensity of three surfaces of the cell are known at a given step of the propagation scheme (e.g., S_{left}, S_{bottom}, S_{front}; note that the concept of $left$, $bottom$ and $front$ depends on the selected Ω_m). Intensities on the other three surfaces of the cell (which are unknown) can

be obtained by introducing assumptions between the values of the radiative intensities on these surfaces and those at its center P. These relationships usually take the form of linear interpolations (in which α is a coefficient that may depend on the direction, on the value of the absorption coefficient, $etc.$; the main constraint is to be between 0 and 1, although most usual values restrict the range of variation from 1/2 to 1):

$$\begin{aligned} I_{\lambda,p,m} &= I_{\lambda,S_{left},m} + \alpha(I_{\lambda,S_{right},m} - I_{\lambda,S_{left},m}) \\ &= I_{\lambda,S_{front},m} + \alpha(I_{\lambda,S_{back},m} - I_{S_{\lambda,front,m}}) \\ &= I_{\lambda,S_{bottom},m} + \alpha(I_{\lambda,S_{top},m} - I_{\lambda,S_{bottom},m}) \end{aligned} \tag{3.23}$$

Combining the previous set of relationships, one can ultimately obtain the following equation for the radiative intensity at the center of the cell (assuming the same value of α for the three directions):

$$\begin{aligned} I_{\lambda,p,m} &= \frac{\Lambda_{x,m} I_{\lambda,S_{left},m} + \Lambda_{y,m} I_{lambda,S,m} + \Lambda_{z,m} I_{\lambda,S_{bottom},m} + S_{\lambda,p} dv}{\Lambda_{x,m} + \Lambda_{y,m} + \Lambda_{z,m} + \kappa_\lambda \delta v} \\ \Lambda_{x,m} &= \frac{\mu_m A x}{\alpha} \\ \Lambda_{y,m} &= \frac{\eta_m A y}{\alpha} \\ \Lambda_{z,m} &= \frac{\xi_m A z}{\alpha} \end{aligned} \tag{3.24}$$

Then, using the linear approximations set by Eq. 3.23, estimates on the unknown radiative intensities at the surface of the cell can be obtained. The process is iterated over the whole mesh, starting from some boundary of the computational domain, and propagates until some stopping criterion is attained on the values of intensities between two successive steps of the iterative process. In the DOM, the choice of the interpolating coefficient α has a strong influence on the quality of the results. Various possible choices for this coefficient are presented in the next section.

3.3.2 Linear interpolation schemes

In this section, a brief description of different schemes encountered in the literature to interpolate values of radiative intensities over cells is provided. These schemes use different values of α in Eqs. 3.23 and 3.24. Other schemes (exponential, CLAM, etc) exist. They are detailed, for instance, in Ref. [93].

3.3.2.1 The upwind (step) scheme

In this case, the radiative intensity on the downstream surfaces is assumed to be the same as the intensity at the center of the cell, $L_{\lambda,p}$.

$$\alpha = 1 \tag{3.25}$$

This assumption provides relatively stable results. However, its main drawback is to neglect the influence of one half of the cell in each direction, which can lead to rather poor accuracy. Nevertheless, as considered in [93], it appears to be the only scheme that never produces physically unrealistic results.

3.3.2.2 The centered (linear-diamond) scheme

This approximation assumes that the radiative intensity at the middle point $I_{\lambda,p,m}$ is the arithmetic mean of the radiative intensities in direction m on the two opposite surfaces in the upstream and downstream directions:

$$\alpha = 0.5 \tag{3.26}$$

This approach provides more accurate results than the upwind scheme for the calculation of mean values over surfaces made of numerous cells. However, it suffers from oscillation issues and may yield physically unrealistic negative angular fluxes.

3.3.2.3 The hybrid (directional weighted) scheme

The method described hereafter was introduced by F. Liu, H. A. Becker, and A. Pollard in [136]. It consists of the definition of interpolating coefficients α that depend on the chosen direction Ω_m through the following set of relationships:

$$\begin{aligned} \alpha_x^m &= max(0.5, \alpha_x^{m'}) \\ \alpha_y^m &= max(0.5, \alpha_y^{m'}) \\ \alpha_z^m &= max(0.5, \alpha_z^{m'}) \end{aligned} \tag{3.27}$$

where:

$$\begin{aligned} \alpha_x^{m'} &= 1 - \frac{a}{2 \times (b+c) + \kappa_\lambda} \\ \alpha_y^{m'} &= 1 - \frac{b}{2 \times (a+c) + \kappa_\lambda} \\ \alpha_z^{m'} &= 1 - \frac{c}{2 \times (a+b) + \kappa_\lambda} \end{aligned} \tag{3.28}$$

with:

$$\begin{aligned} a &= \frac{\mu_m}{\Delta x} \\ b &= \frac{\eta_m}{\Delta y} \\ c &= \frac{\xi_m}{\Delta z} \end{aligned} \tag{3.29}$$

This scheme performs better than the upwind (step) and centered (diamond) schemes. Its only disadvantage, compared to the two other methods, is to be more computationally demanding because it requires additional calculations related to the use of the previous set of relationships to define direction-dependent interpolating coefficients.

3.3.2.4 Comparative study

A comparative study of the performance of the DOM for various interpolating schemes is performed in this part. For this purpose, three cubic geometries are considered. Each cube

Cube 1				
	Surface number	Temperature(K)	Emissivity	Reflectivity
Left surface	S1	280	0.9	0.1
Right surface	S2	280	0.9	0.1
Top surface	S3	273	0.5	0.5
Bottom surface	S4	290	0.9	0.1
Front surface	S5	280	0.9	0.1
Back surface	S6	280	0.9	0.1
Cube 2				
	Surface number	Temperature(K)	Emissivity	Reflectivity
Left surface	S1	300	0.9	0.1
Right surface	S2	295	0.9	0.1
Top surface	S3	285	0.5	0.5
Bottom surface	S4	320	0.9	0.1
Front surface	S5	290	0.9	0.1
Back surface	S6	305	0.9	0.1
Cube 3				
	Surface number	Temperature(K)	Emissivity	Reflectivity
Left surface	S1	273	0.9	0.1
Right surface	S2	275	0.8	0.2
Top surface	S3	255	0.6	0.4
Bottom surface	S4	285	0.85	0.15
Front surface	S5	270	0.9	0.1
Back surface	S6	273	0.85	0.15

Table 3.5: Inputs for the cube test cases

has the same dimension $1\ m \times 1\ m \times 1\ m$. The emissivities and temperature of the surfaces of the cubes considered for the analysis are given in Table 3.5

The first cube is the simplest one and is used to simulate cold ambient conditions. The second cube is representative of a summer setting: The temperatures of the surfaces differ from the previous configuration. The last case uses variations in both temperatures and emissivities. The air temperature in the cube is calculated as the mean value of the temperatures at the surfaces. The absorption coefficient is 0.1 for each case, and the gas is assumed to be gray.

The results of the DOM using the centered scheme are first assessed against results provided by an MC ray tracing engine developed by G.Mathieu of the CETHIL laboratory. One hundred points on each surface are chosen for the comparisons. The mean absolute error (MAE), root mean square error (RMSE), maximum (MAX) and minimum (MIN) errors on each surface are depicted in Figure 3.16:

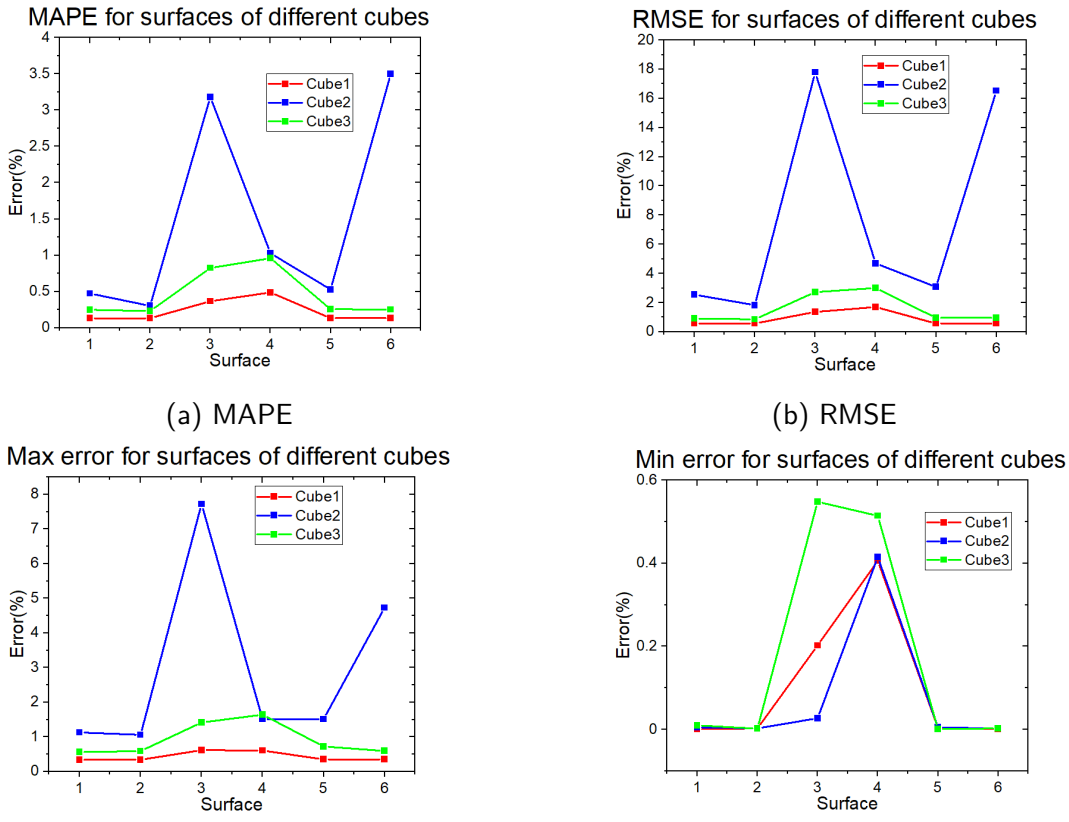

(a) MAPE

(b) RMSE

(c) Maximum

(d) Minimum

Figure 3.16: Results for different cubes with center scheme

The overall difference between the two methods (DOM and MC) is small except for the second cube. With a relatively high emission, the error increases, especially for surfaces 3 and 6, where the incident flux is higher than that of the other 4 surfaces.

The same calculations are carried out with the hybrid scheme. The results for the second cube are shown in Figure 3.17.

The hybrid scheme succeeds in reducing the error compared with the MC calculations. The performance of the DOM is improved substantially with this scheme while avoiding the oscillations and negative values observed with the centered scheme.

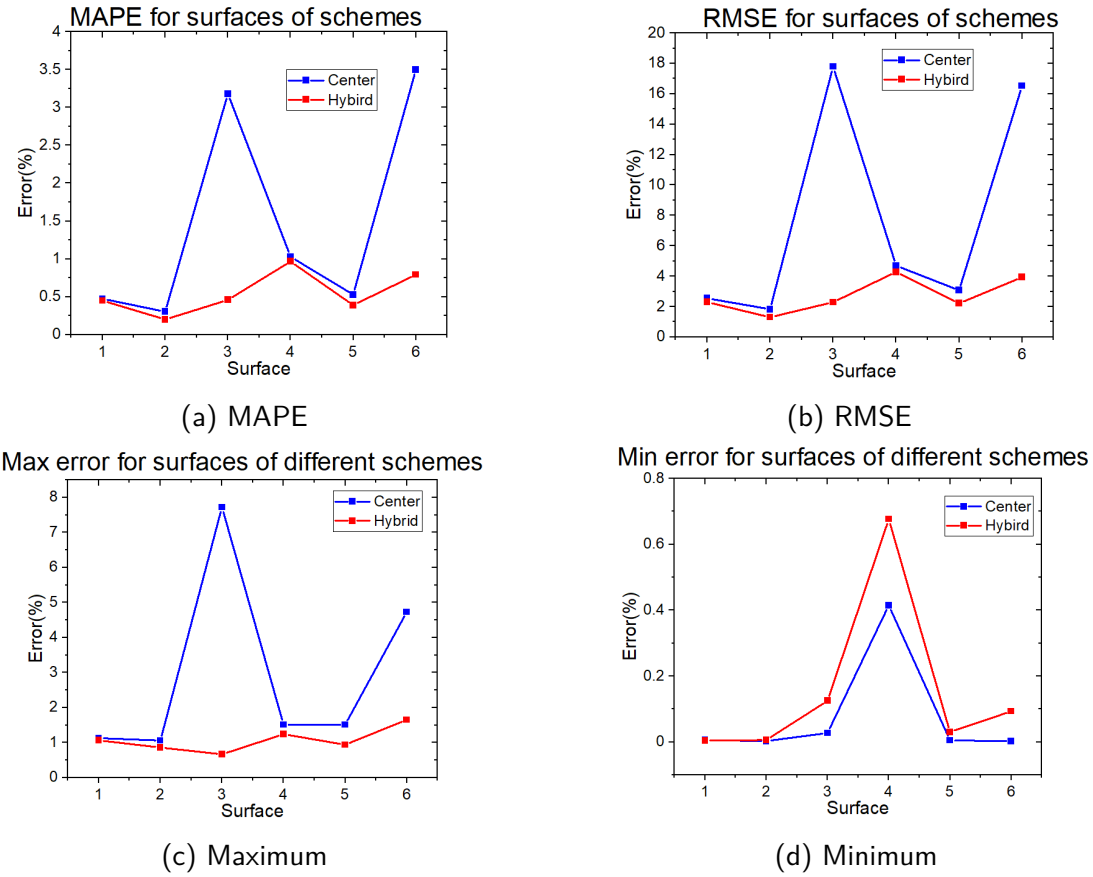

(a) MAPE

(b) RMSE

(c) Maximum

(d) Minimum

Figure 3.17: The results for cube 2 with the center and hybirde schemes

In conclusion, among the schemes considered here, the hybrid scheme is found to perform the best. The centered scheme suffers from oscillation issues and provides physically unrealistic negative results. The step scheme is not found to provide accurate results. The disadvantage of the hybrid scheme is its time consumption compared to the fixed coefficient methods (centered and step), which may increase with an increasing number of directions selected.

3.3.3 Angular quadrature schemes

In this section, different quadrature schemes for the angular integration of the RTE are presented. Quadrature is a numerical integration which uses a finite number of coordinates and the corresponding weight to approximate an integral. According to [137; 138; 139], the principles to generate a quadrature are suggested as:

- The discrete ordinates $\Omega_m(\mu_m, \eta_m, \xi_m)$ must be placed on a unit sphere.

$$\mu_m^2 + \eta_m^2 + \xi_m^2 = 1 \tag{3.30}$$

- The weight factors must be all positive and the zeroth moment condition should be respected:

$$\sum_{m=1}^{N} \omega_m = 4\pi \tag{3.31}$$

- The number of photons (also called the first moment condition) should be preserved which requires:

$$\sum_{m=1}^{N} \omega_m . \vec{\Omega}_m = 0 \tag{3.32}$$

- The diffusion condition (also called the second moment condition) should be satisfied:

$$\sum_{m=1}^{N} \omega_m . \vec{\Omega}_m^2 = \frac{4\pi}{3} \tag{3.33}$$

- The quadrature must be invariant by any rotation of the discrete directions with reference to the center of the sphere.

Besides, in a more general frame, the quadrature should also satisfy as many moments as required to integrate accurately the phase function if the scattering of the radiant energy is non-isotropic in the practical heat transfer applications [140].

One can notice that it is almost impossible for a discretization with a finite number of directions to satisfy the last constraint [139].

Most angular quadrature scheme were initially developed to solve problems in neutron transport theory [141**?**]. During the last several decades, these schemes were adopted [**?**] and extended [140] to solve the RTE. In this thesis, we select the Fibonacci and constant weight for discrete ordinate method (CWDOM) quadratures as well as schemes used in quasi Monte Carlo (qMC) methods. A brief description of the widely used level symmetric quadrature, defined by Carlson and Lee in [141], is also given. Comparisons of these various schemes on test cases are carried out in the next chapter. Here, we introduce only the various methods.

3.3.3.1 Level symmetric quadrature sets

This quadrature is referred to as the S_N method, and was developed by K. D. Lathrop and B. G. Carlson in [142]. It provides directions which are symmetric with respect to a $\pi/2$ rotation inside eight octants. If one direction vector (μ, η, ξ) is chosen, then the seven other combinations of the same μ, η, ξ with different plus-minus signs are also elements of the quadrature set. The main formula to evaluate the cosine values of points on the unit sphere is:

$$\begin{aligned} \mu_i^2 = \mu_1^2 + 2(i-1)\frac{1-3\mu_1^2}{n-1} \\ \mu_i = \eta_i = \xi_i \end{aligned} \tag{3.34}$$

The first base point μ_1 can be determined by Eq. (3.34) together with the constraint:

$$\sum_{i=1}^{\frac{n}{2}} \omega_i \mu^k = \frac{1}{k+1} \tag{3.35}$$

Basically μ_1 is chosen by selecting which moment conditions meed to be satisfied. Level symmetric quadratures can be categorized into 3 classes of quadrature:

- Level Symmetric Even quadrature (LSE): the value k in Eq. (3.35) is an even number to satisfy the even moment condition. This quadrature restricts n to be lower than 22 to avoid negative weights caused by numerical truncation errors [143].

- Level Symmetric Odd quadrature (LSO): the value k is any positive integer. Compared with LSH, the LSO yields negative weights when $n \geq 12$.

- Level Symmetric Hybrid quadrature (LSH): the value k is chosen in the sequence $(0, 1, 2, 4, 6, n-2)$. It also restricts the maximum value of n to 10 in order to avoid negative weights.

The S_N method is widely used at low orders (small values of N). For higher orders, the method is known to provide negative weights when N reaches 20 [143]. I order to compare the quadrature performance with different direction numbers, the SN method along with other method which base on neutron transport theory are not chosen in this thesis, except the CWDOM method.

3.3.3.2 Constant Weights for Discrete Ordiantes Method(CWDOM)

This quadrature set was developed by Taoufik Gassoumi and Rachid Said in [144]. This is an extension of the S_N method in which all the directions are given the same weights. Using the same notations as for the S_N quadrature of the previous section, the number of directions in one octant with this new scheme is equal to $\frac{N(N+1)}{2}$. The corresponding weights, assumed to be independent of directions, are:

$$\omega = \frac{\frac{\pi}{2}}{\frac{N(N+1)}{2}} = \frac{\pi}{N(N+1)} \tag{3.36}$$

The coordinates of the directions are then given as:

$$\begin{aligned} x &= \sin\theta_i \cos\phi_z = \sqrt{1-z_i^2}\cos\phi_z \\ y &= \sin\theta_i \sin\phi_z = \sqrt{1-z_i^2}\sin\phi_z \\ z &= \cos\theta_i = 1 - \frac{i^2}{N(N+1)} \\ d\phi &= \frac{\pi}{2N} \\ \phi_0 &= -\frac{d\phi}{2} \\ \phi_z &= \phi_{z-1} + d\phi \end{aligned} \tag{3.37}$$

Table 3.6 provides coefficients of this quadrature scheme for the case $N = 3$:

The CWDOM quadrature is also one of quadrature set which based on the S_N method. It indicates that these scheme is symmetry to any axis and it satisfies the zeroth, first and second moment condition as the LSO scheme does.

X	Y	Z	weight
0.2825971	0.2825971	0.9166667	0.2617994
0.6886191	0.2852354	0.6666667	0.2617994
0.2852354	0.6886191	0.6666667	0.2617994
0.9352537	0.2506005	0.2500000	0.2617994
0.6846532	0.6846532	0.2500000	0.2617994
0.2506005	0.9352537	0.2500000	0.2617994

Table 3.6: Constant weights for discrete ordinates method $N = 3$

3.3.3.3 The Fibonacci sets

This distribution of points is founded on spherical Fibonacci lattices [145] [146] [147], which are defined as:

$$\begin{aligned} \theta_i &= \arccos(1 - \frac{2i}{F_m}) \\ \phi_i &= 2\pi i \frac{F_{m-1}}{F_m} \end{aligned} \tag{3.38}$$

where (θ_i, ϕ_i) are the angular coordinates of the i_{th} points of the quadrature and F_m is the m_{th} Fibonacci number. F_m can be obtained as solution of the sequence:

$$\begin{aligned} F_0 &= 0 \\ F_1 &= 1 \\ F_m &= F_{m-1} + F_{m-2} \end{aligned} \tag{3.39}$$

With increasing m, the ratio $\frac{F_m}{F_{m-1}}$ converges quickly toward the golden ratio ϕ_{golden}. This provides the generator:

$$\begin{aligned} \theta_i &= \arccos(1 - \frac{2i}{N}) \\ \phi_i &= 2\pi i \phi_{golden}^{-1} \end{aligned} \tag{3.40}$$

Swinbank and Purser [148] improved this set by introducing an offset equal to $\frac{1}{N}$ on the z coordinate. This gives the so-called spherical Fibonacci point sets:

$$\begin{aligned} \theta_i &= \arccos(1 - \frac{2i+1}{N}) \\ \phi_i &= 2\pi i \phi_{golden}^{-1} \end{aligned} \tag{3.41}$$

The Fibonacci quadrature satisfy only the zeroth moment condition as the weight factors of each discrete direction are equal. It is able to satisfy the first moment condition with a huge number of direction. But the higher moment condition could not be satisfied no matter what number of direction it has. Also this scheme is not symmetry like other scheme present in the previous sections.

3.3.3.4 The qMC sets

qMC methods are similar to MC methods [149], but instead of relying on (pseudo)random numbers to generate statistical events (location of absorption, scattering direction, etc), low-discrepancy sequences (LDSs) [150] are used in the qMC method.

If two random numbers $(R_{\theta_i}, R_{\phi_i})$ are sampled in the MC method from a uniform distribution within the interval $[0, 1]$, a point on the unit sphere can be defined. Its angular coordinates are given by:

$$\begin{aligned} \theta_i &= \arcsin(\sqrt{R_{\theta_i}}) \\ \phi_i &= 2\pi R_{\phi_i} \end{aligned} \tag{3.42}$$

The same idea can be used in the qMC method by simply replacing the random numbers with elements of a LDS. LDSs are constructed in such a way that they map the unit hypercube more uniformly than random numbers and thus allow faster convergence than MC methods for the calculation of integrals over $[0, 1]^n$. In the present work, we choose Sobol's and Halton's LDS. The coordinates of the quadrature points on the unit sphere, based on [151], are in this case given as:

$$\begin{aligned} x &= 2\cos(2\pi R_1)\sqrt{R_2 - R_2^2} \\ y &= 2\cos(2\pi R_1)\sqrt{R_2 - R_2^2} \\ z &= 1 - 2R_2 \end{aligned} \tag{3.43}$$

where R_1 and R_2 are two numbers from the LDS. Notice than in qMC, equal weights are used for all directions, as in standard Monte Carlo techniques. It means this scheme could satisfy the zeroth moment condition. But it could not satisfy higher moment condition and it is also not symmetry to any axis.

3.4 Concluding remarks

In the present chapter, we have studied radiative transfer in a participating medium. The usual solution to this problem requires solving the RTE with an appropriate air gas model.

Two global gas methods were described to treat air absorption: the gray and SLW models. Several line-of-sight radiation tests were carried out to assess their performance against LBL calculations chosen as references. These tests had two objectives. The first was to estimate the air absorption to determine whether air could be treated as a transparent medium; the second was to find the most appropriate full-spectrum model for our application.

Concerning the first objective, in the solar spectral range, the ability of air to absorb radiation is weak. Indeed, less than 10% of solar incident energy is absorbed in the most extreme case. In the thermal IR, air plays a more significant role, as approximately 65% of radiative energy is absorbed by air in the most extreme case: Air thus needs to be treated as a participating medium.

Concerning the second objective: as expected, the SLW method was found to give more accurate results than the gray model at a slightly higher computational cost. The choice of the model needs to be made based on the complexity (geometry, coupled or noncoupled calculations, etc.) of the problem studied and the precision requested. For a microclimate simulation, the space between the building surfaces is usually small (a few meters). The distance for solar radiation transfer is often similar to the values considered for the test considered in this section, which may reduce the influence of the error if we consider the air transparent. In summer, with a relatively high air temperature and RH, the air absorption coefficient increases.

At the same time, the difference between the air and building surface temperatures can be significant [152], which may further increase the error of a transparent model in the IR region. The SLW model thus appears to be a good compromise and is applied in the subsequent chapters for radiative transfer calculations in a geometry representative of a set of buildings.

Once the SLW air model was chosen, we focused on the method to solve the RTE. The DOM was described in this chapter, and a comparison of several differencing schemes was carried out. Other factors, such as the discretization schemes over angles and space, may also be critical in DOM calculations. However, as these parameters are strongly connected with the complexity of the geometry, we discuss them in the next chapter in two realistic configurations: a steady-state simulation in a canyon geometry and a transient simulation over an area located on the INSA Lyon campus.

Chapter 4

Evaluation of radiative heat transfer

Contents

4.1 Steady-state simulation: urban canyon

The first calculation is a steady-state calculation with the geometry of an urban canyon. The canyon can be seen as the basic unit of the urban area [153]. Two approaches presented in the previous chapters are applied for the simulation. A ray tracing approach developed by Blaise RAYBAUD [154] joins the comparison in the solar radiation part.

4.1.1 Geometry

Calculation parameters (distances and heights) of the canyon are provided in Figure 4.1.

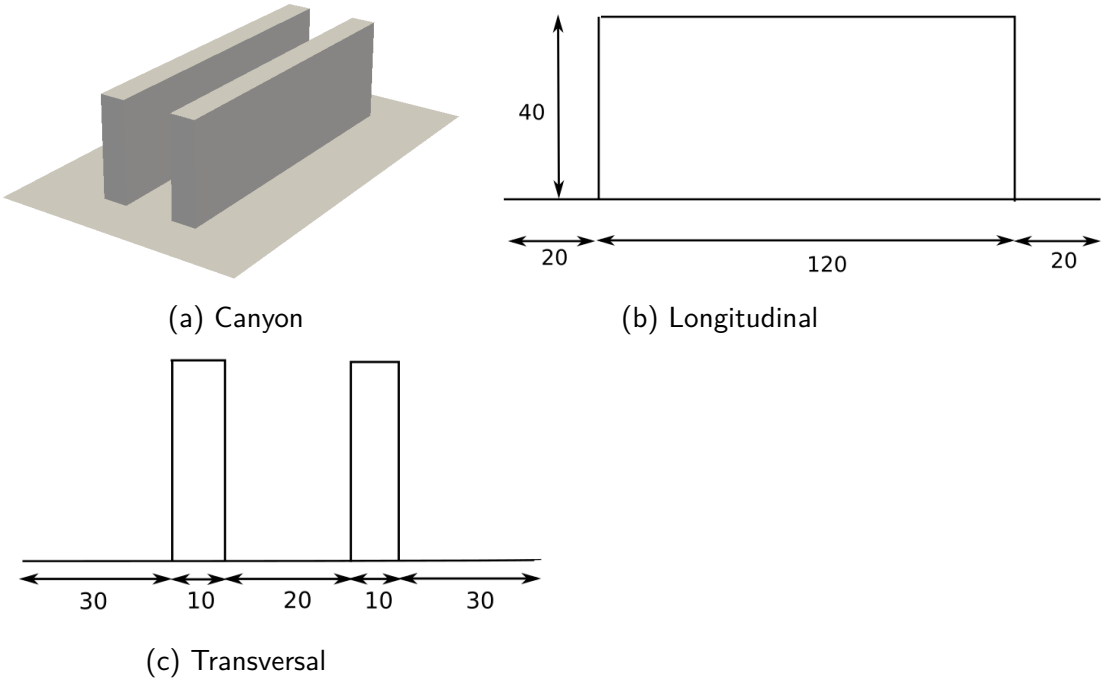

(a) Canyon (b) Longitudinal

(c) Transversal

Figure 4.1: Model for the solar radiation calculation

4.1.2 Boundary conditions

Because the simulation contains both the solar radiation part and the IR radiation part, the parameters for the boundary conditions are defined to be different for the two kinds of radiation.

For solar radiation, the parameters are given in Table 4.1.

The IR radiation is presented in Table 4.2.

The surface is divided into triangle patches in the radiosity method with a maximum size around severals meters. A structured hexahedron mesh is applied in the DOM calculation with a size of 1m in all three dimensions. The direction number used in DOM calculation is set to 100. The Fibonnaci quadrature is first applied for the comparison of the different methods. Then an analysis of different quadratures is discussed in the later of this section.

Soil albedo	0.05
Wall albedo	0.09
Roof albedo	0.12
Sky absorbility	1
Azimuth angle	43.8983°
Elevation angle	62.3438°
Sun direction	(0.3218,0.3348,-0.8857)
Solar radiation received by horizontal surface	842.2396 W/m^2

Table 4.1: Boundary condition for solar radiation

Soil emissivity	0.95
Soil temperature	300K
Wall emissivity	0.91
Roof emissivity	0.88
Building temperature	285K
Sky absorbility	1
Sky temperature	273K

Table 4.2: Boundary condition for infrared radiation

4.1.3 DOM modification for the urban radiation simulation

The DOM is applied mainly in combustion reactor problems. The configuration is quite different in the urban radiation transfer field. For a better implementation, modifications are required to obtain precise results. The most important modification focuses on the boundary conditions and building detection as an obstacle to thermal heat transfer inside the global scene enclosure.

4.1.3.1 Setting DOM boundary conditions

Urban radiation consists of two parts: solar radiation and thermal IR radiation due to radiative emission by the various surfaces in the scene. The boundary conditions for each kind of radiation are quite different from each other.

Solar radiation As presented in chapter 1, global solar radiation has two parts:

$$I_{sw} = I_{dir} + I_{dif} \tag{4.1}$$

I_{dir} is the solar radiation that comes directly from the sun. This part of the total radiative intensity is the highest among all three terms (including thermal IR radiation emitted by the elements of the scene). The solar beam reaches the surfaces in the sunlight direction. With respect to its directional phenomena, a special quadratude is used to calculate the beam solar radiation with the DOM: Only the solar direction is considered in the quadrature. The weight for all the other directions is set to zero. As presented in Figure 4.3, only five of the six faces of the enclosure of the scene are potential source surfaces because the direct solar beam cannot enter the field by the bottom surface (S4). For a given sun direction, only three surfaces act as sources. They are determined by the solar direction. For example, if the sun

beam comes in a direction with (X>0, Y>0, and Z<0), the left surface (S1), the top surface (S3) and the front surface (S5) are considered the entry surfaces of solar radiation. In general, the top surface is always in the group of source surfaces.

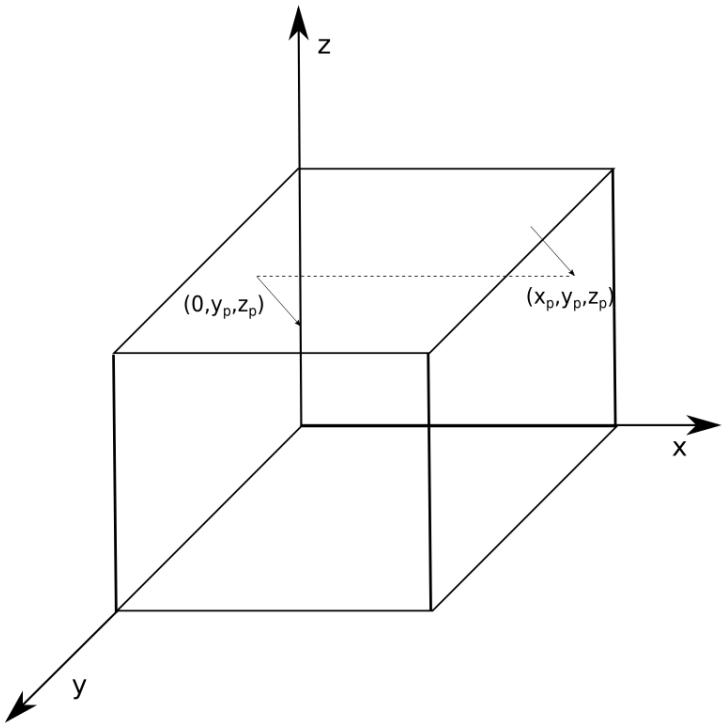

Figure 4.2: The periodic boundary condition

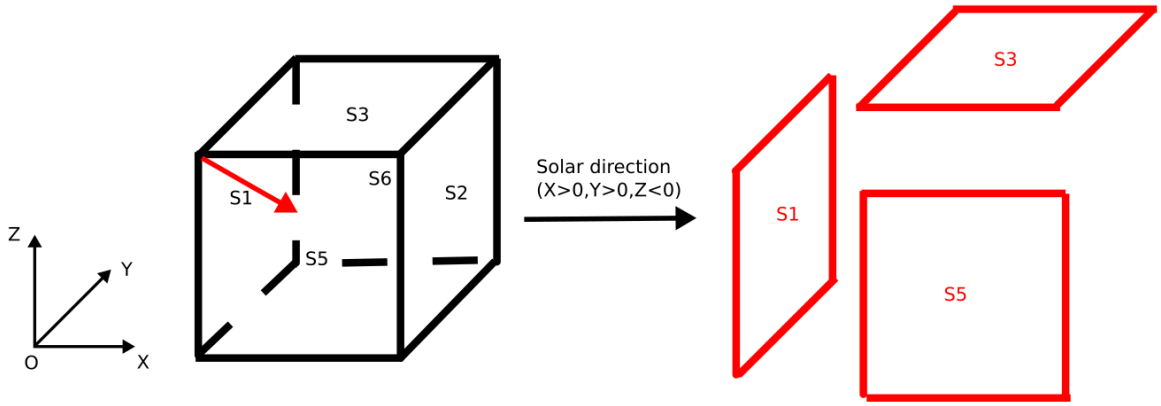

Figure 4.3: Source surface determined by the solar direction

In addition, a periodic boundary condition is used for all the vertical surfaces to address the solar radiation transfer inside the model. If a ray with intensity I_{ray} strikes a vertical surface at a location with coordinates (x_p, y_p, z_p), then the same value of intensity is assumed at the point $(0, y_p, z_p)$ in the same direction of propagation, as depicted in Figure 4.2. To realize this, we first reverse the sun direction and calculate the distance between the center of each patch on the vertical source surface and the level of the top surface $(Z = H_{model})$. Then, we calculate the solar intensity for each center of the patch on the vertical surface by the application of the Lambert Beer Law.

The boundary condition for the I_{dif} part is almost the same as for a normal DOM calculation. All the vertical surfaces share the same solar radiance. A full quadrature set is applied because the diffuse part is not as directional as the direct part.

A simulation of a selected urban area normally contains a third part of solar radiation I_{ref}. This refers to the solar energy reflected by the surface outside of the selected area, which is ultimately diverted into the area. This part of the energy is neglected in this thesis because of the lack of information. In the same fashion, buildings outside of the scene enclosure acting as solar masks are neglected.

IR radiation Similar to the solar reflected part, it is difficult to know the exact value of radiance because of the unknown outside ambiance. The scene is thus assumed to stand alone on a horizontal plane. The boundary condition for S1 to S6 is chosen as a diffuse gray surface, where the temperature of the vertical surface is determined by the direction of the quadrature set. If the direction is ascending, all the temperatures of the vertical surfaces are equal to the ground temperature. If it is descending, all the temperatures switch to the sky temperature (Figure 4.4). The emissivity of the vertical surface is defined as a constant. The horizontal surface S3 is assumed to be at sky temperature.

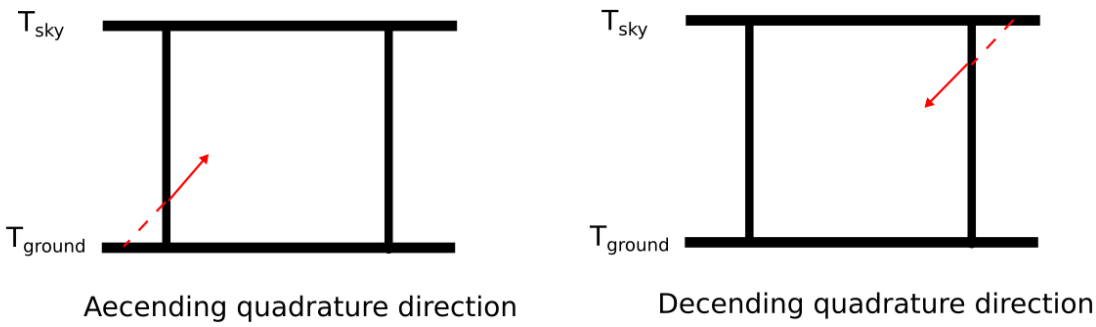

Figure 4.4: Boundary condition for the infrared part

In comparisons with the radiosity results in the following section, the boundary conditions in the IR radiation calculation can lead to vast differences. In the radiosity method, a vertical patch facing "outside" the scene has thermal radiative exchanges with the sky vault (usually a hemisphere) and the ground (part of which can be unmeshed), and the influence of each (sky and ground) is difficult to estimate. Therefore, when comparing with the radiosity results in this thesis, the vertical boundaries in the DOM are changed to sky patches regardless of the chosen discretization direction. If the comparison contains only the DOM, the comparison uses the boundary conditions presented in this section.

4.1.3.2 DOM building simulation

The DOM is a well-known method in combustion problems. In a combustion reactor, normally, there is no obstruction inside the simulation volume. However, in the simulation of urban areas, buildings are the main object of interest, and the simulation addresses events *outside* buildings, not *inside* a combustion chamber. The buildings in the scene are set inside a bounding volume, the simulation enclosure, which is a cuboid. The DOM consequently has to be modified to detect internal boundaries inside the whole simulation volume. This is done in two steps, one while preprocessing the simulation and the other during the simulation:

- Meshing period: Typically, the DOM uses 3D structured meshes composed of cubic patches. Instead of fitting the structured grid to the buildings inside the scene, the dimensions of the buildings are rounded to the closest value inside the grid. Hence, the buildings inside the model can be identified as groups of cubic patches with a tag to distinguish them from "void" air patches. If there is more than one building in the field, every building is specified with a different tag. Patches adjacent to the buildings are marked as "skin patches". This refers to the very first patch outside the building surface, where the DOM propagation has to be stopped. If the building is cuboid or can be divided into several cuboids, the skin patches are categorized by the facing direction (left, right, front, back and top), which is easy to identify in the calculation. If the building is in another shape or has a differently shaped component (cylinder or triangle), only the skin patch is noted (Figure 4.5).
- Calculation period: In the calculation, for each chosen quadrature direction and for every patch traversed, the patch can be air (in this case, we proceed with the DOM) or a skin patch. The first skin patch encountered along a direction is an entry patch (Figure 4.5), and the second patch is an exit patch. When the calculation comes to an entry patch, it is treated as a normal boundary patch. Then, for the following patches (that are inside a building), RTE solution stops until the corresponding exit patch is identified. The RTE is calculated with the boundary condition of the exit patch. For a cylinder- or triangle-shaped building, no enter or exit patch is specified. Upon contact with the skin patch, the incident flux is calculated, and RTE calculation for the following patch stops until another skin patch is identified. This general method can also be applied in the cuboid-shaped case, although it is easier for later surface data recovery to identify the entry/exit patches along each direction for each building first. This is why, when possible, the first method (definition of the entry and exit patches) is applied in this thesis.

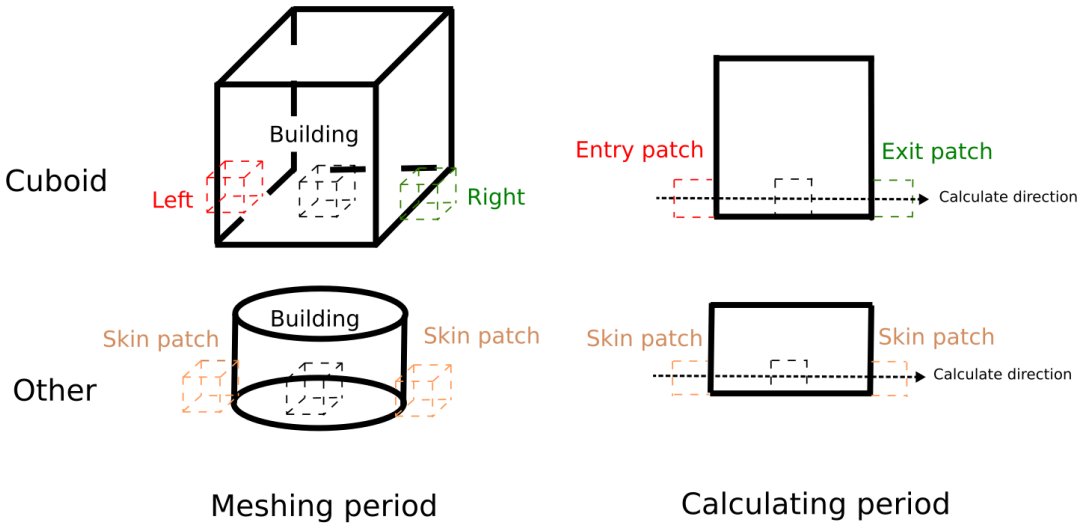

Figure 4.5: Conception of building simulation with mod

4.1.3.3 Surface data mesh conversion

As different meshes are used for the radiosity method and DOM, an interpolation of the results obtained by these two techniques on the same mesh is required to allow fair and

relevant comparisons.

For the DOM, a structured discretization of space is used. Surfaces are represented by numerous rectangles (as shown in red in Figure 4.6). With the radiosity method, on the other hand, surfaces are approximated by triangles (shown in black in Figure 4.6). The connection between the two meshes is as follows:

1: The location of the radiosity triangle mesh is searched inside the DOM mesh by locating the triangle center. As shown in Figure 4.6a, if the triangle mesh is small enough to be entirely located inside the yellow area in the figure, we assume that it has the same value as that on the DOM mesh at the same location.

2: If the triangle center is in the white area in Figure 4.6a, we approximate the intensity at the center of the triangle by a bilinear interpolation (shown in Figure 4.6b):

$$I_{center} = L(m,n) + \frac{cx}{\Delta x}(I(m,n+1) - I(m,n)) + \frac{cy}{\Delta y}(I(m+1,n) - I(m,n)) + (I(m,n) + I(m+1,n+1) - I(m+1,n) - I(m,n+1))\frac{cx}{\Delta x}\frac{cy}{\Delta y} \tag{4.2}$$

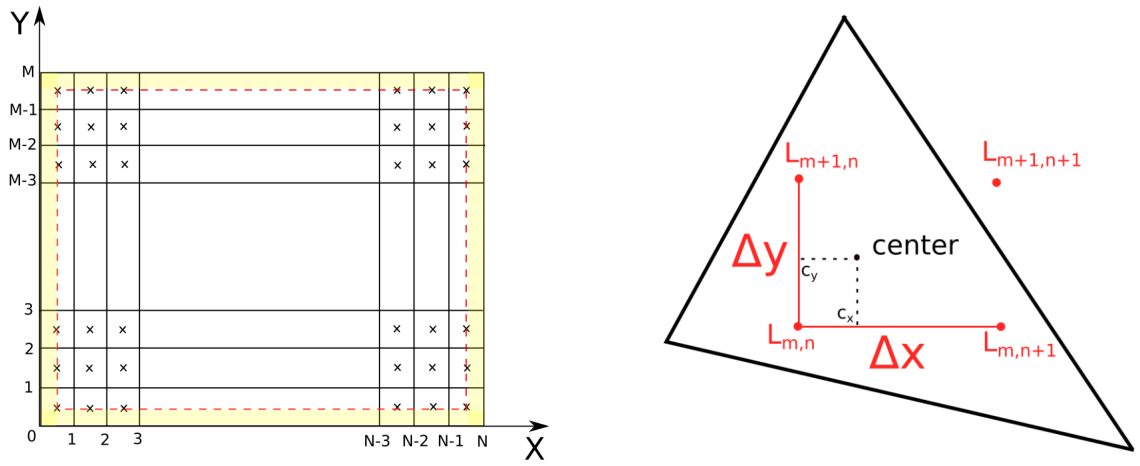

(a) DOM mesh field

(b) Bilinear interpolation

Figure 4.6: Different discretization on surface

4.1.4 Radiosity modification for the urban radiation simulation

Not only does the DOM require modification for the urban radiation transfer simulation, but the radiosity also needs some modification to allow for a fair comparison. First, the sky vault geometry is chosen. Then, the calculation of the direct solar radiation (also called beam solar radiation) is detailed.

4.1.4.1 Testing geometries for the sky vault

For modeling urban areas, not only the urban morphology but also the sky that covers all these buildings needs to be developed. In terms of radiation transfer, the sky participates in the following ways:

- Emission of diffuse solar energy: As mentioned in the first chapter, part of the solar energy is diffused by the different components in the atmosphere. This solar energy passes through the atmosphere and impinges upon the building. Separated from the direct solar radiation, the diffuse radiation is unbiased in direction, which suggests a Lambertian surface for the sky patch. Different sky models are presented in the first chapter, and for most of the models mentioned, sky information such as clearness and brightness is needed, which is not easy to find for a determined area.
- Emission in the IR range: The longwave radiation emitted by the sky also plays a significant role in the urban area energy budget [155]. Since 1918, when the first sky model to estimate the sky was proposed, numerous sky models have been developed. A comparison was made for these sky models [55]. However, the best sky model remains undetermined.

For a building simulation that takes the sky into consideration, the sky geometry is often described by a hemisphere that covers the entire scene. The radius of the hemisphere R_{sky} is much larger than the dimension of the study area. The whole system is not enclosed (due to the ground outside the scene but inside the hemisphere not being meshed), which leads to a nonconservative system. Indeed, the view factors of each scene (and sky) patch with the "missing" ground are not calculated, corresponding to an energy loss through this unmeshed surface. In this section, we aim to determine whether this sky modeling can affect the flux received by the building surface and the relation between the difference in flux and the radius of the hemisphere.

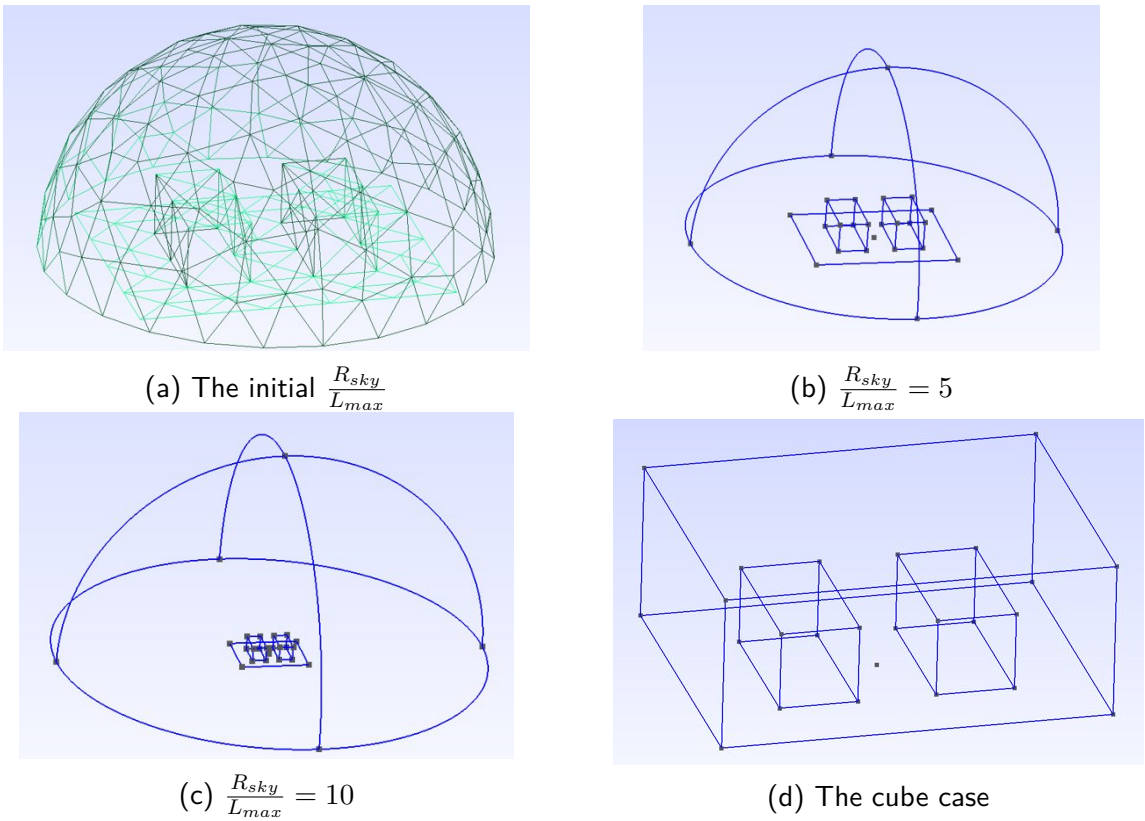

(a) The initial $\frac{R_{sky}}{L_{max}}$ (b) $\frac{R_{sky}}{L_{max}} = 5$

(c) $\frac{R_{sky}}{L_{max}} = 10$ (d) The cube case

Figure 4.7: The different sky model to test the incident flux on the building surface

In this test, we build two blocks that represent the buildings, with dimensions of 2 m×1 m×1 m. The dimensions of the area are 5 m for the length and 4 m for the width. For the beginning, the radius of the sky is 3.5 m, which slightly surpasses the maximum dimension L_{max} (Figure 4.7a). Then, the ratio $\frac{R_{sky}}{L_{max}}$ is changed to 5 and 10 to determine the difference

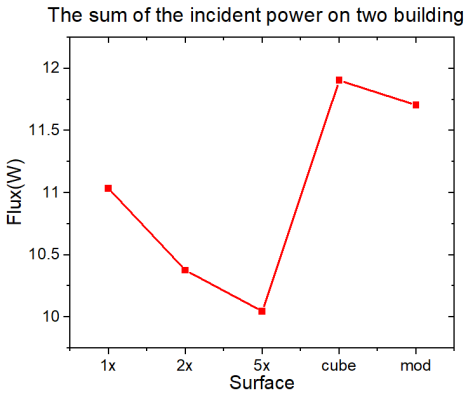

Figure 4.8: The difference of the sum of incident flux on the building

in flux on the building surface. Finally, a cuboid sky model is tested to compare with the results obtained by the DOM (Figure 4.7d). The sky is assumed to emit a normalized power of 1 W/m^2. The emissivities of the sky, ground and building patch are fixed at 1, 0.9, and 0.8, respectively. The difference in the total incident energy on the surface is shown in Figure 4.8.

The figure clearly shows the fall of incident flux on the building with the rise of the sky hemisphere radius. Due to the building height remaining constant, the difference in the building roof between each case is 0. This means that increasing the radius of the sky has a no negligible impact on the incident flux on the vertical surface. The roof is affected only by the reflection of the vertical surface. For the closed system, the cuboid, there is no loss for the power received by the building. In contrast, the radiation is slightly concentrated on the building. The result means that if we wish to compare the results obtained from the radiosity method and DOM, it is better to use the same sky geometry.

4.1.4.2 Beam solar radiation for radiosity

For the radiosity method, the calculation of direct solar radiation is slightly more challenging than that of the diffuse part. The calculation of the direct energy is formulated in two steps:

1: The direct solar beam simulation. A backtracing method is applied to evaluate the first impact of the solar beam.

2: The calculation of the inter reflection in the model is realized by the radiosity method.

The backtracing method has the same principle as the ray tracing method. The process is simple because the reflection calculation is not executed in this section. For each mesh element in the model, a ray is launched from the center of the element along the reversed sun direction. If the scalar product of the ray direction and the normal of the element is positive, the element has the potential to receive solar energy, and the calculation proceeds to the intersection test. If the results are negative (Mesh 1 in Figure 4.9), the element is considered a nonilluminated surface, and we move on to the next element. For the intersection test, if the ray is intersected by another element in the model, it is considered obscured by another object and receives no direct solar energy for the first impact (Mesh 2). Otherwise, this element sees the sun directly, and the incident power can be obtained by [156] with the scalar product calculated at the beginning (Mesh 3).

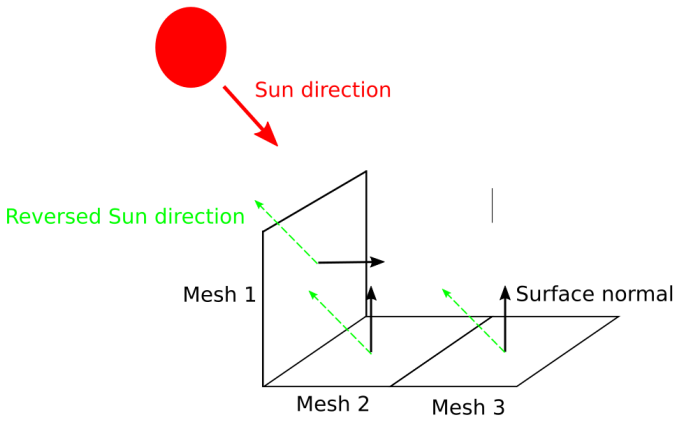

Figure 4.9: The tracing back method

After these modifications are performed for the DOM and radiosity, the calculation of the radiation transfer in the canyon is launched. Regarding solar radiation, only direct solar radiation and its reflection are calculated because the ray tracing approach in general (and the algorithm designed by R.Blaise in particular) is not suited to handle diffuse solar radiation. The IR radiation is simulated only with the DOM and radiosity approaches.

4.1.5 Comparison of the shortwave fluxes

The result of direct solar radiation by the three methods is illustrated in Figure 4.10. The upper range for the ray tracing method is much higher than that of the other two methods. Additionally, a "white" shading boundary exists in the ray tracing and DOM cases, while it is not observed with the radiosity method.

At the ground level, all three methods create a similar shading area shape. The major differences are observed at the edge of the shadowed area. With the ray tracing method and the DOM, there is a transition area between the shadow and the illuminated ground (patches in white). This space is larger when using the DOM. There is no transition zone in the radiosity method, as a surface patch is either lit or shadowed based on the back-tracking described earlier.

The difference between each pair of methods is presented in Figure 4.11. Differences are calculated by the result of the first method minus the second one on the captions provided with these figures.

The main cause of the difference at the ground level is due to the principle of each method:

Radiosity: The determination of the obstruction is calculated by a line-triangle intersection. As shown in Figure 4.12, if there exists a third surface S3 between S1 and S2, even if it is very small, it intersects the vector from the center of S1 to the center of S2. The two surfaces are considered to be unable to definitively see each other. The heat transfer between them is 0.

Ray tracing: The ray is launched from somewhere on surface S1 with a determined

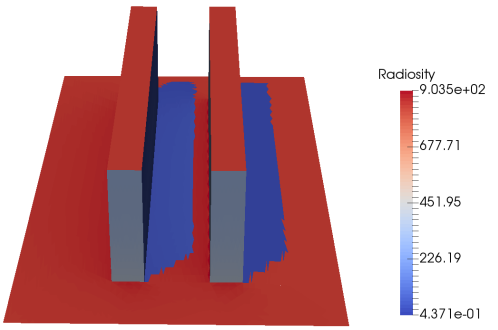

(a) Radiosity

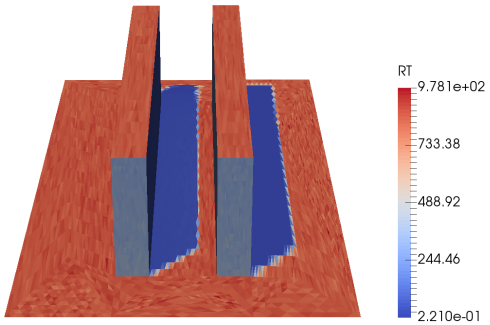

(b) Ray tracing

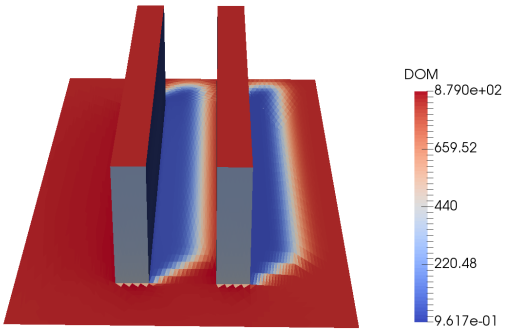

(c) DOM

Figure 4.10: Incident heat flux (W/m^2) calculated by different methods

direction. Even if there is a small surface that intercepts a part of the rays. A part of the energy succeeds in reaching S2. The heat transfer between S1 and S2 is a value above 0.

DOM: This method calculates the radiative transfer progressively. The large gap between two points is realized by a relatively slow variation.

The difference between ray tracing and the radiosity method is concentrated on one line of the mesh (Figure 4.11c). It is the threshold whether sunlight can pass the top of the vertical surface. The difference is somewhere between the maximum value of heat flux (approximately 860 W/m^2) and 0 W/m^2. The result of ray tracing has a higher value if this mesh is considered obstructed by the building with the radiosity method. It has a lower value if this mesh is considered fully illuminated by the sun.

The difference between the DOM and radiosity method is due to the calculation of the DOM. The radiosity method passes directly from a value near 0 to the maximum value. With the DOM, the variation is smoother, which requires more mesh to transit from shading to the normal ground surface. The DOM-ray tracing difference is the combination of the two effects above.

At the building level, we take the result of radiosity as the reference, and the difference between the methods is shown in Figure 4.13. The main difference between the DOM and the radiosity method is located at the bottom of the building. This is caused by the method chosen for the view factor calculation. As we presented in the radiosity section, the ISA generates an error when two surfaces are too close. Even with a subdivision, there can still be a small error for two close surfaces. The random direction generation in the ray tracing method generates an unstructured distribution, which leads to the difference shown in 4.13b.

In this model, different building surfaces receive different kinds of solar radiation, as

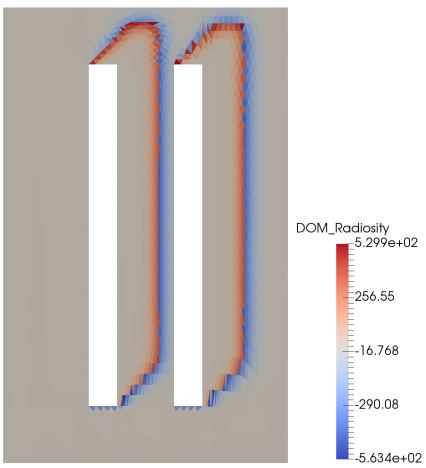

(a) DOM-Radiosity

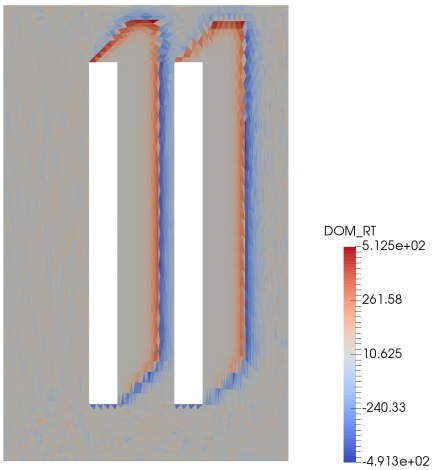

(b) DOM-Ray tracing

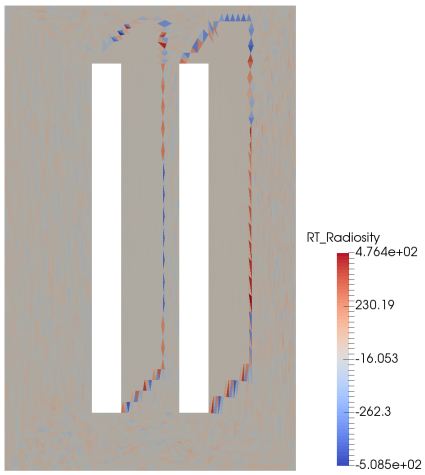

(c) Ray tacing-Radiosity

Figure 4.11: The difference of incident heat flux (W/m^2) on the ground between each two method

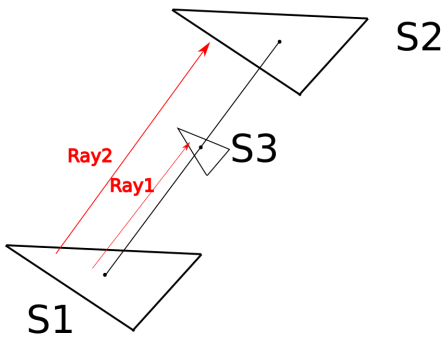

Figure 4.12: Determination of the intersection

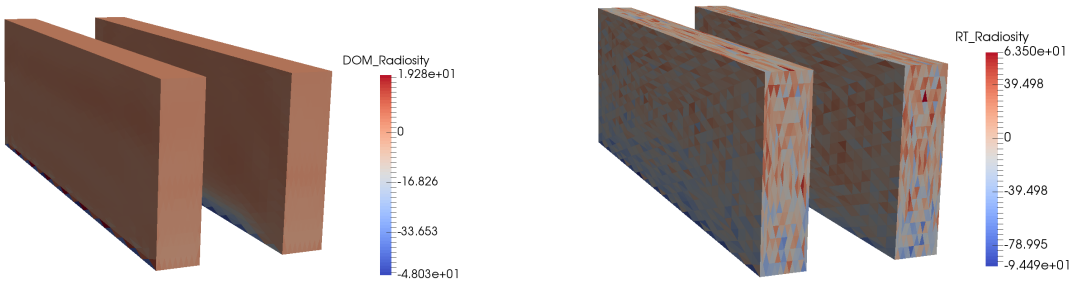

(a) DOM-Radiosity (b) Ray tracing-Radiosity

Figure 4.13: The difference of incident heat flux (W/m^2) on the building surfaces between the methods

shown in Figure 4.14. Three surfaces are chosen to be analyzed:

Left-side vertical surface of building 1: This surface is exposed directly under the sun. The incident radiation contains a direct part and a reflected part from the ground.

Roof of building 1: Due to the same height of the building, both roofs receive only the direct solar beam (the sky albedo equals 0).

Right-side vertical surface of building 2: This surface receives only a small portion of the sun energy reflected by the ground.

Due to the interreflection inside the canyon, the surface of the U shape is avoided.

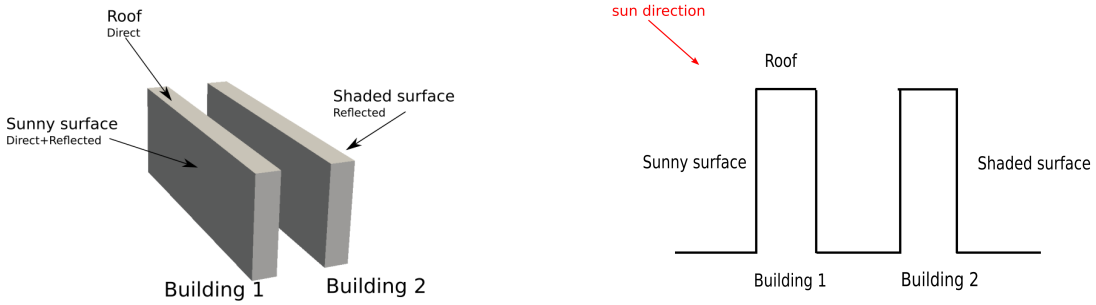

Figure 4.14: The difference surface chosen of buildings

Left-side vertical surface of building 1: Figure 4.15 illustrates the difference in irradiance on the left surface of building 1. The error produced by the view factor calculation dominates in the comparison of radiosity with the others. For the area less influenced by this impact, the difference between the DOM and radiotherapy remains at a relatively low level. Both of these methods obtain the result that the flux decreases progressively from the bottom to the top of the building. For the ray tracing method, the distribution is unstructured by the random reflection of the ground surface. The gradient of flux also decreases and is hard to visualize (Figure 4.16; the profile is the vertical middle line of the surface). Table 4.3 shows that the difference in the sum of incident power is quite small between the DOM and the radiosity method because the surface reflection model is the same for these two methods. Due to the random direction generation of the ground reflection, a part of the energy misses the surface of the building and is ultimately be absorbed by the sky, which causes no negligible gap between ray tracing and the other two methods.

Roof of building 1: The roofs of two buildings receive only direct solar energy, which obtains an equal result for the DOM and the radiosity method (Figure 4.17a). The difference

(a) DOM-Radiosity

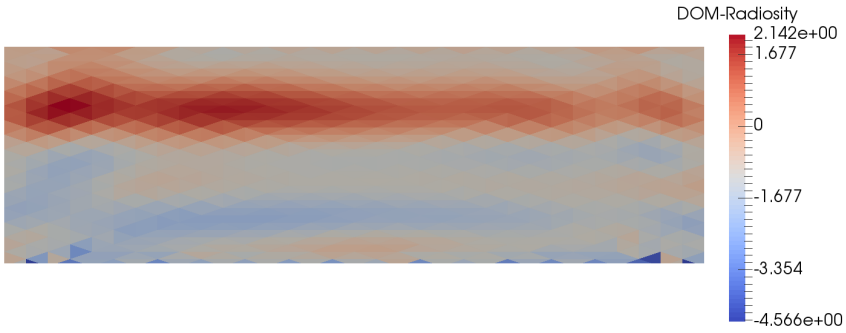

(b) DOM-Radiosity ($Z > 3m$)

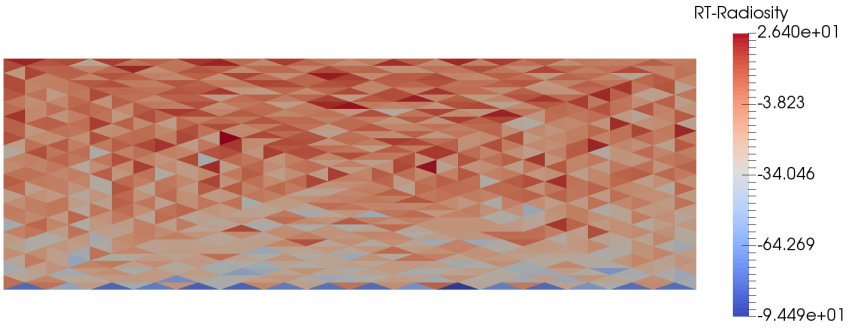

(c) Ray tracing-Radiosity

Figure 4.15: The difference of incident heat flux (W/m^2) on the building sunny surface between the methods

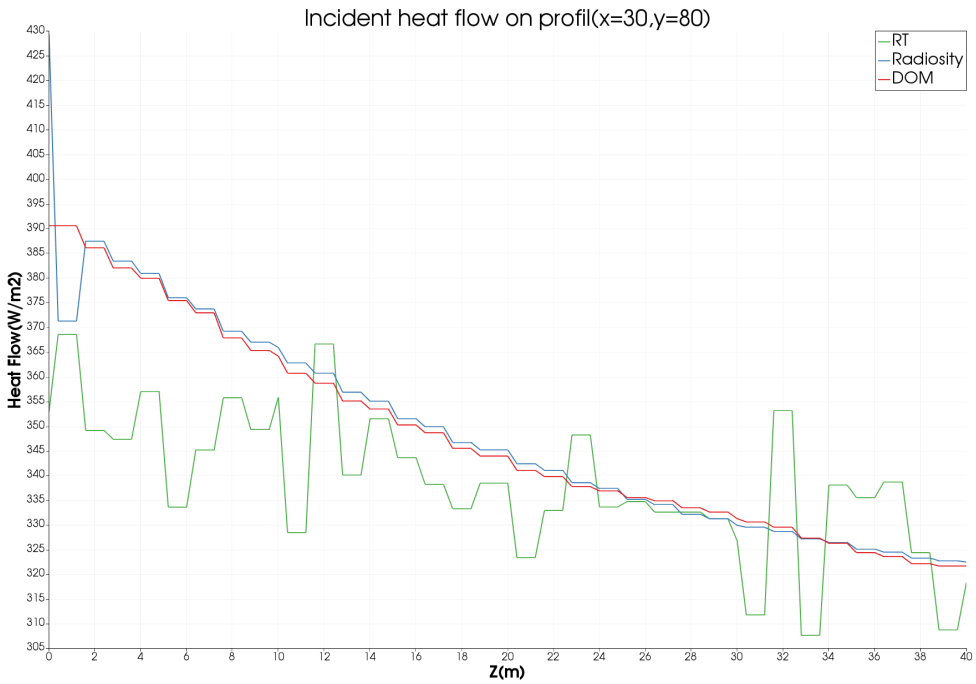

Figure 4.16: The incident heat flux on the sunny surface

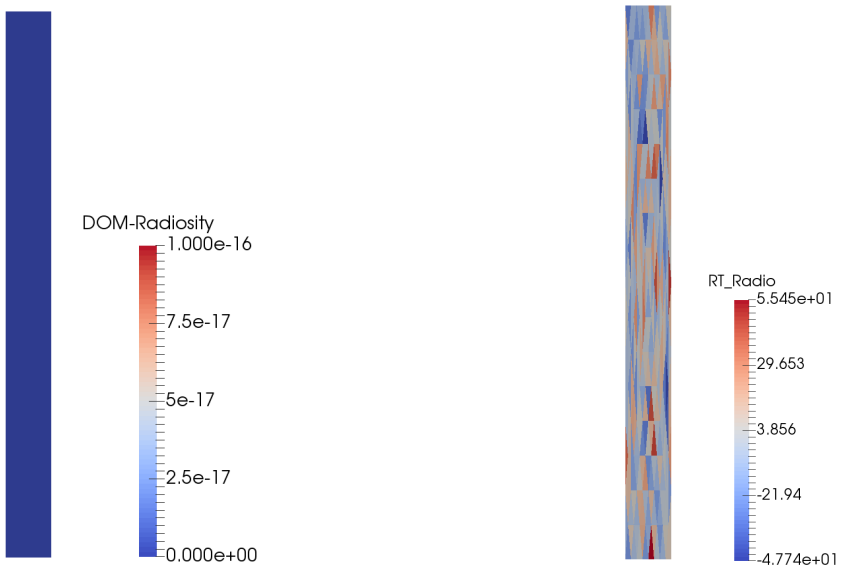

(a) DOM-Radiosity (b) Ray tracing-Radiosity

Figure 4.17: The difference of incident heat flux (W/m^2) on the roof between the methods

between ray tracing and the other methods is caused by the randomized points of shooting at the boundary surface (Figure 4.17b). Table 4.3 shows that the difference in solar energy received for the roof is quite small among these methods.

(a) DOM-Radiosity

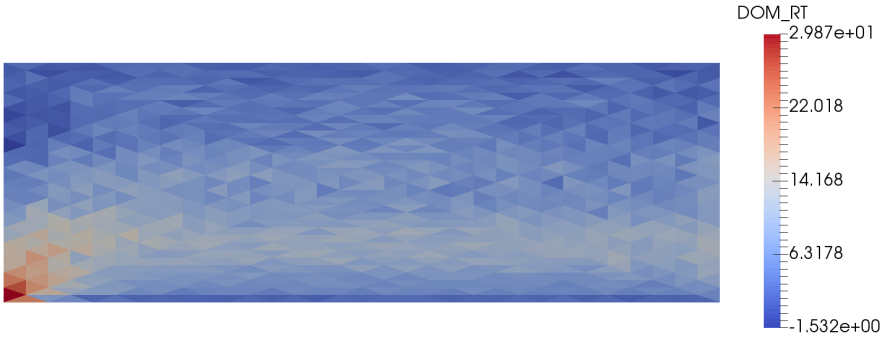

(b) DOM-Ray tracing

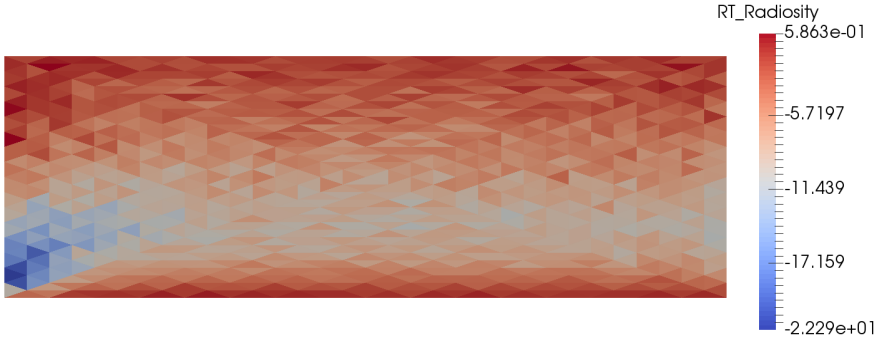

(c) Ray tracing-Radiosity

Figure 4.18: The difference of incident heat flux (W/m^2) on the building shaded surface between the methods

Right-side vertical surface of building 2: The difference on this surface is concentrated in the bottom-left corner. This area receives more energy than anywhere else on the surface because it is closer to the illuminated ground surface. For the radiosity method, the view factor error also has an impact on this area (Figure 4.18a). By Figures 4.18b and 4.18c, a gap of over 20 W/m^2 is produced by ray tracing and the other two methods in this area, which is far larger than elsewhere on the surface. Based on Table 4.3, ray tracing involves a much smaller overall incident power on the shading surface cause of the reflection model. The impact is much more obvious because no backward direction is chosen for the reflection.

To conclude, the result shows that the reflection model of the surface is a determining factor for these methods. Both the radiosity method and the DOM apply a perfect diffuse reflection, which leads to quite similar results for these two methods. The ray tracing method

	Ray Tracing	DOM	Radiosity
Incident heat flux on sunny surface(W/m2)	337.027	346.981	348.226
Incident heat flux on roof(W/m2)	840.56	842.23	842.23
Incident heat flux on shaded surface(W/m2)	11.62	18.40	17.68

Table 4.3: Irradiance on the different surface of building

cannot apply the normal diffuse model due to the computational cost, which results in a larger difference in irradiance value and distribution. However, this model does not contain specular reflection elements (windows and some metal surfaces), which are easier to handle with the ray tracing method than the radiosity method and DOM.

4.1.6 Comparison of the longwave fluxes

In this part, we concentrate on the IR radiation transfer in this canyon. Only the DOM and the radiosity method are implemented in this part. A calculation of the difference between the two methods is shown in Figure 4.19.

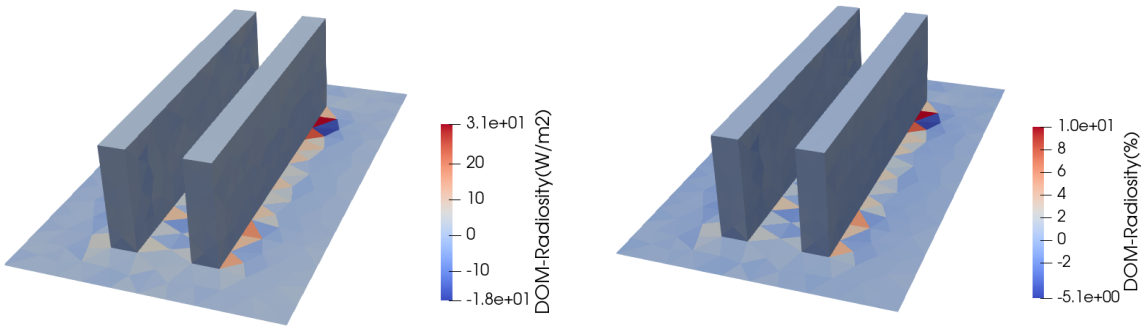

(a) Difference of flux in $[W/m^2]$ (b) Difference of flux in %

Figure 4.19: The difference of incident flux with DOM and radiosity

Figure 4.19a presents the difference in flux of every single patch in the canyon:

$$Dif(W/m^2) = \Phi_{DOM} - \Phi_{radiosity} \tag{4.3}$$

Figure 4.19b calculates this difference in percentage for all the patches:

$$Dif(\%) = \frac{100(\Phi_{DOM} - \Phi_{radiosity})}{\Phi_{radiosity}} \tag{4.4}$$

A difference, ranging from -18 W/m^2 to 31 W/m^2, can be observed for the patches located on the ground near the building bottom, presumably due to the view factor calculation by the ISA method. In the previous case (solar radiation), the view factor is calculated with the mesh generated for the ray tracing method. The patch size is quite small at the leaf level of the hierarchy tree structure. However, in the IR calculation, we redesign the mesh to save calculation time. The larger size of the mesh leads to this magnitude of error for the adjacent case even with the subdivision method. However, this time, the results of the patches on the building are not heavily influenced by this error.

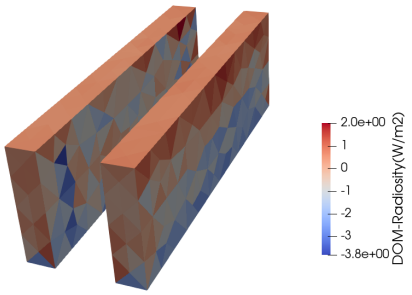

(a) Difference of flux in $[W/m^2]$

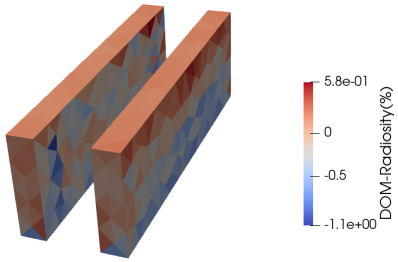

(b) Difference of flux in %

Figure 4.20: The difference of incident flux for the building patches with DOM and radiosity

As presented in Figure 4.20, the difference between the methods is limited between -3.8 W/m^2 and 2 W/m^2, which gives -1.1% to 0.58% of the local value. A more precise result can be obtained with a more refined mesh for the radiosity method. However, with this magnitude of error ($<$1% absolute), we can conclude that our DOM model works well in the IR radiation calculation with a transparent air model.

4.1.7 Influence of the angular and spatial discretization schemes

Demonstrated by the comparison between the DOM and radiosity with the canyon test in the previous section, our DOM model is proven to be able to precisely calculate the radiation transfer in a relatively complex geometry. Then, we concentrate on increasing the calculation performance to obtain a more precise result with less time consumption.

The principle of the DOM is discretizing both angular and spatial information to calculate the radiation transfer. The discretization over both angle and space can affect the method's performance. In this section, a study on these discretizations is carried out.

4.1.7.1 Angular quadrature schemes

In this part, this test of the canyon is carried out with different quadrature schemes (Fibonacci, CWDOM and qMC) presented in the previous chapter. We first fix the discretization number to 100 and compare the different quadratures' performances. Then, we change the number and determine the magnitude of the difference as a function of the discretization number.

Solar radiation The results of simulations for the canyon geometry are depicted in Figure 4.21. All three quadrature sets share the same kind of patterns. The performances of these different quadrature schemes are illustrated on a profile located on the ground $(y = 80,\ z = 0)$ (Figure 4.22). In general, for the simulations at the ground level, the differences observed using the different quadrature sets are more important on the shadowed area than on the illuminated parts of the buildings.

Figure 4.23a illustrates the error between the Fibonacci outcomes and the radiosity method for the building at the right. The largest errors are located at the bottom of the building. This is because the soil mesh and this specific part of the building mesh are very close to each other, which generates large errors in view factor calculations [100]. At the building

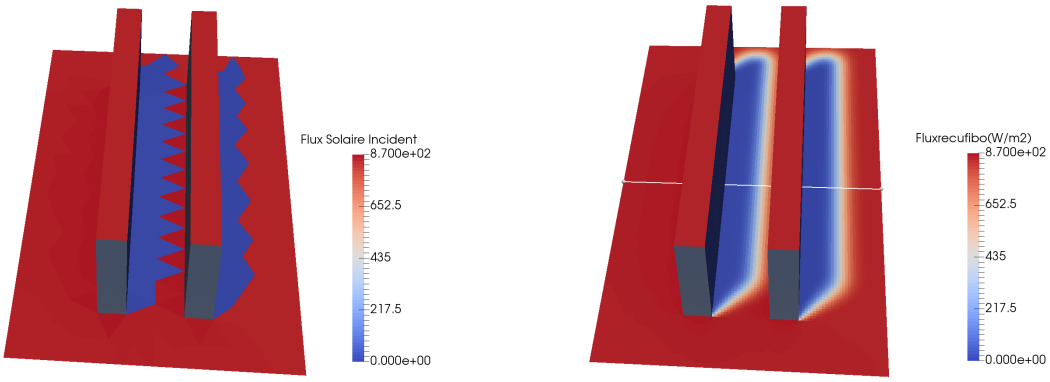

(a) Radiosity (b) DOM

Figure 4.21: Result of the solar radiation test

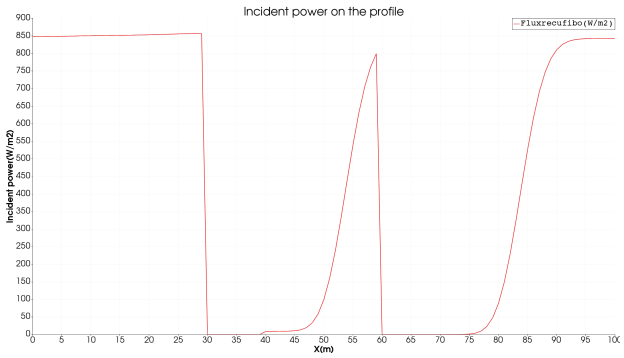

(a) Incident power of Fibo set

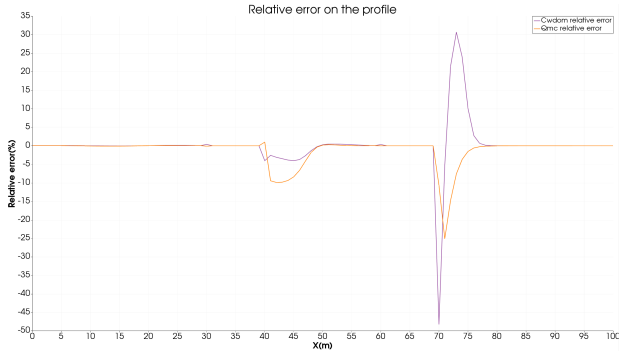

(b) Relative error for CWDOM and QMC set

Figure 4.22: Result on the profile$(y = 80, z = 0)$

level, the comparison excludes the bottom of each building to eliminate the undesirable effect from view factors.

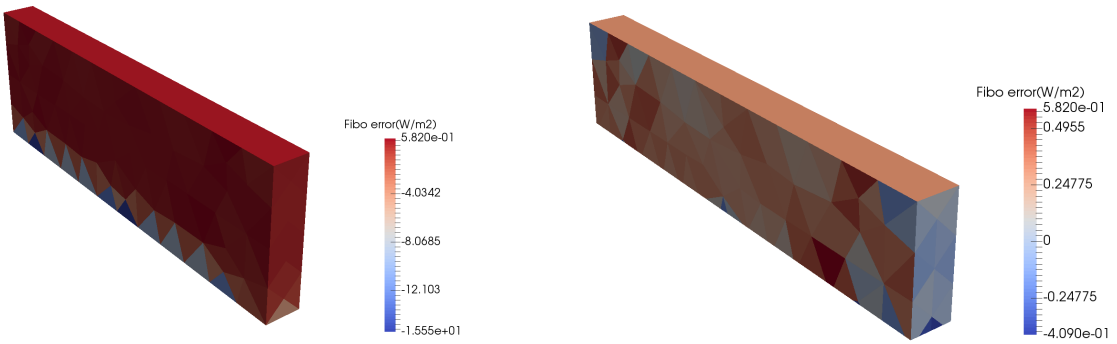

(a) Full right building (b) Right building above 12m

Figure 4.23: Error between Radiosity and Fibonacci set

For further comparisons, the points of the mesh located above $z = 12\,m$ are selected. The radiosity method is chosen as the reference. The relative errors for each surface using the different angular schemes are shown in Figure 4.24.

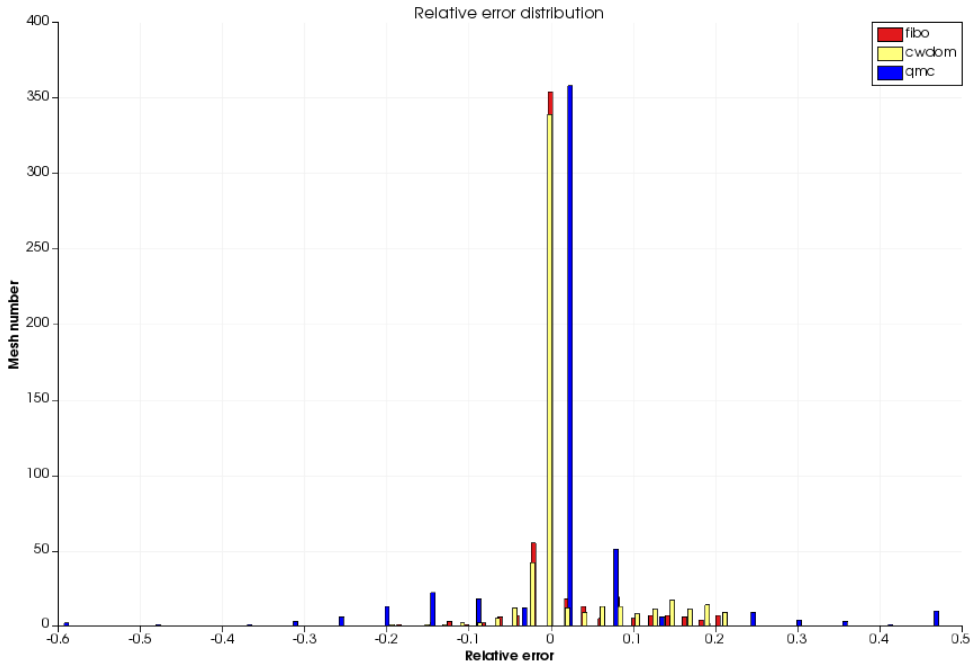

Figure 4.24: Distribution of relative errors for the three quadrature sets

For all quadrature sets, differences are small over a large number of calculation points. Most of the errors are located in the shadowed parts of the mesh. The intensities received by these points are too small. The moderate number of directions ($N = 120$) chosen for the qMC quadrature leads to poor performance for this method in solar radiation calculations compared to the two other quadrature sets. At several locations over the shadowed area, the error increases up to 60%. For the Fibonacci and CWDOM quadratures, on the other hand, the largest errors are approximately 20%. The MAE and RMSE for the entire building at location $z > 12\,m$ are given in Table 4.4.

Infrared radiation On the side of the Infrared radiation, the result of incident flux on each patch is shown in Figure 4.25

	Fibonacci set	CWDOM set	QMC set
MAE full building(W/m2)	0.6262	0.6834	0.8738
MAE building above 12m(W/m2)	0.2855	0.3396	0.5183
RMSE full building (W/m2)	1.506	1.4537	1.5569
RMSE building above 12m (W/m2)	0.24	0.235	0.456

Table 4.4: MAE and RMSE of incident solar radiation on the building surfaces for three quadrature sets

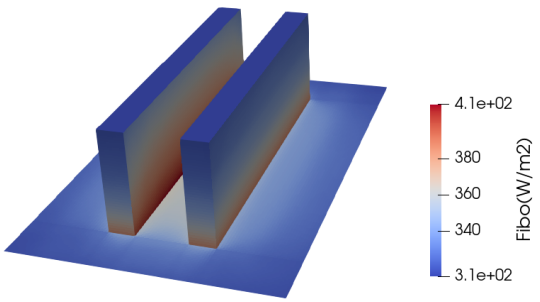

(a) Fibonacci

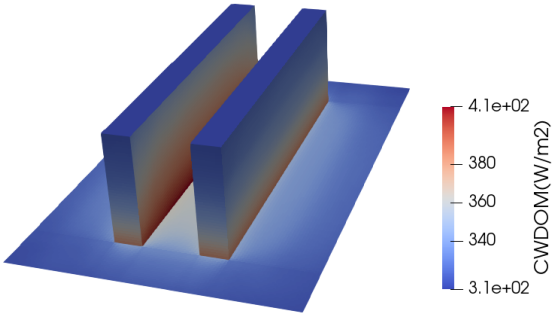

(b) CWDOM

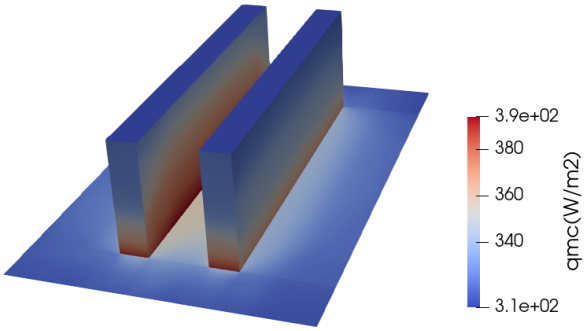

(c) qMC

Figure 4.25: The incident infrared radiation on each patch with different quadrature algorithms

The range of incident flux is almost the same for the Fibonacci method and CWDOM. For the qMC method, there is a difference of 20 W/m^2 in the upper limit. In fact, the difference is concentrated on the ground. If we focus on the average incident flux on each of the building surfaces, which can be seen in Figure 4.26, we find that the difference between the quadrature schemes is quite small. As shown in Figure 4.26, the differences between the methods are within several W/m^2. Moreover, by the calculation of the MAE and RMSE for the entire patches on the building surface (Table 4.5), we are able to determine that the Fibonacci method is the best performing method among these three. Despite a 20 W/m^2 gap on the upper limit of the incident flux range, the difference between the qMC and radiosity method results is only approximately 1 W/m^2 on average larger than the CWDOM results. Table 4.5 shows that the error in view factor calculation due to the adjacent patch reduces its impact compared with the results in Table 4.4.

Direction number For the discretization in the DOM, the number of discretization angles is also a critical factor that can strongly impact the final result. In the previous calculation, the number is fixed at 100. In this part, we vary this value in every quadrature method used in the previous part and aim to find the change in their performance with different discretization numbers. The calculation of the mean absolute percentage error (MAPE) of IR radiation is

	Fibonacci set	CWDOM set	QMC set
MAE full building(W/m2)	0.908	5.04	5.33
MAE building above 12m(W/m2)	0.73	4.5	4.3
RMSE full building (W/m2)	0.704	2.24	4.89
RMSE building above 12m (W/m2)	0.61	2.16	3.53

Table 4.5: MAE and RMSE of incident infrared radiation on the building surfaces for three quadrature sets

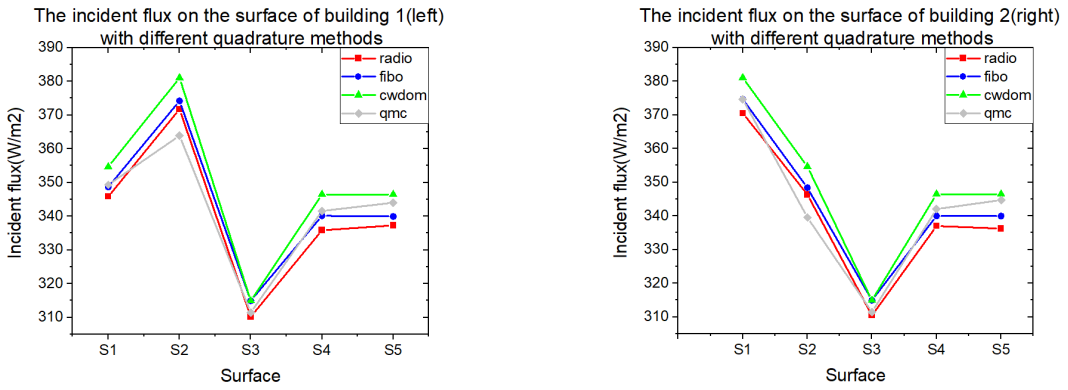

(a) Building 1(Left) (b) Building 2(Right)

Figure 4.26: The average incident flux on the surfaces of buildings

carried out for all building patches by the function 4.5:

$$MAPE = 100 \times \frac{1}{n_{patch}} \sum_{1}^{n_{patch}} \frac{\Phi_{DOM} - \Phi_{Radiosity}}{\Phi_{Radiosity}} \tag{4.5}$$

With Φ_{DOM} calculated with different quadrature methods, the result is illustrated in Figure 4.27

With a relatively low direction number, the Fibonacci method is clearly the best choice. Even with just 10 directions for the entire solid angle of 4π, the error is limited within 5%. In the same circumstances, the qMC method shows a value of 12%, more than twice that of the Fibonacci method. The CWDOM increases this error to near 25% under the same conditions. With an increasing direction number, the error of all quadrature methods drops. The MAPE of the Fibonacci method stabilizes at 1% when the direction number passes 50. In terms of the qMC method, this value changes considerably before 100 direction numbers. Subsequently, it continues to drop, but the variation is much smaller. For the CWDOM, the increasing direction number improves the performance substantially. This method needs only to double the number from 10 to 20 to decrease the error from 25% to less than 10%. When we come to a high-direction-number calculation, for example, 1000 in this case, the Fibonacci method still has an MAPE over 1%, and the qMC method and CWDOM exhibit decreased errors to a level of 0.8%.

We thus confirm that the Fibonacci scheme is our best choice. This scheme can provide a relatively precise result when the discretization number is insufficient, allowing the number to be decreased to save calculation costs. For the other two quadrature schemes, even though they can provide better results with a high discretization number, their relative error with a low direction number is too large. To obtain better results from the qMC method and CWDOM, the direction number must be increased, which correspondingly increases the time consumption.

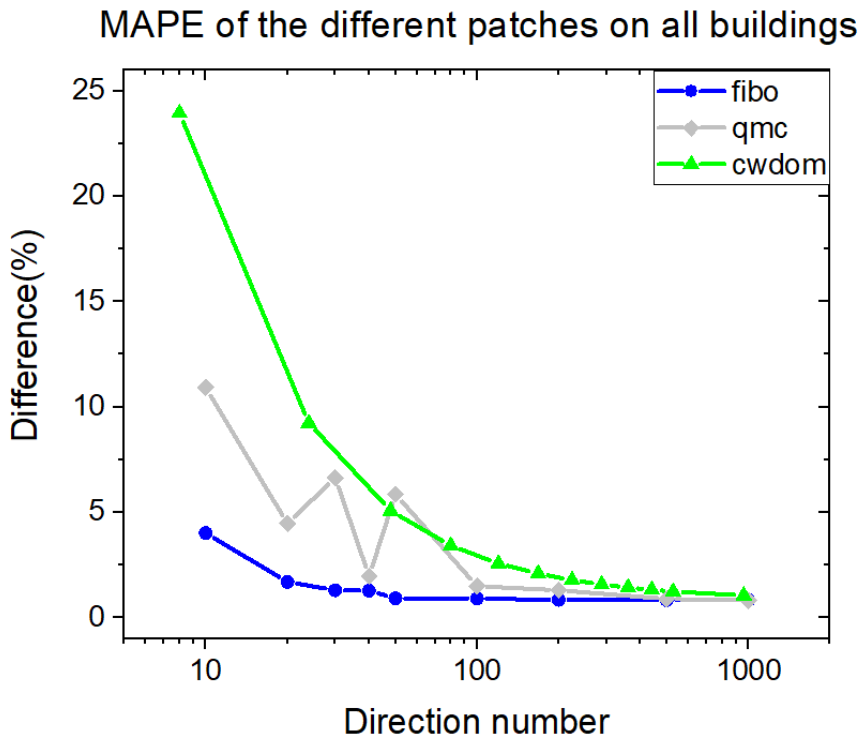

Figure 4.27: Mean Absolute Percentage Error(MAPE) for the building surfaces patches with different quadrature algorithms in function of direction number, compared with the radiosity result

Note that the full calculation in the quadrature section is carried out with a spatial discretization of a 1 m cube. If the discretization in space changes, the direction number requirement also varies. A study of the spatial discretization schemes is discussed in the following section.

4.1.7.2 Spatial discretization schemes

Application of the DOM requires discretization of both solid angles and space. Compared with the number of angles, spatial discretization is more critical. Indeed, for a structured DOM mesh (the space is divided into numerous identical cubes), if the discretization number over each dimension of space is multiplied by 2, the calculation cost is multiplied by 8 compared with that of the initial mesh. Therefore, it is important to evaluate the influence of the spatial discretization on the calculation results. This is the aim of this section.

The test is carried out with the canyon configuration. Solar and IR thermal radiation are both considered in this test. In this section, air is still assumed to be transparent.

Solar radiation In this part, the same configuration as in the quadrature section is used. Instead of fixing the spatial discretization over each axis as we do in the quadrature section, however, both angular and spatial discretization are varied. We first evaluate the impact of the mesh size on the accuracy of the results. The reference calculation uses 100 directions and a 1 m mesh. Then, the size of the spatial mesh is changed within $0.5\ m, 1\ m, 2\ m, 5\ m, 10\ m$. The incident flux on the ground and buildings are as shown in Figures 4.28 and 4.29

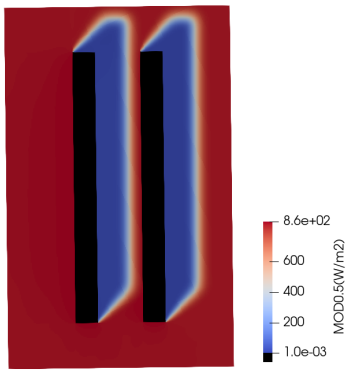

(a) 0.5m cube mesh

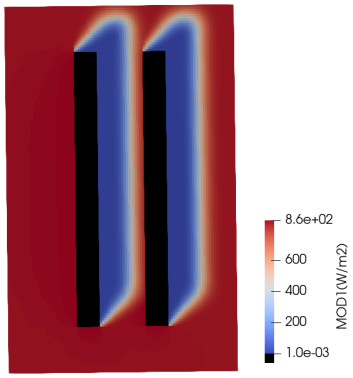

(b) 1m cube mesh

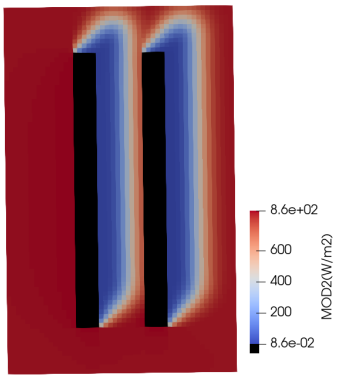

(c) 2m cube mesh

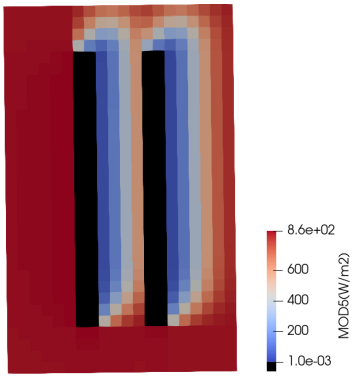

(d) 5m cube mesh

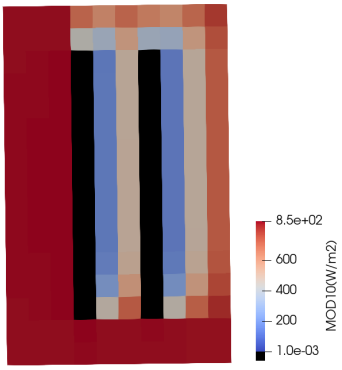

(e) 10m cube mesh

Figure 4.28: The incident flux on the ground for different mesh sizes

Building 1					
	0.5m	1m	2m	5m	10m
S1	316.318	316.2766	316.1962	315.98	315.6826
S2	17.7469	17.7745	17.7605	17.5956	17.3056
S3	842.2736	842.2736	842.2736	842.2736	842.2736
S4	0	0	0	0	0
S5	325.8717	315.8291	325.752	325.5426	325.24
S6	4.9179	4.9473	4.9941	5.053	5.0362
Building 2					
	0.5m	1m	2m	5m	10m
S1	310.2695	309.01	304.85	291.59	273.92
S2	4.5744	4.5674	4.5784	4.67	4.86
S3	842.2736	842.2736	842.2736	842.2736	842.2736
S4	0	0	0	0	0
S5	325.8024	325.77	325.71	325.5192	325.2336
S6	4.2973	4.3025	4.3164	4.33	4.3294

Table 4.6: The incident flux (W/m^2) on each building with 100 directions

Figure 4.28 shows that most of the parts on the ground are not highly influenced by the variation in the mesh size. Even with a 10 m size, the difference for the illuminated surfaces is below 10 W/m^2. This amount can be neglected compared with the 860 W/m^2 incident flux value. The problem is more critical on the shadowed areas. Figures 4.28a and 4.28b clearly reveal a separation between the shadow of building 1 and the left surface of building 2. In Figures 4.28c, 4.28d and 4.28e, this area disappears gradually. Because of the increasing mesh size, it becomes difficult to visualize this separation zone. More importantly, this leads to a decreased value of the incident flux on the surface of the building if the two buildings are too close.

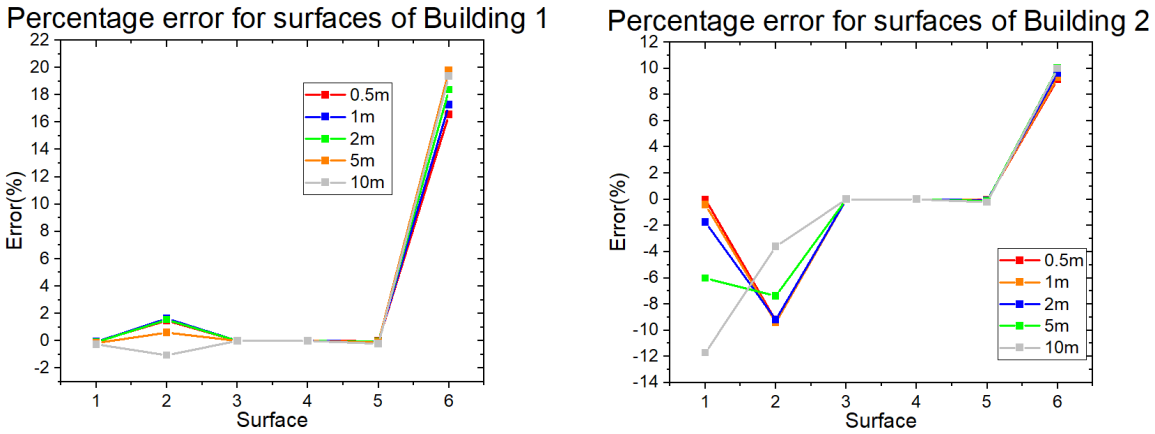

(a) Building left

(b) Building right

Figure 4.29: Percentage error of the incident flux on each building with 100 quadrature direction

In the same case, we can see in Table 4.6 that the flux on the left side of building 2 decreases significantly. This is because the mesh size is too large to correctly model the influence of building 1 on building 2. Figure 4.29 shows the error of each case compared with the results from the radiosity method. Except for surface S1 from building 2, the results are not extremely sensitive to variations in the mesh size. The result for the top surface (S3) is always the same because this surface always sees the same solar intensity. The largest differences are

observed on the right (S2) and back (S6) surfaces, which are shadowed faces. The incident flux on these surfaces is due to reflection by the ground. Differences remain; however, they are small (Table 4.6) and can be neglected.

Then, the number of directions is varied for the largest mesh size cases (2 m, 5 m and 10 m). The goal is to determine whether, with a refined discretization of the solid angles, it is possible to compensate for the errors observed with the largest meshes.

The numbers of directions are chosen from a set of values ranging from 10 to 100000. The results are again compared with those of the radiosity method. The results on the top and bottom surfaces are always the same for all calculations. We thus focus on the other 4 surfaces. The comparison is presented in Figures 4.30 and 4.31.

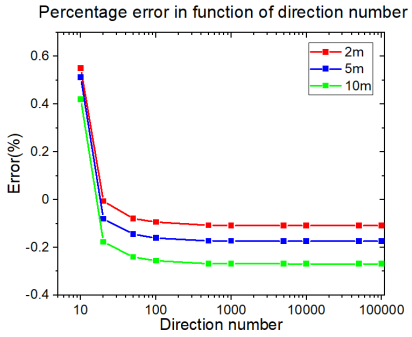

(a) Left surface(S1)

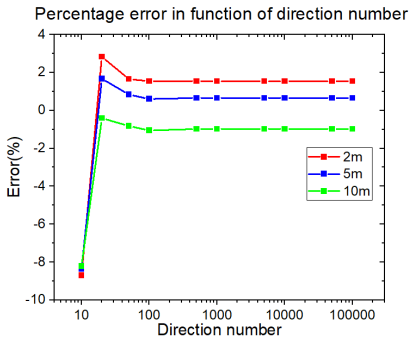

(b) Right surface(S2)

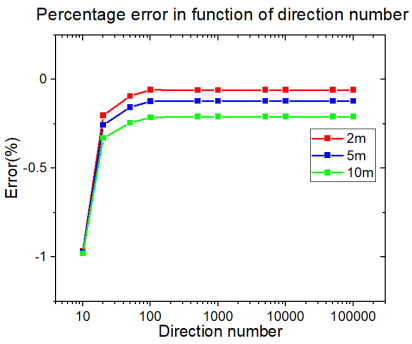

(c) Front surface(S5)

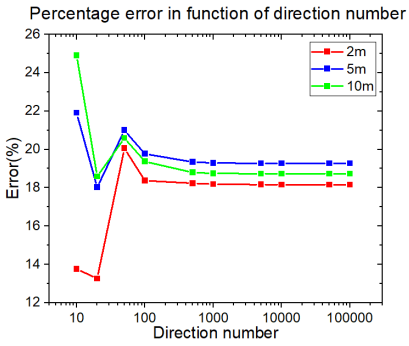

(d) Back surface(S6)

Figure 4.30: Percentage error of incident flux on building 1 in function of direction number

With this configuration, almost all cases stabilize with 100 directions, except the right and back surfaces of building 2. As expected, increasing the number of directions reduces the error of the DOM calculation. In some cases, the results obtained with the largest meshes are close to the radiosity results, especially over the shadowed surfaces.

Infrared radiation Figure 4.32 shows the differences among the various cases considered. The error still varies for some surfaces when the number of directions is above 100, especially for building 1. With increasing cell size, the accordance with the radiosity method globally increases, but the differences remain small in all cases.

Based on the present analysis, the DOM is chosen for the calculations in "real" cases (see the following chapters) to set the ray number to 100 and to divide the geometry into cubes of 1 m side length. A 1 m cube is small enough to accommodate the different scenarios considered in this thesis.

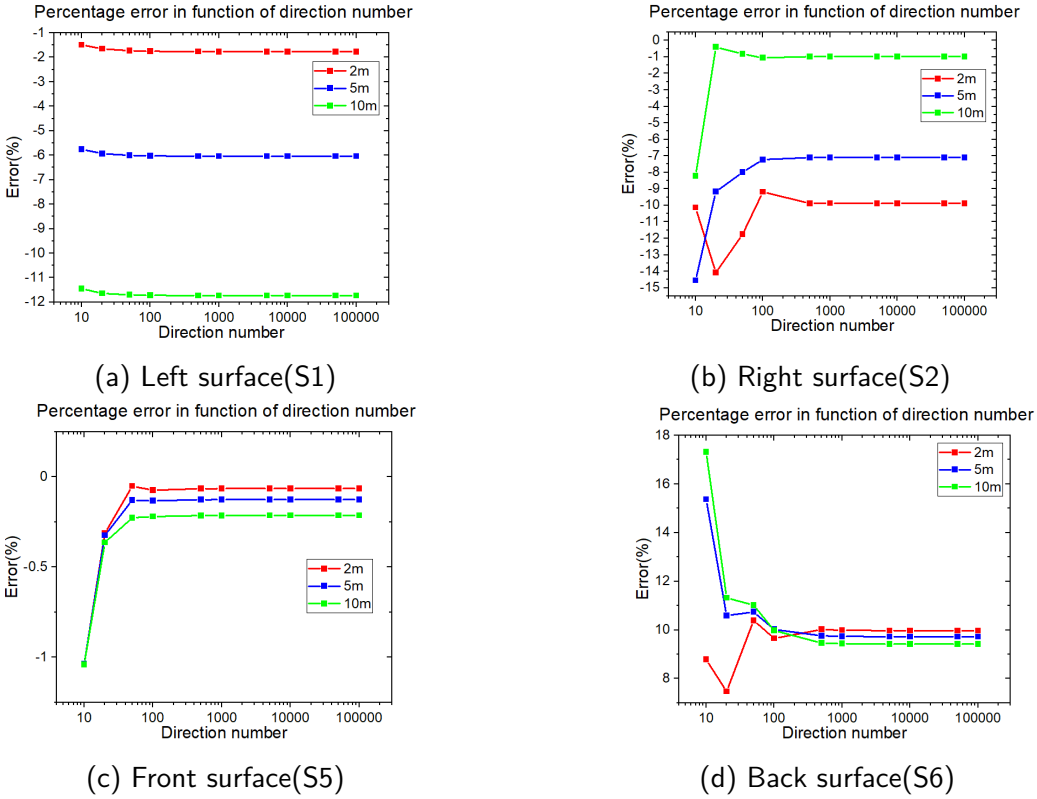

(a) Left surface(S1)

(b) Right surface(S2)

(c) Front surface(S5)

(d) Back surface(S6)

Figure 4.31: Percentage error of incident flux of building 2 in function of direction number

4.2 Transient simulation: La Doua campus

In the previous section, a steady-state test was carried out to identify the difference between the two approaches in the transparent medium. In this part, we implement a nonstationary simulation for the two approaches. This simulation contains two parts: The first part is the comparison of DOM and radiosity with the hypothesis that the air is a transparent medium; the second part contains only the DOM. Different air models presented in the air chapter are implemented in the DOM to calculate the air absorption in the long term of an urban area and its impact on the building surface temperature.

4.2.1 Geometry

Our study location lies in Villeurbanne France, with latitude $45°46'55.9"N$ and longitude $4°52'26.4"E$. It is a part of the campus of "Institut national des sciences appliquées de Lyon" (INSA). The simulation area is circled in red in Figure 4.33.

There are five main buildings in this area. Dimensions and positions are taken from the GIS geoportail.fr. The DOM simulation is carried out on $1\ m^3$ cubes. The position and dimensions on the buildings are accordingly rounded to the closest value with $1\ m$ spacing in every direction. The presentation of each building and its model in this simulation is listed below:

- The Sadi Carnot building: This building is shared by the laboratories CETHIL and DEEP((Déchets Eaux Environnement Pollutions), and the Energy and Environment Engineering Department of INSA is also located here. The building itself is a cuboid of 89

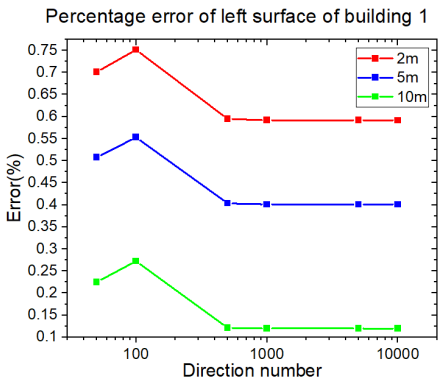

(a) Left surface(S1) of building 1

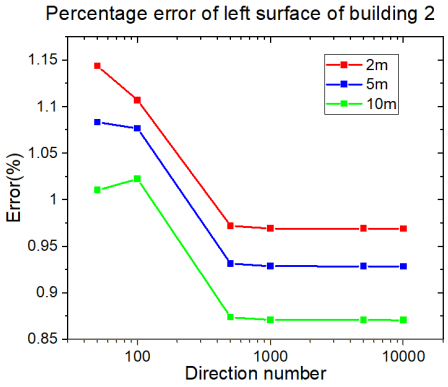

(b) Left surface(S1) of building 2

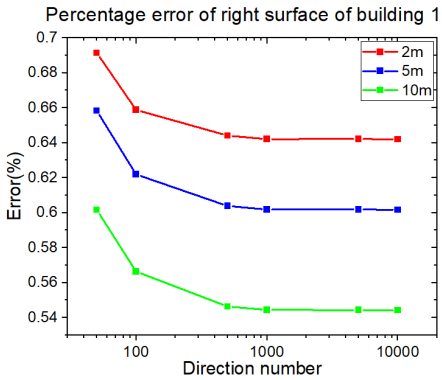

(c) Right surface(S2) of building 1

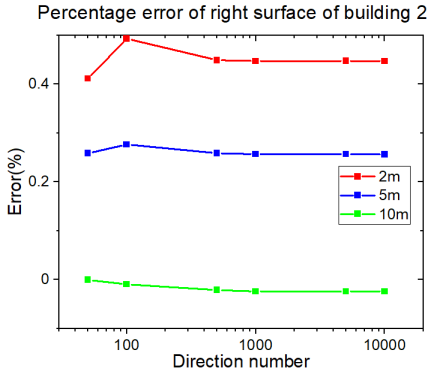

(d) Right surface(S2) of building 2

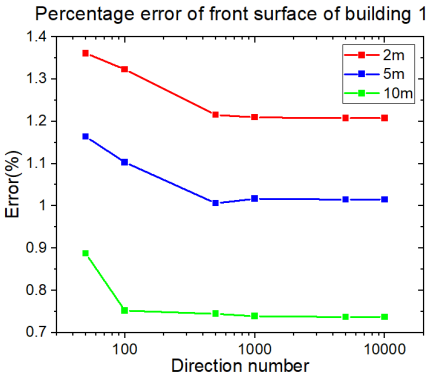

(e) Front surface(S5) of building 1

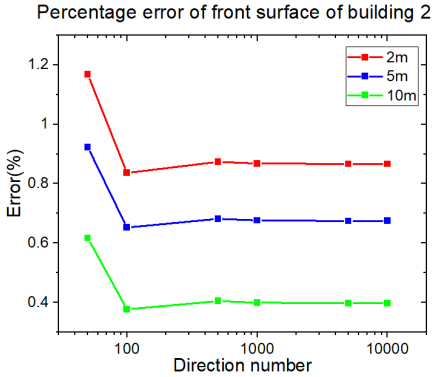

(f) Front surface(S5) of building 2

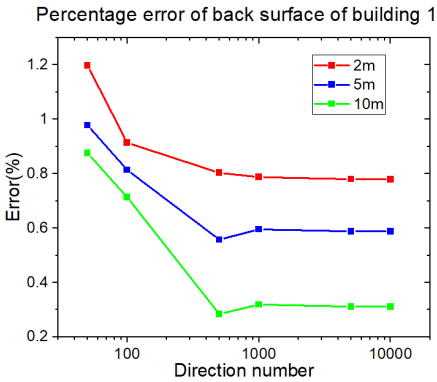

(g) Back surface(S6) of building 1

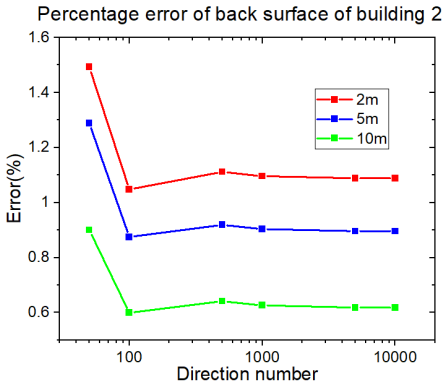

(h) Back surface(S6) of building 2

Figure 4.32: Percentage error of incident infrared fluxes for the surfaces of the buildings.

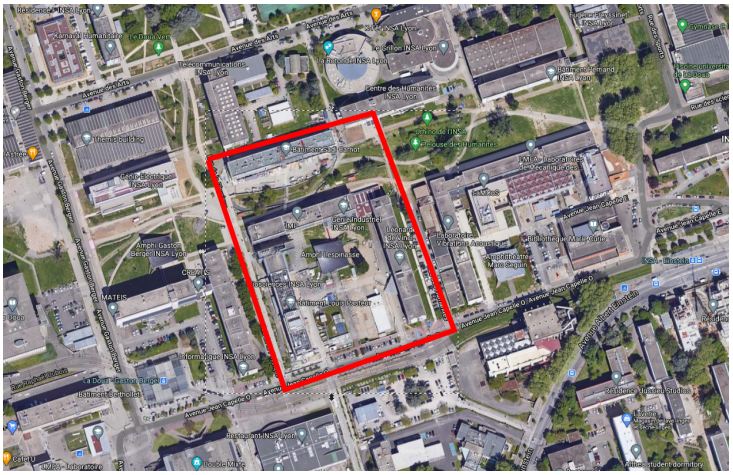

Figure 4.33: The location of the simulation area

m length, 13 m width and 19 m height.

- The Jules Verne building: This building is occupied mainly by the Industrial Engineering Department. The building is also a cuboid with the same dimensions as the Sadi Carnot building. There is an additional building that connects the Jules Verne and Leonardo da Vinci buildings, as presented later.

- The Leonardo da Vinci building: Laboratory Ampere is located here. The building is a cuboid 104 m in length, 15 m in width and 19 m in height.

- The connection part: A connection building exists between the Jules Verne and da Vinci buildings. This part is divided into two small regions: a cuboid with dimensions of 24 m$\times$13 m$\times$5 m and another cuboid with dimensions of 42 m$\times$4 m$\times$6 m.

- The Louis Pasteur building: This T-shaped building is used by the BF2I laboratory. It is modeled as a combination of two cuboids: a larger cuboid 86 m in length, 15 m in width and 19 m in height and a smaller one 30 m in length, 6 m in width and 19 m in height.

- The Lespinasse amphitheater: This building, which belongs to INSA, is an amphitheater for classes and conferences. The base of the building is a 23 m$\times$22 m rectangle. The roof is a curved surface that is replaced with a cuboid. Its height is the mean value of the curved surface, approximately 15 m.

The whole area is a rectangle with size 200 m$\times$250 m. The existence of buildings outside of the area is neglected. The boundary surfaces are considered to be a plane surface with an emissivity fixed before the simulation. No vegetal elements are taken into account, which means that neither trees nor lawns appear in this simulation. The model is presented in Figure 4.34.

Due to its T-shape, the Louis Pasteur building is divided into 2 cuboids with the same height of 19 m. The connection building is also divided; however, the resulting two cuboids do not have equal heights. Connection 2 (sometimes called Jules Verne 3, as we consider the full connection part to belong to the Jules Verne building) is a long and thin cuboid with a height of 6 m. Connection 1 (Jules Verne 2) has a small length-to-width ratio. It is 1 m lower than connection 2.

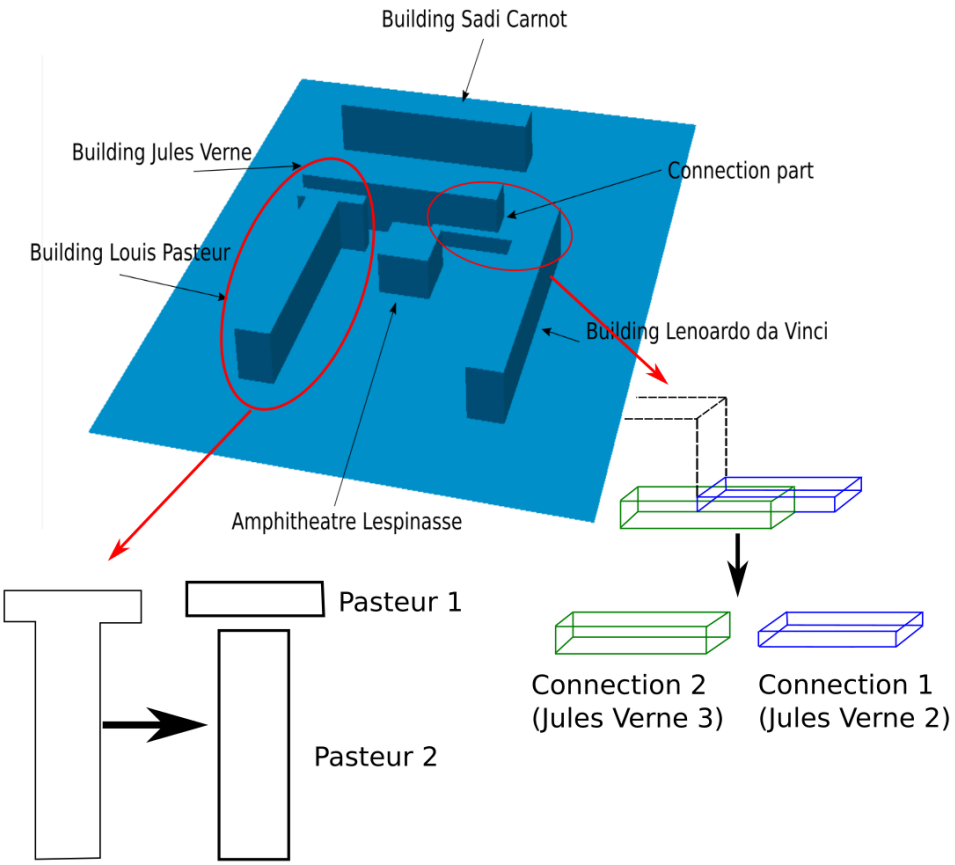

Figure 4.34: The modelling of the area

4.2.2 Weather data

As presented in the chapter on air, the weather data measured for the whole year of 2019 are used for this section. These data are recorded every 12.5 min for the entire year, which can clearly describe the variation in each parameter. This provides important information for the calculation of each term of the energy transfer. The weather data used here are taken from the TRNSYS weather data. It is measured in Lyon–Saint-Exupéry Airport.

4.2.3 Thermal boundary conditions and inputs

4.2.3.1 Convection

Convection is always a complicated aspect of urban simulations. The complicated urban morphology makes it difficult to obtain the exact value of wind speed and direction at every point in the scene, while the convection coefficient is highly related to these parameters [45]. The convection coefficient h is estimated as $h = 4u_{air} + 4$ in this section, with u_{air} being the wind speed, taken at each time step from the weather data.

4.2.3.2 Ground

Conduction is addressed through a surface balance equation. For the building's surfaces, this is detailed in the next section. For the ground, we simply use an equivalent temperature, defined as:

$$T_{ground} = T_{air} + \frac{E_{solar} * \epsilon_{ground}}{h} \tag{4.6}$$

4.2.3.3 Sun radiation

The weather data provide the necessary inputs to calculate the solar radiation: azimuth and elevation of the sun and direct and overall solar radiation received by a horizontal surface. The sky temperature, air temperature and humidity are also taken from the TRNSYS weather data.

4.2.3.4 Thermal balance on the buildings

As the main objective of this part is to analyze the air influence on the radiation transfer, more details are implemented for the radiation part. In terms of convection and conduction, we apply simple modeling. The building surface is assumed to be a 2 mm exterior aluminum panel with perfect insulation. The aluminum has a density of 7800 $kg.m^{-3}$ and a notably large heat capacity of 900 $Jkg^{-1}k^{-1}$.

The local nonstationary energy balance for a surface with $1\ m^2$ is written as:

$$\rho Cp\Delta z\frac{\partial T}{\partial t} = E_{Solar} + E_{IR} + E_{conduction} + E_{convection} \tag{4.7}$$

ρ: Density of the surface

Cp: Heat capacity of the surface

Δz: Thickness of the surface

4.2.3.5 Radiative properties of surfaces

There are several other modifications of the building model: Due to the lack of information about the buildings' surfaces and their renovation during this thesis, it is not possible to know the exact emissivity value. The buildings, except the amphitheater, have a large percentage of glazed surfaces. In particular, for the longitudinal side of the building, many windows appear on this kind of surface. Neither of the two methods applied in this calculation can accommodate glazed surfaces. Unlike the ray tracing method, which is very well suited for specular reflection, the radiosity and the MOD can only treat the surface as a parfait diffuse surface. In fact, among all the radiation categories that participate in the transfer in this area, the direction of sun radiation is probably the most influential parameter in the presence of a specular surface. The other radiation types do not have the strong directional characteristics as the direct solar radiation. To simplify the simulation procedure, we consider the surfaces to all be Lambertian surfaces, and no glazed surface is present in this model. The absorbility for the building surface is set to 0.9.(Even if the 0RC model is used in this part, we still consider that the building surface is built with concrete. So the absorbility of concrete is applied here) The value for the ground is 0.95, and the value for the sky is 1. These values are applied for both solar radiation and IR radiation.

4.2.3.6 Radiative properties of air

The air plays an important role in this simulation. On the one hand, the radiosity method can treat air as a transparent material only. The result can be used as a benchmark for the DOM. On the other hand, the DOM can incorporate different air models, which are presented in the chapter on air.

- Transparent air model: This is the simplest air model in this thesis. The air absorption coefficient κ_λ equals 0.
- Gray model: The absorption coefficient varies as a function of air temperature and wavelength. The temperature changes 8 times in one hour, and it is impossible to obtain the coefficient from each different temperature in the simulation. Before the calculation, we predefine the air temperature range, from 263 K to 313 K. For each 10 K, we calculate the monochromatic absorption coefficient with the help of HITRAN, assuming an RH of 100%. With Eq. 3.11, we obtain a 100% humidified air absorption coefficient for every 10 K increment in temperature. This can be used to construct a grid of temperature and RH. For any point located in the grid, its absorption coefficient can be obtained by interpolation. This approximation provides the coefficient based on the temperature and the RH. All air calculations are carried out before the simulation to avoid excessively increasing the time consumption. The interpolation time in each iteration can be negligible.
- SLW model: This is the most complicated air model we use in this thesis. Based on the absorption cross section of air, this model divides this cross section into groups, with

each group having a mean value and a weight. A calculation is performed for each group, which means that the time of calculation is n_{group} times that of the initial calculation. To incorporate this air model into the DOM, we first define a default temperature and obtain the monochromatic absorption cross section with the HITRAN database. Then, we divide the samples into 7 groups and calculate each group's absorption coefficient and weight. It is critical to note that the result from HITRAN contains only part of the spectrum. This means that the coefficient we obtain cannot represent all the air absorption at this temperature and RH condition. Most of the time, the wavelengths we choose in HITRAN contain approximately 95% of the energy for this air gas emission. Therefore, the weight of each group should be compensated with a 95% coefficient. For the part of spectrum beyond the range when we use HITRAN, we consider that 5% of the energy is transferred in a transparent air model with κ_λ equal to 0. Finally, a list of air absorption coefficients and corresponding weights is used in the DOM. In each iteration, a weight and a coefficient are taken to calculate the incident flux, and the results are summed to obtain the appropriate value of incident power on the building surface.

4.2.3.7 Simulation flowchart

The flowchart of the radiosity and DOM calculation is illustrated in Figures 4.35 and 4.36.

For the radiosity method after mesh generation by GMSH, the view factor calculation is carried out, which takes the majority of the time consumption for the entire radiosity simulation. With the weather data and the time period, we first determine the solar radiation for the entire duration (direct+diffuse+reflection). The solar radiation result is independent of the building surface temperature. For timestep i, we calculate the IR radiation transfer with the building surface temperature obtained in the previous timestep i-1. For the first timestep, the flux is calculated from a hypothesis of surface temperature, which is the air temperature at the starting time point. Then, the energy budget for each patch is calculated, and the new surface temperature can be obtained. If the difference in temperatures is under a threshold we define, we proceed to the next timestep. If not, the temperature of each patch is updated, and the new energy budget for each patch is calculated.

On the side of the DOM, after the loading of weather data and the determination of time period, the method proceeds directly to the calculation in one timestep. First, the solar radiation (direct+diffuse+reflection) is calculated. Then, the ground surface is determined by the incident solar power on the ground. Similar to the radiosity method, the surface energy budget is calculated with the temperature obtained in the previous timestep. The variation in temperature determines whether the calculation moves to the next step or returns to the recalculation of the surface energy budget with a new surface temperature.

The analysis consists of two parts. The first part is the comparison between the radiosity method and the DOM. In this part, we wish to determine, along with the other heat transfer, how much of a difference is generated between these two methods within a time duration. This approach also helps validate our DOM model. The second part of the analysis compares the results obtained from different air models. Finally, we determine the impact of the air for a long duration.

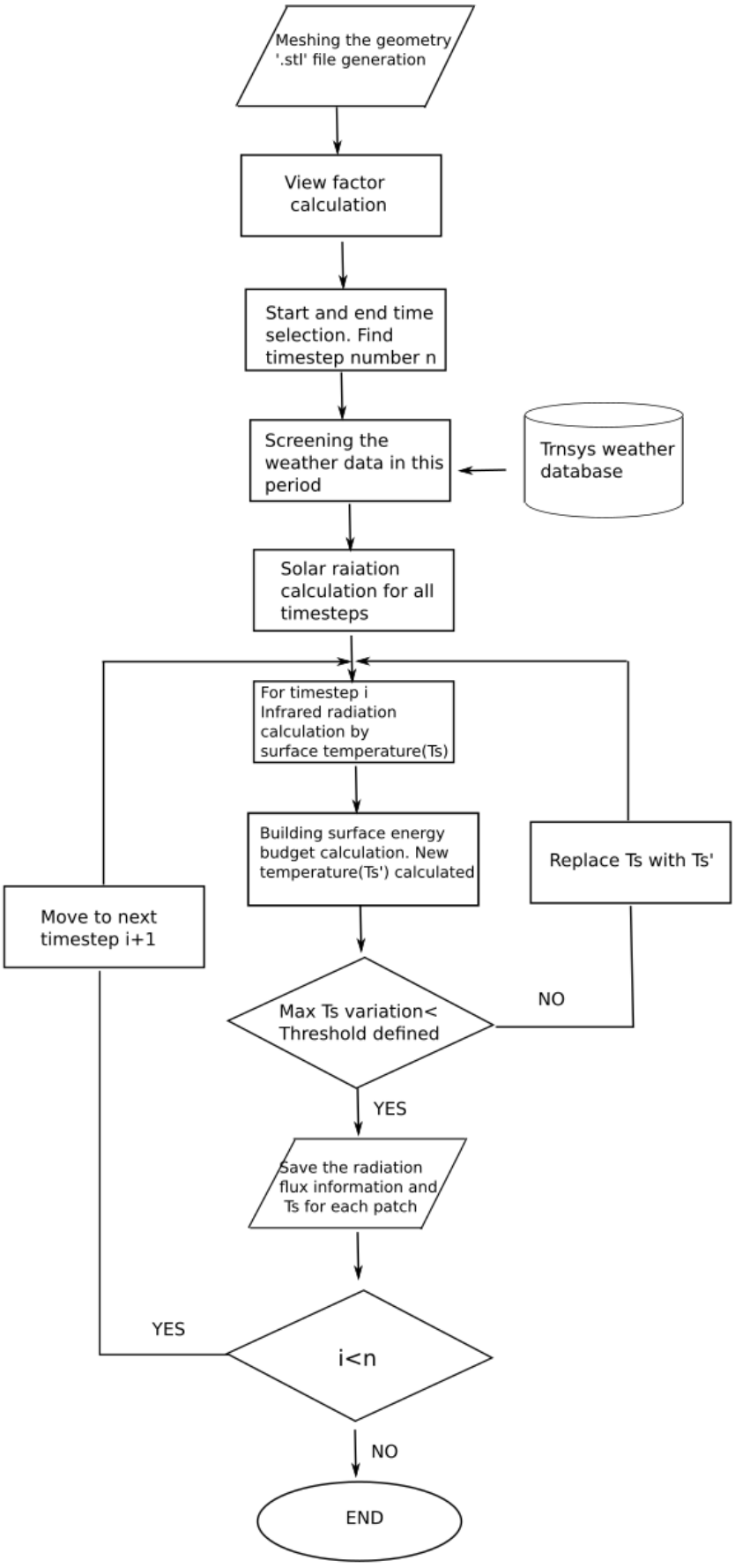

Figure 4.35: The Radiosity calculation flowchart

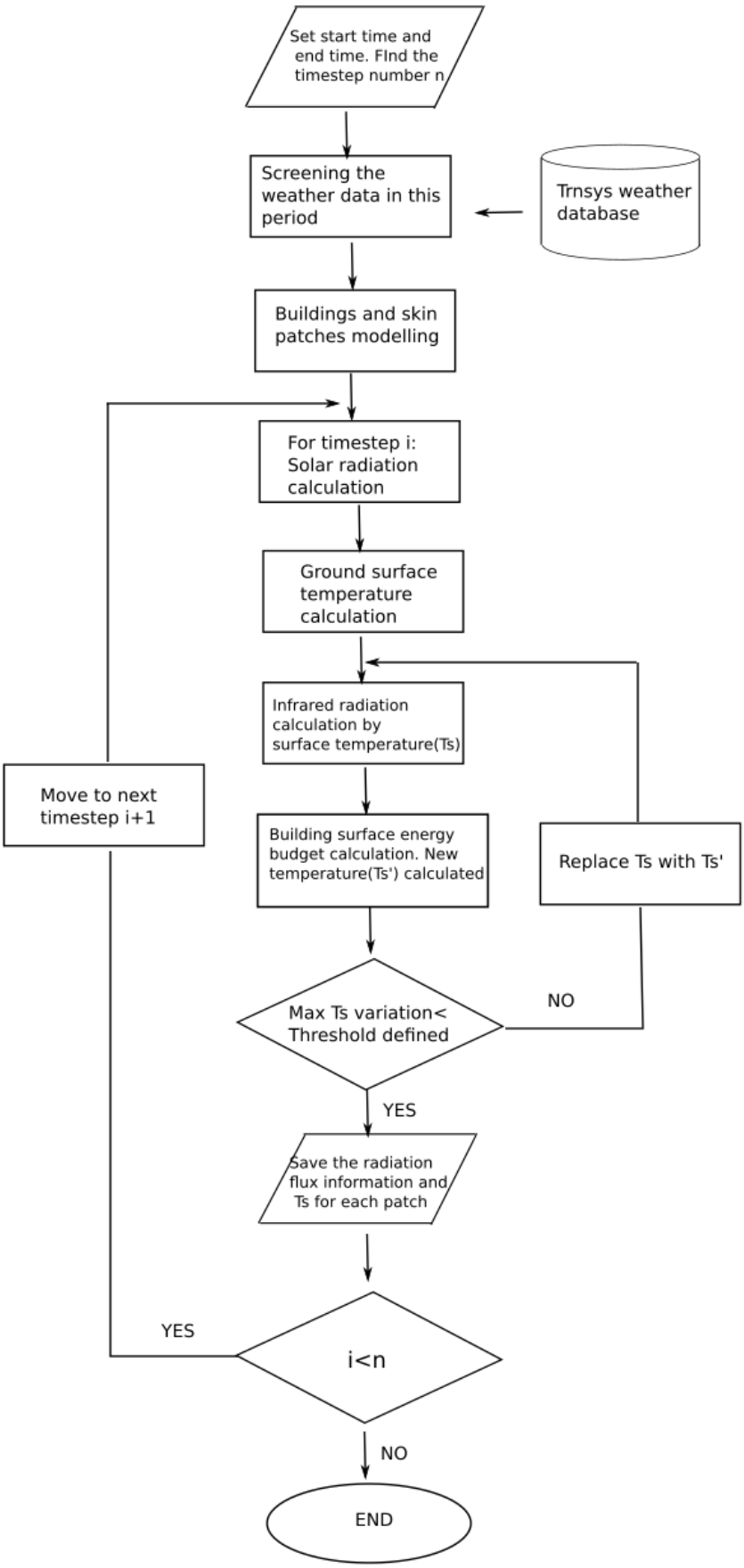

Figure 4.36: The DOM calculation flowchart

4.2.4 Comparing the radiosity method and DOM results for air as a transparent medium

4.2.4.1 Influence of boundary conditions

We start this part by a comparison between the radiosity method and DOM with the aim of finding the magnitude of disparity between the two methods. We compare two methods with a similar configuration as follows.

- The sky is modeled as a cuboid in the radiosity method. The distance between the roof of the highest building and the sky surface is 3 m. This means that both the radiosity method and the DOM have the same geometry model.
- The main reason we cannot easily compare the radiosity method with the DOM is the boundary condition, in particular, the vertical boundary. In terms of radiosity, these surfaces are assumed to be sky surfaces, regardless of the sky shape model. However, in the DOM we defined, the temperature of these vertical surfaces switches between the sky temperature and ground temperature, which depends on the chosen discretized direction. This suggests that a large difference may appear at the surface, which can directly see the vertical boundary. We add another calculation for the DOM with a full sky condition for the vertical boundary. For further comparison of different surfaces, we take the result from the radiosity method and the full sky boundary case.

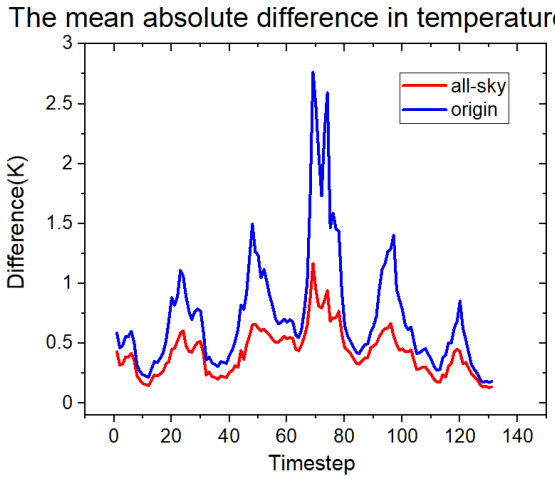

Figure 4.37: Difference of temperature between two DOM cases and radiosity

Figure 4.37 shows the variation in the mean absolute difference in building surface temperature for two DOM cases with different boundaries and the radiosity method. As expected, the normal boundary set for DOM has a larger gap relative to the radiosity than the full sky boundary. The disparity is larger during daytime. Because of the rise in the ground temperature, the IR radiation difference between the ground and sky increases. The vertical surfaces, especially the surfaces with a nonzero view factor to the boundary, can have a large disparity in IR received. For vertical surfaces that do not face the boundary directly (e.g., the vertical surfaces inside the U shape) or the roof of the building, the impact of the different boundaries is reduced. The roofs lower than 19 m in height (the amphitheater and the two parts of the connection building) are slightly influenced by the vertical boundary, as they can partially see it. Overall, the difference in IR received by the vertical surfaces leads to the large gap between the red and blue lines in the figure.

In terms of the value, the maximum distance (exceeding $1\ \mathrm{K}$) is hard to neglect. The mean absolute difference in temperature for each building in the DOM is shown in Figure 4.38 to illustrate this discrepancy.

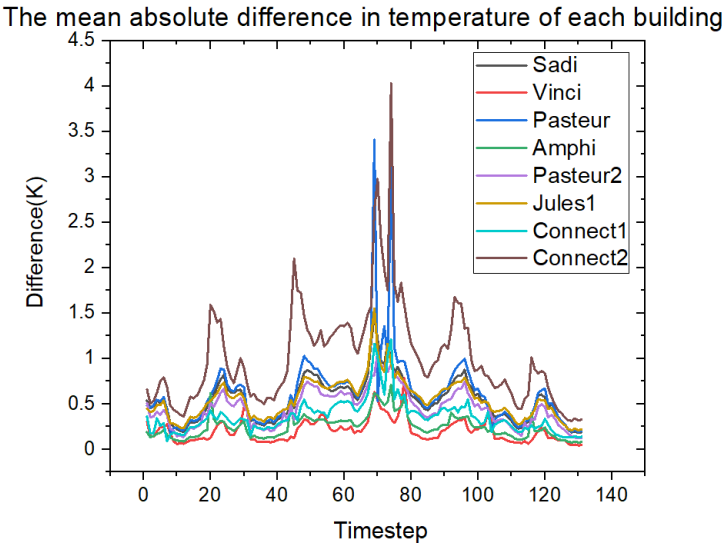

(a) Full sky boundary DOM

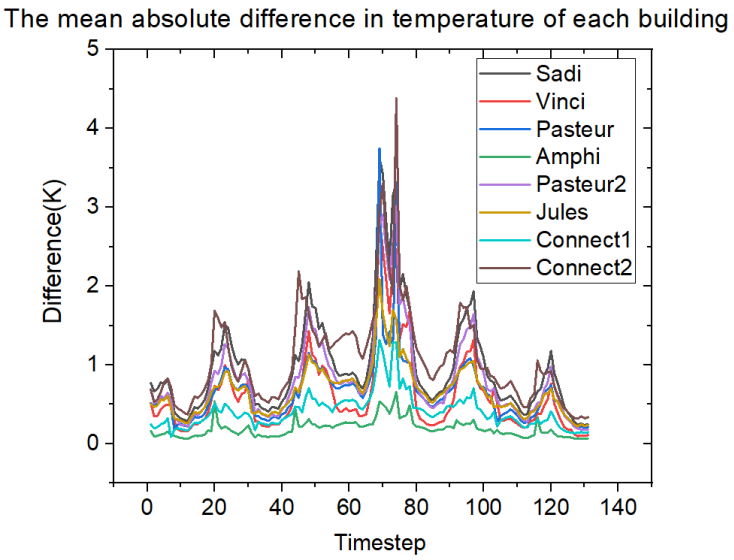

(b) The default boundary DOM

Figure 4.38: The mean absolute difference in temperature for each building in the difference DOM case

The result proves that the difference between DOM and radiosity varies considerably across times and buildings. As shown in Figure 4.37, every building has its difference peak during the daytime, more precisely around noon, when the solar radiation is intense. In addition, the value of the difference for each building varies. Even with the full sky boundary condition, the second part of the connection and the first part of the Pasteur building can reach near $4\ \mathrm{K}$. The reasons for these differences are studied in the next section.

4.2.4.2 Influence of the view factor calculation

The differences between the DOM and radiosity methods can be explained by the way form factors are calculated.

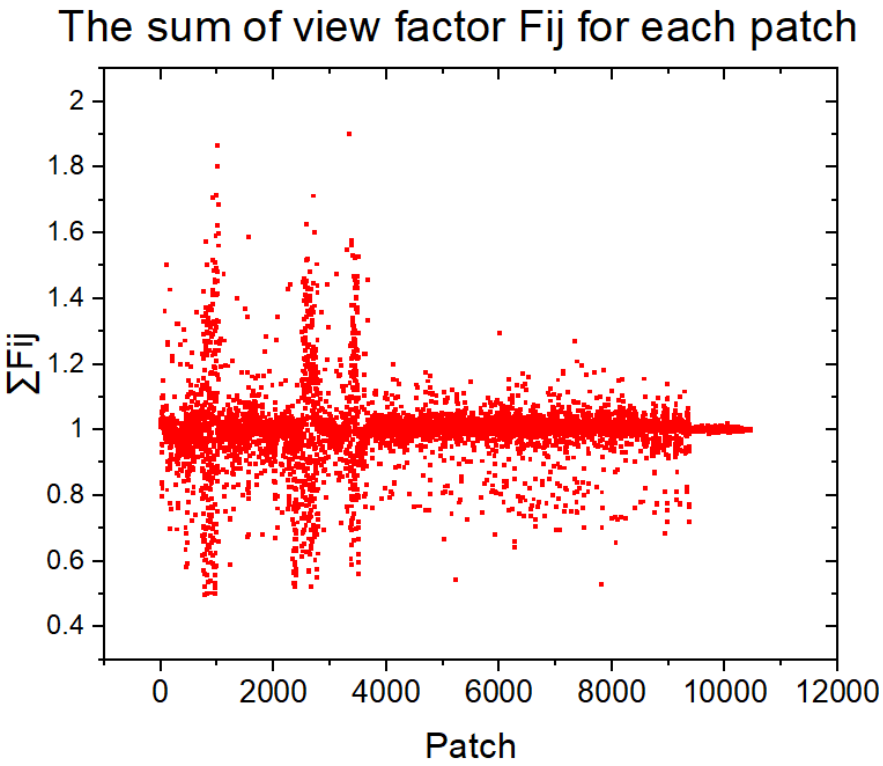

Figure 4.39: The sum of the view factor Fij for each i surface.

To this end, Figure 4.39 presents the sum of the view factor for each surface i. The value normally equals 1 for each surface patch if the system is closed. Even considering the error created during the subdivision and the summation, the absolute difference to 1 should be small. In this case, we have many points that are located far from 1. For some patches, a value near 2 can even be obtained, which is physically impossible.

The reason for this view factor error is the patch size. During the creation of the patch, we divide each segment by adding nodes, similar to the procedure in the radiosity chapter. However, to reduce the calculation time of the view factor, we do not add enough nodes in one segment, and the mesh size is too large. There are nearly 11000 patches in this case, and many of them have a maximum size of approximately 10 m. Moreover, some surfaces have a very large disparity in two dimensions. Flat triangles are created, making the results worse. As we conclude in the radiosity section, the subdivision cannot neutralize all the error if the patch size is large. The only method to realize successful calculation is to refine the mesh. In this calculation, a large patch size ultimately leads to poor results.

The patch size generates an error for both wall and roof flux calculations.

The roofs are defined as described in case 1 in the radiosity chapter. The sky is designed to be close to the roofs, as it is only 3 m higher than the height of most of the buildings. This leads to the parallel case we discussed previously. In this case, the sky patches have a maximum dimension of approximately 10 m. As the distance between the parallel surface is 3 m, approximately 8% error remains in the view factor calculation, even with subdivision (Figure 2.21).

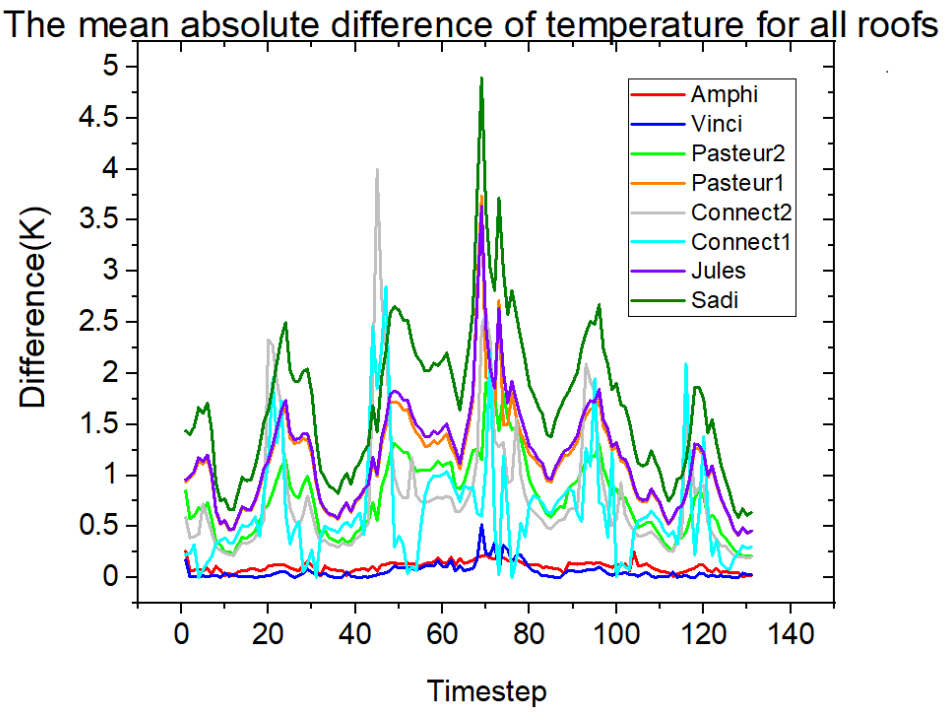

Figure 4.40: The mean absolute difference for the patches on the roof comparing the DOM and radiosity

As shown in Figure 4.40, except for the roof of the da Vinci building, all the other roofs that have a height of 19 m suffer from large differences. For the three roofs with lower heights (15 m for the amphitheater, 5 m and 6 m for the two parts of the connection), the situation differs. For the roof of the amphitheater, the difference stabilizes at a very low level. The reason is that its roof is relatively far from any surrounding surface, which includes the sky surface and the vertical surface of the surrounding buildings. Consequently, the amphitheater results are more accurate than the other results. In contrast, the roofs of the connection building are both connected with the other buildings' vertical surfaces. An error arises as in the perpendicular case in the radiosity chapter. This finally leads to the error magnitude being similar to that for the other 19 m roofs.

The large error ranging from 0.5° to 5° in the roof is compensated by the vertical surface result. Only a small area of the vertical surface produces an error during the view factor calculation. This error is negligible for only some vertical surfaces. This can have an impact on the mean surface temperature calculation.

In Figure 4.39, we find approximately 1000 patches that have an absolute difference over 0.2. We list these 1000 patches and look for their locations. Figure 4.41 shows the patches on the building vertical surfaces. There are two conditions.

- Bottom case: As the buildings are connected with the ground, the classical perpendicular case is created. There can be an error for the patches close to the connection.
- The top case: It is rare to see this case. However, because of the close sky as defined, the patch located at the top area of the wall can generate a problem with the sky patch during the view factor calculation.

On most of the vertical surfaces, the incidents of a mistaken patch are few. For these

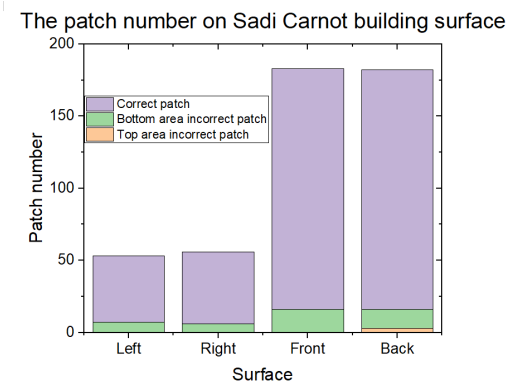

(a) Sadi Carnot

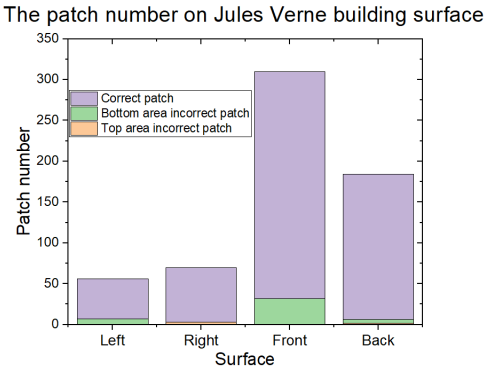

(b) Jules Verne

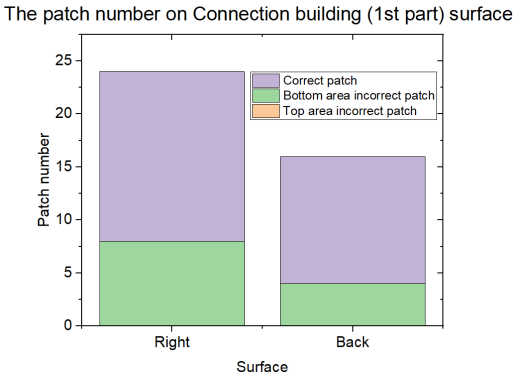

(c) 1st part of connection building

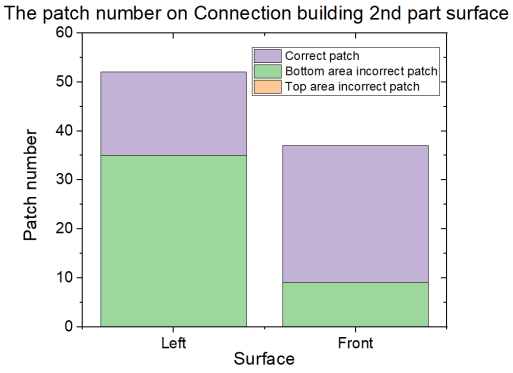

(d) 2ed part of connection building

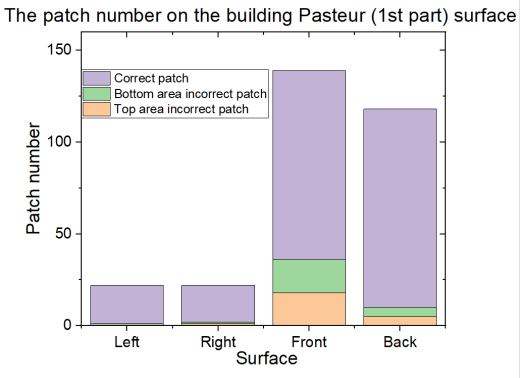

(e) 1st part of Pasteur

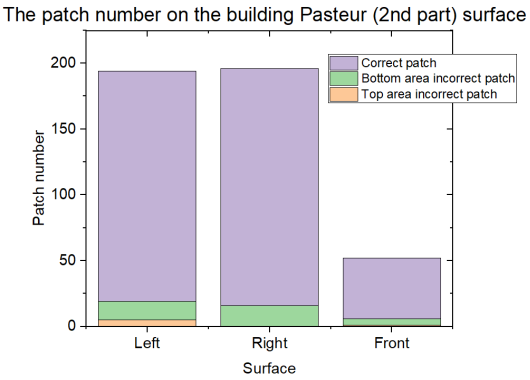

(f) 2nd part of Pasteur

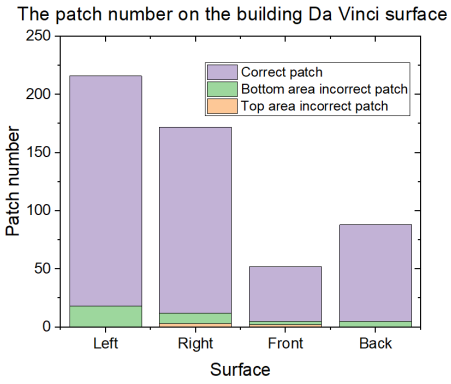

(g) Da Vinci

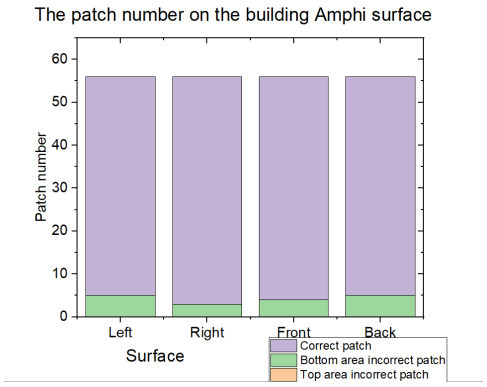

(h) Amphitheatre

Figure 4.41: The number of patches for each surface of building. Containing the correct patch and the patch whose view factor is incorrectly calculated

surfaces, the difference in results between the DOM and the radiosity method is usually small. However, for the surfaces of the connection building, the patch with the error in the view factor accounts for a larger proportion, in particular the left surface of the second part of the connection building. This is because it is close to the front surface of the Jules Verne building, the back surface of the amphitheater and the ground. The surface has more problematic patches than correct patches.

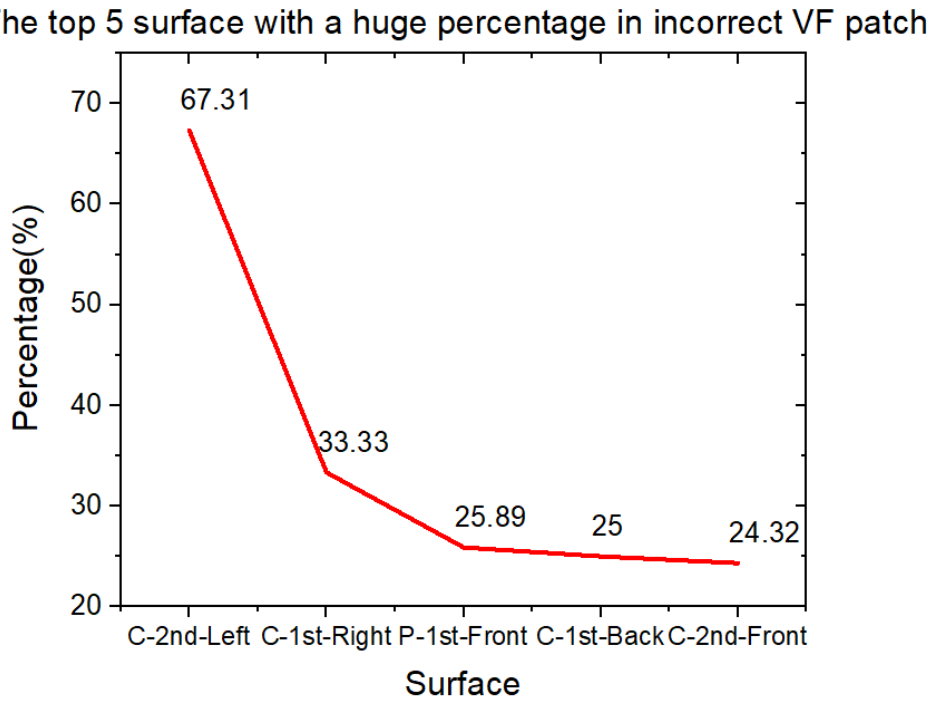

Figure 4.42: The 5 surfaces with the biggest problem patch occupation

Through ranking by the problem patch frequency, Figure 4.42 calculates the percentage of the problem patch in total. The left surface of the second part of the connection building leads the order (C2L), followed by the right surface of the 1st part of the connection building (C1R), front surface of the 1st part of the Pasteur building (P1F), back surface of the 1st part of the connection building (C1B) and the front surface of the second part of the connection building (C2F). The profiles of the difference in mean temperatures for these 5 surfaces are illustrated in Figure 4.43.

A very poor result for C2L is shown, as most of the patches exhibit an incorrect view factor. During the third day, the result can be $15°C$ cooler than the DOM result. For the other surface, the situation is better, as most of the patches correctly calculate the view factor.

In terms of calculation time, it takes approximately 1 day to calculate the view factor matrix, 87 min to calculate the solar radiation transfer (direct+diffuse) and another 55 min for the IR radiation and the energy budget for each building surface patch. In total, approximately 27 h are needed to finish a simulation with a 132-h duration.

On the side of the DOM, with a 1 m size for all cube meshes, the time consumption of each timestep is as shown in Figure 4.44. Because of the solar radiation, this scenario takes more time to calculate in every timestep during the daytime. At night, there is only IR radiation transfer in the radiation budget, which leads to a shorter calculation time. Figure 4.44 shows that it usually takes approximately 225 s for a timestep in the daytime and between 75 s and 100 s at night. In total, approximately 6 h are spent in this simulation.

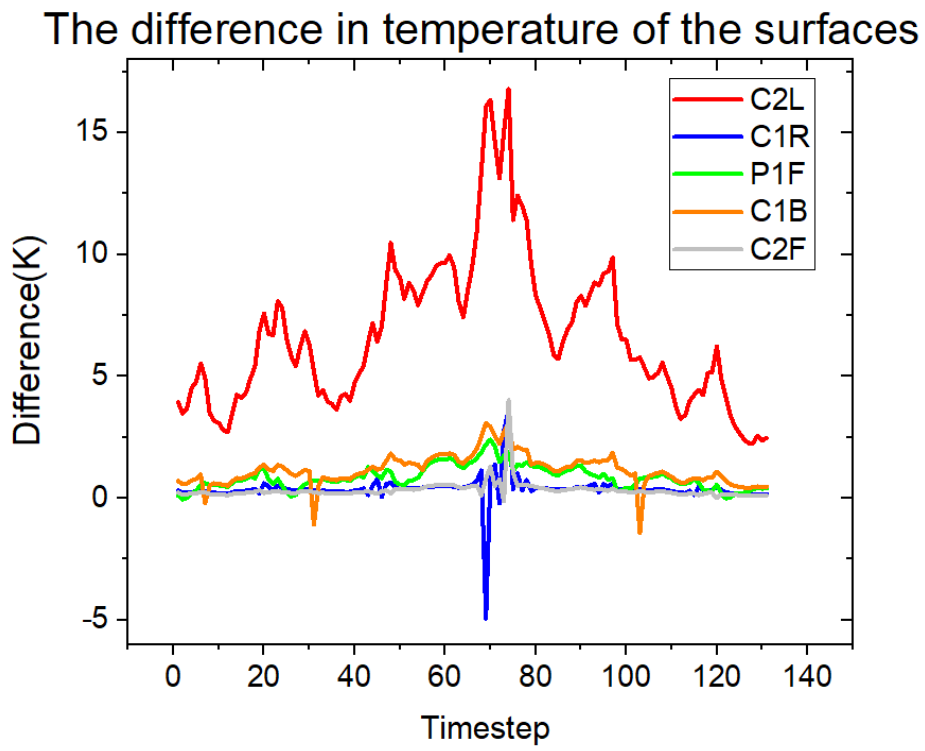

Figure 4.43: The difference in mean value of 5 surfaces temperature

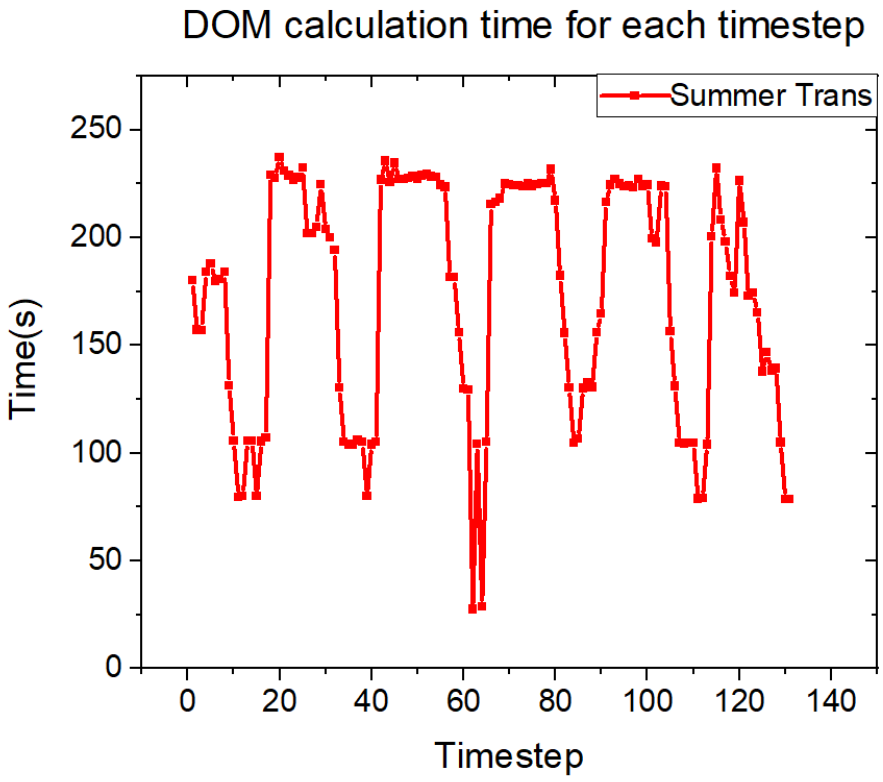

Figure 4.44: The time consumption of DOM for each timestep

In summary, the radiosity method takes a lot of time to calculate the view factor, as expected. However, the time consumption on each timestep to calculate the surface energy budget is small. In contrast, the DOM does not contain a step-like view factor calculation that consumes substantial initial time. However, the mean time consumption for each step is larger than in the radiosity method. The mean time consumption for the DOM at each timestep is approximately 150 s. Meanwhile, this value for radiosity is slightly more than 1 min. This means that the radiosity method consumes less time than the DOM if the timestep exceeds 1000 (41.67 days).

For the conclusion of this part, we apply this calculation to validate our DOM model. This results in a large difference between the two methods. The use of an unfavorable setting to create the mesh eventually leads to a difference in surface temperatures that cannot be neglected. To better compare the two methods with this geometric model, the view factor should be re-evaluated.

In the next part, we focus on the DOM model and apply the different air models to determine the magnitude of the air absorption in this area.

4.2.5 Influence of air absorption

In this part, we concentrate on the air impact on the radiation transfer in this area. The results of the transparent air model are seen as the benchmark for the other two models. Moreover, we introduce the software HélioBIM to simulate solar radiation to verify the DOM result. HélioBIM software is used at the EDF company in France. It applies the ray tracing method to calculate the solar radiation transfer.

An example of the results is shown by the figures 4.45. It was 13 h on 10th June 2019, which was the second time step.

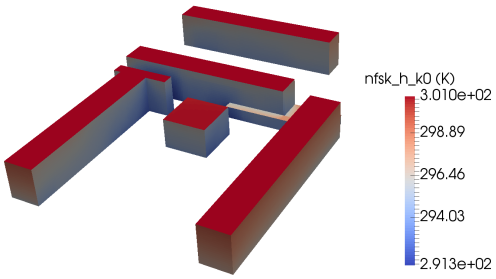

(a) The transparent model

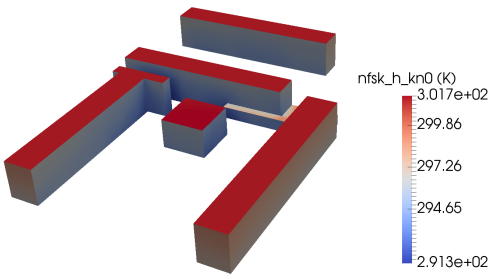

(b) The gray gas model

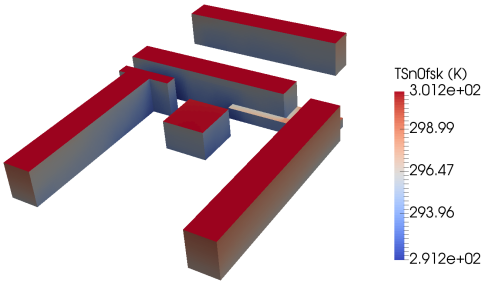

(c) The SLW model

Figure 4.45: The surface temperature at 13h 10th June 2019

The results show that the difference in range of surface temperatures is not wide

among all these models at this moment. The distribution stays at almost the same pattern. However, if we try to determine the difference between the two participatory models and the transparent model at every patch (Figure 4.46), we find that the difference is concentrated on the roof of the amphitheater and the top of the vertical surface, especially for the gray model. In the following section, we analyze the difference at these two places for each kind of radiation transfer.

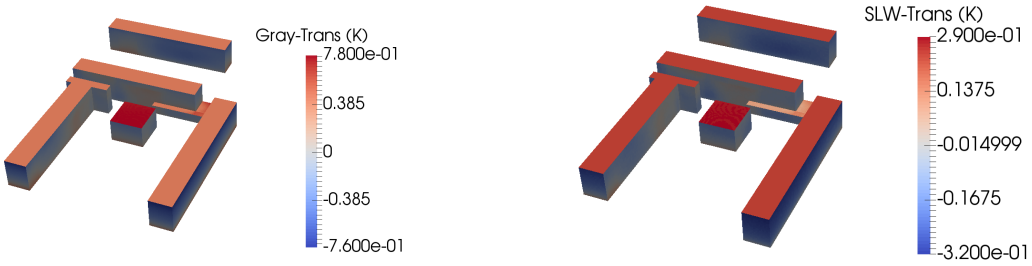

(a) The gray gas model (b) The SLW model

Figure 4.46: The difference of building surface for each patch compared with the transparent model

4.2.5.1 Horizontal surfaces

Figure 4.47 reveals the results of each term of radiation and surface temperature at the second iteration (except Figure 4.47f) with the transparent air model. We distinguish the direct solar radiation and its reflection to more clearly see the first impact of the sun beam and whether it is blocked by the other surface.

Beam solar radiation For direct solar radiation ($E_{solar.dir}$), due to the boundary condition chosen for the DOM, all horizontal patches that can see the sun should have the same value of 86.5 W/m^2 in the transparent air model (Figure 4.47a).

Due to the different heights of the building, there is a chance that only part of the amphitheater roof can see the sun. In this case, the mean incident energy can differ from the input value. As shown in Figure 4.48a, there are peaks of difference ranging from -3 W/m^2 to -11 W/m^2 for the incident direct solar energy between the roof of the amphitheater and the da Vinci building. The latter is one of the highest buildings in the model, which means that its roof always receives the input value of $E_{solar.dir}$. The peak is mainly due to the difference in height, which blocks part of the energy. This difference is also verified by HélioBIM (Figure 4.48b).

Figure 4.49 shows the variation in direct solar radiation received by the roof during the entire simulation duration. The negligible difference of approximately 1 W/m^2 between the DOM and HélioBIM verifies our DOM model. Furthermore, the insignificant difference shows that $E_{solar.dir}$ is not the factor that provokes a difference in temperature for the roof of the amphitheater.

Reflected beam solar radiation Because of the high emissivity value for the building surface, there is normally very little reflection of direct radiation (Figure 4.47b. The variation in the mean reflection of solar direct radiation is shown in Figure 4.50. There are disparities

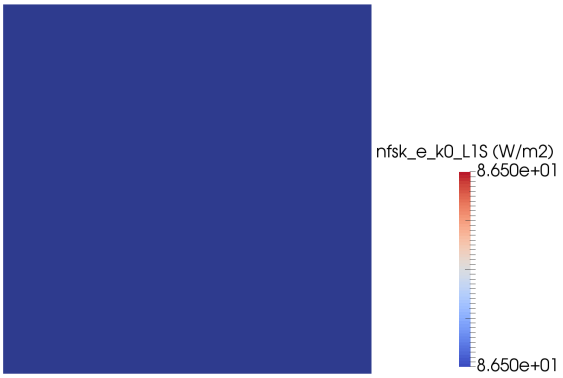

(a) The direct solar radiation $E_{solar.dir}$

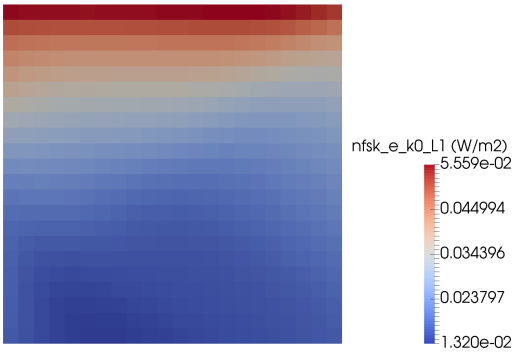

(b) The direct solar radiation reflection $E_{solar.ref}$

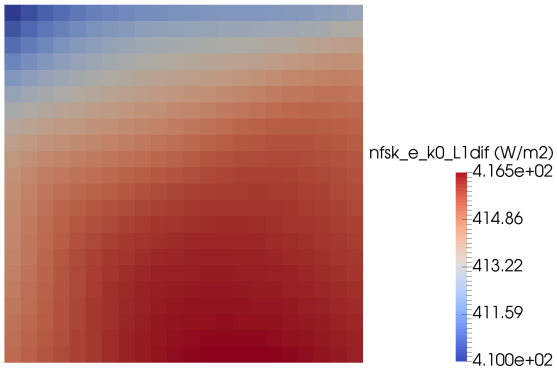

(c) The diffuse solar radiation $E_{solar.dif}$

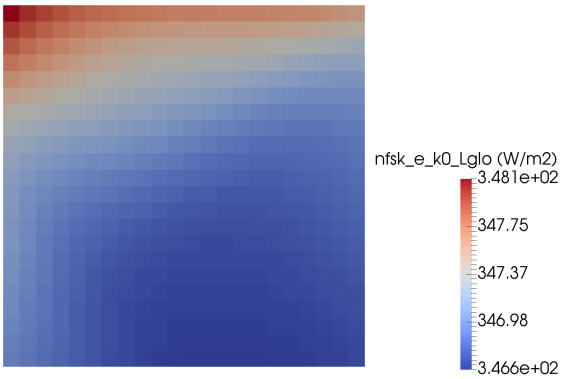

(d) The infrared thermal radiation $E_{solar.glo}$

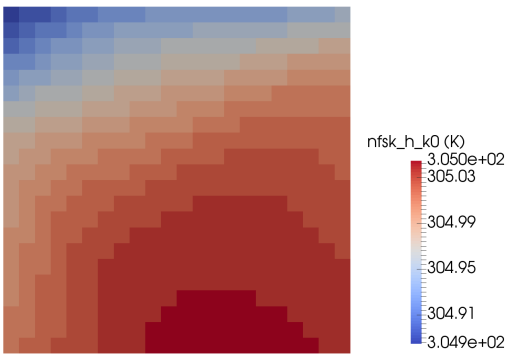

(e) The surface temperature T_s

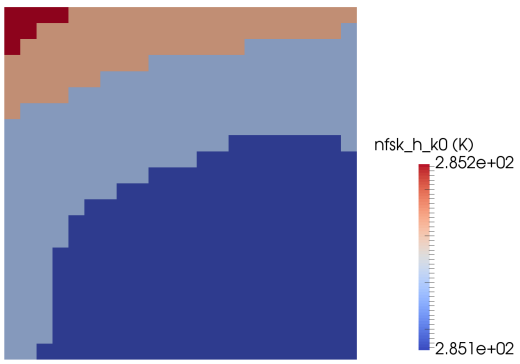

(f) The surface temperature $T_{s.midnight}$

Figure 4.47: The result for the roof at 13h 10th 2019(except the $T_{s.midnight}$ which is the value for 0h 11th 2019)

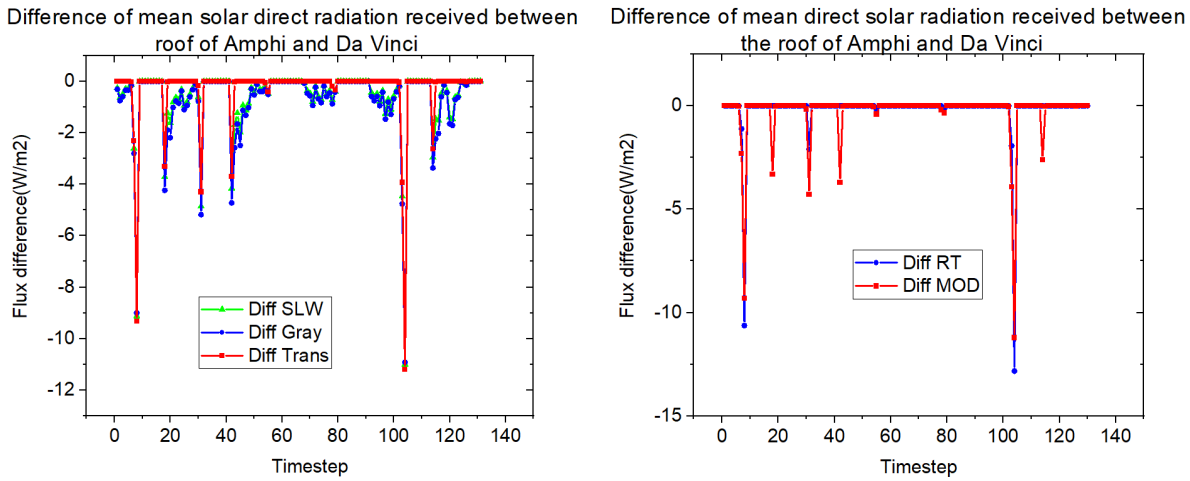

(a) Different air models (b) Different methods

Figure 4.48: The difference of the solar radiation between the roof of amphi and DaVinci with different air models and methods (RT for ray tracing, calculated by HélioBIM)

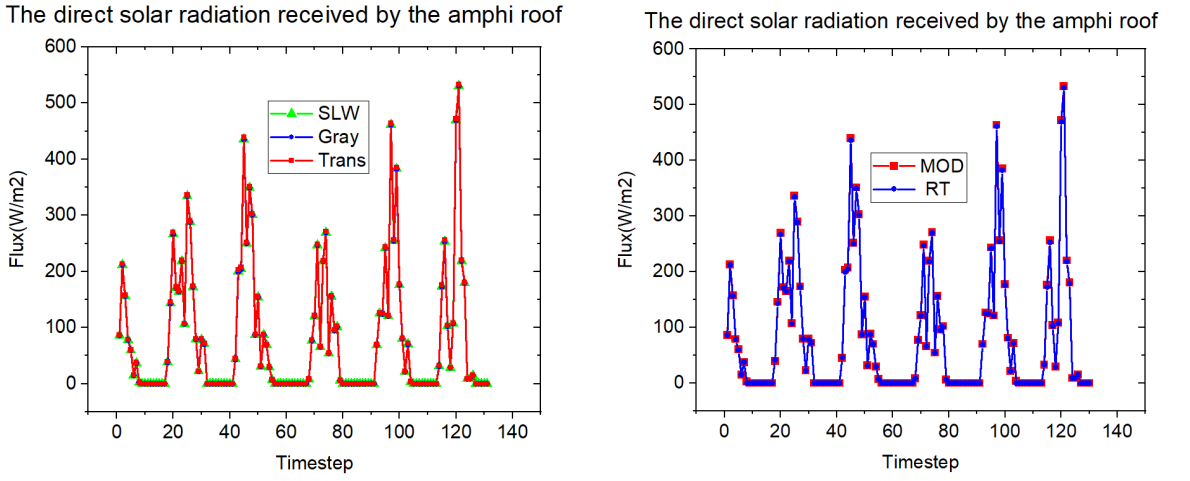

(a) Different air models (b) Different methods

Figure 4.49: The comparison of the incident direct solar radiation on the roof of amphi with different air models and methods (RT for ray tracing, calculated by HélioBIM)

at some time points, especially when $E_{solar.dir}$ is strong. However, the value is too small to generate an impact on the building surface.

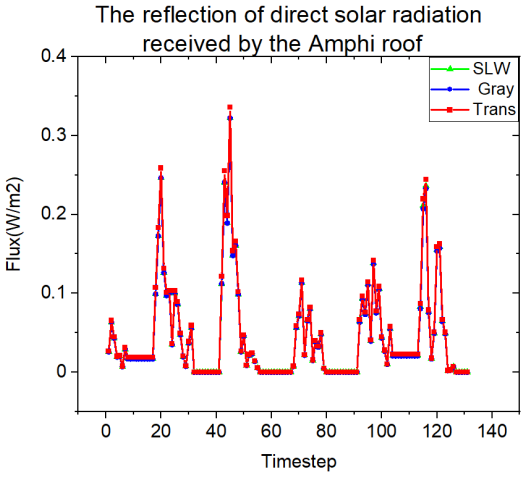

Figure 4.50: The comparison of the reflected direct solar radiation received by the roof of amphi

Diffuse solar radiation In terms of the diffuse solar energy ($E_{solar.dif}$), which can be seen in Figure 4.47c, we observe a gradient of incident flux on the surface. The power is more concentrated on the southern part of the roof. This is because the Jules Verne building is located just behind the amphitheater. Although they have the same height as the former, the Pasteur and da Vinci buildings are located slightly farther away, which reduces their impact on $E_{solar.dif}$ as received by the amphitheater's roof.

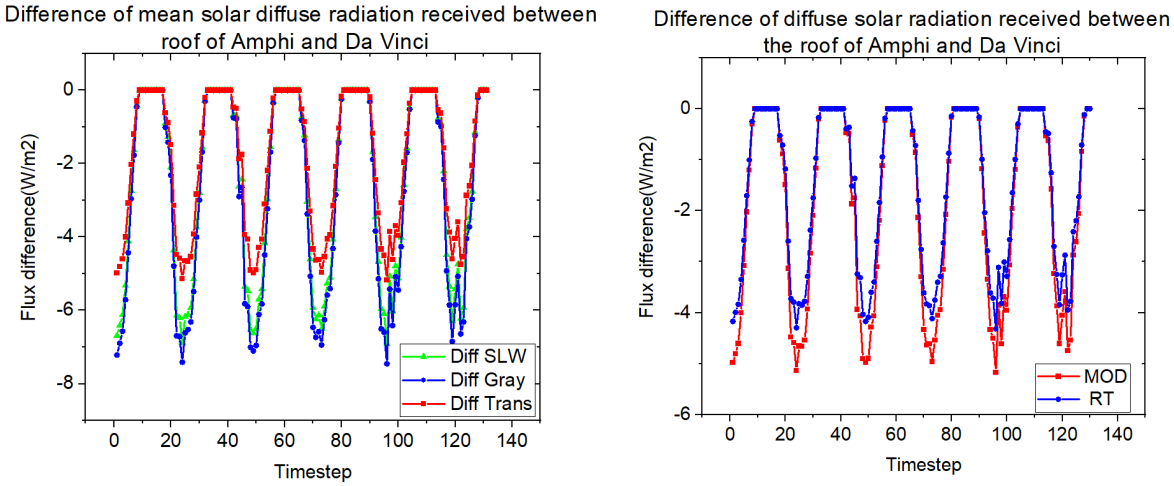

(a) Different air models

(b) Different methods

Figure 4.51: The comparison of the incident diffuse solar radiation between the roof of amphi and Da Vinci with different air models and methods (RT for ray tracing, calculated by HélioBIM)

Compared with the mean $E_{solar.dif}$ received by the roof of the da Vinci building, the roof of the amphitheater receives slightly less (Figure 4.51), which is confirmed by HélioBIM. The amphitheater roof receives a maximum of 5 W/m^2 shortage when $E_{solar.dif}$ reaches its highest value in the daytime. The participatory air model enlarges this difference in heat flux, particularly for the gray gas model. Note that the DOM results have already increased slightly in the transparent model 4.51b and that the participatory model can amplify this difference.

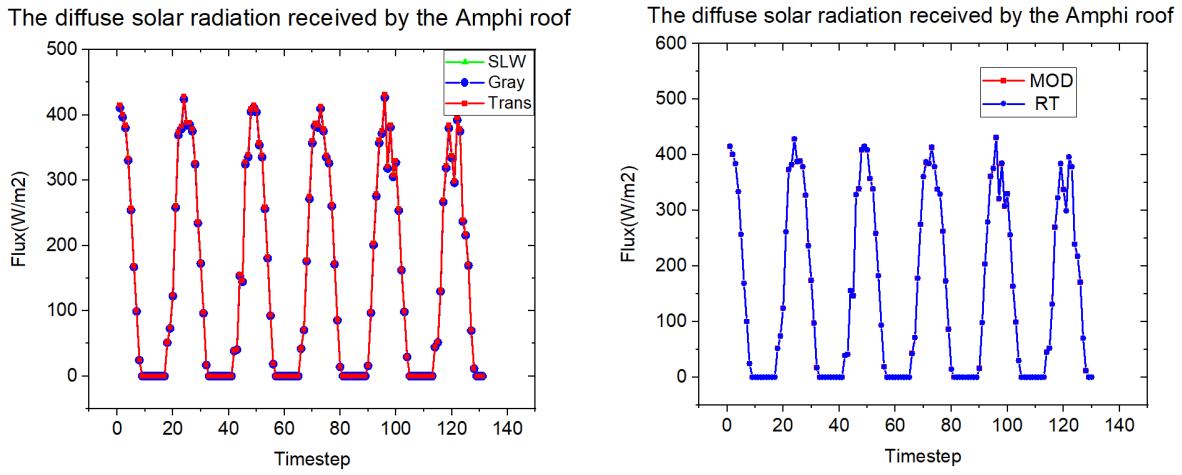

(a) Different air models (b) Different methods

Figure 4.52: The variation of the incident diffuse solar radiation on the roof of amphi with different air models and methods (RT for ray tracing, calculated by HélioBIM)

From the perspective of the entire simulation period (Figure 4.52), the difference between the air models is still hard to observe. This leads to the conclusion that even with a large input for solar radiation, the poor air absorptivity on shortwaves does not have a significant impact on the surface temperature within a microclimate scale. Furthermore, this calculation already exaggerates the air shortwave absorption for the participatory model. For the band where air absorptivity is strong, the energy is already considerably reduced during the transverse direction of the entire atmosphere.

Long wavelengths (thermal IR) In terms of IR radiation ($E_{solar.glo}$), as shown in Figure 4.47d, the building behind the amphitheater becomes an important longwave incoming source. However, the IR radiation increase is compensated by the difference in incident solar energy in the daytime. At night, when the solar factor disappears, this gap in IR radiation can reverse the surface temperature map (Figures 4.47e and 4.47f).

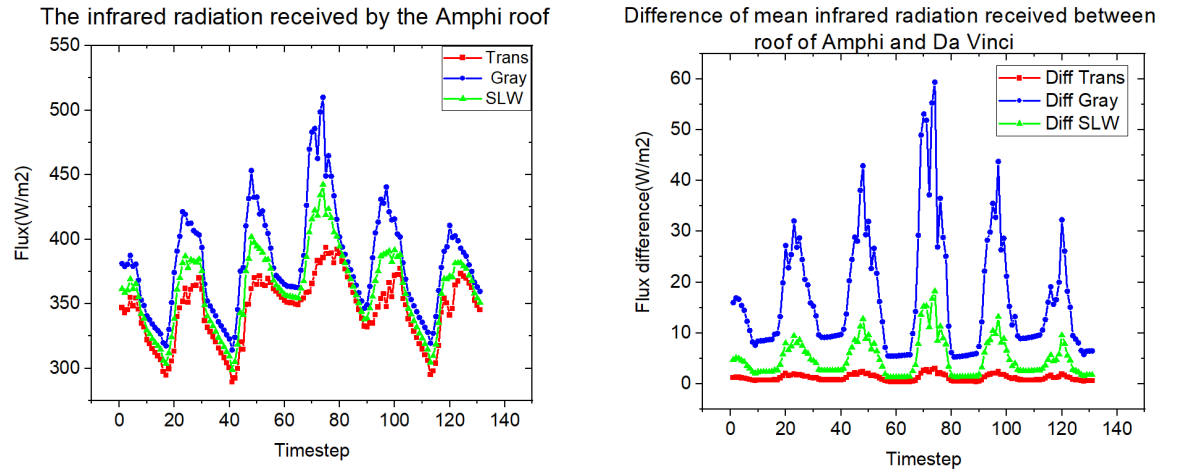

(a) Different air model for the amphi's roof (b) Difference between the roof

Figure 4.53: The variation of the infrared radiation with different air models

Figure 4.53 shows the incident IR radiation for the amphitheater's roof, as well as the difference between it and the da Vinci building's roof. A large gap exists during the

daytime when the building surfaces are warmed up with solar energy. For noon on 13th June in particular, the amphitheater's roof predictions differ by over 100 W/m^2 between the gray and transparent models.

To explain this gap, we should first concentrate on the difference between the two roofs with the transparent model. During the daytime of 13th June, the maximum difference is limited near 5 W/m^2. This difference arises from the emission of the building around the amphitheater's roof. The roof of the da Vinci building can receive only longwave sky emissions. Moreover, the amphitheater can receive emissions from the top of the vertical surface of the surrounding building. As the building surface temperature is higher than the sky temperature, the amphitheater receives slightly more longwave radiation than the da Vinci building. With the participatory air model, the sky's emissions are absorbed by the air between the boundary and the roof surface. At the same time, the air emits its own longwave radiation towards the roofs. For the same values of absorbility and emissivity and the higher temperature of the air than the sky, the IR radiation on the roof increases. For the gray gas model, which is known to overestimate the absorption of gas, the increase is more evident. Additionally, with a longer distance to the boundary, the amphitheater roof is more severely influenced by the existence of the air. Ultimately, a difference of over 50W/m^2 arises in the IR radiation between the two surfaces.

The roof surface temperature is presented in Figure 4.54a. With respect to the amphitheater's roof, the impact of additional IR radiation is substantial. During the daytime, the difference in E_{glo} can lead to a temperature disparity of over 8 K with the gray gas model. The situation is slightly improved with the SLW model, but there is still a maximum difference of approximately 2.5 K. Compared with the temperature of the da Vinci building's roof (4.54b), the amphitheater's roof can reach a lead of approximately 3.6 K with the gray air model and 0.6 K with the SLW model. Considering the distance from each roof to the top boundary (7 m for the amphitheater's roof and 3 m for the da Vinci building's roof), the gray gas model easily overestimates the air absorption, which can lead to a poor result.

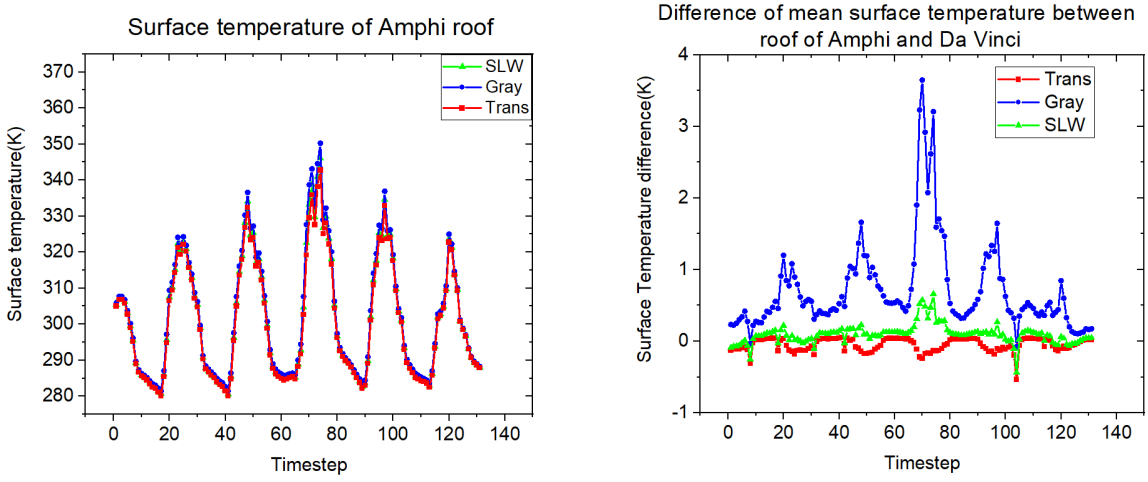

(a) Different air model for the amphi's roof

(b) Difference between the roof

Figure 4.54: The variation of the surface temperature with different air models

4.2.5.2 Vertical surfaces

Figure 4.46 shows that almost all the vertical surfaces have the same trend of difference distribution. For all participatory air models, the temperature of the top part is slightly lower

than the transparent model result. In addition, the temperatures difference contrast at the bottom part for the gray air model. Among all vertical surfaces, we choose the right surface of the da Vinci building, which provides a relatively large gradient of temperature differences. Additionally, factors such as reflection from other building surfaces do not exist, which helps analyze the results more clearly. An example of the results for this surface is presented in the figure. In the following section, we draw the profile of each result as a function of its height. A mean value is calculated by the results for the patch with the same height. This time, the results cannot be compared with HélioBIM because the latter calculates only a mean value for a planar surface.

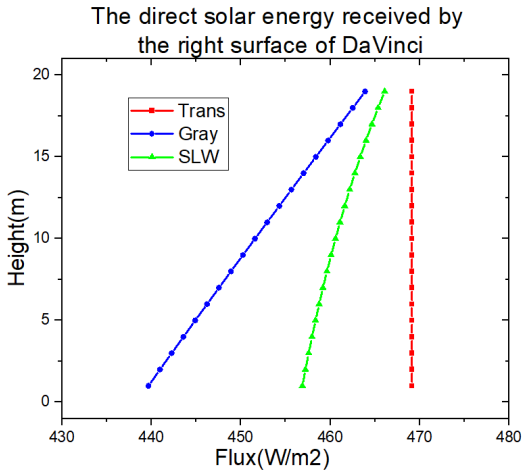

Figure 4.55: The variation of the direct solar energy in function of building height(9h 11th June)

Beam solar radiation In terms of solar direct radiation, the mean value of every 1 m along the z-axis is exhibited in Figure 4.55. In the transparent case, a stable value is obtained for all patches, regardless of the z level at which it is located. Upon switching to the participatory air model, the incident solar energy starts to drop. The longer the transfer distance is, the larger the flux value decreases. This slightly favors the SLW model because the gray model results in overestimation. For the maximum decrease in the two air models, the gray model has over 5% loss, and the SLW model has 3% loss.

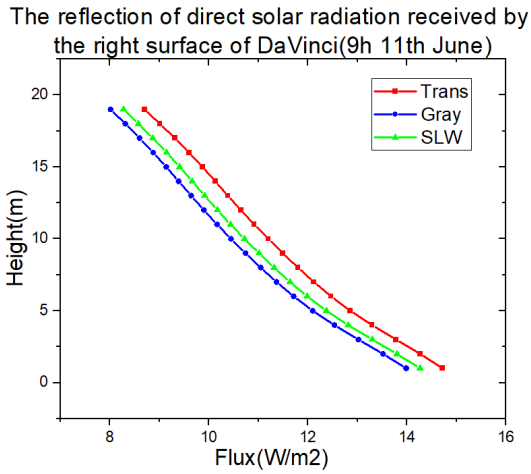

Figure 4.56: The variation of the direct solar energy reflection in function of building height(9h 11th June)

Reflected beam solar radiation In regard to the reflection of direct solar energy, the gradient reverses (Figure 4.56). More energy received by the bottom of the wall causes a higher reflectivity of ground than sky. Broadly, it is poor reflectively for both sky and ground patches, and the difference is small.

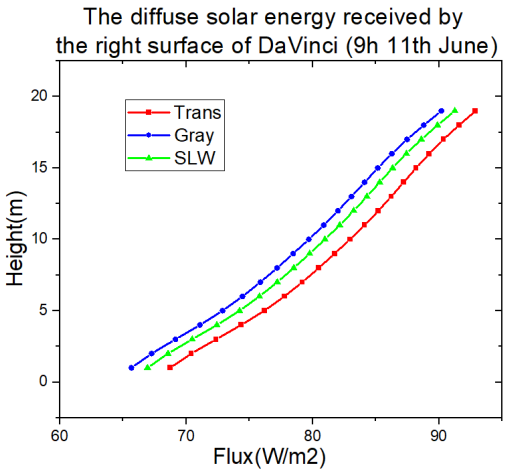

Figure 4.57: The variation of the diffuse solar energy in function of building height(9h 11th June)

Diffuse solar radiation In terms of diffused solar energy, the pattern approaches the direct pattern. This is because the source of energy returns to the sky patch. At this moment, the amount of diffuse solar energy is small, which shows a 3 W/m^2 gap between the gray and transparent models. It is not even possible to cancel the gradient of the reflection energy.

Long wavelengths (thermal IR) The IR radiation is presented with the results for two time points. We add a time point at midnight of the 12th, as the direction of IR radiation is reversed compared with the daytime case. The longwave radiation received by the vertical surface is presented in Figure 4.58. The wall is not the same as the amphitheater roof in the previous part. For this roof, the incident IR radiation is contributed mainly by the sky. Only a small fraction comes from the reflection of the surrounding building. In this case, this wall receives longwave energy from both sky and ground. When the sun rises, the air and ground temperatures both start to increase. Moreover, the ground temperature increases more quickly than the air temperature. For the surface located at the bottom of the wall, the incoming radiation from the ground does not change much, as the transfer distance is short. On the other hand, because of the long transfer distance, most of the sky longwave radiation is absorbed by the air. The IR downwards radiation that reaches the bottom patches is now emitted by the air gas, whose temperature is much higher than that of the sky. In contrast, for the patches located at the top of the building, the ground's emission decreases sharply as the transfer distance increases. Moreover, the downwards radiation has just started its journey, which cannot compensate for the loss of ground radiation. For this reason, the energy received at the bottom of the wall increases substantially, and that for the top decreases substantially.

At night, the building surface becomes the source as its temperature becomes higher than the environment. The difference in temperature between sky and air shrinks to a relatively low level. With our boundary condition for the ground, the temperatures of the air and ground are the same. For the patches near the ground, the incident energy rises as sky emission is replaced by air emission. The difference in temperature between them is smaller than in the

daytime. The increase in energy received also drops. Moreover, because the air and ground are at the same temperature, the ground emission factor decreases. This leads to the climbing of the intersection point of the transparent and gray curves. The lower energy received by the upper patches is caused by the same reason as in daytime. The difference decreases because the ground and air are at the same temperature.

For the SLW model, the idea is almost the same. The only difference is that the air absorption is smaller than in the gray model. Normally, the resulting predictions are lower than those of the transparent model. During the daytime, the variation is similar to that of the gray model, but the inclination is much smaller, as is the surplus value at the bottom.

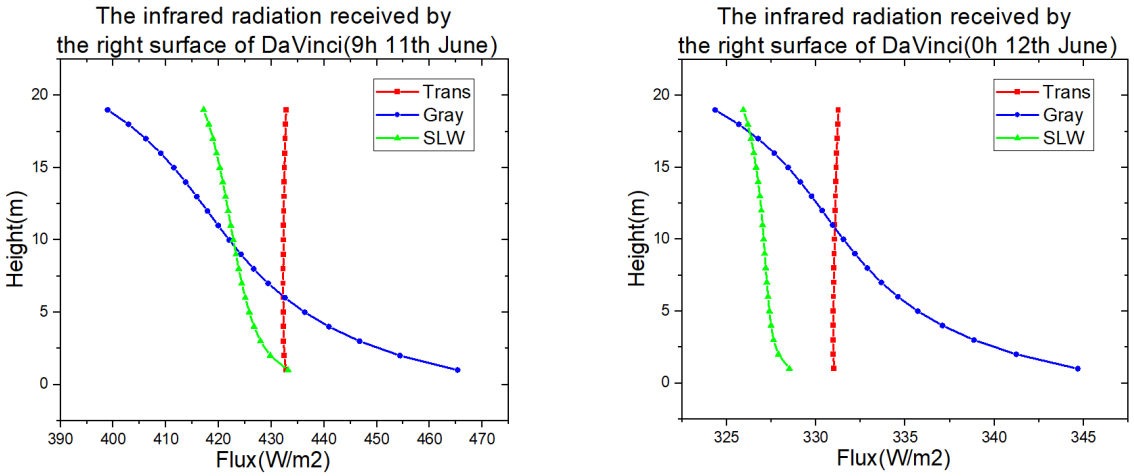

(a) Day time(9h 11th June) (b) Night time(0h 12th June)

Figure 4.58: The infrared radiation received by the right surface of DaVinci

The profile of the mean temperature as a function of height is presented in Figure 4.59. During the daytime, even with higher IR radiation received at the bottom, the surface temperature of the participatory air model declines. At night, with the influence of solar energy, longwave radiation becomes the only factor affecting surface temperature. This is the reason that the received IR radiation and surface temperature are highly similar.

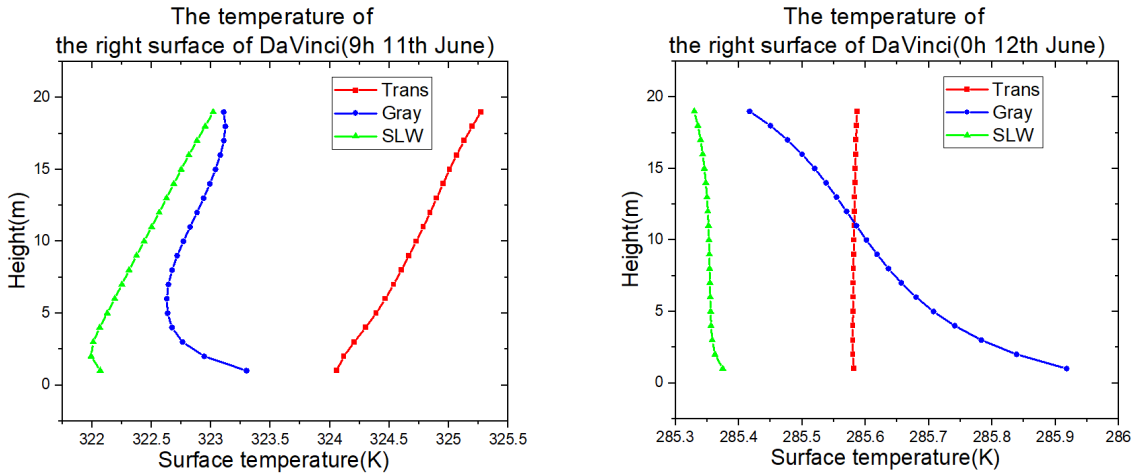

(a) Day time(9h 11th June) (b) Night time(0h 12th June)

Figure 4.59: The surface temperature of right surface of the building DaVinci

For the last part of this analysis, the mean absolute value and the mean absolute deviation are calculated for all patches in this model during the entire period. The results of

the first iteration of calculation are not noted, and the graphics describing the variation depart from the second iteration. The variation in surface temperature is shown in Figure 4.60. The results of different types of radiation are shown in Figure 4.61.

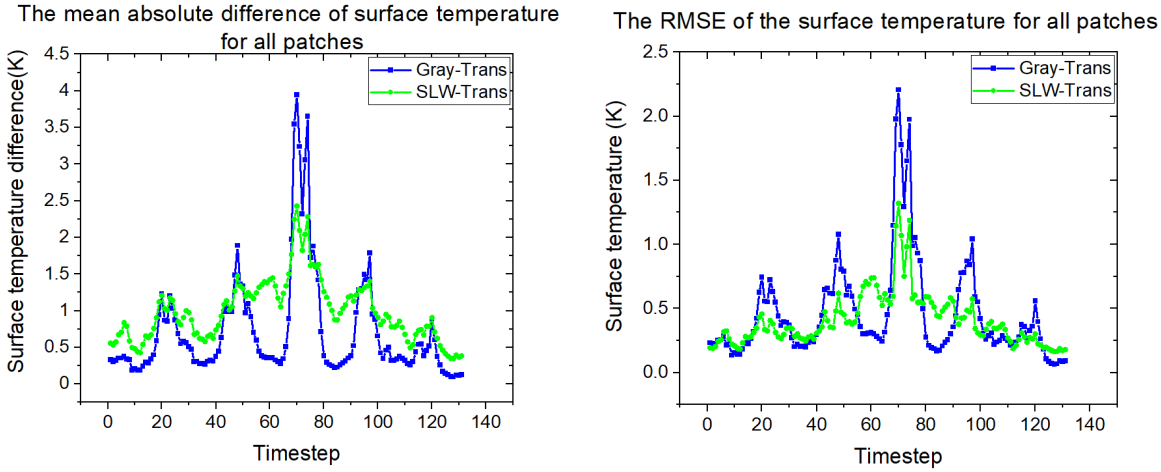

(a) MAE (b) RMSE

Figure 4.60: The variation of the difference in surface temperature

During the daytime, with impinging strong solar radiation, the difference between the gray and transparent models starts to climb. The temperature difference can exceed the SLW value and reach its maximum when the sun reaches its zenith. The reason is that as the sun rises, the air temperature increases, corresponding to an increase in the incident IR radiation for all horizontal surfaces. Furthermore, for the vertical surfaces, the gray model can increase the gradient of incident IR flux along the height, which leads to a large difference in temperature as a function of height. When the solar radiation starts to decrease, the impact of air absorption decreases at the same time. For the horizontal surfaces, the difference in IR radiation with different air models drops to a negligible level (Figure 4.53a). In terms of vertical surfaces, the longwave radiation profile starts to approach the transparent profile, which decreases the sum of the differences between the two air models. In contrast, the SLW profile stays at almost the same position. This leads to a difference in IR radiation between the SLW model and transparent radiation exceeding the gray model's difference. In terms of solar radiation, the difference in every type of solar radiation remains at a low level, which cannot generate a substantial impact compared with IR radiation.

Regarding time consumption, both transparent and gray models take approximately 6 h to finish, whereas the SLW model takes approximately 26.5 h. This is less than the expected value of 42 h (7 times that of the transparent model), but the time consumed is still much longer than that of the other two models.

4.3 Concluding remarks

In this chapter, we concentrated on the different calculations with the two approaches to determine their difference and the impact of air absorption.

The first calculation was carried out for a canyon with a transparent air model. Different modifications over the DOM and the radiosity method were made to obtain a more precise result for solar and IR radiation transfer. In terms of solar radiation, a ray tracing

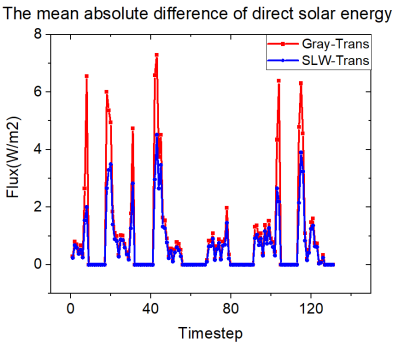

(a) The MAE of direct solar radiation

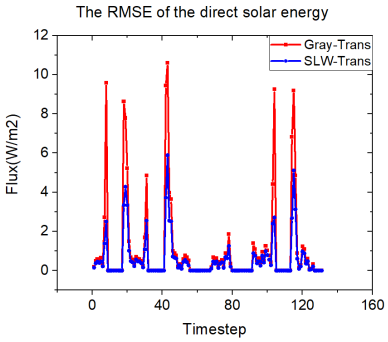

(b) The RMSE of direct solar radiation

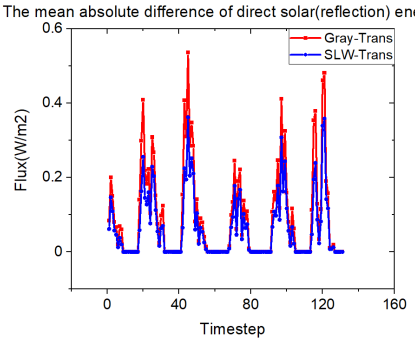

(c) The MAE of direct solar radiation reflection

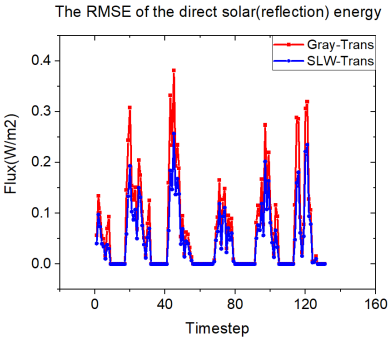

(d) The RMSE of direct solar radiation reflection

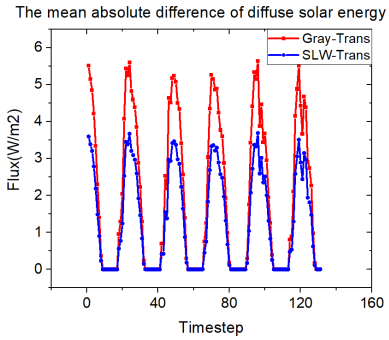

(e) The MAE of diffuse solar radiation

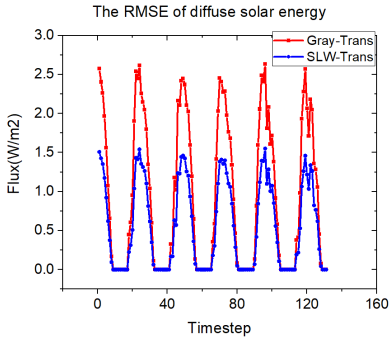

(f) The RMSE of diffuse solar radiation

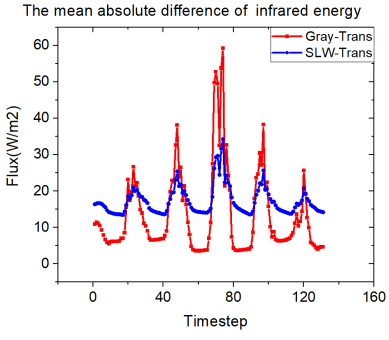

(g) The MAE of infrared radiation

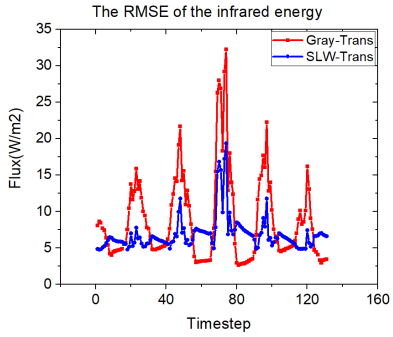

(h) The RMSE of infrared radiation

Figure 4.61: The result of every term of radiation during the entire period

approach was applied for comparison. With the different surface reflection models used by ray tracing and the other two approaches, differences were generated at the ground patches and the building-shaded surface patches. Especially for building surfaces that could not see the sun directly, the difference in averages reached 40% compared with the DOM and radiosity results. The difference between the DOM and radiosity method remained at a very small level for both solar and IR radiation (1.1% of the maximum difference). This result suggests that our DOM approach is valid in this case.

The second calculation is a nonstationary state simulation. With geometry on the INSA campus and weather data from the TRNSYS software, we aimed to validate our DOM approach in this transient simulation and determine the air absorption impact on the surface temperature. However, due to the inappropriate mesh designed for the radiosity approach, it was difficult to fully validate our DOM approach. A well refined mesh is required for this validation. Regarding air absorption, we found a nonnegligible gap between the surface temperatures obtained by different air models. The gray gas model showed a difference in temperature from the transparent model, ranging from $0.4\mathrm{K}$ to $4\mathrm{K}$ for all building surface patches. The SLW showed that this value varied from $0.5\mathrm{K}$ to $2.5\mathrm{K}$. This magnitude of difference proves that air absorption can modify the building surface temperature by up to a few K.

This heat flux difference (a few tens of W/m^2) can be compared to other orders of magnitude: The sky vault geometry has an influence on the radiation received (chapter 2), and the DOM boundary condition (full sky or sky and ground) can affect the surface temperature (Figure 4.37).

This means that if absorption of radiation by air has a nonnegligible impact on the temperatures of the buildings and thus if air should be treated as a participating medium, a suitable definition of the boundary conditions for the simulation (walls, sky vault, etc.) is required to ensure the quality of the results.

Chapter 5

Conclusion and perspective

5.1 Work done in the thesis

With the enormous population boost in urban areas, not only the energy demand but also climate change due to human activities has exploded. This change in climate can drive higher energy requirements. This vicious circle has been adversely affecting the world for a long time. To decrease building energy consumption, regulations have been developed in many regions, including France. Since its release in 1974, RT has been dedicated to increasing building thermal performance to reduce energy consumption. However, there is a vast gap between the design and the real behavior of a building, and this gap is caused by many unknown parameters and variables. In this thesis, we concentrate on radiation transfer in air. We aim to determine whether air can reasonably be considered a transparent model for energy transfer at the microclimate scale. If not, what is the impact of such an assumption on the building heat budget? The objective of this thesis is to develop a tool capable of accurately describing the thermal environment outside of buildings. The focus in particular is on the most computationally expensive and least well characterized mode of heat transfer, i.e., radiation.

To achieve this goal, we first need an approach to simulate the outdoor radiation transfer with the hypothesis that the air is a transparent medium. Chapter 2 concentrates on the development of this approach, and a typical S2S method was chosen, the radiosity method. As a S2S method to calculate the radiation transfer, the radiosity method neglects the variation in intensity during the transfer between the surfaces. As a popular method to evaluate radiation transfer, this method focuses on view factor calculations. In this thesis, several view factor calculation methods are listed in the this chapter. Among them, the ISA method is the method of interest. The method contains no integration, leading to a reduction in the calculation time. However, it performs poorly in calculating the view factor of adjacent surfaces. In this chapter, we applied the subdivision method to improve its performance for the adjacent surface. By respecting the so-called 5 times rule, we aimed to determine how much of the improvement could a subdivision method bring to ISA and how much is the magnitude of error that is not easily neutralized.

Using two test cases, we first evaluated the ISA performance on close surfaces without subdivision. Both of the results showed a poor ability to solve this problem. In the parallel case, the error was depended on the distance between the walls. An error of over 180% compared with the DCI result could be generated if the two surfaces were extremely close. For the perpendicular case, the sum of errors was as high as 88% of the reference value within

the area that did not satisfy the 5 times rule. Then, subdivision was incorporated into the ISA to solve the same problem. The results showed that in both cases, the subdivision was able to reduce the error considerably, by over 90%. Nevertheless, it was not possible to fully cancel this error. For the parallel surface, 20% error still existed in an extreme case. The only method to reduce this residual error was to refine the mesh. On the other hand, a -5% error may still be excessive for the perpendicular case. More importantly, the error could not readily be reduced even with a smaller patch. The only benefit of mesh refinement is to reduce the area associated with the error.

Next, a comparison of the methods was carried out with the ISA, DCI and MC methods. The ISA performed well with a relatively small mesh size. Its error was limited at -1% in terms of the view factor and -4.6% in terms of the incident flux. As expected, the DCI was the best-performing method, with only a -0.4% value for the view factor calculation. The performance of the MC method was found to be highly dependent on the number of samples and size of the mesh. This method was not very stable compared with the other two methods. In terms of time cost, the MC leads to competition. The ISA method can save much time compared with the DCI method, even with the time increase associated with the subdivision. Moreover, the DCI method is impractical for complex model calculations in terms of computational time.

At the end of chapter 2, we chose the ISA method to calculate the view factors for the rest of the thesis, and an approach to calculate the radiation transfer in the transparent medium was developed based on the radiosity method. Subsequently, the question switched to calculation within a nontransparent medium.

In chapter 3, we focused on the development of a nontransparent radiative transfer approach. With this objective, we solved the RTE to determine the air attenuation. The solution was split into 2 parts: How can we represent the air absorption in the RTE, and how can we solve the RTE?

Starting with the first question, we needed to find a suitable air model to represent the air in the RTE. The global air model was selected to reduce the time consumption of calculation compared with the time consumption of the LBL model and band model. Two global models were chosen in this thesis: the gray model, which has a single air absorption coefficient for all wavelength bands, and the SLW model, which is the most sophisticated global air model. The transparent model was also considered in this part to compare the result with the transparent approach developed in the previous chapter.

Different configurations of air gas were designed to evaluate the performance of the three air models. According to these configurations, the database HITRAN was capable of providing the absorption coefficient or absorption cross section as a function of wavenumber. With the help of HITRAN, we could estimate the air absorption for each air model within different distances of transfer.

The results showed that compared to the transparent model, the gray model overestimated the air absorption, especially in the IR radiation range. Within 100 m, the intensity of the IR radiation dropped to 1% for the case with the lowest temperature. The attenuation was much more severe in the hottest case, as only 7% energy remained after 10 m of propagation. The identical absorption coefficient for all wavelengths substantially increased the air absorption for the band where the coefficient was relatively smaller. In terms of the visible field, the performance of the gray model was not truly improved. The only advantage of this model was the calculation time. It took almost the same time as the transparent model, as

the only change in these two models was one calculation of the absorption coefficient. To avoid error, this model is best applied only under conditions where the distance between the surface is not too long.

Regardless of the wavelength, the SLW model provided more accurate results than other methods. However, the simulation time was increased, as we repeated the calculation several times. This increase could be unacceptable for simulations with a complex geometry. Overall, in this part, we found that air attenuation could not be neglected, especially for IR radiation in hot and wet environments. The SLW model was the best-performing method, despite the requirement of a longer calculation time.

Then, we turned to the second question to determine the way to solve the RTE. The DOM was chosen. This method is actually well developed in the combustion field but not often applied in the building simulation field. We started by studying parameter changes with the aim to apply this method to the urban simulation. The linear interpolation scheme interpolates the values of radiative intensities in every cell. The default schemes, such as upwind or centered schemes, both have shortcomings when encountering buildings. The upwind scheme provides realistic results. However, due to the neglected transfer in the second half of the cell, the precision is not satisfactory. The center scheme has the problem of creating unrealistic results, especially in the shaded areas of buildings. A hybrid scheme was tested in this chapter, which was found to successfully reduce the error and erase the noise. Factors such as discretization of angles and spaces are critical to DOM calculation. Because these factors are highly related to the complexity of the geometry, the corresponding discussion was presented in the subsequent chapter.

Chapter 4 compared the two approaches. A steady-state simulation was performed on the geometry of a canyon, and a transient simulation was performed on an area in the INSA campus.

The steady-state simulation was carried out with a canyon, which is the traditional configuration of the urban surface. The objective of this test was to validate our nontransparent approach. To compare with the radiosity method, the air in this part was assumed to be transparent. Both solar radiation transfer and IR radiation transfer were calculated after numerous modifications to the radiosity method and DOM. Regarding solar radiation, a ray tracing approach developed by RAYBAUD Blaise was also considered in the comparison. The results showed that all of the methods could handle this kind of problem. The main difference involved the boundary of the shading surface. Because the view factor in the radiosity method was determined according to the center of the patch, there were some patches that were determined to be blocked from the solar radiation by the radiosity method, actually receiving a part of the energy in the ray tracing method. For the DOM, the variation from the shading to the sunny surface was progressive. On the other hand, radiosity and ray tracing predicted a jump in value for this area. For the other part, the results of the DOM and radiosity method were highly similar, as they both assume a Lambertian surface for all the patches. However, for ray tracing, influenced by the BRDF of each surface, the distribution was not close to that of the other two methods. Thus, the forwards-biased BRDF also caused a decrease in energy on the shady side of the building.

Regarding IR radiation, only the radiosity method and the DOM were applied due to the difficulty of ray tracing to calculate diffuse reflection. As shown in the solar calculation part, the results of these two methods were similar because the same reflection model was used for the surface patch. The error was concentrated on some ground surface patches caused by the ISA view factor calculation issue mentioned above. For the incident flux on the building

surface, a negligible maximum absolute error of 1.1% was generated.

Then, we discussed the impact of the quadrature scheme and discretization spatial on the DOM with this canyon test. The traditional quadrature SN could generate a negative value with a high direction number. We tested the CWDOM, which is a relatively new quadrature set initially designed for a spherical case; the Fibonacci set, which applies the Fibonacci number to generate the direction; and the qMC quadrature, which uses LDSs, which is in contrast to the radiation MC method. The results proved that the Fibonacci quadrature was the best choice for this work, as it was capable of giving a precise result with a relatively low direction number. Subsequently, the impact of the number of directions and cells was discussed. The results showed for both solar and IR radiation terms that the DOM is not too sensitive to cell changes. Even with a large cell size, the DOM could provide results with good precision. The only problem arose with the space between two buildings. This required enough cells to eliminate the building influence. If the cell number is not large enough, a significant decrease in energy can appear on the vertical surfaces of the other building. In addition, the error created by the size of the mesh cannot be compensated by the increase in the quadrature directions. Adding directions can reduce the error, but reducing the upper limit of error requires a smaller cell.

The second simulation in chapter 4 was a transient simulation. The calculation was based on the geometry of an area on the INSA campus. It contained 5 main buildings with a connection between two buildings. The boundary condition was taken from the weather data of Lyon in 2019. We calculated the energy transfer over a period of approximately 5.5 days. The variation in each element, such as the surface temperature, solar radiation and IR radiation, was recorded every hour. Our DOM approach was intended to be first verified by the radiosity method for IR radiation and HélioBIM for the solar part. The shortwave calculation was successfully verified by HélioBIM. However, due to the unfavorable mesh designed for the radiosity method, the longwave radiation could not be verified. The surface, in particular the regions severely influenced by the view factor calculation error, showed a large difference in surface temperature between the radiosity method and the DOM. Regarding time consumption, the radiosity took approximately one day to finish the view factor calculation and slightly more than 2 h for the rest of the calculation. The DOM spent more time on the timestep during the daytime (225 s) and less time on the timestep at night (75 s). This suggests that the DOM would take more time to calculate than the radiosity method if the timestep number was to exceed 1000.

Then, different air models were implanted in the model to determine the impact of the various assumptions. The results showed that in terms of solar radiation, the difference between the air models was not high, regardless of the kind of solar radiation. The maximum error was often located at the bottom of the building, where the transfer distance of solar radiation was the highest. Note also that all the participatory air models overestimated the air absorption at the near-ground level because for the band where the absorption coefficient was high, the intensity was already consumed when it passed through the entire atmosphere. At the boundary layer, little solar energy remained at these wavelength bands. Several hundred meters of propagation distance did not create the same losses as the solar beam just entering the atmosphere. Moreover, in terms of IR radiation, the overestimation of the gray model had a much more influence: Over 100 W/m^2 of difference was observed for the roof of the amphitheater, which led to an $8\mathrm{K}$ gap. For the vertical surfaces during the daytime, the surplus IR radiation obtained with the gray model at the bottom of the wall led to a smaller disparity in temperature compared with the SLW model. Furthermore, at night, when there was no more solar radiation for the wall, the difference in incident IR radiation resulted in a higher temperature at the bottom and a lower temperature at the top compared with the

transparent model. The SLW model performed more stably than the gray model, and the air absorption was more promising. However, the SLW took too much time to finish the calculation. Overall, during the daytime with a higher amount of solar energy, the mean difference in surface temperature between the gray and transparent models for all patches could reach $4\mathrm{K}$, while the value for SLW exceeded $2\mathrm{K}$. After the sunset, the SLW difference was higher, with a $1\mathrm{K}$ gap; in addition, the gray model's value dropped to near $0.5\mathrm{K}$. In terms of time consumption, the transparent model and gray model performed at essentially the same level, consuming approximately 6 h. In contrast, the SLW took more than 26 h to finish the calculation.

To conclude, no negligible difference was observed in the calculations between the participatory air model and the transparent model. This means that air absorption is capable of affecting the building energy budget by varying the incident radiation on the building outside the surface, in particular the IR energy. However, this difference may be influenced by several factors. To obtain a more precise value, a higher accuracy of the setup for the simulation is required, which could lead to a large increase in the simulation cost.

5.2 Future perspective

To evaluate the radiation transfer more precisely, we developed a detailed numerical model in 3 dimensions. However, there are still some points to be improved:

- The boundary condition: The improvement of modeling requires the improvement of the boundary conditions, corresponding to how we define the sky, ground and building patch. For the sky patch, it is possible to implement the sky models mentioned in the chapter on radiosity. For the diffuse solar radiation in this thesis, we directly took the value given by the weather data file. Because of the lack of information about these data, such as sky clearness and brightness, we could not implement a more precise sky diffuse model for diffuse solar energy. In terms of ground, we aimed to save calculation time by avoiding a complex RC model for the ground as well as the building.

- Energy transfer: At the beginning of this thesis, we stated a need to develop a tool to accurately simulate all three terms of energy transfer. Because of the concentration on the radiation part, we did not have enough time to develop heat transfer by convection and conduction. Both of these transfers were modeled in a very simple way, which must be addressed in future studies.

- The air model: The air absorption ability highly corresponds to the temperature and RH of air gas. With the help of the HITRAN database, we succeeded in creating air samples for different conditions and calculated the resulting absorption coefficients. For a long simulation, the air temperature and RH vary over time. This means that a precise evaluation of air absorption requires real-time absorption data. In this thesis, interpolation of temperature and humidity was realized, which can differ from reality. Moreover, the SLW model offers good results, but its calculation time is far too long and cannot be reduced. This means that this model may be impractical to apply in complex conditions.

- Reflection model: The traditional DOM cannot calculate specular reflection, which means that the window cannot be correctly modeled. The problem also exists in the

radiosity method. DART has combined the DOM with the ray tracing technique to realize specular reflection [91] [157].

Bibliography

[1] H. Ritchie, "Urbanization," *Our World in Data*, 2018. https://ourworldindata.org/urbanization.

[2] L. Merlier, *On the interactions between urban structures and air flows : A numerical study of the effects of urban morphology on the building wind environment and the related building energy loads*. PhD thesis, 2015. Thèse de doctorat dirigée par Kuznik, Frédéric Génie civil Lyon, INSA 2015.

[3] Wikipedia, "Rayonnement solaire."

[4] I. Ashdown, *Radiosity - a programmer's perspective*. 01 1994.

[5] R. Goody and Y. Yung, *Atmospheric Radiation: Theoretical Basis*. Oxford University Press, 1995.

[6] W. Haynes, *CRC Handbook of Chemistry and Physics*. CRC Press, 2016.

[7] H. R. Max Roser and E. Ortiz-Ospina, "World population growth," *Our World in Data*, 2013. https://ourworldindata.org/world-population-growth.

[8] A. Khan, "The industrial revolution and the demographic transition," *Business Review*, no. Q1, pp. 9–15, 2008.

[9] M. Anderson, *Population Change 1750–1850*, pp. 21–26. London: Macmillan Education UK, 1988.

[10] U. Nations, "68% of the world population projected to live in urban areas by 2050, says un," 2018.

[11] Y. Wang, L. Chen, and J. Kubota, "The relationship between urbanization, energy use and carbon emissions: evidence from a panel of association of southeast asian nations (asean) countries," *Journal of Cleaner Production*, vol. 112, pp. 1368 – 1374, 2016. Preventing Smog Crises.

[12] M. M. Alam, M. W. Murad, A. H. M. Noman, and I. Ozturk, "Relationships among carbon emissions, economic growth, energy consumption and population growth: Testing environmental kuznets curve hypothesis for brazil, china, india and indonesia," *Ecological Indicators*, vol. 70, pp. 466 – 479, 2016. Navigating Urban Complexity: Advancing Understanding of Urban Social – Ecological Systems for Transformation and Resilience.

[13] S. S. Sharma, "Determinants of carbon dioxide emissions: Empirical evidence from 69 countries," *Applied Energy*, vol. 88, no. 1, pp. 376 – 382, 2011.

[14] L. Yang, H. Yan, and J. C. Lam, "Thermal comfort and building energy consumption implications – a review," *Applied Energy*, vol. 115, pp. 164 – 173, 2014.

[15] W. Liu, H. Lund, B. V. Mathiesen, and X. Zhang, "Potential of renewable energy systems in china," *Applied Energy*, vol. 88, no. 2, pp. 518 – 525, 2011. The 5th Dubrovnik Conference on Sustainable Development of Energy, Water and Environment Systems, held in Dubrovnik September/October 2009.

[16] K. Wang, Y.-M. Wei, and X. Zhang, "Energy and emissions efficiency patterns of chinese regions: A multi-directional efficiency analysis," *Applied Energy*, vol. 104, pp. 105 – 116, 2013.

[17] Q. Zhu and X. Peng, "The impacts of population change on carbon emissions in china during 1978–2008," *Environmental Impact Assessment Review*, vol. 36, pp. 1 – 8, 2012.

[18] O. Allen M.R. and K.Zickfeld, "Chapter1: framing and context.," in *Global Warming of 1.5 C*, ch. 1, pp. 49–91, 2018.

[19] M. E. Mann, R. S. Bradley, and M. K. Hughes, "Northern hemisphere temperatures during the past millennium: Inferences, uncertainties, and limitations," *Geophysical Research Letters*, vol. 26, no. 6, pp. 759–762, 1999.

[20] M. Röck, M. R. M. Saade, M. Balouktsi, F. N. Rasmussen, H. Birgisdottir, R. Frischknecht, G. Habert, T. Lützkendorf, and A. Passer, "Embodied ghg emissions of buildings – the hidden challenge for effective climate change mitigation," *Applied Energy*, vol. 258, p. 114107, 2020.

[21] ADEME, "les chiffres clés du bâtiment," tech. rep., 2013.

[22] M. Emmanuella and H. Alibaba, "The assessment of indoor thermal comfort in a building: A case study of lemar, salamis road, famagusta, cyprus," pp. 109–127, 10 2018.

[23] A. S. Committee, *Thermal Environmental Conditions for Human Occupancy*. 2004.

[24] B. Aebischer, M. Jakob, and G. Catenazzi, "Impact of climate change on thermal comfort, heating and cooling energy demand in europe," 2007.

[25] T. Frank, "Climate change impacts on building heating and cooling energy demand in switzerland," *Energy and Buildings - ENERG BLDG*, vol. 37, pp. 1175–1185, 11 2005.

[26] J. A. Dirks, W. J. Gorrissen, J. H. Hathaway, D. C. Skorski, M. J. Scott, T. C. Pulsipher, M. Huang, Y. Liu, and J. S. Rice, "Impacts of climate change on energy consumption and peak demand in buildings: A detailed regional approach," *Energy*, vol. 79, pp. 20 – 32, 2015.

[27] D. J. Sailor, "Relating residential and commercial sector electricity loads to climate—evaluating state level sensitivities and vulnerabilities," *Energy*, vol. 26, no. 7, pp. 645 – 657, 2001.

[28] H. Wang and Q. Chen, "Impact of climate change heating and cooling energy use in buildings in the united states," *Energy and Buildings*, vol. 82, pp. 428 – 436, 2014.

[29] G. Franco and A. Sanstad, "Climate change and electricity demand in california," *Climatic Change*, vol. 87, pp. 139–151, 03 2008.

[30] N. Levermore, G.J.; Doylend, "North american and european hourly based weather data and methods for hvac building energy analyses and design by simulation," *Ashrae Trans*, no. 10, 2002.

[31] M. Herrera, S. Natarajan, D. A. Coley, T. Kershaw, A. P. Ramallo-González, M. Eames, D. Fosas, and M. Wood, "A review of current and future weather data for building simulation," *Building Services Engineering Research and Technology*, vol. 38, no. 5, pp. 602–627, 2017.

[32] S. Wilcox and W. Marion, "Users manual for tmy3 data sets," 01 2008.

[33] I. Rahman and J. Dewsbury, "Selection of typical weather data (test reference years) for subang, malaysia," *Building and Environment*, vol. 42, no. 10, pp. 3636 – 3641, 2007.

[34] W. Wong and K. Ngan, "Selection of an "example weather year" for hong kong," *Energy and Buildings*, vol. 19, no. 4, pp. 313 – 316, 1993.

[35] J. Hacker, S. E. Belcher, and A. White, "Design summer years for london," 05 2014.

[36] T. Oke, "Towards better scientific communication in urban climate," *Theoretical and Applied Climatology*, vol. 84, pp. 179–190, 02 2006.

[37] J. E. Thornes, "Ipcc, 2001: Climate change 2001: impacts, adaptation and vulnerability, contribution of working group ii to the third assessment report of the intergovernmental panel on climate change, edited by j. j. mccarthy, o. f. canziani, n. a. leary, d. j. dokken and k. s. white (eds). cambridge university press, cambridge, uk, and new york, usa, 2001. no. of pages: 1032. price: £34.95, isbn 0-521-01500-6 (paperback), isbn 0-521-80768-9 (hardback).," *International Journal of Climatology*, vol. 22, no. 10, pp. 1285–1286, 2002.

[38] B. Ferguson, K. Fisher, J. S. Golden, L. Hair, L. Haselbach, D. Hitchcock, K. Kaloush, M. Pomerantz, N. Tran, and D. Waye, "Reducing urban heat islands: Compendium of strategies - cool pavements," 2008.

[39] S. Peng, S. Piao, P. Ciais, P. Friedlingstein, C. Ottle, F.-M. Breon, H. Nan, L. Zhou, and R. Myneni, "Surface urban heat island across 419 global big cities," *Environmental science technology*, vol. 46, pp. 696–703, 12 2011.

[40] M. Santamouris, "Analyzing the heat island magnitude and characteristics in one hundred asian and australian cities and regions," *Science of The Total Environment*, vol. 512-513, pp. 582 – 598, 2015.

[41] W. Zhou, J. Wang, and M. L. Cadenasso, "Effects of the spatial configuration of trees on urban heat mitigation: A comparative study," *Remote Sensing of Environment*, vol. 195, pp. 1 – 12, 2017.

[42] X. Li, Y. Zhou, G. R. Asrar, M. Imhoff, and X. Li, "The surface urban heat island response to urban expansion: A panel analysis for the conterminous united states," *Science of The Total Environment*, vol. 605-606, pp. 426 – 435, 2017.

[43] E. A. Arens and P. B. Williams, "The effect of wind on energy consumption in buildings," *Energy and Buildings*, vol. 1, no. 1, pp. 77 – 84, 1977.

[44] D.-E. A. Bauman, FredErnest, "The effects of surrounding buildings on wind pressure distributions and natural ventilation in long building rows," 1988.

[45] E. Sartori, "Convection coefficient equations for forced air flow over flat surfaces," *Solar Energy*, vol. 80, no. 9, pp. 1063 – 1071, 2006.

[46] F. J. S. de la Flor, R. Ortiz Cebolla, J. Luis Molina Félix, and S. Álvarez Domínguez, "Solar radiation calculation methodology for building exterior surfaces," *Solar Energy*, vol. 79, no. 5, pp. 513 – 522, 2005.

[47] G. Kopp and J. L. Lean, "A new, lower value of total solar irradiance: Evidence and climate significance," *Geophysical Research Letters*, vol. 38, no. 1, 2011.

[48] P. Würfel and U. Würfel, *Physics of Solar Cells: From Basic Principles to Advanced Concepts*. No Longer Used, Wiley, 2016.

[49] C. Gueymard, D. Myers, and K. Emery, "Proposed reference irradiance spectra for solar energy systems testing," *Solar Energy*, vol. 73, no. 6, pp. 443 – 467, 2002.

[50] F. Causone, S. P. Corgnati, M. Filippi, and B. W. Olesen, "Solar radiation and cooling load calculation for radiant systems: Definition and evaluation of the direct solar load," *Energy and Buildings*, vol. 42, no. 3, pp. 305 – 314, 2010.

[51] S. Pal, B. Roy, and S. Neogi, "Heat transfer modelling on windows and glazing under the exposure of solar radiation," *Energy and Buildings*, vol. 41, no. 6, pp. 654 – 661, 2009.

[52] W. C. Tam and W. Yuen, "Numerical study on the importance of radiative heat transfer in building energy simulation1," 03 2016.

[53] A. Gros, E. Bozonnet, and C. Inard, "Modelling the radiative exchanges in urban areas: A review," *Advances in Building Energy Research*, vol. 5, no. 1, pp. 163–206, 2011.

[54] T. M. Crawford and C. E. Duchon, "An Improved Parameterization for Estimating Effective Atmospheric Emissivity for Use in Calculating Daytime Downwelling Longwave Radiation," *Journal of Applied Meteorology*, vol. 38, pp. 474–480, 04 1999.

[55] J. Kjaersgaard, F. Plauborg, and S. Hansen, "Comparison of models for calculating daytime long-wave irradiance using long term data set," *Agricultural and Forest Meteorology*, vol. 143, no. 1, pp. 49 – 63, 2007.

[56] B. Y. Liu and R. C. Jordan, "The interrelationship and characteristic distribution of direct, diffuse and total solar radiation," *Solar Energy*, vol. 4, no. 3, pp. 1 – 19, 1960.

[57] T. Klucher, "Evaluation of models to predict insolation on tilted surfaces," *Solar Energy*, vol. 23, no. 2, pp. 111 – 114, 1979.

[58] J. E. Hay, "Calculating solar radiation for inclined surfaces: Practical approaches," *Renewable Energy*, vol. 3, no. 4, pp. 373 – 380, 1993. Solar radiation, environment and climate change.

[59] D. Reindl, W. Beckman, and J. Duffie, "Evaluation of hourly tilted surface radiation models," *Solar Energy*, vol. 45, no. 1, pp. 9 – 17, 1990.

[60] R. Perez, P. Ineichen, R. Seals, J. Michalsky, and R. Stewart, "Modeling daylight availability and irradiance components from direct and global irradiance," *Solar Energy*, vol. 44, no. 5, pp. 271 – 289, 1990.

[61] B. T. Phong, "Illumination for computer generated pictures," *Commun. ACM*, vol. 18, p. 311–317, June 1975.

[62] J. F. Blinn, "Models of light reflection for computer synthesized pictures," in *Proceedings of the 4th Annual Conference on Computer Graphics and Interactive Techniques*, SIGGRAPH '77, (New York, NY, USA), p. 192–198, Association for Computing Machinery, 1977.

[63] K. E. Torrance and E. M. Sparrow, "Theory for off-specular reflection from roughened surfaces∗," *J. Opt. Soc. Am.*, vol. 57, pp. 1105–1114, Sep 1967.

[64] M. Oren and S. K. Nayar, "Generalization of lambert's reflectance model," in *Proceedings of the 21st Annual Conference on Computer Graphics and Interactive Techniques*, SIGGRAPH '94, (New York, NY, USA), p. 239–246, Association for Computing Machinery, 1994.

[65] E. P. F. Lafortune, S.-C. Foo, K. E. Torrance, and D. P. Greenberg, "Non-linear approximation of reflectance functions," in *Proceedings of the 24th Annual Conference on Computer Graphics and Interactive Techniques*, SIGGRAPH '97, (USA), p. 117–126, ACM Press/Addison-Wesley Publishing Co., 1997.

[66] G. J. Ward, "Measuring and modeling anisotropic reflection," *SIGGRAPH Comput. Graph.*, vol. 26, p. 265–272, July 1992.

[67] C. M. Goral, K. Torrance, D. P. Greenberg, and B. Battaile, "Modeling the interaction of light between diffuse surfaces," in *SIGGRAPH '84*, 1984.

[68] A. iversen, N. Roy, M. Hvass, M. Jørgensen, J. Christoffersen, W. Osterhous, and K. Johnsen, *Daylight calculations in practice: An investigation of the ability of nine daylight simulation programs to calculate the daylight factor in five typical rooms*. 01 2013.

[69] D. Immel, M. Cohen, and D. Greenberg, "A radiosity method for non-diffuse environments," vol. 20, pp. 133–142, 08 1986.

[70] P. Hanrahan, D. Salzman, and L. Aupperle, "A rapid hierarchical radiosity algorithm," *SIGGRAPH Comput. Graph.*, vol. 25, p. 197–206, July 1991.

[71] G. Larson and R. Shakespeare, *Rendering with Radiance: The Art and Science of Lighting Visualization*. Computer Graphics and Geometric Modeling Series, Morgan Kaufmann, 1998.

[72] E. Lafortune and Y. Willems, "Bi-directional path tracing," *Proceedings of Third International Conference on Computational Graphics and Visualization Techniques (Compugraphics'*, vol. 93, 01 1998.

[73] PETER.S.SHIRLEY, *Physically based lighting calculations for computer graphics*. PhD thesis, Reed College, 1985.

[74] M. Kalos and P. Whitlock, *Monte Carlo Methods*. Wiley, 2008.

[75] P. Shirley, C. Wang, and K. Zimmerman, "Monte carlo techniques for direct lighting calculations," *ACM Trans. Graph.*, vol. 15, p. 1–36, Jan. 1996.

[76] N. Jakica, "State-of-the-art review of solar design tools and methods for assessing daylighting and solar potential for building-integrated photovoltaics," *Renewable and Sustainable Energy Reviews*, vol. 81, pp. 1296 – 1328, 2018.

[77] H. W. Jensen, "Global illumination using photon maps," in *Proceedings of the Eurographics Workshop on Rendering Techniques '96*, (Berlin, Heidelberg), p. 21–30, Springer-Verlag, 1996.

[78] S. Heugang, H. T. Kamdem Tagne, and F. Pelap, "A discrete transfer method for radiative transfer through anisotropically scattering media," *American Journal of Heat and Mass Transfer*, vol. Vol. 3, pp. pp. 396–411, 11 2016.

[79] J. Howell, R. Siegel, and M. P. Mengüç, *Thermal Radiation Heat Transfer*. 09 2010.

[80] G. Pietrek, "Fast calculation of accurate formfactors," 1993.

[81] J. Bouyer, C. Inard, and M. Musy, "Microclimatic coupling as a solution to improve building energy simulation in an urban context," *Energy and Buildings*, vol. 43, no. 7, pp. 1549 – 1559, 2011.

[82] D. Robinson, F. Haldi, J. Kämpf, P. Leroux, D. Perez, A. Rasheed, and U. Wilke, "Citysim: Comprehensive micro-simulation of resources flows for sustainable urban planning;," pp. 1083–1090, 01 2009.

[83] D. Robinson and A. Stone, "Solar radiation modelling in the urban context," *Solar Energy*, vol. 77, no. 3, pp. 295 – 309, 2004.

[84] D. Robinson, "A simplified radiosity algorithm for general urban radiation exchange," *Building Service Engineering*, vol. 26, 11 2005.

[85] A. Keller, "Instant radiosity," in *Proceedings of the 24th Annual Conference on Computer Graphics and Interactive Techniques*, SIGGRAPH '97, (USA), p. 49–56, ACM Press/Addison-Wesley Publishing Co., 1997.

[86] A. Willmott, P. Heckbert, and M. Garl, "Face cluster radiosity," *Rendering Techniques 99 (Proceedings of EG Workshop on Rendering)*, 07 1999.

[87] J. Srinivasan, "Climate change, greenhouse gases and aerosols," *Resonance*, vol. 13, pp. 1146–1155, 12 2008.

[88] A. Maurellis and J. Tennyson, "The climatic effects of water vapour," *Physics World*, vol. 16, 05 2003.

[89] M. Etminan, G. Myhre, E. J. Highwood, and K. P. Shine, "Radiative forcing of carbon dioxide, methane, and nitrous oxide: A significant revision of the methane radiative forcing," *Geophysical Research Letters*, vol. 43, no. 24, pp. 12,614–12,623, 2016.

[90] H. Ritchie and M. Roser, "Co and greenhouse gas emissions," *Our World in Data*, 2017. https://ourworldindata.org/co2-and-other-greenhouse-gas-emissions.

[91] F. GASCON, *Modélisation physique d'images de télédétection optique*. Theses, Université Paul Sabatier - Toulouse III, Dec. 2001.

[92] M. Planck, *The Theory of Heat Radiation*. Dover publications,inc, 1914.

[93] M. F. Modest, *Radiative Heat Transfer – Third edition*. Academic Press, 2013.

[94] G. Kirchhoff and R. Bunsen, "Chemische analyse durch spectralbeobachtungen," *Annalen der Physik*, vol. 186, no. 6, pp. 161–189, 1860.

[95] D. Baum, H. Rushmeire, and J. Winget, "Improving radiosity solutions through the use of analytically determined form-factors," vol. 23, pp. 325–334, 07 1989.

[96] M. Cohen, D. Greenberg, D. Immel, and P. Brock, "An efficient radiosity approach for realistic image synthesis," *Computer Graphics and Applications, IEEE*, vol. 6, pp. 26 – 35, 04 1986.

[97] J. Bouyer, *Modélisation et simulation des microclimats urbains - Étude de l'impact de l'aménagement urbain sur les consommations énergétiques des bâtiments*. Theses, Université de Nantes, Sept. 2009.

[98] E. Sparrow, "A new and simpler formulation for radiative angle factors," 1963.

[99] M. Sbert, "Error and complexity of random walk monte carlo radiosity," *Visualization and Computer Graphics, IEEE Transactions on*, vol. 3, pp. 23 – 38, 02 1997.

[100] J. MacFarlane, "Visrad—a 3-d view factor code and design tool for high-energy density physics experiments," *Journal of Quantitative Spectroscopy and Radiative Transfer*, vol. 81, no. 1, pp. 287 – 300, 2003. Radiative Properties of Hot Dense Matter.

[101] R. Mistrick and D. DiLaura, "A new finite orthogonal transform applied to radiative transfer calculations," *Journal of the Illuminating Engineering Society*, vol. 16, pp. 115–128, 09 2013.

[102] A. EMERY, O. JOHANSSON, M. LOBO, and A. ABROUS, *A comparative study of methods for computing the diffuse radiation viewfactors for complex structures*.

[103] N. Max, "Optimal sampling for hemicubes," *IEEE Transactions on Visualization and Computer Graphics*, vol. 1, p. 60–76, Mar. 1995.

[104] M. Sbert, "An integral geometry based method for fast form-factor computation," *Computer Graphics Forum*, vol. 12, no. 3, pp. 409–420, 1993.

[105] J. Mahovsky and B. Wyvill, "Fast ray-axis aligned bounding box overlap tests with plucker coordinates," *Journal of Graphics Tools*, vol. 9, pp. 35–46, jan 2004.

[106] J. Goldsmith and J. Salmon, "Automatic creation of object hierarchies for ray tracing," *IEEE Computer Graphics and Applications*, vol. 7, no. 5, pp. 14–20, 1987.

[107] H. Sulaiman and A. Bade, *Bounding Volume Hierarchies for Collision Detection*. 03 2012.

[108] J. P. Mena-Chalco, "Ray/box intersection," 2020.

[109] C. Geuzaine and J.-F. Remacle, "Gmsh: A 3-d finite element mesh generator with built-in pre- and post-processing facilities," *International Journal for Numerical Methods in Engineering*, vol. 79, no. 11, pp. 1309–1331, 2009.

[110] D. R. Nicolas Lauzier, "View factors," 2020.

[111] T. Bergman, F. Incropera, D. DeWitt, and A. Lavine, *Fundamentals of Heat and Mass Transfer*. Wiley, 2011.

[112] D. Jacob, "The role of water vapour in the atmosphere. a short overview from a climate modeller's point of view," *Physics and Chemistry of the Earth, Part A: Solid Earth and Geodesy*, vol. 26, no. 6, pp. 523 – 527, 2001. Proceedings of the First COST Action 716 Workshop Towards Operational GPS Meteorology and the Second Network Workshop of the International GPS Service (IGS).

[113] T. R. Anderson, E. Hawkins, and P. D. Jones, "Co2, the greenhouse effect and global warming: from the pioneering work of arrhenius and callendar to today's earth system models," *Endeavour*, vol. 40, no. 3, pp. 178 – 187, 2016.

[114] L. H. Allen, "Uv radiation as related to the greenhouse effect," in *Stratospheric Ozone Depletion/UV-B Radiation in the Biosphere* (R. H. Biggs and M. E. B. Joyner, eds.), (Berlin, Heidelberg), pp. 15–26, Springer Berlin Heidelberg, 1994.

[115] R. Penndorf, "Tables of the refractive index for standard air and the rayleigh scattering coefficient for the spectral region between 0.2 and 20.0 μ and their application to atmospheric optics," *J. Opt. Soc. Am.*, vol. 47, pp. 176–182, Feb 1957.

[116] W. C. Malm and D. E. Day, "Estimates of aerosol species scattering characteristics as a function of relative humidity," *Atmospheric Environment*, vol. 35, no. 16, pp. 2845 – 2860, 2001.

[117] P.-S. Wei, H.-H. Chiu, Y.-C. Hsieh, D.-L. Yen, C. Lee, Y.-C. Tsai, and T.-C. Ting, "Absorption coefficient of water vapor across atmospheric troposphere layer," *Heliyon*, vol. 5, no. 1, p. e01145, 2019.

[118] F. Moupfouma, "Electromagnetic waves attenuation due to rain: A prediction model for terrestrial or l.o.s shf and ehf radio communication links," *Journal of Infrared, Millimeter, and Terahertz Waves*, vol. 30, pp. 622–632, 06 2009.

[119] D. Harris, "The attenuation of electromagnetic waves due to atmospheric fog," *International Journal of Infrared and Millimeter Waves*, vol. 19, p. 1091–1108, 1955.

[120] M. A. Fares, S. C. Fares, and C. A. Ventrice, "Attenuation of the electromagnetic waves due to dry snow," in *Proceedings of SOUTHEASTCON '96*, pp. 680–683, 1996.

[121] M. Fares, S. Fares, and C. Ventrice, "Attenuation of the electromagnetic waves due to moist and wet snow," pp. 99–104, 01 2007.

[122] N. R. T. S. U. T. Harvard-Smithsonian Center for Astrophysics (CFA), V.E. Zuev Insitute of Atmosperic Optics (IAO), "Hitran."

[123] Atomic and H.-S. C. f. A. Molecular Physics Division, "Hitran."

[124] I. Gordon, L. Rothman, C. Hill, R. Kochanov, Y. Tan, P. Bernath, M. Birk, V. Boudon, A. Campargue, K. Chance, B. Drouin, J.-M. Flaud, R. Gamache, J. Hodges, D. Jacquemart, V. Perevalov, A. Perrin, K. Shine, M.-A. Smith, J. Tennyson, G. Toon, H. Tran, V. Tyuterev, A. Barbe, A. Császár, V. Devi, T. Furtenbacher, J. Harrison, J.-M. Hartmann, A. Jolly, T. Johnson, T. Karman, I. Kleiner, A. Kyuberis, J. Loos, O. Lyulin, S. Massie, S. Mikhailenko, N. Moazzen-Ahmadi, H. Müller, O. Naumenko, A. Nikitin, O. Polyansky, M. Rey, M. Rotger, S. Sharpe, K. Sung, E. Starikova, S. Tashkun, J. V. Auwera, G. Wagner, J. Wilzewski, P. Wcisło, S. Yu, and E. Zak, "The hitran2016 molecular spectroscopic database," *Journal of Quantitative Spectroscopy and Radiative Transfer*, vol. 203, pp. 3 – 69, 2017. HITRAN2016 Special Issue.

[125]

[126] W. Malkmus, "Random lorentz band model with exponential-tailed s1 line-intensity distribution function∗," *J. Opt. Soc. Am.*, vol. 57, pp. 323–329, Mar 1967.

[127] J. Taine and A. Soufiani, "Gas ir radiative properties: From spectroscopic data to approximate models," vol. 33 of *Advances in Heat Transfer*, pp. 295 – 414, Elsevier, 1999.

[128] V. P. Solovjov, F. Andre, and B. W. Webb, *Thermal Radiation Heat Transfer: radiative properties of gases, Handbook of Thermal Science and Engineering*. Springer, 2017.

[129] P. Rivière, A. Soufiani, and J. Taine, "Correlated-k and fictitious gas methods for h2o near 2.7 m," *Journal of Quantitative Spectroscopy and Radiative Transfer*, vol. 48, no. 2, pp. 187 – 203, 1992.

[130] M. Modest and H. Zhang, "The full-spectrum correlated-k distribution and its relationship to the weighted-sum-of-gray-gases method," *American Society of Mechanical Engineers, Heat Transfer Division, (Publication) HTD*, vol. 366, 01 2000.

[131] H. C. Hottel and A. F. Sarofim, *Radiative transfer*.

[132] M. Denison and B. Webb, "k-distributions and weighted-sum-of-gray-gases-a hybrid model," 1994.

[133] V. Ambartzumian, "The effect of the absorption lines on the radiative equilibriul of the outer layers of the stars," *Publ. Obs. Astron. Univ. Leningrad*, 1934.

[134] M. F. Modest, *Radiative Heat Transfer*. Academic Press, 2003.

[135] "Beer-lambert law."

[136] F. Liu, H. A. Becker, and A. Pollard, "Spatial differencing schemes of the discrete-ordinates method," *Numerical Heat Transfer, Part B: Fundamentals*, vol. 30, no. 1, pp. 23–43, 1996.

[137] M. F. Modest, "Chapter 16 - the method of discrete ordinates (sn-approximation)," in *Radiative Heat Transfer (Second Edition)* (M. F. Modest, ed.), pp. 498–538, Burlington: Academic Press, second edition ed., 2003.

[138] R. Koch, W. Krebs, S. Wittig, and R. Viskanta, "Discrete ordinates quadrature schemes for multidimensional radiative transfer," *Journal of Quantitative Spectroscopy and Radiative Transfer*, vol. 53, no. 4, pp. 353–372, 1995.

[139] R. Koch and R. Becker, "Evaluation of quadrature schemes for the discrete ordinates method," *Journal of Quantitative Spectroscopy and Radiative Transfer*, vol. 84, no. 4, pp. 423–435, 2004. Eurotherm Seminar 73 - Computational Thermal Radiation in Participating Media.

[140] W. A. Fiveland, "The selection of discrete ordinate quadrature sets for anisotropic scattering," *Fundamantals of radiative heat transfer*, vol. 160, pp. 89–96, 1991.

[141] B. Carlson, C. Lee, L. A. S. Laboratory, and U. A. E. Commission, *Mechanical Quadrature and the Transport Equation*. LAMS (Los Alamos Scientific Laboratory), Los Alamos Scientific Laboratory of the University of California, 1961.

[142] K. D. Lathrop and B. G. Carlson, "Discrete ordinates angular quadrature of the neutron transport equation,"

[143] K. Manalo, C. D. Ahrens, and G. Sjoden, "Advanced quadratures for three-dimensional discrete ordinate transport simulations: A comparative study," *Annals of Nuclear Energy*, vol. 81, pp. 196 – 206, 2015.

[144] T. Gassoumi and R. Said, "Application of a new quadrature scheme for the discrete ordinate method to investigate radiative heat transfer in a spherical geometry," 12 2019.

[145] J. Hannay and J. Nye, "Fibonacci numerical integration on a sphere," *Journal of Physics A: Mathematical and General*, vol. 37, p. 11591, 11 2004.

[146] R. Marques, C. Bouville, L. P. Santos, and K. Bouatouch, *Efficient Quadrature Rules for Illumination Integrals: From Quasi Monte Carlo to Bayesian Monte Carlo*. Morgan & Claypool, 2015.

[147] D. Svergun, "Solution scattering from biopolymers: Advanced contrast variation data analysis," *Acta Crystallographica Section A - ACTA CRYSTALLOGR A*, vol. 50, pp. 391–402, 05 1994.

[148] R. Swinbank and R. Purser, "Fibonacci grids: A novel approach to global modelling," *Quarterly Journal of the Royal Meteorological Society*, vol. 132, pp. 1769 – 1793, 02 2006.

[149] W. L. Dunn and J. K. Shultis, *Exploring Monte Carlo Methods*. Academic Press, 2012.

[150] C. Lemieux, *Monte Carlo and Quasi-Monte Carlo Sampling*. Springer Series in Statistics, Springer, 2009.

[151] J. S. Brauchart and J. Dick, "Quasi-monte carlo rules for numerical integration over the unit sphere s 2," *Numerische Mathematik*, vol. 121, 01 2011.

[152] H. Künzel, T. Schmidt, and A. Holm, "Exterior surface temperature of different wall constructions comparison of numerical simulation and experiment," *Proceedings TU Dresden Sept*, vol. 11, pp. 441–449, 01 2002.

[153] M. Núñez and T. Oke, "The energy balance of an urban canyon," *Journal of Applied Meteorology*, vol. 16, pp. 11–19, 01 1977.

[154] B. Raybaud, P. Thony, E. Vergnault, L. Merlier, and J. Roux, "Preliminary numerical evaluation of the bipvs potential in urban areas: Which method to use for solar radiation calculation?," 2020.

[155] V. Sridhar, "Land surface modeling of energy-balance components: Model validation and scaling effects," 01 2001.

[156] C. Rigollier, O. Bauer, and L. Wald, "On the clear sky model of the ESRA - European Solar Radiation Atlas with respect to the Heliosat method," *Solar Energy*, vol. 68, no. 1, pp. 33–48, 2000.

[157] J. P. G.-E. C. author, E. Martin, and F. Gascon, "Dart: a 3d model for simulating satellite images and studying surface radiation budget," *International Journal of Remote Sensing*, vol. 25, no. 1, pp. 73–96, 2004.

Chapter 6

Appendix

6.1 ISA case equations

6.1.1 Parallel case equation

The fundamental equation of the ISA can be expressed as:

$$F_{ji} = -\frac{1}{2A_j\pi}\frac{2A_jA_i}{|\vec{R}|^4}(\vec{n}_j.\vec{R})(\vec{n}_i.\vec{R}) \tag{6.1}$$

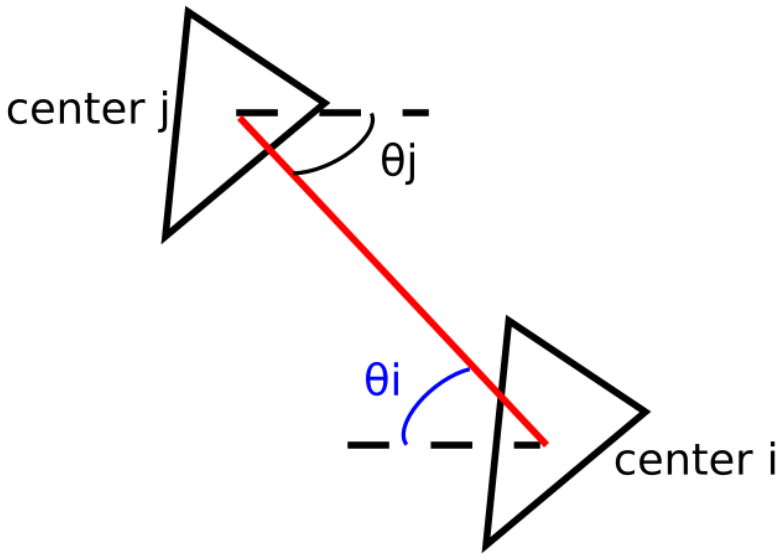

Figure 6.1: The parallel case

In the parallel case, as Figure 6.1 shows, θ_j equals θ_i. The triangles are superficially identical. The dot product in Eq. 6.1 changes to:

$$(\vec{n}_j.\vec{R})(\vec{n}_i.\vec{R}) = |\vec{R}|^2 cos(\pi - \theta_j)cos\theta_i \tag{6.2}$$

$$= -|\vec{R}|^2 cos^2\theta_i \tag{6.3}$$

The initial equation to calculate the view factor becomes:

$$F_{ji} = \frac{A}{\pi}\frac{1}{|\vec{R}|^2}cos^2\theta_i \tag{6.4}$$

As $|\vec{R}|$ equals $\frac{X}{cos\theta_i}$, Eq. 6.4 becomes:

$$F_{ji} = \frac{Acos^4\theta_i}{\pi X^2} \tag{6.5}$$

6.1.2 Perpendicular case

6.1.2.1 Case 1

The case is presented in Figure 6.2. The emitting surface moves along the bottom of the wall, and z_j always equals $\frac{\sqrt{3}}{6}$.

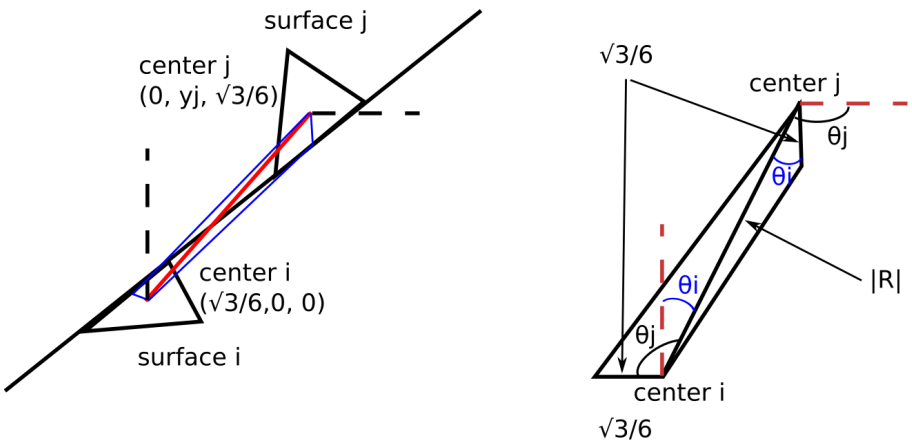

Figure 6.2: The perpendicular case 1

The angles θ_j and θ_i can be expressed with a polygon. Both of them equal

$$cos\theta = \frac{\frac{\sqrt{3}}{6}}{|\vec{R}|} \tag{6.6}$$

Eq. 6.1 than becomes:

$$F_{ji} = \frac{A}{12\pi|\vec{R}|^4} \tag{6.7}$$

The parameter $|\vec{R}|$ can be calculated by the coordinates of triangle center j:

$$|\vec{R}| = \sqrt{y_j^2 + 2 * (\frac{\sqrt{3}}{6})^2} \tag{6.8}$$

The final equation of view factor in this case simplifies to:

$$F_{ji} = \frac{A}{12\pi(y_i + \frac{1}{6})^2} \tag{6.9}$$

6.1.2.2 Case 2

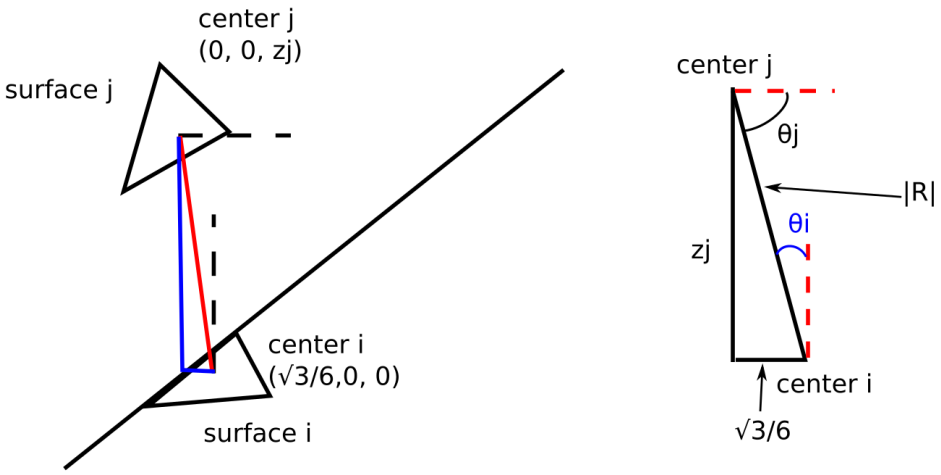

Figure 6.3: The perpendicular case 2

In this case, surface j moves along axis z, which suggests that y_i is 0. The sum of θ_j and θ_i is $\frac{\pi}{2}$. Their values can be calculated by:

$$|\vec{R}| = \sqrt{z_j^2 + \frac{1}{12}} \tag{6.10}$$

$$cos\theta_i = \frac{z_j}{|\vec{R}|} \tag{6.11}$$

$$cos\theta_j = \frac{\frac{\sqrt{3}}{6}}{|\vec{R}|} \tag{6.12}$$

The view factor calculation equation can be simplified to the following form:

$$F_{ji} = \frac{\sqrt{3}Az_j}{6\pi(z_j^2 + \frac{1}{12})^2} \tag{6.13}$$

This case is just a special boundary case, as the quadrant we study is only $z_j > \frac{\sqrt{3}}{6}, y_j > 0$. It could be concluded in the general case, the case 3.

6.1.2.3 Case 3

This is the general case for the perpendicular intersection scenarios. The source surface is located in the area $z_j > \frac{\sqrt{3}}{6}, y_j > 0$. The problem is illustrated in Figure 6.4.

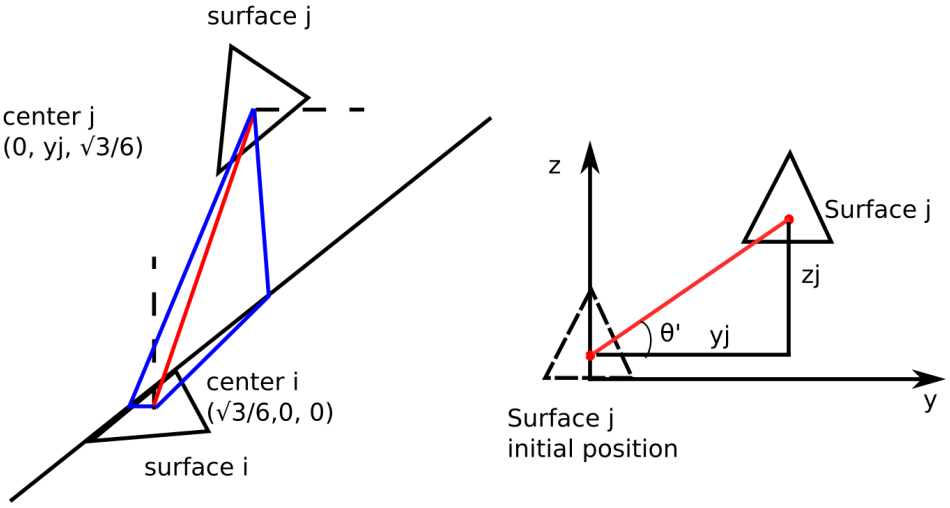

Figure 6.4: The perpendicular case 3

The angles θ_i and θ_j can also be found in the polygon as in case one. However, this time, their values are calculated by the equation in case 2:

$$|\vec{R}| = \sqrt{z_j^2 + y_j^2 + \frac{1}{12}} \tag{6.14}$$

$$cos\theta_i = \frac{z_j}{|\vec{R}|} \tag{6.15}$$

$$cos\theta_j = \frac{\frac{\sqrt{3}}{6}}{|\vec{R}|} \tag{6.16}$$

The equation 6.1 becomes:

$$F_{ji} = \frac{\sqrt{3}Az_j}{6\pi(z_j^2 + y_j^2 + \frac{1}{12})^2} \tag{6.17}$$

In our MATLAB code for this part, we used the cylinder coordinates for the location of triangle j. This means that the value z_j is represented by:

$$z_j = \frac{\sqrt{3}}{6} + y_j tan\theta' \tag{6.18}$$

where θ' is the azimuth angle. This leads to the final form of our equation to calculate the view factor:

$$F_{ji} = \frac{\sqrt{3}A(\frac{\sqrt{3}}{6} + y_j tan\theta')}{6\pi((\frac{\sqrt{3}}{6} + y_j tan\theta')^2 + y_j^2 + \frac{1}{12})^2} \tag{6.19}$$

6.2 Air absorption in different cases

6.3 The error of each patch with different view factor calculation methods

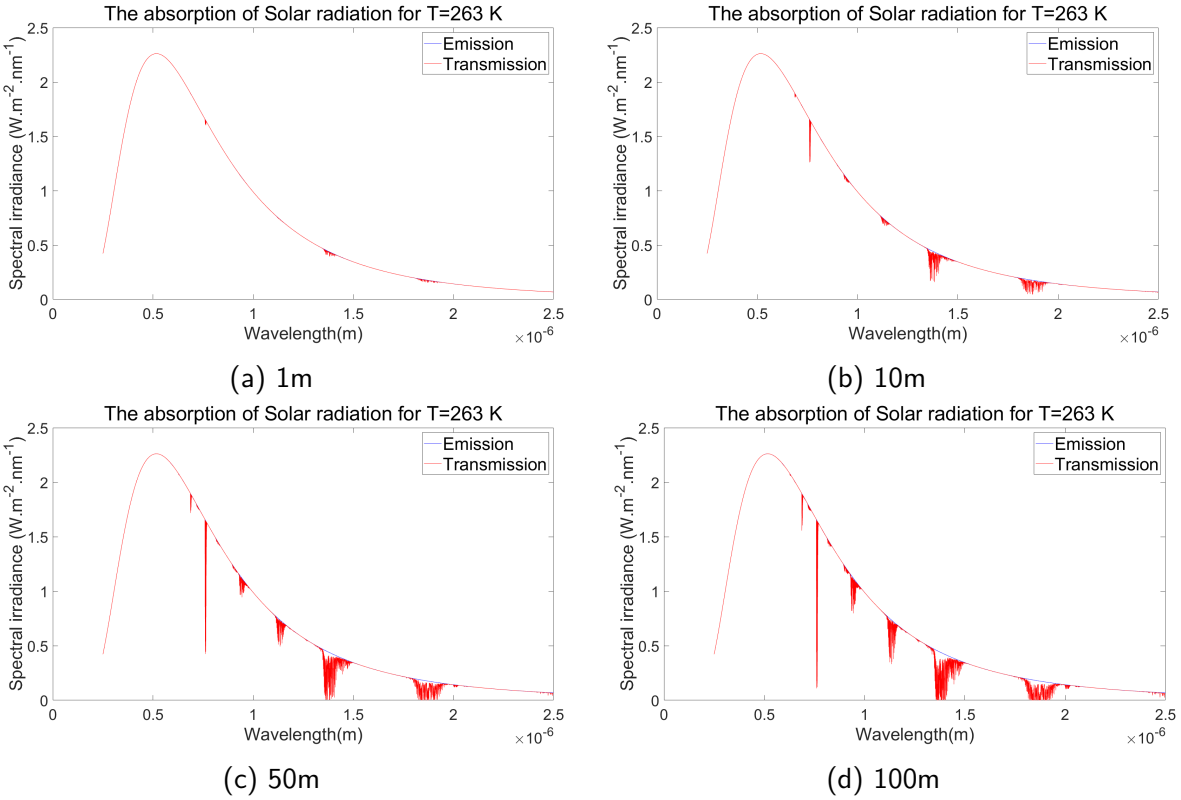

(a) 1m (b) 10m

(c) 50m (d) 100m

Figure 6.5: Transmission of Solar radiation for different air layer (at 263 K) thicknesses

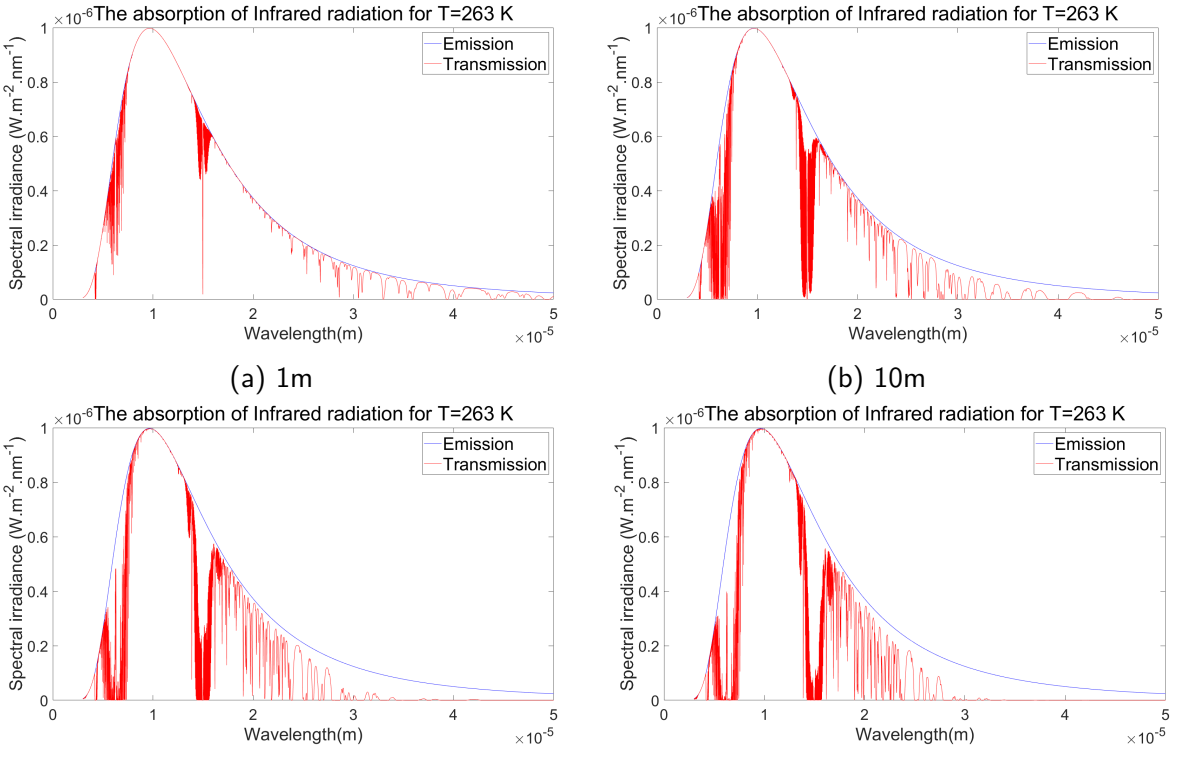

(a) 1m (b) 10m

(c) 50m (d) 100m

Figure 6.6: Transmission of infrared radiation for different air layer (at 263 K) thicknesses

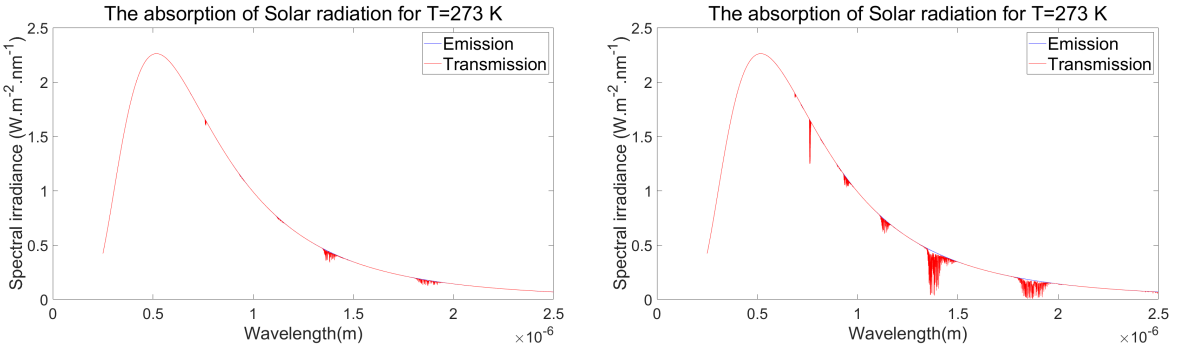

(a) 1m (b) 10m

(c) 50m (d) 100m

Figure 6.7: Transmission of Solar radiation for different air layer (at 273 K) thicknesses

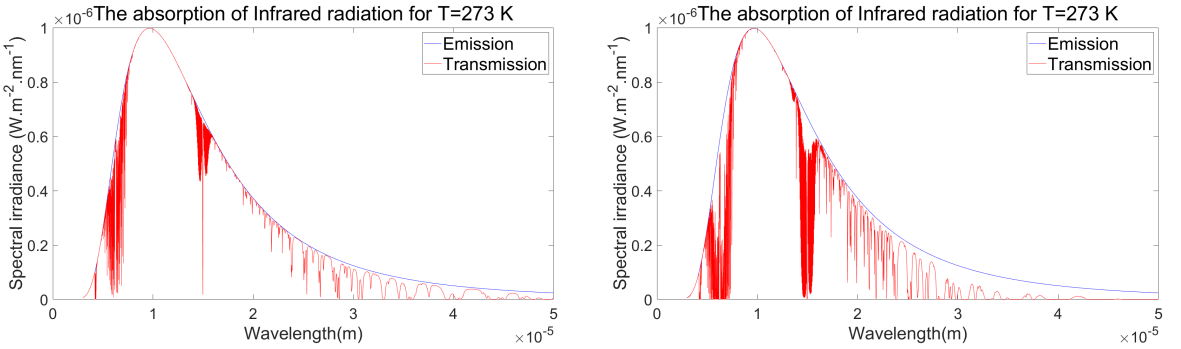

(a) 1m (b) 10m

(c) 50m (d) 100m

Figure 6.8: Transmission of infrared radiation for different air layer (at 273 K) thicknesses

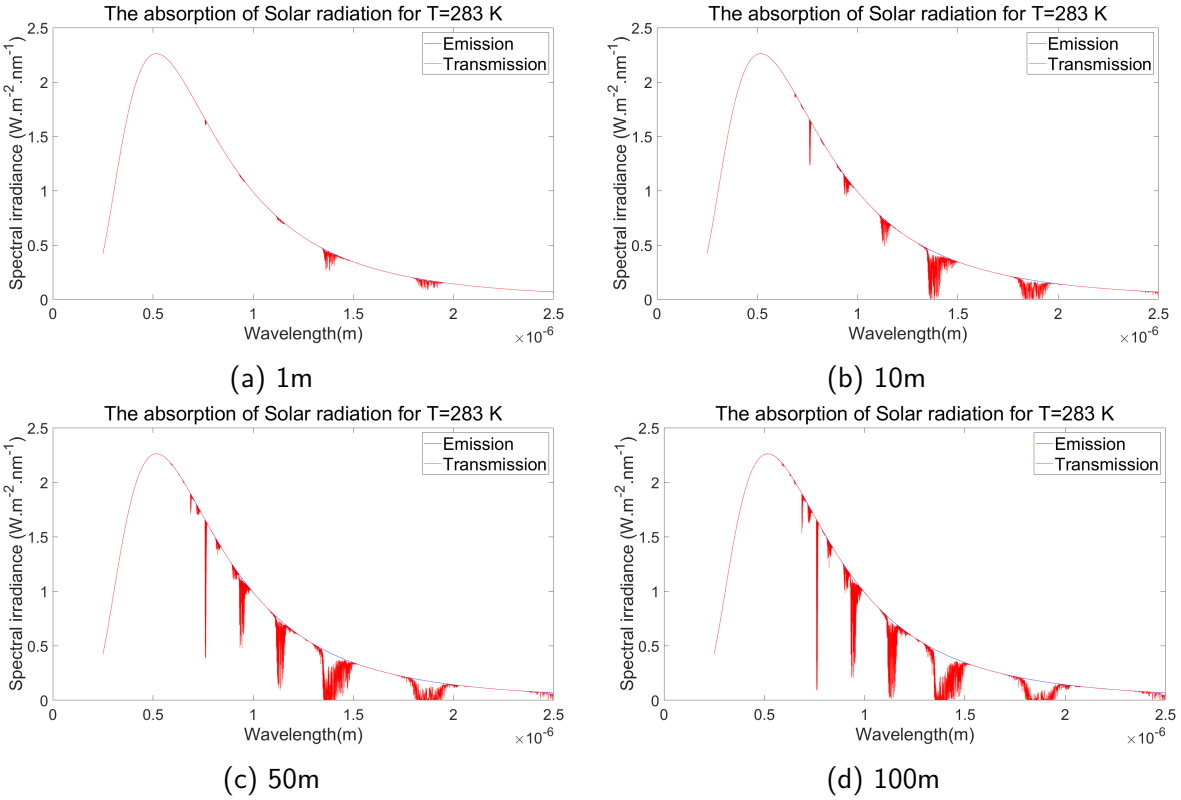

(a) 1m (b) 10m

(c) 50m (d) 100m

Figure 6.9: Transmission of Solar radiation for different air layer (at 283 K) thicknesses

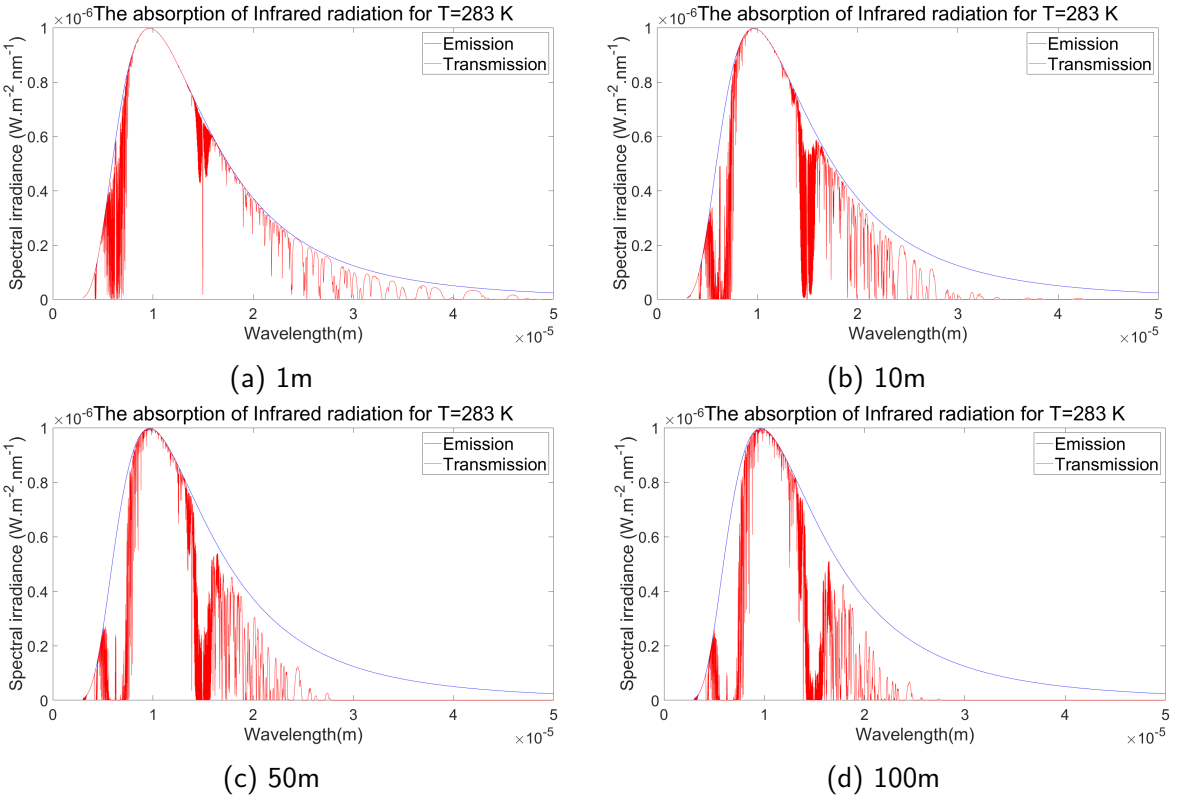

(a) 1m (b) 10m

(c) 50m (d) 100m

Figure 6.10: Transmission of infrared radiation for different air layer (at 283 K) thicknesses

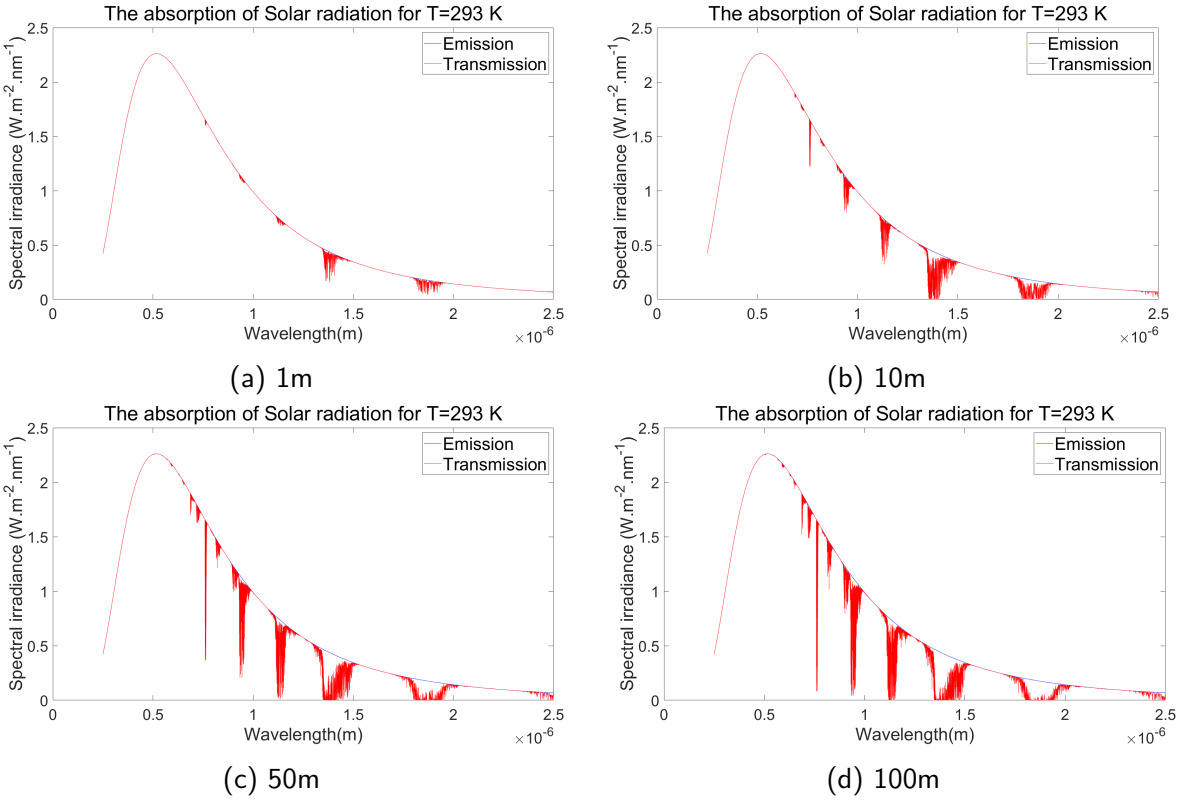

(a) 1m (b) 10m

(c) 50m (d) 100m

Figure 6.11: Transmission of Solar radiation for different air layer (at 293 K) thicknesses

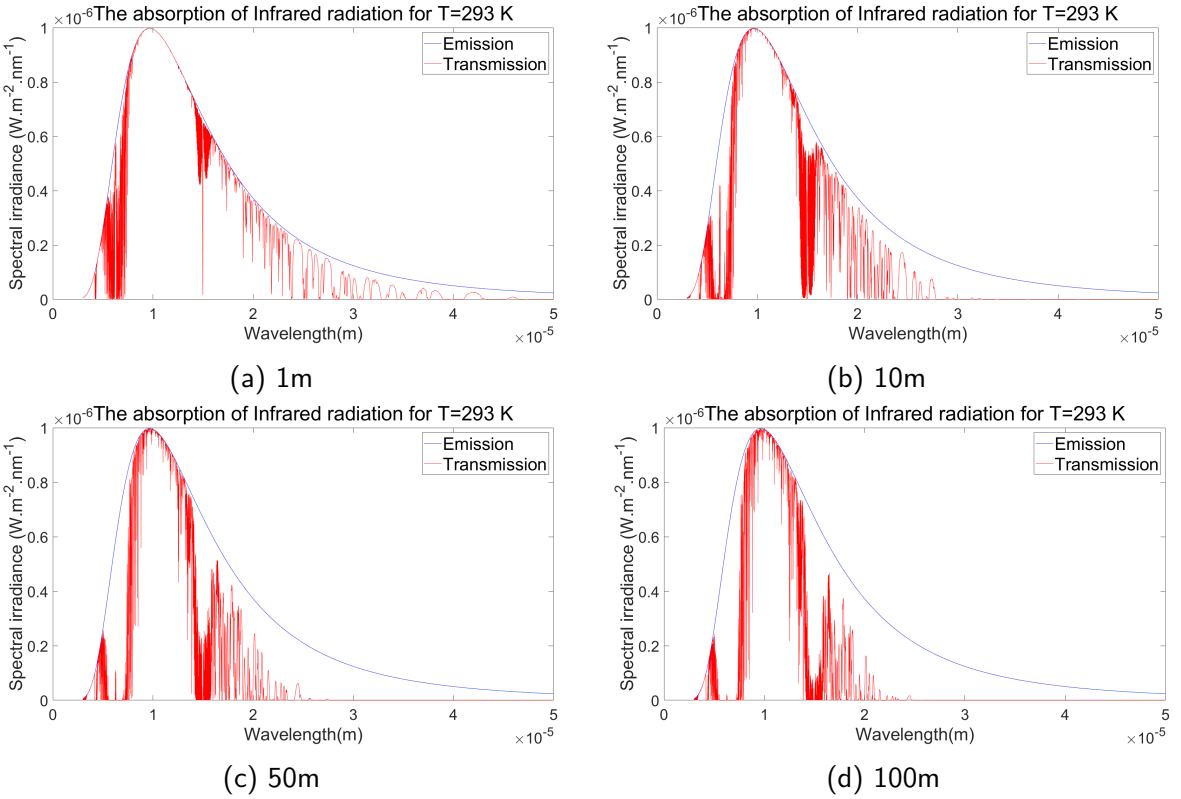

(a) 1m (b) 10m

(c) 50m (d) 100m

Figure 6.12: Transmission of infrared radiation for different air layer (at 293 K) thicknesses

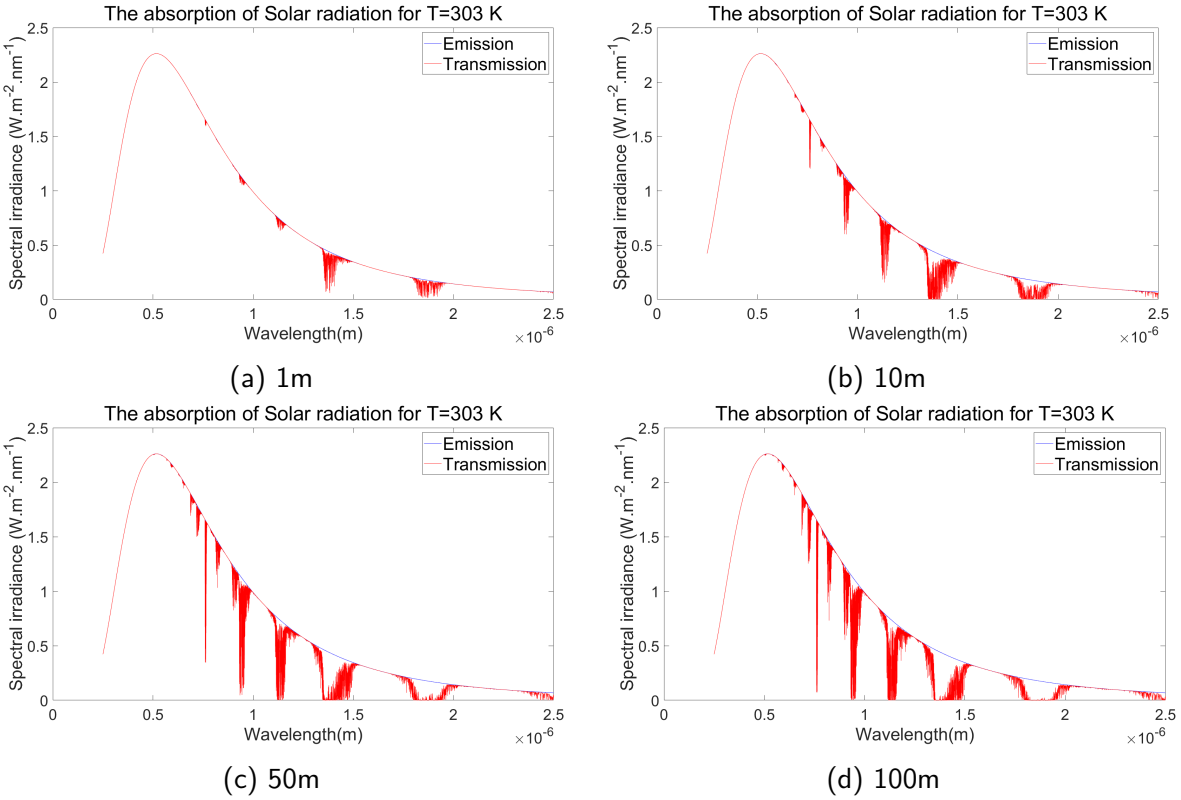

(a) 1m (b) 10m

(c) 50m (d) 100m

Figure 6.13: Transmission of Solar radiation for different air layer (at 303 K) thicknesses

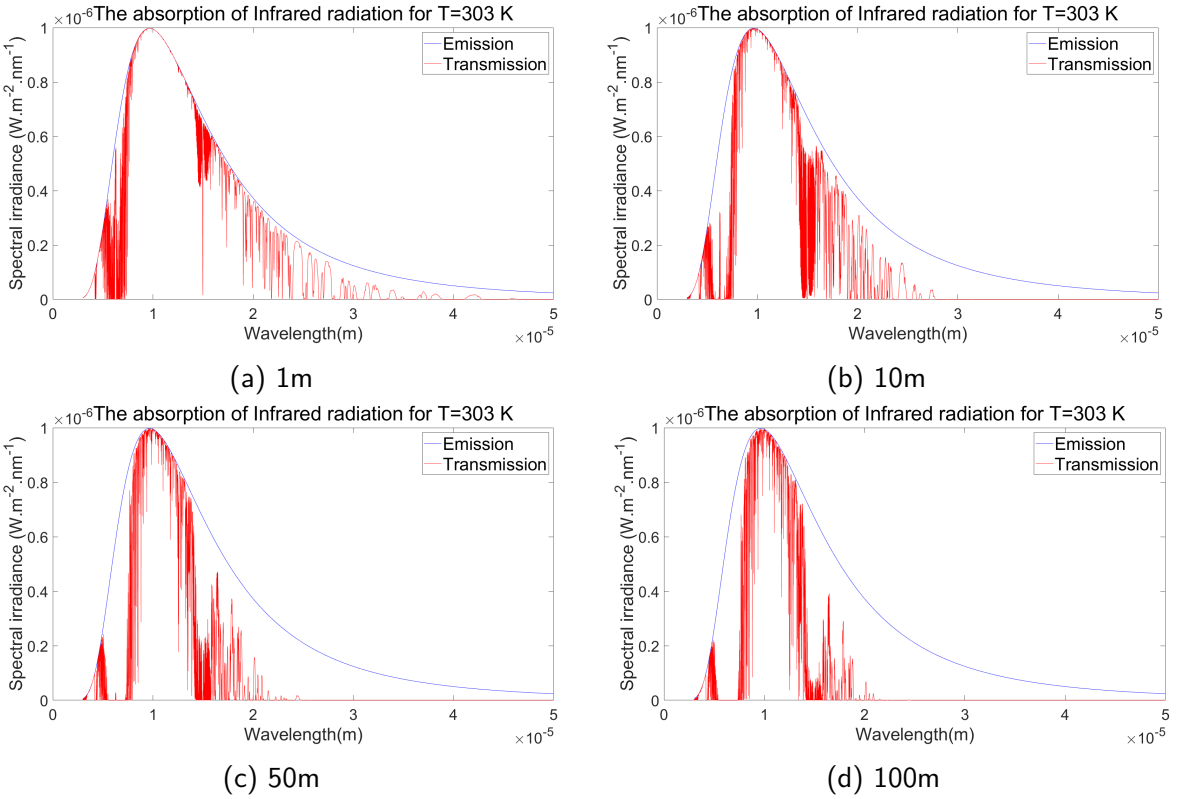

(a) 1m (b) 10m

(c) 50m (d) 100m

Figure 6.14: Transmission of infrared radiation for different air layer (at 303 K) thicknesses

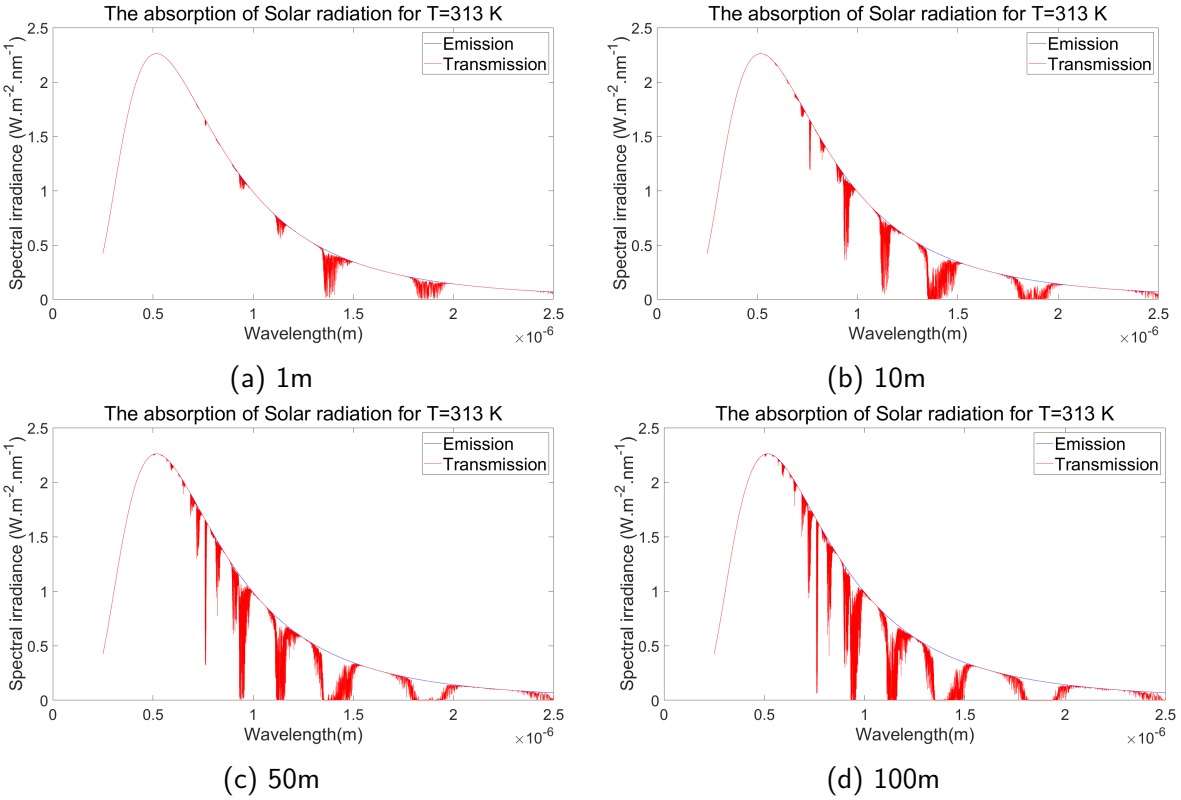

(a) 1m (b) 10m

(c) 50m (d) 100m

Figure 6.15: Transmission of Solar radiation for different air layer (at 313 K) thicknesses

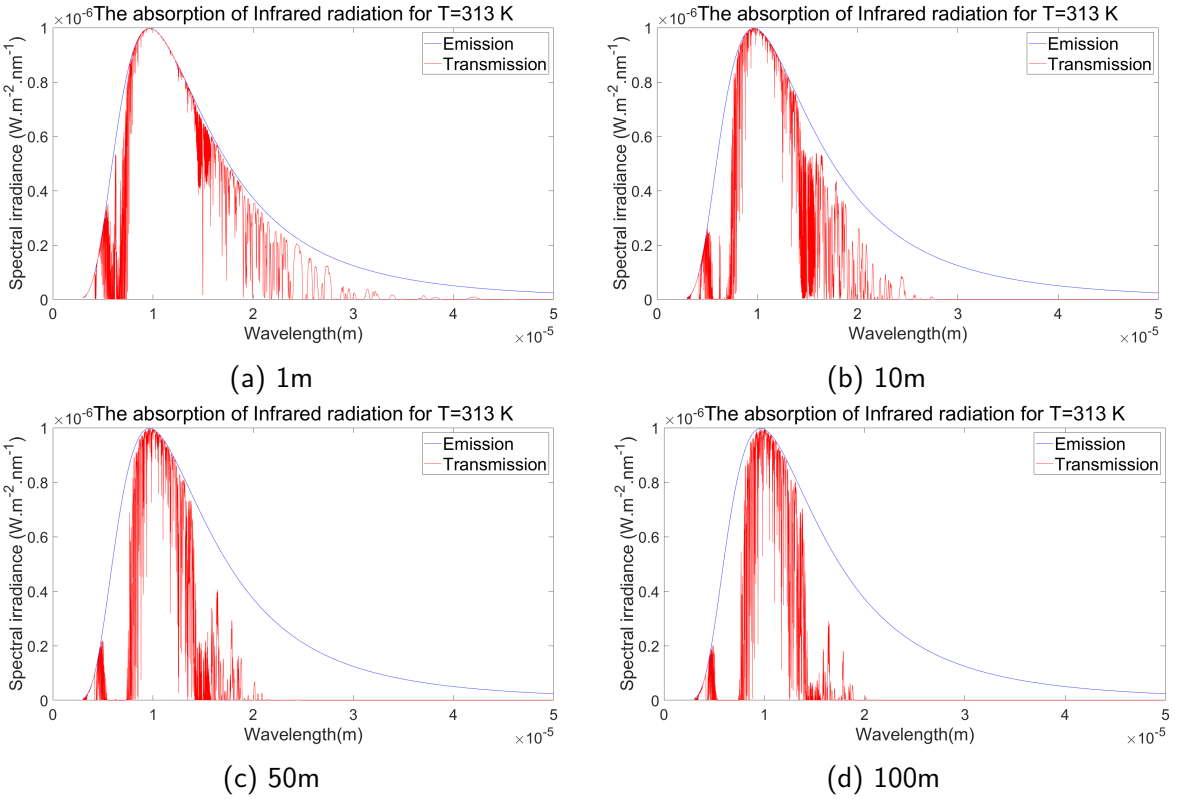

(a) 1m (b) 10m

(c) 50m (d) 100m

Figure 6.16: Transmission of infrared radiation for different air layer (at 313 K) thicknesses

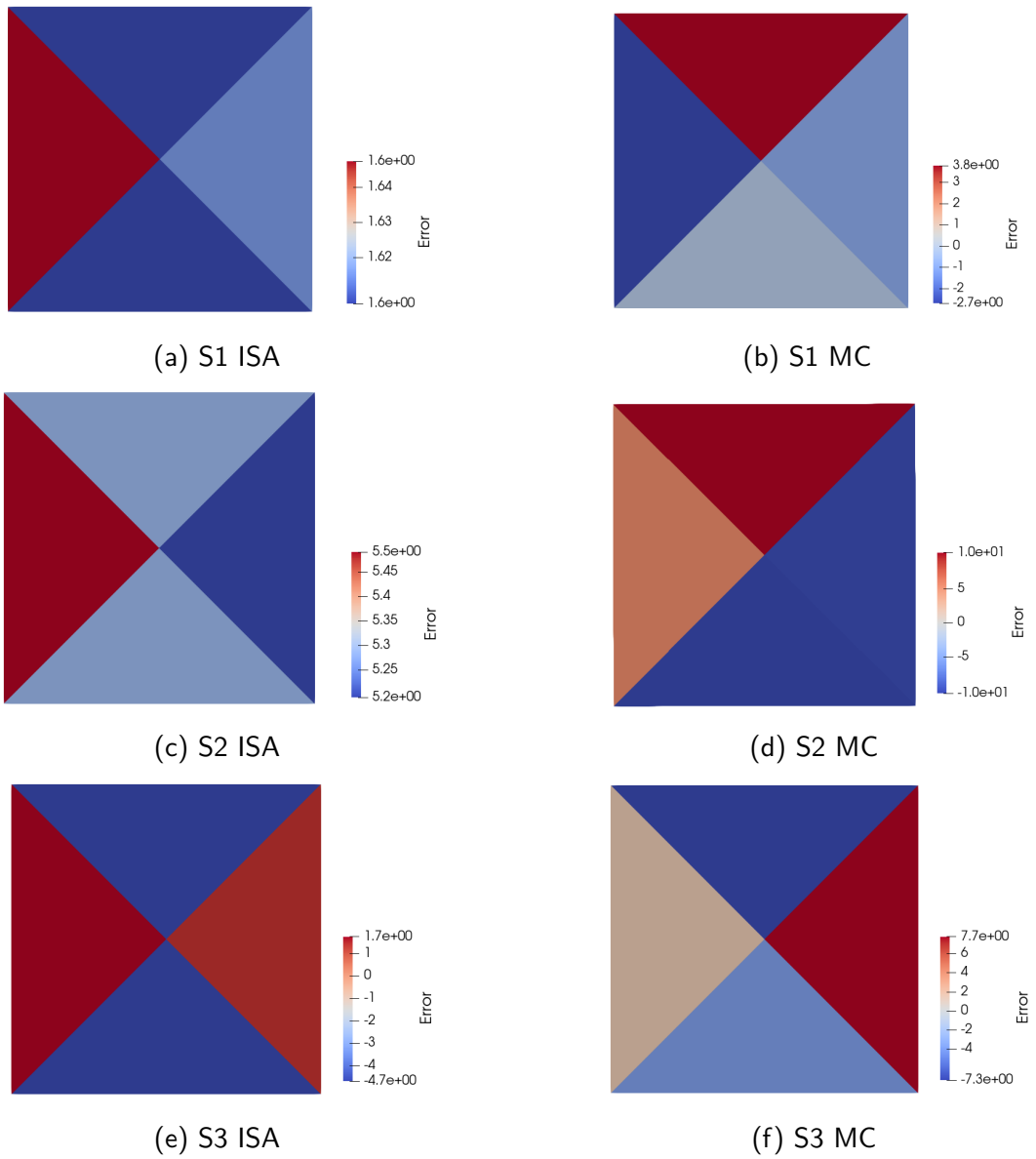

(a) S1 ISA (b) S1 MC

(c) S2 ISA (d) S2 MC

(e) S3 ISA (f) S3 MC

Figure 6.17: The percentage error of each patch on the three chosen surfaces(4 patches)

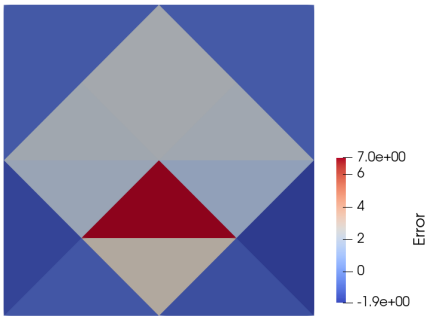

(a) S1 ISA

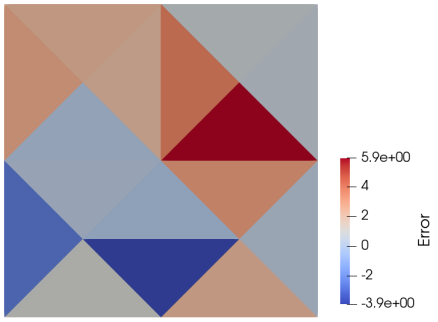

(b) S1 MC

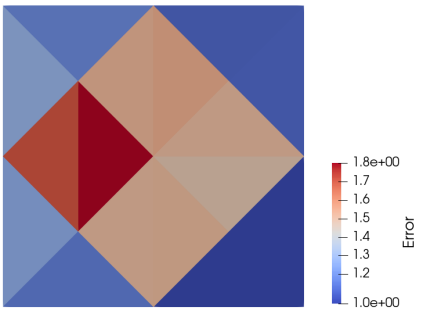

(c) S2 ISA

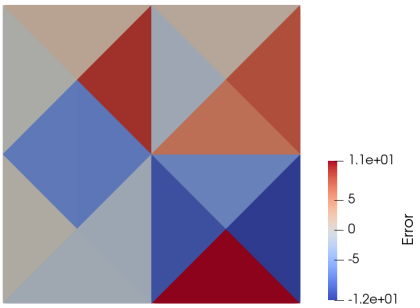

(d) S2 MC

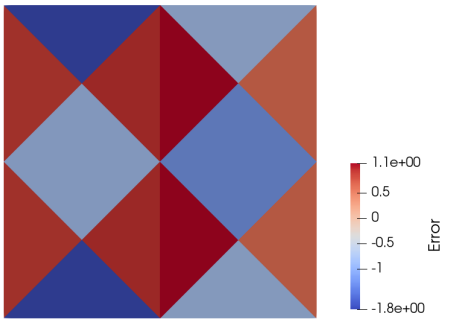

(e) S3 ISA

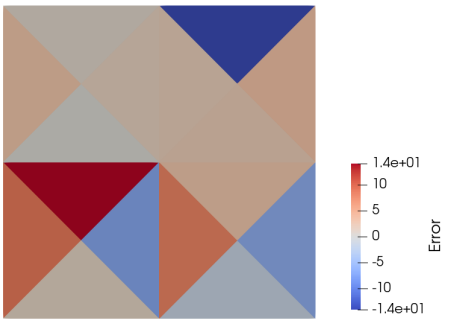

(f) S3 MC

Figure 6.18: The percentage error of each patch on the three chosen surfaces(16 patches)

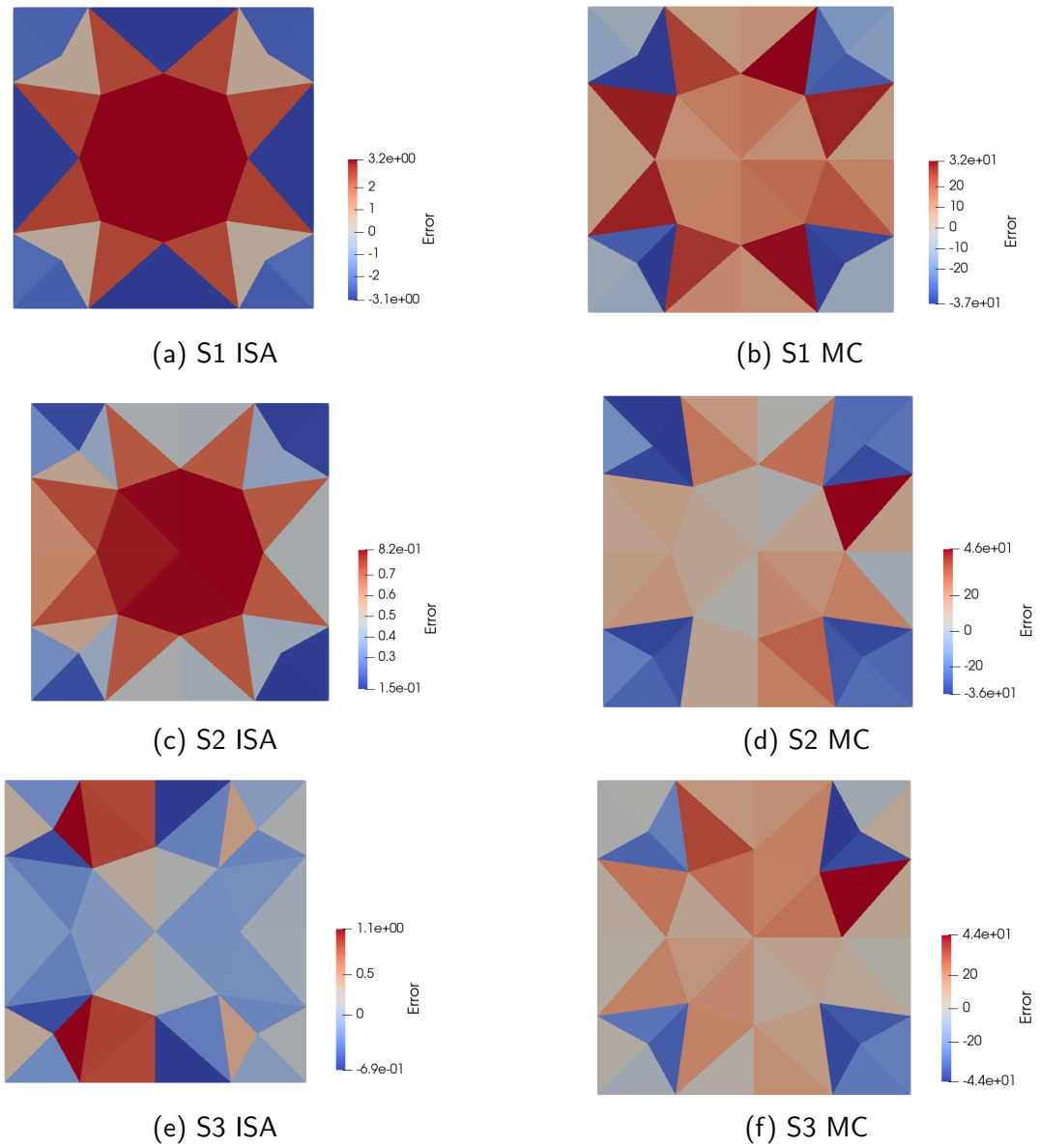

(a) S1 ISA (b) S1 MC

(c) S2 ISA (d) S2 MC

(e) S3 ISA (f) S3 MC

Figure 6.19: The percentage error of each patch on the three chosen surfaces(40 patches)